Elucidating the Evolution Histories of Giant Planets with *K2* and *TESS*

by

Liang Yu

B.S., Astronomy & Physics, Yale University (2014)

Submitted to the Department of Physics
in partial fulfillment of the requirements for the degree of

Doctor of Philosophy

at the

MASSACHUSETTS INSTITUTE OF TECHNOLOGY

June 2019

Author .....
Department of Physics
May 21, 2019

Certified by .....
Ian Crossfield
Assistant Professor of Physics
Thesis Supervisor

Accepted by .....
Nergis Mavalvala
Professor of Physics
Associate Department Head of Physics

Elucidating the Evolution Histories of Giant Planets with *K2* and *TESS*

by

Liang Yu

Submitted to the Department of Physics
on May 21, 2019, in partial fulfillment of the
requirements for the degree of
Doctor of Philosophy

Abstract

Giant planets play a fundamental role in shaping the architecture of planetary systems and the formation and evolution of smaller planets. Over the last few decades, over 1000 giant planets have been discovered outside the Solar System, yet many open questions remain about their formation and evolution histories. How do close-in giant planets – the so-called "hot Jupiters" – reach orbits as short as ~ 0.01 AU, where they could not have accreted their gaseous envelopes? How do many hot Jupiters attain radii larger than predicted by standard models of planetary structure? How do giant planets form, and what determines their final masses? To answer these questions, we need to amass a large and diverse population of giant planets that will allow us to uncover their evolution histories through both case studies and statistical analyses.

In this thesis, I focus on the discovery and characterization of unusual systems that may provide some insight into the pasts of giant planets. In particular, I present detailed analyses of systems that have not been subject to the overwhelming tidal forces capable of erasing many traces of orbital evolution. These include young systems that may still be actively undergoing planetary migration, giant planets with wider orbits than most hot Jupiters, and planets orbiting predominantly radiative stars, which exert weak tidal forces. Some of these newly discovered planets have spent their entire lifetimes near the stellar irradiation threshold at which giant planets become larger than expected, and are valuable in constraining planet inflation models. Some are also favorable targets for transit spectroscopy to study the atmospheres and chemical compositions of giant planets. Although these discoveries do not by themselves answer the questions posed above, they represent a necessary step toward that goal.

I also develop methods and tools to further expand our collection of known giant planets using data from the *K2* and *TESS* space missions. After demonstrating the traditional human vetting approach to planet candidate identification, I present two convolutional neural networks, `AstroNet-Triage` and `AstroNet-Vetting`, capable of automatically performing triage and vetting on *TESS* light curves. These are the first machine learning-based classifiers to be trained and tested on real *TESS* data,

and can rapidly and accurately eliminate false positives. These models not only allow humans to focus on the strongest planet candidates instead of false positives, but also identify candidates in an unbiased, homogeneous manner so as to facilitate planet occurrence rate calculations.

Thesis Supervisor: Ian Crossfield
Title: Assistant Professor of Physics

When I heard the learn'd astronomer,
When the proofs, the figures, were ranged in columns before me,
When I was shown the charts and diagrams, to add, divide, and measure them,
When I sitting heard the astronomer where he lectured with much applause in the lecture-room,
How soon unaccountable I became tired, and sick,
Till rising and gliding out I wander'd off by myself,
In the mystical moist night-air, and from time to time,
Look'd up in perfect silence at the stars.

Walt Whitman
When I Heard the Learn'd Astronomer, 1865

Contents

Acknowledgments **17**

1 Introduction **21**

1.1 The Mysterious Pasts of Giant Planets 23

1.2 The Era of Large-Scale Transit Surveys 28

1.3 This Thesis 31

2 PTFO 8-8695b: A Young Giant Planet Caught in Migration? **33**

2.1 Introduction 34

2.2 Time-series photometry 37

2.2.1 Overview 37

2.2.2 Ground-based observations of fading events 41

2.2.3 Ground-based observations of predicted occultations 44

2.2.3.1 Magellan observations 44

2.2.3.2 Spitzer observations 47

2.2.4 Departure from periodicity 52

2.3 Spectroscopic observations 53

2.3.1 Search for the Rossiter-McLaughlin effect 54

2.3.2 Projected rotation rate 57

2.3.3 Time variations in emission-line profiles 60

2.4 Discussion 65

2.4.1 Dust-emitting rocky planet 67

2.4.2 Starspots 68

2.4.3 Eclipses by a circumstellar disk or dust 69

2.4.4 Occultations of an accretion hotspot 71
2.4.5 Summary 73

3 The Road to More Data: *K2* and Data Processing Techniques 75
3.1 Introduction 76
3.2 *K2* Targets and Photometry 77
3.2.1 Target Selection and C16 Data Characteristics 77
3.2.2 Time-Series Photometry 77
3.2.3 Transit Search 79
3.3 Triage and Vetting 80
3.4 Discussion 84
3.4.1 Host Star Parameters 84
3.4.2 Characteristics of the Planet Candidate Sample 85
3.4.3 HD 73344 88
3.4.4 Conclusions 90

4 New Discoveries: Two Warm, Low-density Sub-Jovian Planets Orbiting Bright Stars in *K2* Campaigns 13 and 14 113
4.1 Introduction 114
4.2 Observations 117
4.2.1 *K2* Photometry 118
4.2.2 Ground-based Followup 119
4.2.2.1 Spectroscopic followup 120
4.2.2.2 Keck/NIRC2 Adaptive Optics Imaging 123
4.2.2.3 Ground-Based Photometry 126
4.3 Host Star Characterization 127
4.3.1 Spectral Analysis 127
4.3.2 Evolutionary Analysis 128
4.3.3 UVW Space Motions, Galactic Coordinates, and Evolutionary States of the Host Stars 128
4.3.3.1 HD 89345 128

4.3.3.2 HD 286123 . . . 129
4.4 Planet Characterization . . . 131
4.4.1 EXOFASTv2 Global Fit . . . 131
4.4.2 RV Analysis with `RadVel` . . . 138
4.5 Discussion . . . 138
4.5.1 Potential for Atmospheric Characterization . . . 138
4.5.2 The Evolutionary History of Close-in Giant Planets . . . 140
4.5.3 Constraining Planet Inflation Models . . . 143
4.5.4 HD 89345b and the Transition between Ice Giants and Gas Giants 145

5 Constraining Giant Planet Migration Pathways through Spin-Orbit Alignment and Stellar Companions 149
5.1 Introduction . . . 150
5.2 Observations . . . 152
5.2.1 K2 Light Curve . . . 152
5.2.2 Ground-Based Follow-Up . . . 154
5.2.2.1 Spectroscopy . . . 155
5.2.2.2 Keck/NIRC2 Adaptive Optics Imaging . . . 158
5.2.2.3 Ground-Based Photometry . . . 162
5.3 Host Star Characterization . . . 163
5.3.1 Spectral Analysis . . . 163
5.3.2 UVW Space Motion . . . 165
5.4 EXOFASTv2 Global Fit . . . 165
5.5 Discussion . . . 166
5.5.1 The Stellar Companion . . . 166
5.5.2 Spin-Orbit Alignment . . . 171
5.5.3 Future Prospects . . . 176

6 Identifying New Planet Candidates in the Era of *TESS*: Deep Learning 177
6.1 Introduction . . . 178

6.2 Data set 180
6.2.1 Identifying Threshold-Crossing Events 180
6.2.1.1 Light Curve Production 181
6.2.1.2 Transit Search 182
6.2.2 “Ground Truth" Labels 182
6.2.3 Preparing Input Representations 185
6.3 Neural Network 187
6.3.1 Architecture 187
6.3.1.1 Triage Mode 188
6.3.1.2 Vetting Mode 190
6.3.2 Training 192
6.4 Evaluation of Neural Network Performance 192
6.5 Application to Previously Unseen TCEs 197
6.6 Future Work 199

7 Conclusion **209**

List of Figures

1-1 Planet radius vs. stellar irradiation for giant planets with radii larger than 0.5 $R_{\rm J}$. 27

2-1 Dates of observations of fading events with the FLWO 1.2m and TRAPPIST 0.6m telescopes, along with previous observations by VE+12. . 37

2-2 Time-series photometry of fading events of PTFO 8-8695. 39

2-3 Same as Figure 2-2, but after "flattening" the out-of-transit flux variation by dividing by the best-fitting polynomial function of time. . . . 40

2-4 Depths and durations of the fading events of PTFO 8-8695. 44

2-5 Phase-folded light curves of PTFO 8-8695 based on all data from FLWO and TRAPPIST. 45

2-6 Multiband observations of fading events. 46

2-7 Near-infrared photometry of PTFO 8-8695 spanning the predicted time of occultation. 48

2-8 The expected occultation depth vs. dayside effective temperature for PTFO 8-8695. 49

2-9 *Spitzer* time-series 4.5 μm photometry of PTFO 8-8695 from 2012 Apr 28. 51

2-10 Close-up of the "transit" and "occultation" data, after rectification to unit flux outside of the events. 52

2-11 Transit timing residuals after subtracting the best-fitting linear and quadratic functions of epoch. 54

2-12 Perkins-Mimir 1.65 μm photometry of PTFO 8-8695. 55

2-13 Time variations of the CCF during the night of 2013 Dec. 11/12. . . 57

2-14 Same as Figure 2-13, but in this case an artificial signal of a transiting planet has been injected. 58
2-15 CCF for the pre-transit observation from Dec. 2013, along with the best-fitting model with $v \sin i_\star = 103$ km s^{-1}. 60
2-16 The Hα line profile of PTFO 8-8695 on 2013 Dec 12. 62
2-17 The Ca II H line profile of PTFO 8-8695 on 2013 Dec 12. 63
2-18 Spectral energy distribution of PTFO 8-8695 based on publicly available broadband photometry. 64
2-19 Illustrations of the five hypotheses discussed in Section 2.4. 67

3-1 *K2* photometry of HD 73344 ($V = 6.9$) and its planet candidate, EPIC 212178066.01. 79
3-2 Orbital periods of transit-like signals identified *K2* C16. 81
3-3 Phase-folded light curves of our 30 high-quality planet candidates, and their best-fit Mandel & Agol [190] transit models. 82
3-4 Phase-folded light curves of our 48 lower-quality planet candidates, and their best-fit Mandel & Agol [190] transit models. 83
3-5 Distribution of EPIC stellar $T_{\rm eff}$ for the entire C16 target sample and for our planet candidate sample. 86
3-6 Transit depth and stellar magnitude for planetary candidates from *K2* C16. 87
3-7 Approximate radii and incident insolation for our planetary candidates from *K2* C16. 88

4-1 Calibrated *K2* photometry for HD 89345 and HD 286123 and best-fit light curve models. 119
4-2 AO images and K_S-band contrast curves for HD 89345 and HD 286123. 125
4-3 Detrended ground-based light curve of HD 286123 and *K2* light curve phase-folded to the same ephemeris and overplotted with the transit model from our global fit in Section 4.4.1. 126
4-4 The RV time series of HD 89345. 132

4-5 Same as Fig. 4-4, but for HD 286123. 132
4-6 SED fits to HD 89345 and HD 286123 from EXOFASTv2. 133
4-7 The locations of HD 89345 solution 1, HD 89345 solution 2 and HD 286123 in the Kiel diagram. 134
4-8 Estimated SNR per transit for transmission spectroscopy, relative to that of WASP-107b, as a function of planetary mass for planets with 0.01 $M_{\rm J} < M_p < 0.5\ M_{\rm J}$. 141
4-9 Orbital eccentricity versus the log of the orbital period for transiting planets. 142
4-10 Radius-Mass diagram of transiting planets with measured masses and radii, for planets with $R_p > 0.3\ R_{\rm J}$. 146
4-11 Planet radius vs. stellar irradiation at the planets' orbits for transiting planets with measured mass and radius, for planets with $R_p > 0.3\ R_{\rm J}$. 147
4-12 Models of the orbital evolution of HD 89345b solution 1, HD 89345b solution 2 and HD 286123b for tidal quality factors $Q'_\star \sim 10^5$ and $Q'_{\rm planet} \sim 10^6$. 148

5-1 *K2* light curves of EPIC 246851721. 154
5-2 Doppler tomographic map for the transit of EPIC 246851721 b, as observed with MIKE/Magellan on 2018 Jan 04. 159
5-3 AO images and K_S-band contrast curves for EPIC 246851721, taken with Keck/NIRC2, and 2MASS J-band image showing EPIC 246851721 and its nearby companion.. 161
5-4 POSS-I red band, POSS-II red band, Pan-STARRS g band, and *K2* pixel-level images of EPIC 246851721. 162
5-5 Individual transit observations of EPIC 246851721 from DEMONEXT with the best-fit model from the global fit (Section 5.4) overplotted. . 164
5-6 The RV time series of EPIC 246851721 from TRES. 168
5-7 SED fits to EPIC 246851721 from EXOFASTv2. 169
5-8 The location of EPIC 246851721 in the Kiel diagram. 170

5-9 Polar plot showing all planets with known obliquities. 172
5-10 Absolute values of the projected obliquities, λ, of Jovian planets as a function of scaled orbital distance, a/R_*, for systems with $T_{\rm eff} > 6100$ K and $T_{\rm eff} < 6100$ K. 173
5-11 Lomb-Scargle periodogram of the *K2* light curve of EPIC 246851721 b, with transits masked out. 175

6-1 Phase-folded, depth-normalized representations of light curves of TCEs in the following four categories: PC (planet candidates), EB (eclipsing binaries), V (stellar variability) and IS (instrumental artifact). 186
6-2 The architecture of `AstroNet-Triage` (identical to that of the best-performing neural network from Shallue & Vanderburg [253]). 189
6-3 Same as Fig. 6-2, but for `AstroNet-Vetting`. 191
6-4 Precision-recall curve of our neural network in both triage and vetting modes. 194
6-5 Histogram of predictions on the test set by `AstroNet-Triage` and `AstroNet-Vetting`. 195
6-6 Phase-folded light curves of our 25 highest-quality planet candidates from Sector 6, along with their TIC IDs. 198

List of Tables

2.1 Best-fitting parameters of fading events (see Eq. 2.1). 38
2.2 Best-fitting parameters of phase-folded light curves (see Eq. 2.2) . . . 38

3.1 Candidate Parameters for HD 73344 90
3.2 High-quality candidate parameters 92
3.3 Plausible candidate parameters 94
3.4 Systems with secondary eclipses 98
3.5 Systems showing periodic variability 106

4.1 Stellar parameters of HD 89345 and HD 286123 from the literature and spectroscopy 117
4.2 Radial velocities for HD 89345 122
4.3 Radial velocities for HD 286123 122
4.4 Median values and 68% confidence intervals for the physical and orbital parameters of the HD 89345 and HD 286123 systems 135

5.1 Parameters of EPIC 246851721 from the literature and spectroscopy 155
5.2 TRES radial velocities 157
5.3 Median values and 68% confidence interval for EPIC 246851721 . . . 167
5.4 Median values and 68% confidence interval for the Telescope parameters of EPIC 246851721 168

6.1 Ensembled results achieved on the test set 193
6.2 New TCEs from Sector 6 with the highest likelihood of being planet candidates and manually assigned PC labels 201

Acknowledgments

As I sit down to write this thesis, scenes from my teenage days in South Africa flash before my eyes one by one. I see myself rummaging through a pile of discarded textbooks I had found at my dad's former university. It was from this yellowed, dusty pile of books that I learned calculus. I see myself standing in a corner of our garage, trying to recreate an experiment from my chemistry textbook with whatever makeshift reactants I could find in the house (in hindsight, that was perhaps not safe at all). I see myself poring over my first application for a research internship. With no research experience or mentor whatsoever, I had no idea how to write such an application, and instead wrote a poetic description of the moments in which I had felt awestruck by the beauty of science. I didn't get the internship, of course. In those days, I liked to sit in the back of an empty classroom after school with a science book. And while reading, I would dream of pursuing an education outside my country, where merely being able to study science was a luxury. But even then, I did not dare dream of receiving a PhD in physics at a school like MIT. When I think of myself now, and of the teenage girl sitting alone in that high school classroom, I still cannot believe how far I've come.

This incredible journey would not have been possible without the many individuals who supported and guided me along the way. It all started with my family: my parents, who implanted in me a passion for science and courage to pursue my dreams, and believed in me even when I didn't believe in myself; and my younger brother, who kept me company all these years and grew to share my nerdy sense of humour. After coming to grad school, I met my husband, Dan, who spent countless hours studying for quals with me and made MIT feel like home. All the difficult times we've survived

together are now special memories I'll carry with me for the rest of my life.

I'm also greatly indebted to my mentors and research advisers. Ian Crossfield, my thesis adviser, has only known me for two years, but I've come to see him as a friend as well as an adviser. He helped me get back on track very quickly after numerous disruptions to my PhD and gave me ample freedom and support to try out new ideas. Ian not only approves of all the time I spend singing opera instead of doing research, but also came to my concerts to cheer me on. I could not have asked for a better adviser. My academic adviser, Deepto Chakrabarty, has also played an irreplaceable role during my time at the MKI. When I felt lost, frustrated, or depressed, Deepto always checked in on me to make sure that I was all right, and offered me sage advice whenever I needed it. Scott Gaudi, who adopted me unofficially as his student during my third year, offered me words of encouragement and taught me many invaluable skills as a scientist. Sara Seager kindly reached out to me after the abrupt departure of my first adviser, and took time out of her busy schedule to supervise me until I found a permanent adviser. Saul Rappaport always made me feel welcome in his office, whether to talk about science or just to look at the photos he took during his trips to China and Africa. Nevin Weinberg has served on both my oral exam committee and thesis committee, and guided me towards my goals with benevolence and compassion. I would also like to thank Al Levine for helping me prepare for my oral exam. And I would not have gotten into MIT in the first place without three important mentors from my undergraduate years: Daisuke Nagai, Andrey Kravtsov and Debra Fischer. Daisuke, in particular, made a lasting impact as my senior thesis supervisor. His passion inspired me to pursue a PhD, and his kindness helped me achieve that goal.

During my time at the MKI, I came to know many wonderful graduate students. I want to thank Ani Chiti, my first and closest friend here, who taught me by example to live in gratitude and optimism; Stephanie O'Neil, who maintained an endless supply of candies whenever I felt like ranting about work and life; Lu Feng, Uchupol Ruangsri and David Hernandez, who helped me navigate my first days at MIT; Champ Somboonpanyakul, Michael Calzadilla and Sherry Guo, for the hilarious games of

Dungeons and Dragons that we played in the conference room; Alex Ji, Tom Cooper, Keaton Burns, Aaron Ewall-Wice, Greg Dooley and Abraham Neben, who administered my mock oral exams and never begrudged me their kindness and wisdom; Nick Mehrle and David Berardo, my fellow research group members; Halston Lim, for the beautiful music that we played together; Ryan McKinnon, who survived classes and interviews with me; Honggeun Kim, Kaley Brauer, Kaitlyn Shin, Mason Ng and Calvin Leung, for distracting me with Pokémon GO. I am also grateful to have a number of beloved friends outside the department. I thank Jennifer Cheung, Andrea Scarinci, Brandon Araki, Melina Sánchez, Claire Boine, Alisa Knizel, Xingchen Zhou and Wojciech Osowiecki for always being there for me and for lending me your ears and your shoulders to lean on. Of course I cannot forget Marna Wessels and AJ du Plessis, who treated me like family throughout my time at MIT.

It has been a joy to work with many brilliant colleagues in the field. I learned a lot from each and every one of them while collaborating on projects. Some have become friends and role models to me over the years. I'd like to thank Andrew Vanderburg, Chelsea Huang, Diana Dragomir, Jenn Burt, Natalia Guerrero, Avi Shporer, Joey Rodriguez, George Zhou, Zach Berta-Thompson, Jason Eastman, Laura Kreidberg, David Latham, Allyson Bieryla, Sam Quinn, Chris Shallue, Steven Villanueva, Josh Schlieder, David Ciardi, Molly Kosiarek, and many others. Although our time together has been short, the postdocs in my group, Elisabeth Matthews and Tom Evans, have patiently sat through many of my practice talks and given me plenty of good advice. I'm also grateful for that unforgettable summer at Totsa Total Oil Trading in Geneva, Switzerland and my coworkers there, who had great faith in me and helped pave the way for my machine learning projects.

Many thanks to the administrators at the MKI and in the physics department. Cathy Modica knew me by name right from the beginning. I knew that I could always turn to her to talk about anything, and that she would listen patiently and sympathetically. I will also miss Debbie Meinbresse and the administrative staff on the second floor of Building 37, who never failed to put a smile on my face.

My time at MIT would not have been complete without karate. I would like to

thank all my friends from Isshinryu Karate-do at MIT and my sensei, Yelena Tsitkin, who trained me for the last five years from white belt to almost black belt. Music has also been an integral part of my life, and brought me hope and joy when times were hard. I am really fortunate to have been able to pursue that passion at MIT, especially in the last three semesters. I want to thank the MIT Chamber Chorus, its conductor Bill Cutter, and my singing teachers Kerry Deal and Emily Romney. I am grateful to have met a number of friends through singing: Piotr Suwara, Srinivasan Raghuraman, Oron Propp, Alexey Balitskiy, Thao Nguyen, and Carles Boix, among others, filled my last days of grad school with laughter. I will always cherish the memories of our long, amusing lunch conversations, the camaraderie we built up during many hours of rehearsal, the adventure of planning and performing our very own show, and the standing ovation we received at the end of it.

Chapter 1

Introduction

> *"There are countless suns and countless earths all rotating around their suns in exactly the same way as the seven planets of our system. ... The countless worlds in the universe are no worse and no less inhabited than our earth. ... Open the door through which we can look out into the limitless, unified firmament composed of similar elements and show us that the other worlds float in an ethereal ocean like our own! Make it plain to us that the motions of all the worlds proceed from inner forces and teach us in the light of such attitudes to go forward with surer tread in the investigation and discovery of nature! Take comfort, the time will come when all men will see as I do."*
>
> —Giordano Bruno, *De l'infinito, universo e mondi*, 1584

Few branches of the sciences have generated as much curiosity, excitement, and speculation as the search for other worlds in the cosmos. Over thousands of years, human beings have looked up at the night sky and wondered what sort of planets, possibly similar to our own, might exist out there. Until recently, these speculations were based on observations of a single sample: our own Solar System. Many, like Giordano Bruno, believed that all planetary systems looked like the Solar System. Planets were thought to orbit their host stars on coplanar, nearly circular, prograde

orbits. By the 18th century, a widely accepted model had emerged to explain the formation and evolution of planetary systems [270, 150, 170]: stars form in dense clouds of nebulous material, which collapse into disks that rotate in the stars' equatorial planes and eventually give birth to orderly sets of planets. This formation picture is further supported by the compositions of the Solar System planets. Near the Sun, the temperature is high enough to prevent the condensation of water ice and other substances into grains, while icy materials exist in abundance in the outer Solar System, so that protoplanets can form large enough cores to accrete massive gaseous envelopes before the gas disk dissipates. As a result, inner planets are small, dense and metal-rich, while lower density gas and ice giants lie farther out from the Sun [e.g. 174, 175, 176].

The discovery of the first exoplanets – planets outside our Solar System – immediately uprooted all existing models of planet formation. The first exoplanet known to orbit a main sequence star is 51 Peg b, a gas giant [196]. But instead of orbiting its host star beyond a few AU like the Solar System's giant planets, 51 Peg b has an orbital semi-major axis of just 0.05 AU and an orbital period as short as 4.2 days. 51 Peg b opened the door to the discovery of many more similar gas giants on extremely close-in orbits – known as "hot Jupiters" – which forced astronomers to accept that giant planets can exist at such short distances from their stars, where they could not have accreted their gaseous envelopes [233]. Since then, we have gone on to discover and confirm nearly 4000 exoplanets, many of which harbor even more surprises than the original hot Jupiter. We have found planets that orbit their host stars on retrograde orbits (e.g. WASP-17b [8]), polar orbits (e.g. WASP-79b [3]), extremely eccentric orbits (e.g. HD 20782b [217]), and ultra-short-period orbits (e.g. KOI-1843.03 [236]). What we now know to be the most common type of planet in the universe – planets between the size of Earth and Neptune [e.g. 193] – does not even have an analog in the Solar System. The existence of so many planetary systems whose formation cannot be explained by our Solar System-centric theories points to the existence of much more diverse planet formation and migration pathways than previously believed.

Clearly, much remains to be understood about the evolution histories of planets. Fortunately, we have at our disposal the necessary techniques and tools to answer these questions. The field of exoplanet research has undergone explosive growth over the last few decades. Large-scale transit surveys, including *Kepler* [158, 34], *K2* [136] and *TESS* [241], have provided us with an unprecedented volume of photometric observations of exoplanets. Transit surveys are complemented by powerful ground-based telescopes capable of spectroscopically confirming transiting planet candidates and characterizing their host stars. Soon we will be able to amass a large and diverse enough population of known planets to help us piece together the mysterious pasts that led to the perplexing array of properties we observe today.

This thesis represents a step towards the solution of this planetary evolution puzzle. I focus specifically on giant planets, which I define to be planets with masses $\gtrsim 0.1$ $M_{\rm J}$. To date, over 1000 extrasolar giant planets have been confirmed and characterized by spectroscopic and photometric methods. These planets play a fundamental part in shaping the architecture of planetary systems and the evolution of terrestrial planets. Even though they are the oldest known class of transiting planets, many open questions remain about the processes that lead to their present-day orbital and compositional traits. Uncovering their evolutionary histories would help answer some of the most pressing questions in modern astronomy: How do hot Jupiters reach their extremely close-in orbits? How do many of the known transiting hot Jupiters attain radii larger than expected by standard models of giant planet formation? What is the formation mechanism of gas giants? In our quest to answer these questions, data from large transit surveys will play an invaluable role.

1.1 The Mysterious Pasts of Giant Planets

Our inital understanding of giant planet formation was based completely on observations of our Solar System. All four Solar System giants have massive hydrogen/helium envelopes, and exist beyond the snow line – the radial distance in the Solar nebula beyond which it is cold enough for volatile compounds such as water, ammonia,

methane, carbon dioxide and carbon monoxide to condense into solid ice grains. It is commonly understood that giant planets form when solid materials coagulate into rocky cores and subsequently accrete massive gaseous envelopes, and that beyond the snow line, solid materials are sufficiently abundant for giant planet formation to happen. The locations of the Solar System giants beyond the snow line plausibly suggest that they may have formed and remained near their current orbits, and that migration did not play a large role in their evolution histories [e.g. 280]. It was therefore a surprise when 51 Peg b was discovered [196]. It became clear that theories of giant planet formation needed revision. Although *in situ* formation has been considered as a possibility [30, 32, 23], the details and feasibility of *in situ* formation remain unclear (see Dawson & Johnson [84] for a comprehensive review). A more straightforward explanation for the existence of hot Jupiters is that they formed farther out beyond the snow line, and subsequently migrated inward to their present orbits. With the discovery of more hot Jupiters, migration has become an essential component of any planet formation theory.

The mechanism behind planetary migration remains the subject of much contention. Theories attempting to explain giant planet migration fall into two categories: smooth disk migration caused by planet-disk interactions [e.g. 113, 181, 6], and high-eccentricity migration via gravitational interactions between the planet and other planets or stars in the system [e.g. 238, 97]. During disk migration, the planet exchanges angular momentum with the gaseous protoplanetary disk by perturbing and deflecting gas in the disk. The net torque tends to shrink the planet's orbit. High-eccentricity migration, on the other hand, is a violent, two-step process: first, a companion perturbs the planet onto an eccentric orbit via mechanisms such as planet-planet scattering [e.g. 238, 294], Kozai-Lidov cycles [162, 178] or secular chaos [e.g. 299]; then, the planet tidally dissipates its orbital energy through interactions with the central star during close passages at periapse. Strong tides raised on the planet dissipate energy while conserving the orbital angular momentum, eventually leading to orbital circularization.

The three different origin scenarios (*in situ* formation, disk migration and high-

eccentricity migration) should leave different imprints in the properties of giant planet systems, most notably in their eccentricity and stellar obliquity distributions. *In situ* formation and disk migration should result in circular orbits whose angular momentum vectors are well-aligned with the stars' spin angular momentum, while high-eccentricity migration usually alters the eccentricities and angular momentum vectors of planets, leading to some planetary systems with eccentric and/or misaligned orbits. These signatures can, in theory, be used to distinguish between the different migration pathways, but in reality, most known hot Jupiter orbits are consistent with circular and aligned with stellar rotation. It appears that tidal dissipation can circularize hot Jupiters' orbits on relatively short timescales [e.g. 95], while also erasing stellar obliquities [e.g. 251, 296]. To circumvent this tidal dissipation problem and catch a glimpse of the primordial eccentricity and obliquity distributions of giant planet systems, we can search for either young giant planet systems that have not yet had time to tidally interact with their stars (see Chapter 2), or systems that experience weaker tidal effects, e.g. systems with large orbital distances (Chapter 4) or predominantly radiative host stars (Chapter 5). The detection of such planets is intrinsically difficult because young stars tend to be active, far-out planets have low transit probabilities, and radiative host stars have large radii that dimish the sizes of transit signals. This thesis presents a number of valuable new detections.

Another unsolved mystery is the formation mechanism of the so-called "inflated" hot Jupiters. We now know of many transiting hot Jupiters with radii larger than 1.2 $R_{\rm J}$, some reaching almost 2 $R_{\rm J}$ [e.g. 126, 8], even though standard models of planetary structure predict that giant planets should never have radii larger than $\sim 1.2\ R_{\rm J}$ by the time they are several billion years old [e.g. 100]. It remains unclear how inflated planets can exist around mature main sequence and even old, evolved stars, long after the planets should have lost much of their initial heat from formation. One clue is the positive correlation between planet radius R_p and stellar irradiation f (see Fig. 1-1). Radius inflation is observed to be common at irradiation levels above $\sim 2 \times 10^8$ erg s^{-1} cm^{-2}, but mostly absent below this threshold [86, 202]. These observations hint that hot Jupiter inflation is somehow intimately linked to

the amount of stellar irradiation incident on the planet. As a result, many of the proposed hot Jupiter inflation mechanisms invoke irradiation. Following Lopez & Fortney [188], these can be divided into two categories: in class I mechanisms, stellar irradiation is transported to the planet's interior, causing it to expand via adiabatic heating [e.g. 13, 24]; in class II mechanisms, no energy is deposited in the interior, but the planet is able to retain its heat from formation and contract more slowly (delayed contraction, e.g. [51]). Alternatively, some proposed mechanisms suggest that tidal heating, rather than stellar irradiation, provides the heat necessary to inflate planets [e.g. 31, 13, 260]. But, as noted by Socrates [260], no matter what the mechanism, there must be a large range of heating rates, likely spanning 4-5 orders of magnitude, to explain the observed range of inflated radii. A first step to solving the giant planet inflation problem is refining our understanding of the $R_p - f$ correlation. As we can see from Fig. 1-1, the correlation between R_p and f is much less well defined at the low stellar irradiation end. This corresponds to the regime of longer periods and smaller (and likely fainter) host stars, where it is much harder to detect planets. Filling out this region of parameter space will help clarify the role of stellar irradiation in planet inflation.

Furthermore, we have yet to understand the details of giant planet formation (see Lissauer & Stevenson [183] for a detailed review). A widely accepted model that offers a natural explanation for the formation of rocky planets, ice giants like Uranus and Neptune, and gas giants like Jupiter and Saturn is the core accretion model [e.g. 231]. In the core accretion scenario, the initial phases of giant planet formation involve the coagulation of solid material into a planetary core, similar to the process of terrestrial planet formation. Once the planetary core is large enough (typically $\sim 10\ M_\oplus$) that the envelope can no longer maintain a purely hydrostatic equilibrium, runaway gas accretion begins, leading to the formation of a gaseous envelope. The core accretion model is supported by the observed positive correlation between stellar metallicity and the fraction of stars hosting short-period giant planets [e.g. 248, 148], because core formation is more efficient around metal-rich stars. However, core accretion requires that planets form within primordial gas disks, which have a fairly limited

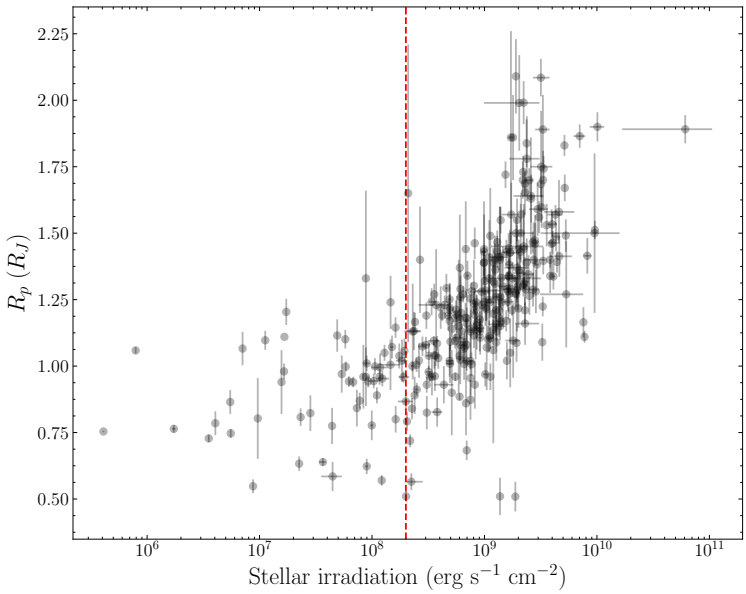

Figure 1-1 Planet radius vs. stellar irradiation for giant planets with radii larger than 0.5 R_J. While a positive correlation is visually apparent for hot Jupiters ($f > 10^9$ erg s^{-1} cm^{-2}), the behavior of planet radius as a function of stellar irradiation at lower irradiation levels is less clear due to low number statistics. The red dashed line marks the Demory & Seager [86] threshold of 2×10^8 erg s^{-1} cm^{-2}, below which there are very few known inflated planets. Data retrieved from the NASA Exoplanet Archive on March 21, 2019.

extent (see, e.g., [179]). In addition, the timescale for giant planet formation through core accretion becomes excessively long at large orbital distances. Detailed studies so far have concluded that core accretion cannot form massive planets beyond ~ 35 AU, even in the most favorable circumstances [e.g. 173, 274, 58]. Yet direct imaging and microlensing surveys are beginning to suggest that giant planets do exist at large orbital distances, possibly in significant numbers [e.g. 167, 213, 114]. Due to the intrinsic difficulty of detecting planets on wide orbits, we do not yet know how common these planets are, nor understand their implications on the core accretion theory. Core accretion also predicts a deficit of planets with masses between those of Neptune and Saturn, because runaway gas accretion should have initiated on such planets and turned them into gas giants [144, 205]. But such planets have been detected in microlensing and transit surveys, and may in fact be quite common (e.g.

[269, 227, 28]; see also Chapter 4). Despite their apparent abundance, there are currently very few planets in this mass regime with precisely measured masses and radii to help us understand the factors that determined their final masses. To answer any of the above questions, we would benefit from a larger sample of known giant planets covering a wide range of masses, eccentricities, obliquities, ages, and orbital periods. With the advent of space-based transit surveys, we are better positioned than ever to expand our collection of exoplanets.

1.2 The Era of Large-Scale Transit Surveys

No other exoplanet detection method has proven as prolific as the transit method[1]. It was proposed as a means of exoplanet detection long before the discovery of the first exoplanet [e.g. 171, 267]. When planets pass in front of their host stars as viewed from Earth, the flux from the host stars should drop because the planets block a fraction of the starlight. The fractional loss in flux is equal to the fraction of the stellar disk blocked. Detecting planets through these flux dips does not require expensive high-resolution spectroscopy, and is sensitive to a relatively large range of planet sizes and periods. In 2000, Charbonneau et al. [59] reported the periodic dimming of HD 209458 due to the transit of a Jupiter-sized planet, registering the first detection of an exoplanet using the transit method. Since then, the transit method alone has yielded over 3000 confirmed exoplanets, while all other methods combined contribute a total of less than 900.

Before the launch of *CoRoT* [15] and *Kepler* [158, 34], transit detection was mostly limited to ground-based surveys[2]. But the yield of such surveys was limited by a stringent timing requirement: a transit can only be detectable if it happens when the host star is above the horizon and the Sun is down. Moreover, scintillation and differential extinction limit the precision of ground-based photometry, making the

[1]Other commonly used exoplanet detection methods include radial velocity, astrometry, transit timing variations, gravitational microlensing, and direct imaging.

[2]A few notable examples include OGLE [281], HAT [16], TrES [7], XO [199], SuperWASP [230], and KELT [257].

detection of smaller transit signals challenging [295]. In 2006, *CoRoT* became the first spacecraft dedicated to the detection of transiting exoplanets to be launched into space, ushering in the era of space-based transit surveys and paving the way for the tremendously successful *Kepler* mission, which would completely revolutionize our understanding of exoplanets.

Kepler was launched in March 2009 into an Earth-trailing orbit, and monitored the brightness of $\sim 200,000$ stars in a $10^\circ \times 10^\circ$ patch of sky for four years with high precision. Over 2000 of these stars were later confirmed to be planet hosts [33]. When the second of four reaction wheels failed in May 2013, the spacecraft was no longer able to maintain precise (sub-pixel) pointing at its original field. The spacecraft was, however, able to balance itself against solar radiation pressure by pointing along the plane of its orbit and using thrusters to mitigate the residual drift. In this configuration, the *Kepler* spacecraft executed a mission called *K2* [136], in which it observed stars along the ecliptic in 80-day campaigns, albeit with decreased pointing precision. *K2* completed observations of 20,000-30,000 stars per campaign for 19 campaigns, before finally running out of fuel in October 2018. ~ 360 *K2* targets are now confirmed planet hosts [e.g. 77, 195, 185, 186], and thousands more have been identified as candidates [e.g. 304, 78].

The recently launched *Transiting Exoplanet Survey Satellite* (*TESS*) [241], *Kepler* and *K2*'s immediate successor, will likely more than double the number of known exoplanets [268, 137]. During its two-year mission duration, *TESS* will observe the sky in $24^\circ \times 96^\circ$ sectors and downlink data twice during every 27-day sector, eventually covering 20 million stars and 90% of the sky [268]. Space-based transit surveys have provided and will continue to provide us with an unprecedented volume and rate of new discoveries.

While large-scale surveys have dramatically transformed our knowledge of exoplanets, the sheer amount of data they present is challenging to process in an efficient yet accurate manner. *Kepler*, *K2* and *TESS* have all relied heavily on manual inspection to identify planet candidates (this process is referred to as "vetting"). In the

earlier *Kepler* planet candidate catalogs [e.g. 35, 36, 20], although an algorithm[3] was used to automatically identify periodic dimming signals ("threshold-crossing events", or TCEs), each TCE was visually examined by trained experts with an understanding of *Kepler* data systematics and common false positive scenarios, and classified as either a planet candidate or one of several types of false positives. Many teams working on *K2* and *TESS* have adopted a similar approach [e.g. 77, 195, 304, 78]. In Chapter 3, I describe in detail how manual vetting can be applied to *K2* data.

Human vetting has a number of weaknesses. First of all, it is a very time-consuming process. For a typical *TESS* sector, it may take one or two experienced humans up to a few days to perform triage, i.e. the procedure of rapidly eliminating the obvious false positives, on tens of thousands of candidates. Then, a team of ~ 10 vetters may spend up to a week classifying the remaining $\sim 1,000$ high-quality candidates if we require each one to be viewed by at least three different people [78]. But prompt candidate identification is crucial to the *TESS* mission, which was designed with follow-up in mind. Because *TESS* observes in the anti-Sun direction, *TESS* targets can be immediately observed from the ground if identified sufficiently rapidly, but the inefficiency of human vetting can limit the number of planet candidates receiving timely follow-up. Moreover, human vetters do not always maintain the same consistent set of standards when evaluating TCEs, and are often prone to errors. Even for a team of experts, the disposition given to the same TCE can vary depending on the vetters' mood, the manner of presentation, other TCEs viewed recently, or the time of day. For example, the *K2* planet catalogs published by different teams are, in fact, quite disjoint. Inconsistencies and errors in candidate classification make the calculation of planet occurrence rates challenging.

Motivated by a desire to classify TCEs rapidly and homogeneously, researchers turned to automated vetting as an alternative. The *Kepler* team developed a robotic vetting procedure known as the "Robovetter", which passes each TCE through a

[3]The most widely used algorithm to identify periodic dimming signals is the Box Least Squares (BLS) algorithm [161]. BLS exploits the box-like shape of transits and fits step functions to a light curve folded at various trial periods. If a combination of trial period and box shape yields a signal-to-noise ratio exceeding a given threshold, we can expect a significant detection of a transit-like signal.

classic tree diagram whose criteria are designed to imitate the manual process for rejecting false positives [74, 210]. By the end of the *Kepler* mission, the Robovetter was fully automated and used to produce planet candidate catalogs. At the same time, machine learning methods have also gained popularity in exoplanet surveys due to their high versatility. One particularly notable example is convolutional neural networks (CNNs), a class of deep learning models inspired by the organization of neurons in the visual cortex. CNNs have been widely used in image recognition and classification, and have been successfully adopted to identify planet candidates in *Kepler* data [253]. Given the scope of the mission and the rate at which data is generated, machine learning classification, CNNs in particular, will likely play an important role in the *TESS* mission.

1.3 This Thesis

The body of this thesis is organized into four parts. In Chapter 2, I present an in-depth analysis of a hot Jupiter candidate, PTFO 8-8695, which could have been a rare and valuable case study of a young hot Jupiter caught in the middle of migration, but is in fact unlikely to be a planet. In Chapter 3, given the need to expand our sample of known giant planets, I present some techniques and methods used to search for more planets in *K2* data. In Chapters 4 and 5, I describe three new giant planets we have discovered with *K2* using these methods: two warm sub-Saturns that have preserved to some degree their primordial eccentricities, and one hot Jupiter on an extremely well-aligned orbit despite the weak tidal forces in the system. In Chapter 6, I present a convolutional neural network that can be used to rapidly and accurately perform triage and vetting on *TESS* data. This neural network will aid humans in their discovery of more planets with *TESS*. Four of these five chapters have been published in peer reviewed journals, and the fifth has been submitted. I am confident that not far in the future, we will be able to gather the population of giant planets needed to answer many of the pressing questions about their formation and evolution.

Chapter 2

PTFO 8-8695b: A Young Giant Planet Caught in Migration?

The content of this chapter was submitted to ApJ *on July 24, 2015 and published [302] on October 10, 2015 as* Tests of the planetary hypothesis for PTFO 8-8695b*, by Liang Yu, Joshua N. Winn, Michaël Gillon, Simon Albrecht, Saul Rappaport, Allyson Bieryla, Fei Dai, Laetitia Delrez, Lynne Hillenbrand, Matthew J. Holman, Andrew W. Howard, Chelsea X. Huang, Howard Isaacson, Emmanuel Jehin, Monika Lendl, Benjamin T. Montet, Philip Muirhead, Roberto Sanchis-Ojeda, and Amaury H. M. J. Triaud.*

The T Tauri star PTFO 8-8695 exhibits periodic fading events that have been interpreted as the transits of a giant planet on a precessing orbit. Here we present three tests of the planet hypothesis. First, we sought evidence for the secular changes in light-curve morphology that are predicted to be a consequence of orbital precession. We observed 28 fading events spread over several years, and did not see the expected changes. Instead we found that the fading events are not strictly periodic. Second, we attempted to detect the planet's radiation, based on infrared observations spanning the predicted times of occultations. We ruled out a signal of the expected amplitude. Third, we attempted to detect the Rossiter-McLaughlin effect by performing high-resolution spectroscopy throughout a fading event. No effect was seen at the expected level, ruling out most (but not all) possible orientations for the hypothetical planetary

orbit. Our spectroscopy also revealed strong, time-variable, high-velocity Hα and Ca H & K emission features. All these observations cast doubt on the planetary hypothesis, and suggest instead that the fading events represent starspots, eclipses by circumstellar dust, or occultations of an accretion hotspot.

2.1 Introduction

The discovery of close-in giant planets around very young stars — less than a few million years old — would provide precious information about the timing of planet formation, the structure of newborn planets still cooling and contracting, and the mechanism for shrinking planetary orbits and creating hot Jupiters. Currently the only candidate for such an object is PTFO 8-8695b, found by van Eyken et al. [284] (hereafter VE+12). PTFO 8-8695 is a T Tauri star in the Orion-OB1a region, with a mass of $\approx$0.4 $M_{\odot}$, a spectral type of M3, and an estimated age of 3 Myr [44]. In addition to the quasi-sinusoidal variability characteristic of T Tauri stars, this star was found to exhibit periodic fading events, during which the star dims by a few percent for an interval of about 1.8 hours. VE+12 reported on these and other properties of the system, and advanced the hypothesis that the fading events are transits of a close-in giant planet.

However, the planetary interpretation is not secure. The system has some puzzling properties that seem incompatible with the planet hypothesis, or at least demand that the system has somewhat exotic properties. In the first place, the "transit" light curves do not have the customary morphology. They were seen to vary in depth and duration over a timespan of a year, and in some cases to lack the expected symmetry around the time of minimum light. Barnes et al. [19] proposed that these changes are caused by a large misalignment between the planet's orbit and the star's equatorial plane. This misalignment, when combined with an asymmetric intensity profile on the stellar disk due to gravity darkening, can produce asymmetric transit light curves. Furthermore, the misalignment leads to nodal precession of the orbit, which could explain the secular changes in morphology.

By itself this would not be too unusual. Hot Jupiters with spin-orbit misalignments are now commonplace [see, e.g. 5], and nodal precession has been observed in at least one other misaligned system [272, 271]. Barnes et al. [19] constructed a model that quantitatively fits the two light curves measured by VE+12 in 2009 and 2010. However, in the case of PTFO 8-8695 the "transit" period is equal to the stellar rotation period (as estimated from the quasi-sinusoidal variability): both are consistent with 0.448 days or 10.8 hours. It seems strange that the system would have reached spin-orbit synchronization without also achieving spin-orbit alignment.[1] The coincidence between the "transit" and rotation periods raises the possibility that the fading events are actually due to starspots, or eclipses by a corotating structure within a circumstellar disk or accretion flow.

Another striking property of PTFO 8-8695 is that the planetary radius inferred by VE+12 was 1.9 $R_{\rm Jup}$, making it essentially tied with WASP-17b [278] for the largest known planetary radius. Perhaps this should be expected, for a planet that is still contracting from an initially distended state. Somewhat more worrying is that the orbital period of 10.8 hours is within or at least near the Roche limit for a gas giant [236]. This suggests that the planet would be actively losing mass through Roche lobe overflow.

The conventional way to confirm the existence of a transiting planet is to detect the expected radial-velocity variation of the host star. VE+12 attempted to detect such a signal but were foiled by the spurious radial-velocity variations caused by stellar activity, which are larger than the amplitude of the expected orbital velocity. Even if an apparently sinusoidal radial-velocity signal were detected, it would be difficult to ascertain whether the signal is planetary in origin or arises from stellar activity, due to the coincidence between the "transit" and rotation periods.

Given the high scientific stakes, we attempted three less conventional tests of the planetary hypothesis:

[1] Kamiaka et al. [149] explored models in which the orbital and rotation periods are not necessarily synchronized, under the premise that the stellar rotation period could have any value up to 16 hours (an upper limit set by the measured $v \sin i_\star$). However, the quasi-sinusoidal flux variations outside the fading events are likely due to rotation, and have a period that agrees with that of the "transit" events to within a percent. Thus it seems unnecessary to consider non-synchronized models.

1. According to the gravity-darkening model of Barnes et al. [19], continued nodal precession should produce variations in the asymmetry, duration, and depth of the fading events, with a period of a few years. Barnes et al. [19] also predicted that there should be intervals of several months during which the fading events cease, because the planet's trajectory does not cross the face of the star. Therefore, we undertook time-series photometry of as many fading events as possible over a timespan of several years, to detect the expected changes in morphology.

2. Close-in giant planets emit relatively strongly at infrared wavelengths, due to a combination of reflected starlight and the planet's own thermal radiation. Therefore, we attempted to detect the loss of light when the planet is hidden by the star, by performing time-series infrared photometry spanning the expected times of occultations (halfway between transits).

3. A key premise of the planet hypothesis is that the orbit is misaligned with the stellar equator. In contrast, starspots move in a prograde direction, aligned with stellar rotation. The angle between the trajectory of a transiting feature and the (sky-projected) stellar equator can be measured by observing the Rossiter-McLaughlin effect [243, 201]. Therefore, we undertook high-resolution optical spectroscopy throughout a fading event to measure the spin-orbit angle of whatever is apparently blocking the starlight. We also used the spectra to check for time variations in the sky-projected rotation rate ($v \sin i_\star$), which would be expected if the star is precessing.

This chapter is organized as follows. Section 2.2 presents time-series photometry of the candidate transits and occultations, using several ground-based telescopes and an archival observation with the *Spitzer* Space Telescope. Section 2.3 presents our time-series spectroscopy and our attempt to detect the Rossiter-McLaughlin effect. Section 2.4 analyzes the preceding results and their implications for the planetary hypothesis as well as other possible explanations for the fading events.

2.2 Time-series photometry

2.2.1 Overview

We conducted time-series photometric observations of fading events between 2012 and 2015. Below, in § 2.2.2, we present ground-based observations of 26 different events. Figure 2-1 shows their distribution in time, and Figure 2-2 shows the light curves (including the 7 highest-quality light curves presented previously by VE+12, for reference). In a few cases we observed the event through multiple broadband filters. The resulting multi-band light curves are shown in Figure 2-6. We also observed a candidate occultation at infrared wavelengths with one of the Magellan 6.5m telescopes; those data are described in § 2.2.3.1 and plotted in Figure 2-7. Finally, we analyzed the available *Spitzer* data, spanning a fading event as well as an expected occultation. Those data are described in § 2.2.3.2 and shown in Figure 2-9. The dates of the *Spitzer* and Magellan observations are also indicated on Figure 2-1, along with the Keck spectroscopic observations described in Section 2.3.

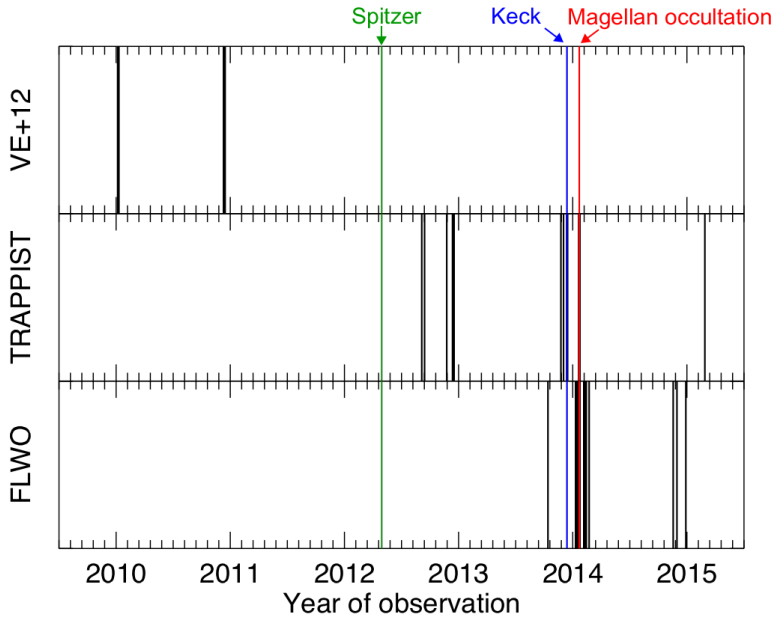

Figure 2-1 Dates of observations of fading events with the FLWO 1.2m and TRAPPIST 0.6m telescopes, along with previous observations by VE+12. Also indicated are the dates of the observations with *Spitzer*, Magellan, and Keck.

Table 2.1. Best-fitting parameters of fading events (see Eq. 2.1).

UT date	Filter	$\chi^2_{\rm min}$	No. of data points	Time of minimum light, t_0 [HJD−2,455,200]	Fractional loss of light, δ	Duration, w [days]
2010 Jan 5	R	193.4	228	1.8053 ± 0.0014	0.0442 ± 0.0052	0.0282 ± 0.0033
2010 Jan 6	R	216.5	244	2.6961 ± 0.0017	0.0789 ± 0.0208	0.0349 ± 0.0059
2010 Jan 9	R	217.0	191	5.8431 ± 0.0014	0.0979 ± 0.0142	0.0370 ± 0.0042
2010 Dec 9	R	169.9	270	339.9069 ± 0.0006	0.0498 ± 0.0023	0.0190 ± 0.0013
2010 Dec 10	R	248.4	298	340.8020 ± 0.0006	0.0425 ± 0.0011	0.0167 ± 0.0007
2010 Dec 13	R	191.1	271	343.9467 ± 0.0010	0.0558 ± 0.0038	0.0229 ± 0.0017
2010 Dec 14	R	473.2	288	344.8401 ± 0.0009	0.0412 ± 0.0018	0.0158 ± 0.0012
2012 Sep 4	$I+z$	194.0	209	974.8427 ± 0.0005	0.0510 ± 0.0027	0.0160 ± 0.0011
2012 Sep 13	$I+z$	388.8	265	983.8121 ± 0.0004	0.0521 ± 0.0014	0.0138 ± 0.0006
2012 Nov 23	$I+z$	240.1	243	1054.6614 ± 0.0009	0.0189 ± 0.0013	0.0128 ± 0.0014
2012 Dec 11	$I+z$	94.2	94	1072.5994 ± 0.0009	0.0366 ± 0.0024	0.0132 ± 0.0015
2012 Dec 14	$I+z$	154.0	176	1075.7379 ± 0.0006	0.0298 ± 0.0014	0.0098 ± 0.0008
2012 Dec 15	$I+z$	152.8	182	1076.6357 ± 0.0005	0.0338 ± 0.0029	0.0128 ± 0.0013
2013 Oct 12	i'	9.7	54	1377.9469 ± 0.0009	0.0324 ± 0.0024	0.0099 ± 0.0012
2013 Nov 23	$I+z$	102.7	93	1419.6524 ± 0.0022	0.0177 ± 0.0029	0.0114 ± 0.0030
2013 Dec 1	$I+z$	245.9	195	1427.7243 ± 0.0007	0.0316 ± 0.0026	0.0163 ± 0.0016
2013 Dec 11	$I+z$	190.3	233	1437.5864 ± 0.0007	0.0385 ± 0.0030	0.0153 ± 0.0016
2013 Dec 14	$I+z$	255.1	262	1440.7266 ± 0.0005	0.0344 ± 0.0016	0.0139 ± 0.0011
2014 Jan 9	i'	127.6	46	1466.7304 ± 0.0007	0.0385 ± 0.0016	0.0156 ± 0.0012
2014 Jan 14	i'	183.0	57	1471.6634 ± 0.0011	0.0337 ± 0.0025	0.0128 ± 0.0015
2014 Jan 17	i'	245.0	59	1474.8039 ± 0.0010	0.0377 ± 0.0042	0.0160 ± 0.0023
2014 Jan 18	i'	177.0	57	1475.7000 ± 0.0007	0.0375 ± 0.0014	0.0144 ± 0.0009
2014 Jan 19	$I+z$	253.6	240	1476.5974 ± 0.0007	0.0326 ± 0.0023	0.0167 ± 0.0016
2014 Jan 23	i'	331.9	136	1480.6289 ± 0.0004	0.0628 ± 0.0044	0.0218 ± 0.0013
2014 Jan 23	$I+z$	549.4	356	1480.6339 ± 0.0010	0.0295 ± 0.0018	0.0149 ± 0.0015
2014 Feb 5	i'	404.4	111	1493.6353 ± 0.0005	0.0349 ± 0.0013	0.0140 ± 0.0008
2014 Feb 9	i'	330.9	107	1497.6729 ± 0.0005	0.0402 ± 0.0013	0.0132 ± 0.0008
2014 Feb 13	i'	246.4	99	1501.7075 ± 0.0005	0.0451 ± 0.0022	0.0147 ± 0.0010
2014 Feb 22	i'	476.4	83	1510.6778 ± 0.0007	0.0463 ± 0.0027	0.0148 ± 0.0013
2014 Nov 17	i'	208.1	119	1778.7654 ± 0.0007	0.0304 ± 0.0020	0.0116 ± 0.0012
2014 Nov 29	i'	259.0	145	1790.8761 ± 0.0009	0.0185 ± 0.0014	0.0088 ± 0.0011
2014 Dec 27	i'	199.7	118	1818.6748 ± 0.0007	0.0222 ± 0.0012	0.0094 ± 0.0008
2015 Feb 27	$I+z$	200.0	206	1880.5567 ± 0.0009	0.0206 ± 0.0017	0.0087 ± 0.0012

Table 2.2. Best-fitting parameters of phase-folded light curves (see Eq. 2.2)

Light curve	Filter	Time of minimum light, t_0 [days]	Fractional loss of light, δ	Ingress duration, w_1 [days]	Egress duration, w_2 [days]
FLWO average	i'	0.0029 ± 0.0028	0.0360 ± 0.0017	0.0166 ± 0.0023	0.0124 ± 0.0018
TRAPPIST average	$I+z$	0.0018 ± 0.0018	0.0336 ± 0.0010	0.0149 ± 0.0014	0.0128 ± 0.0013

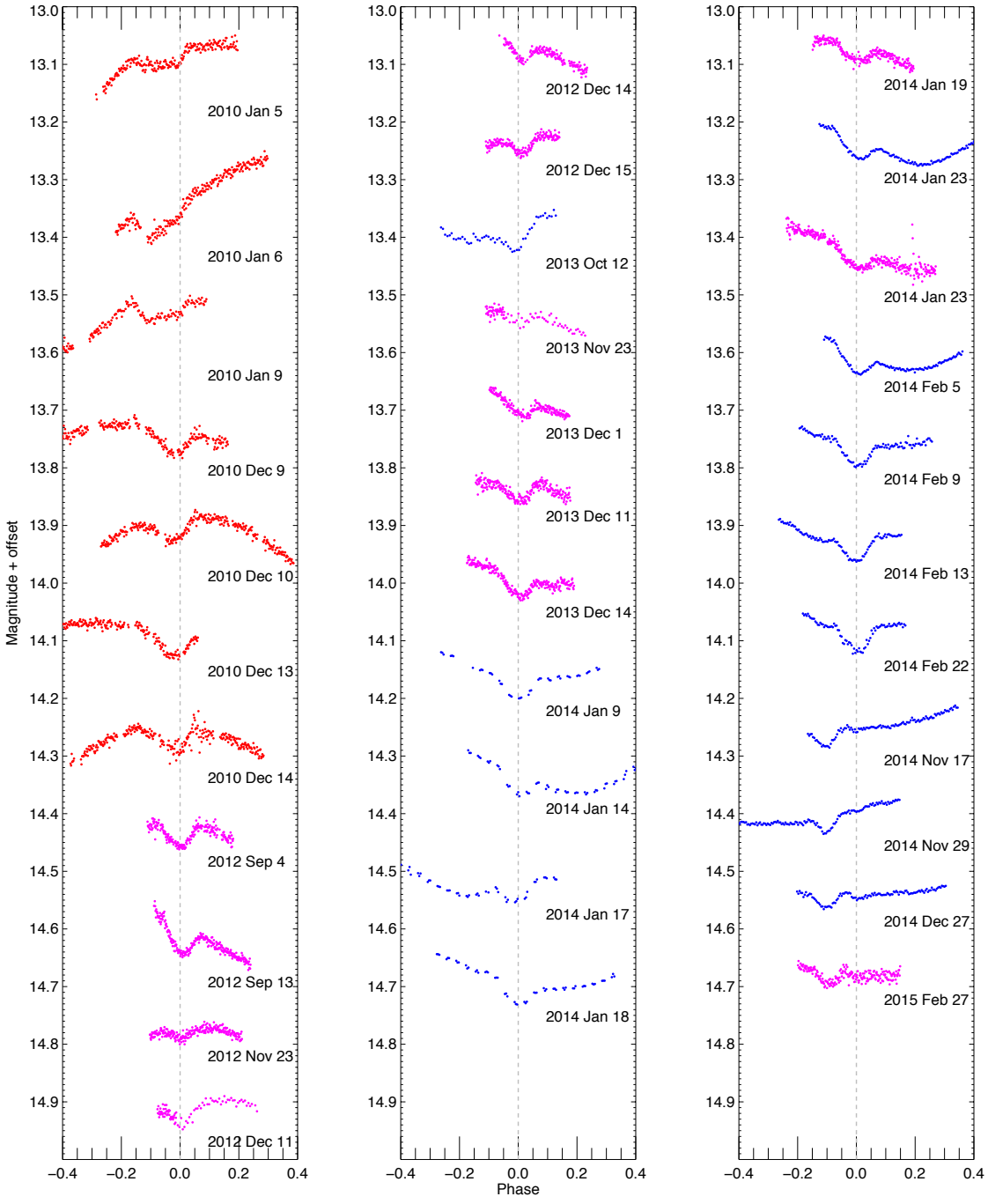

Figure 2-2 Time-series photometry of fading events of PTFO 8-8695. The vertical scale is the same for all events; vertical offsets have been applied to separate the different time series. Included in this plot are the 7 highest-quality light curves from VE+12 (red), as well as 26 new light curves from the FLWO 1.2m telescope (blue) and the TRAPPIST 0.6m telescope (magenta). The FLWO observations between 2014 Jan 9-18 were conducted in both i' and g' band.

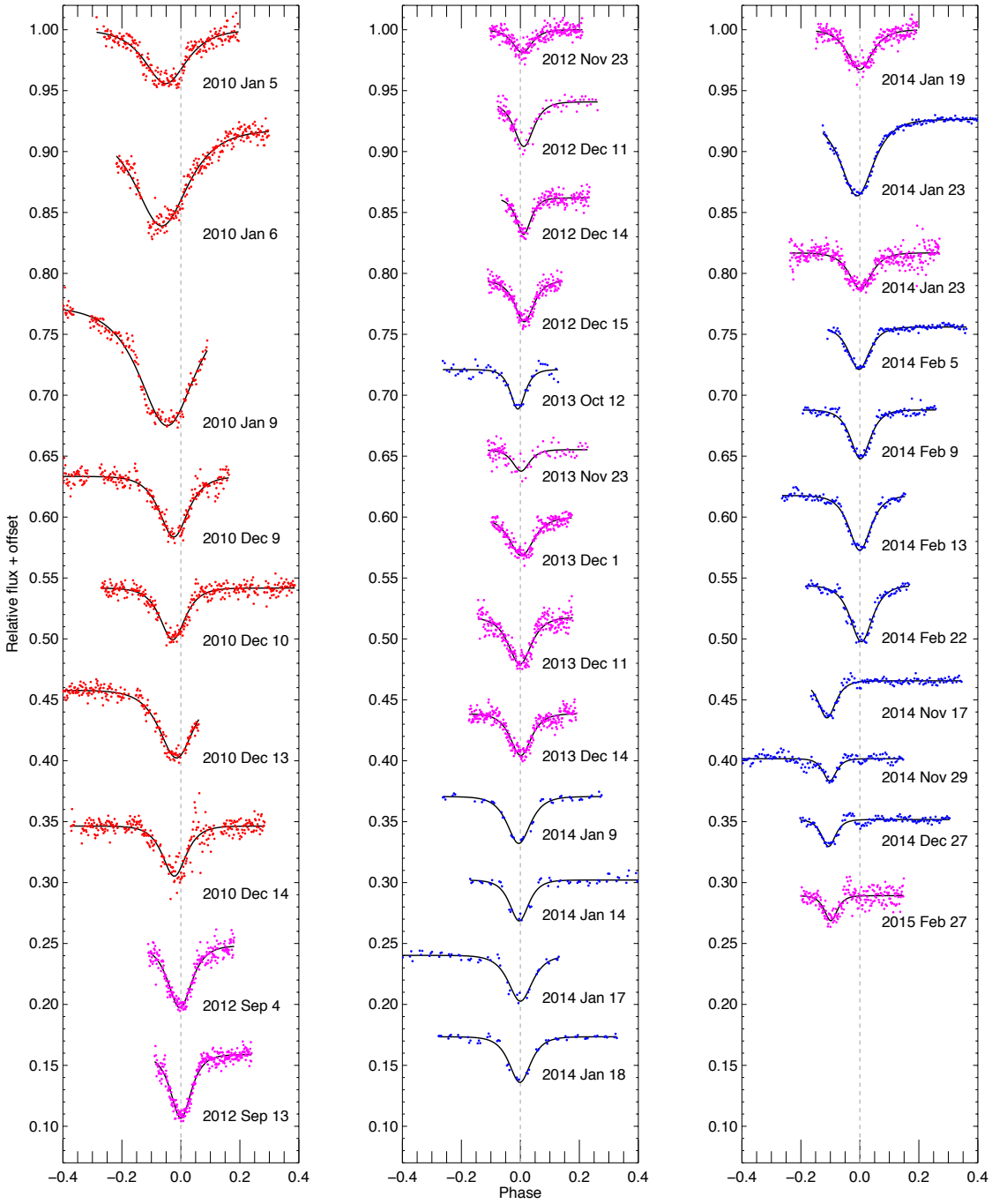

Figure 2-3 Same as Figure 2-2, but after "flattening" the out-of-transit flux variation by dividing by the best-fitting polynomial function of time. Flux values are normalized to unity outside of the transit. The black curves are the best-fitting models (see Eqn. 2.1), from which we derived the transit times, depths, and durations that are reported in Table 2.1.

2.2.2 Ground-based observations of fading events

We observed 13 fading events with the 1.2m telescope at the Fred Lawrence Whipple Observatory (FLWO) on Mt. Hopkins, Arizona. The instrument, Keplercam, has a single 4096×4096 CCD with a $23\farcm1$ field of view. All the events were observed through an i' filter. For the events between 2014 Jan 9–18, we interleaved the i'-band exposures with g'-band exposures, although the g'-band data were only useful in two cases. Calibration was performed using standard IRAF[2] procedures, including bias and flat-field corrections. The time stamps were placed on the $\mathrm{BJD_{TDB}}$ system using the code by Eastman et al. [94]. Circular aperture photometry was performed with the Interactive Data Language (IDL).

Another 13 events were observed with the 0.6m TRAnsiting Planets and PlanetesImals Small Telescope (TRAPPIST), located at ESO's La Silla Observatory in Chile. This telescope is equipped with a thermoelectrically-cooled 2048×2048 CCD with a $22'$ field of view [111, 147]. The observations were conducted with a custom "$I + z$" filter, which has transmittance >90% between 750–1100 nm. We refer the reader to Gillon et al. [112] for descriptions of the procedures for observing and data reduction. The two events of 2012 Dec 14 and 15 were simultaneously observed with a Gunn r' filter, using EulerCam on the 1.2m Euler-Swiss Telescope at the La Silla site, Chile. EulerCam uses a 2048×2048 CCD with a field of view of $14\farcm7$ on a side. For details on the instrument and data reduction procedures, please refer to Lendl et al. [172].

A single event on 2014 Jan 19 was observed with the 6.5m Magellan I (Baade) telescope at Las Campanas Observatory in Chile. The same event was observed simultaneously by TRAPPIST in the $I + z$ band. With Magellan, we observed in the H band using FourStar, a 2048×2048 infrared array with a $10\farcm9$ square field of view. The data were reduced with IRAF and IDL procedures similar to those used on the FLWO data.

[2]The Image Reduction and Analysis Facility (IRAF) is distributed by the National Optical Astronomy Observatory, which is operated by the Association of Universities for Research in Astronomy (AURA) under a cooperative agreement with the National Science Foundation.

In all cases the flux of PTFO 8-8695 was divided by the summed flux from several reference stars, leading to the light curves plotted in Figure 2-2. This figure also shows the 7 light curves presented by VE+12 that cover the entire fading event; those observations were performed with the 1.2m Palomar telescope and an R filter.

Outside of the fading events, the star varies gradually by $\sim$0.1 mag over several hours, in a manner consistent with its young age and late spectral type. Superimposed on those relatively gradual variations are periodic transit-like fading events lasting no more than about 2 hours. The depth and duration of the fading seems to vary from event to event. To derive the basic phenomenological parameters of the dimming events — depth, duration, and time of minimum light — we fitted a parameterized model describing both the gradual out-of-transit variations as well as the transit-like loss of light. We modeled the gradual variations as a polynomial function of time (2nd or 3rd order, depending on the event). The additional loss of light during the fading event, relative to the polynomial-corrected out-of-transit flux, was modeled as

$$\Delta f(t) = \delta \,\mathrm{sech}\left[\frac{t-t_0}{w}\right] = \frac{2\delta}{e^{(t-t_0)/w} + e^{-(t-t_0)/w}}, \tag{2.1}$$

where δ is the maximum fractional loss of light (the "transit depth"), w is the duration, and t_0 is the time of minimum light. We chose this model instead of a more physically-motivated transit model [e.g., the model presented by 190] because the asymmetries and other odd features in the light curves do not fit the standard models. Hence there is no advantage in fitting the physical model when a much simpler model can provide estimates of the basic transit parameters. One might be able to fit the data with a model based on transits of an oblate, oblique, precessing, gravity-darkened star [18], but such a model is far more demanding computationally. Our analytic model suffices to estimate the basic parameters of each event.

Figure 2-3 shows the light curves after dividing out the best-fitting polynomial functions. This gives a clearer view of the "transits" with most of the long-term trends removed. Table 2.1 gives the model parameters, as well as the value of $\chi^2_{\rm min}$ and the number of data points in each time series. In most cases, $\chi^2_{\rm min}$ is too large to

be statistically acceptable, i.e., the simplified model of Eq. 2.1 does not fit the data to within the photometric uncertainties. For this reason, Table 2.1 does not report the formal parameter uncertainties defined by the usual criterion $\Delta\chi^2 = 1$. Rather, the reported parameter uncertainties have been enlarged by a factor of $\sqrt{\chi^2_{\rm min}/N_{\rm dof}}$ where $N_{\rm dof}$ is the number of degrees of freedom. These enlarged uncertainties were also adopted for our subsequent calculations.

Figure 2-4 shows the measured depths and durations. When the transits are deeper, they also tend to have longer durations; the measured depth and duration have a Pearson correlation coefficient of 0.84 ($p < 10^{-5}$).

The VE+12 light curves showed strong asymmetries in at least 5 out of the 7 complete light curves. None of our new light curves show strong asymmetries, at least not as clearly as was seen by VE+12. We tried fitting a model in which the rates of brightness variation are not symmetric about the time of minimum light, by using a non-standard variant of the hyperbolic secant function [see, e.g., 244]:

$$\Delta f = \frac{2\delta}{e^{(t-t_0)/w_1} + e^{-(t-t_0)/w_2}}. \tag{2.2}$$

The asymmetric model does not seem to improve the quality of the fit to a significant degree. The number of cases for which the fitted asymmetry obeyed $w_1 > w_2$ (more prolonged "ingress") was nearly the same as the number of cases with $w_2 > w_1$, without any obvious pattern. Figure 2-5 shows the FLWO and TRAPPIST data as a function of $t-t_0$ (coverted to hours) after some averaging in time to increase the signal-to-noise ratio. In these averaged light curves there does seem to be a slight asymmetry, with a longer "ingress" than "egress" in both cases. The best-fitting asymmetric model is shown in Figure 2-5, and the parameters are given in Table 2.2.

Another finding is that the loss of light is usually strongly chromatic, as shown in Figure 2-6. For those two cases in which we observed the same event in both the i' and g' bands, we found the loss of light to be 30-50% larger in the g' band. For the single case in which we observed in both H and $I + z$, the loss of light was also $\sim$40% larger in the bluer band. We also observed two events simultaneously in the Gunn r'

and $I + z$ bands. On the first night the loss of light was 20-30% larger in the bluer band. On the second night, the loss of light in r' was essentially the same as in $I + z$.

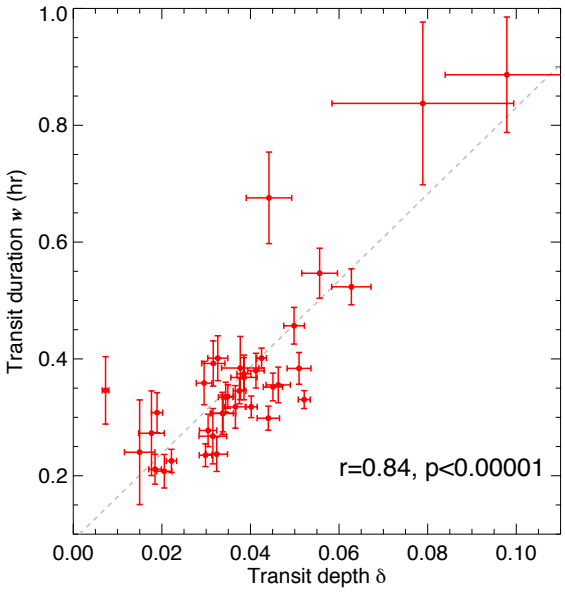

Figure 2-4 Depths and durations of the fading events, estimated for each individual event by fitting a simple analytic model (Eq. 2.2). There is a positive correlation between depth and duration. The best-fit straight line is shown as a dashed line. The Pearson correlation coefficient and its statistical significance are given in the bottom right corner.

2.2.3 Ground-based observations of predicted occultations

The infrared emission from close-in giant planets is often strong enough that it is possible to detect the decrement in total flux when the planet is hidden by the star. The detection of such an occultation would be strong evidence supporting the planet hypothesis. We searched for the predicted occultations in the Magellan and *Spitzer* time-series infrared photometry, as discussed below.

2.2.3.1 Magellan observations

The 6.5m Magellan I (Baade) telescope and FourStar were also used to monitor PTFO 8-8695 for approximately 6 hours on 2014 Jan 21, spanning the predicted time of a planetary occultation. The prediction was based on the assumption that

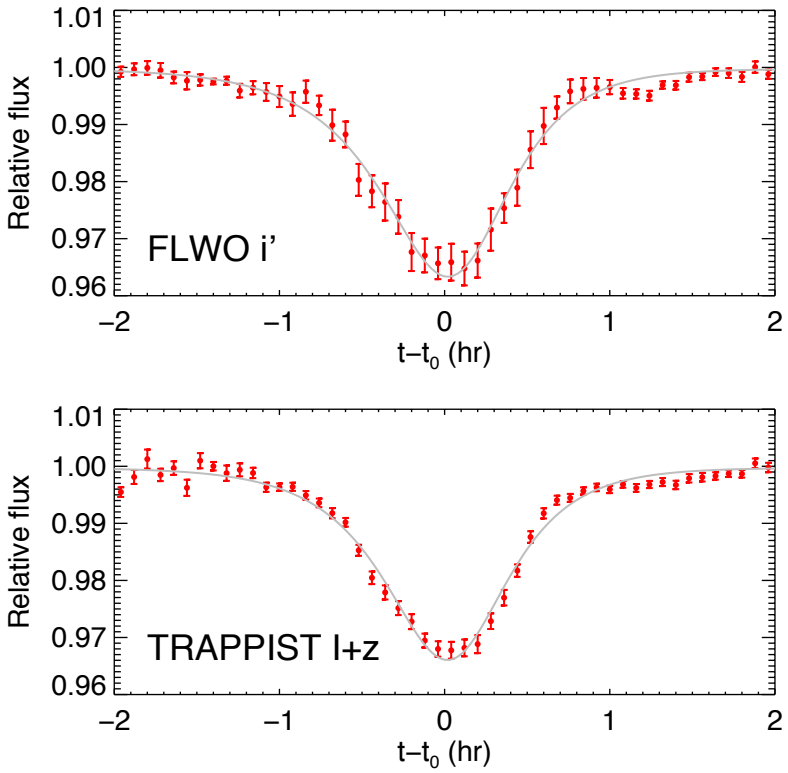

Figure 2-5 *Top.*—Phase-folded light curve based on data from all the fading events observed with the FLWO 1.2m telescope in the i' band. *Bottom.*—Same, but for the $I+z$ data obtained with the 0.6m TRAPPIST telescope. In both cases the data were placed into 50 time bins spanning a 4-hour period bracketing the expected transit time. The grey line represents the best-fit asymmetric model for each light curve. The error bars represent the standard deviation of the mean in each time bin.

the planet's orbit is circular, i.e., that the occultations occur exactly halfway between transits. The observations were conducted in the H band and the data were processed in the manner described in § 2.2.2. Figure 2-7 shows the resulting light curve. No occultation signal is evident, although some gradual variability is seen.

We determined an upper limit on the relative brightness of the planetary dayside by fitting an occultation model to the data. The model had the same total duration and ingress/egress durations as the "transit" light curve observed with Magellan two days earlier. As with the transits, we fitted the gradual variations with a polynomial function of time (in this case, a cubic function). We used a Markov Chain Monte Carlo (MCMC) algorithm to calculate the posterior probability distribution for the parameters describing the cubic function as well as the loss of light during the occul-

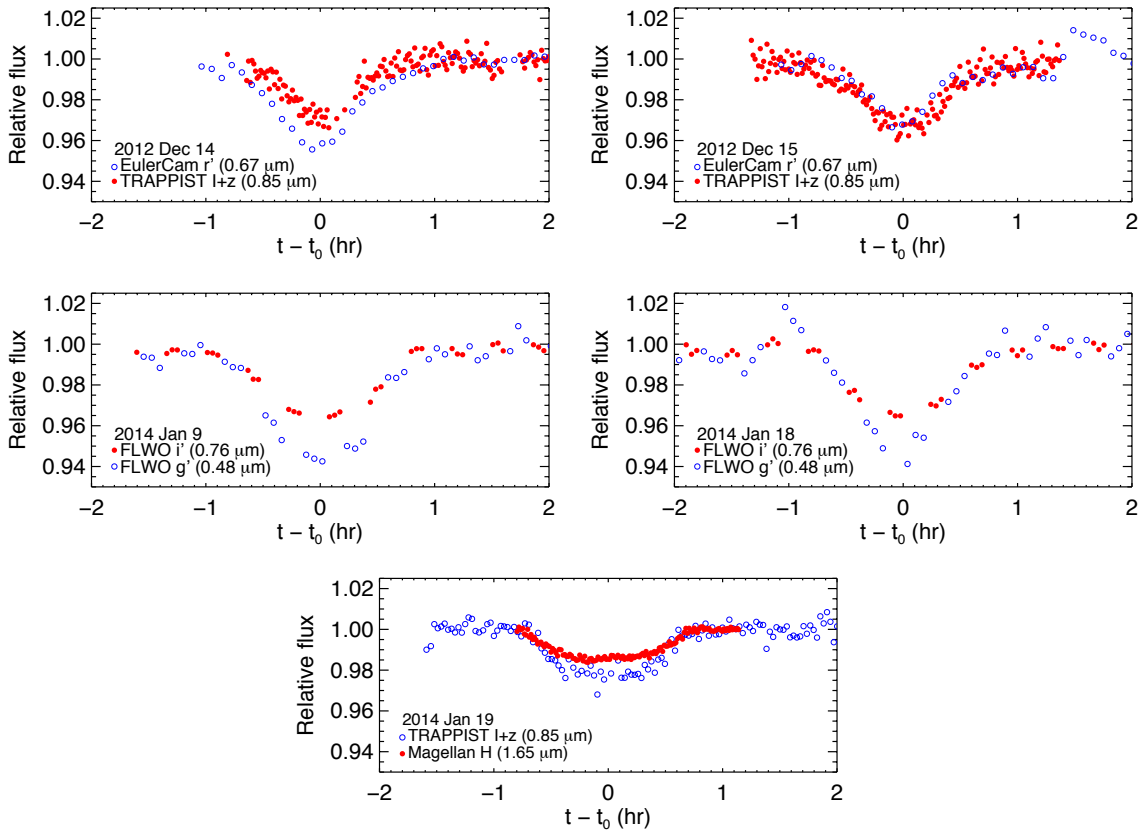

Figure 2-6 Multiband observations of fading events. *Top row.*—Simultaneous observations in the r' and $I+z$ bands (open blue and filled red circles, respectively). *Middle row.*—Interleaved observations in the g' and i' bands (open blue and filled red circles, respectively). *Bottom.*—Simultaneous observations in the $I+z$ and H bands (open blue and filled red circles, respectively). In all but one case, the loss of light is greater in the bluer bandpass.

tation. The minimum χ^2 value was 2082.5, with 1876 degrees of freedom, indicating a statistically unacceptable fit; the cubic function is evidently not a completely satisfactory description of the observed flux variations. Rather than develop more elaborate models we simply inflated the parameter uncertainties by the factor $\sqrt{\chi^2_{\rm min}/N_{\rm dof}}$. The resulting occultation depth was $\delta_{\rm occ} = 0.00024 \pm 0.00016$, corresponding to a 3σ upper limit of $\delta_{\rm occ} < 0.00072$.

To decide if this upper limit rules out the planetary hypothesis, we need to know the expected occultation signal. Following the usual simplified model for transiting

planets, the fractional loss of light during an occultation is

$$\delta_{\rm occ} = A_g \left(\frac{R_p}{a}\right)^2 + \left(\frac{R_p}{R_\star}\right)^2 \frac{\int_{\lambda_1}^{\lambda_2} B_\lambda(T_p) d\lambda}{\int_{\lambda_1}^{\lambda_2} B_\lambda(T_\star) d\lambda}. \tag{2.3}$$

The first term is due to reflected starlight, in which A_g is the geometric albedo, and R_p and $R_\star$ are the planetary and stellar radii. The second term is due to the planet's thermal emission, in which the observing bandpass extends from λ_1 to λ_2 (1.48–1.76 μm, for H band), $B_\lambda(T)$ is the Planck function, $T_\star$ is the star's effective temperature, and T_p is the planet's dayside effective temperature. The latter is calculated from the condition of radiative equilibrium, giving

$$T_p = T_\star \left(\frac{R_\star}{a}\right)^{1/2} \left(\frac{1-A}{f}\right)^{1/4}, \tag{2.4}$$

where A is the Bond albedo and f is a dimensionless number depending on the manner of radiation. If the entire surface radiates isotropically as a blackbody, then $f = 4$. If instead the dayside radiates uniformly and the nightside radiation can be neglected, then $f = 2$. Furthermore, if the angular dependence of the planet's radiation is assumed to follow Lambert's law, then $A_g = 2A/3$.

In this case it is difficult to establish the key parameters $(R_p/R_\star)^2$ and $R_\star/a$, because of the changing morphology of the fading events with time and wavelength. Barnes et al. [19] found $(R_p/R_\star)^2 \approx 0.027$ and $R_\star/a \approx 0.58$ using a model incorporating the effects of gravity darkening and orbital precession. Using those parameters, we calculate the expected value of $\delta_{\rm occ}$ and plot it as a function of the Bond albedo in Figure 2-8, for both $f = 4$ and $f = 2$. The expected $\delta_{\rm occ}$ ranges from a minimum value of 0.0028 for $f = 4$ and $A = 0$, to a maximum value of 0.0061 for $f = 2$ and $A = 1$. Such large occultation depths are ruled out by our Magellan observations.

2.2.3.2 Spitzer observations

The *Spitzer* Space Telescope monitored PTFO 8-8695 on 2012 Apr 28 for about 12 hours, slightly longer than a full photometric period. The data consist of 1369

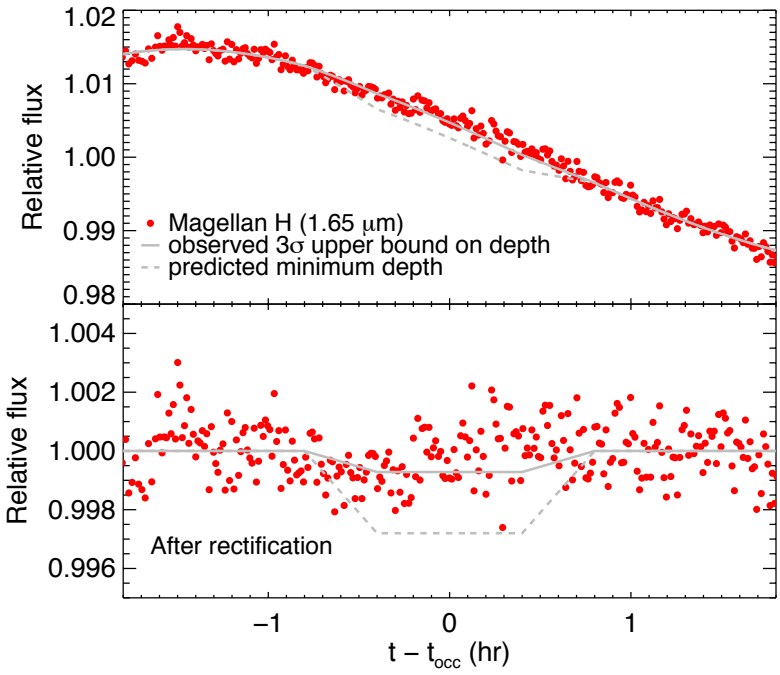

Figure 2-7 *Top.*—Near-infrared photometry of PTFO 8-8695 spanning the predicted time of occultation. The data points are averaged in groups of 5 for clarity. The solid gray line shows the 3σ bound on the maximum depth of the occultation given by this light curve. The dashed grey line shows the minimum predicted occultation depth according to the model of Barnes et al. [19]. *Bottom.*—Same, but after dividing through the light curve by the best-fit cubic function to the out-of-occultation region.

full-array images from the IRAC detector operating at 4.5 μm, with an integration time of 26.8 seconds. The data were calibrated by the *Spitzer* pipeline version S19.1.0. These observations were carried out in non-cryogenic mode under program no. 80257 (PI: Stauffer), and are publicly available on the *Spitzer* Heritage Archive database.[3]

We converted the data from the *Spitzer* units of specific intensity (MJy sr^{-1}) into photon counts, and then performed IRAF aperture photometry on each subarray image. Best results were obtained with an aperture radius of 2.5 pixels and a background annulus extending from 11 to 15.5 pixels from the center of the point-spread function (PSF). The center of the PSF was measured by fitting a two-dimensional Gaussian function to each image. At this stage, 30 discrepant fluxes were discarded by applying a 5σ median clipping algorithm.

[3]While this manuscript was in preparation, Ciardi et al. [63] reported an independent analysis of these same data.

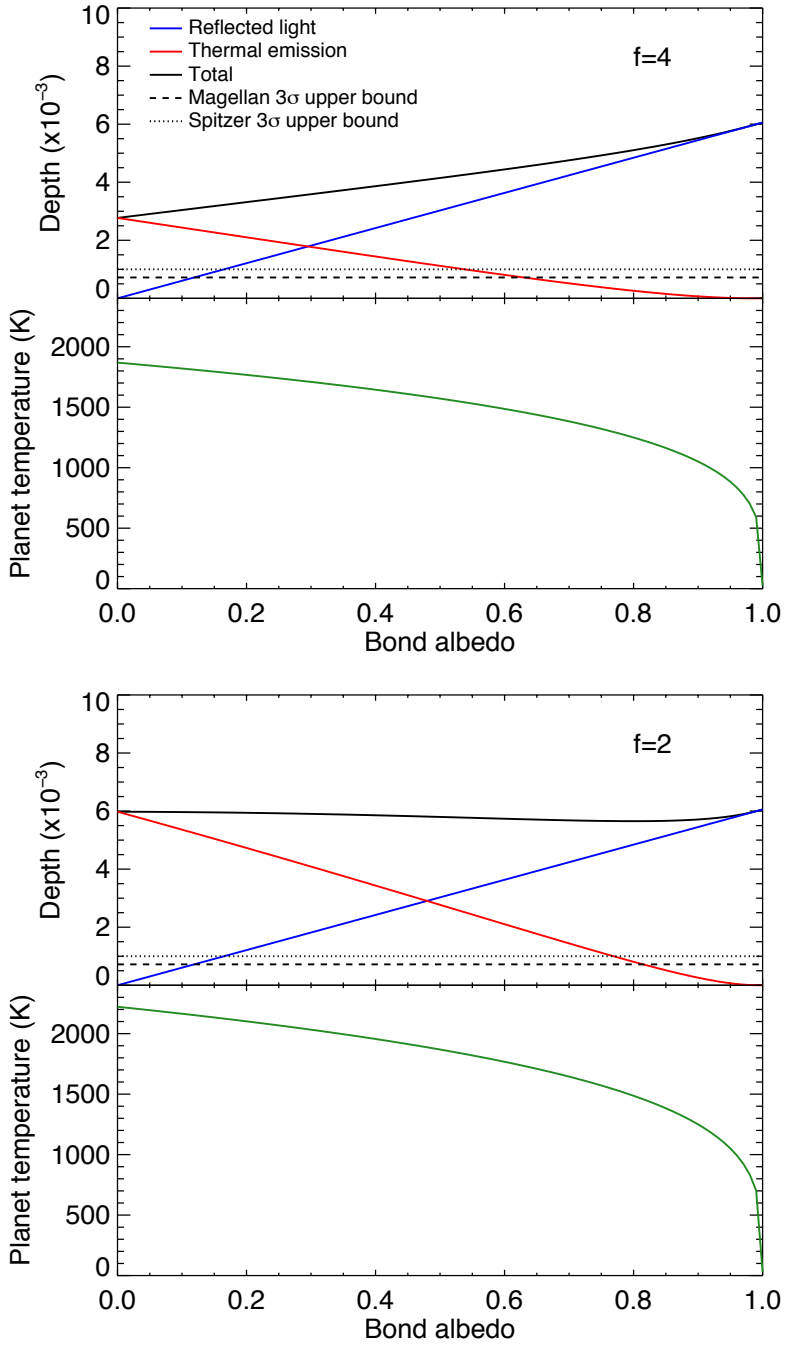

Figure 2-8 *Top.*—The upper panel shows the expected occultation depth $\delta_{\rm occ}$ (solid black line) plotted as a function of the Bond albedo for $f = 4$. The red and blue lines represent the contributions to the total occultation depth from thermal emission of the planet and reflected light, respectively. For comparison, the 3σ upper bounds on $\delta_{\rm occ}$ obtained from Magellan and *Spitzer* are shown as dashed and dotted lines. The lower panel shows the corresponding dayside effective temperature of the planet. *Bottom.*—Same, but for $f = 2$.

Next we needed to remove the apparent flux variations associated with motion of the image on the detector, the main source of systematic effects in time-series photometry with the IRAC InSb arrays [157]. This effect is caused by the combination of (i) the coarse sampling of the PSF, (ii) the significant inhomogeneity of the pixels, and (iii) fluctuations in the telescope pointing. To mitigate this effect we chose the Bi-Linearly-Interpolated Sub-pixel Sensitivity (BLISS) mapping method presented by Stevenson et al. [266]. In this method, the flux data themselves are used to constrain a model for the subpixel sensitivity variations. In our implementation of the method, the detector area probed by the PSF center was divided into a 13×13 grid. With this degree of sampling, the PSF center visited each grid point at least 10 times throughout the course of the observations.

Figure 2-9 shows the *Spitzer* light curve after BLISS correction. The variability can be described as the combination of quasi-sinusoidal variation with a period of $\approx$0.5 day, and the transit-like dip in brightness at the expected time, with an amplitude of 0.5% and a duration of approximately 1.4 hours. No occultation is seen at the expected time (0.224 days after the transit). Figure 2-10 gives a better view of the transit-like event, and the data surrounding the predicted time of occultation. In this figure, only the data within 0.1 days of each event are shown, and the data have been rectified by fitting a quadratic function of time to data outside of the event and then dividing by the best-fitting function.

Just as with the Magellan light curve, we determined an upper limit on the occultation loss of light by fitting a parameterized model to the data. The model included a quadratic function of time to describe the out-of-occultation variations. The occultation model was required to have the same durations between first, second, third and fourth contacts as observed earlier with Magellan. The loss of light $\delta_{\rm occ}$ was a free parameter. We used an MCMC algorithm to calculate the posterior probability distribution of $\delta_{\rm occ}$ and the parameters of the quadratic function. The minimum χ^2 value was 565.9, with 535 degrees of freedom. The result for the occultation depth was $\delta_{\rm occ} = -0.0008 \pm 0.0006$, i.e., the best-fitting value corresponds to a brightness increase rather than a loss of light. This corresponds to a 3σ upper limit of

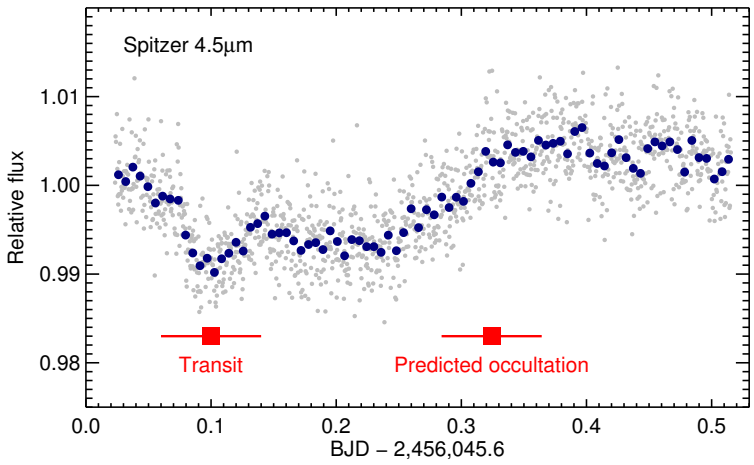

Figure 2-9 *Spitzer* time-series 4.5 μm photometry of PTFO 8-8695 from 2012 Apr 28. The small gray points represent individual measurements; the larger dark blue points are time averages. Red bars show the times of the fading event, and the predicted time of the planetary occultation.

$\delta_{\rm occ} < 0.0010$. Again, as illustrated in Figure 2-8, the upper bound on $\delta_{\rm occ}$ given by *Spitzer* is smaller than the occultation depth implied by the parameters of the Barnes et al. [19] model.

Careful inspection of Figure 2-9 shows a candidate flux dip of centered around a time coordinate of 0.425, with an amplitude of ≈0.3%. One might be tempted to attribute this dip to the occultation of a planet on an eccentric orbit, for which the occultation need not be halfway between transits. However, the statistical significance of this dip is dubious, and the required value of the eccentricity would be $e > 0.35$, using Eq. 33 of Winn [295]. Such a high eccentricity would be unprecedented and unexpected for a short-period planet. In general, giant planets with periods shorter than 3 days have nearly circular orbits, a fact that is attributed to the gradual action of tidal dissipation. Given the youth of the star, it is possible that there has not yet been sufficient time for orbital circularization; however, a higher eccentricity and a potentially smaller pericenter distance would also put the planet in even more danger of violating the Roche limit.

Our non-detections of occultation signals at both 1.7 μm and 4.5 μm bands rule out the existence of a planet that radiates like a blackbody in these two bands. We have

not pursued more realistic models for the planetary emission spectrum, given that the atmospheric composition is unconstrained, but seems unlikely that atmospheric absorption features would suppress the planetary flux in both bands to such a degree that it would be undetectable in our data.

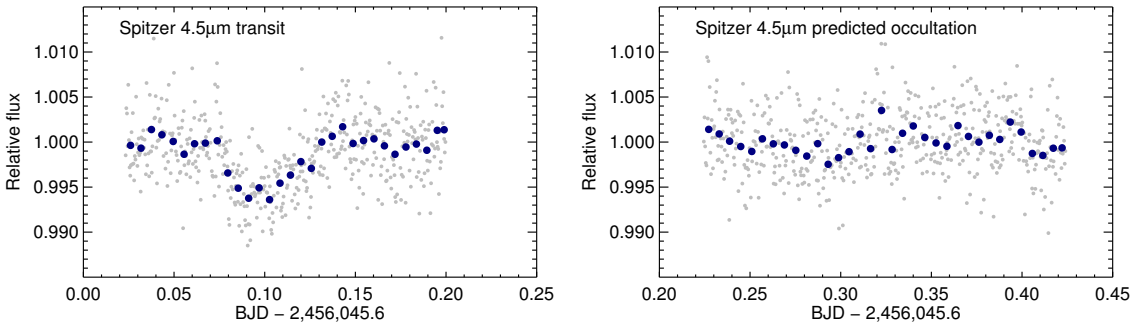

Figure 2-10 Close-up of the "transit" and "occultation" data, after rectification to unit flux outside of the events.

2.2.4 Departure from periodicity

Perhaps the most important finding of all the photometric observations is that the fading events are not strictly periodic. The top panel of Figure 2-11 shows the residuals after subtracting the best-fitting linear function of epoch from the measured times of minimum light,

$$t_n = t_0 + Pn, \tag{2.5}$$

for which $\chi^2_{\rm min} = 15573$ with 35 degrees of freedom. This poor fit is the result of the large scatter (≈15 min) of the residuals within each season, and the even larger deviation (≈1.3 hours) of the most recent season's residuals relative to the earlier data. The pattern of residuals suggests that the period was nearly constant up until the 2014/5 observing season, when the fading events began occurring earlier than expected. This apparent change in period or phase can be readily checked by gathering additional data over the next few seasons. The best-fitting parameters of

the linear ephemeris are

$$\begin{aligned} t_0 &= 2455201.832 \pm 0.007 \text{ days}, \\ P &= 0.448391 \pm 0.000003 \text{ days}. \end{aligned}$$

In these expressions the uncertainties have been scaled up by a factor of $\sqrt{\chi^2_{\rm min}/N_{\rm dof}}$ to account for the statistically poor fit.

We also tried fitting a quadratic function of epoch,

$$t_n = t_0 + P_0 n + \frac{1}{2}\frac{{\rm d}P}{{\rm d}n}n^2, \tag{2.6}$$

for which $\chi^2_{\rm min} = 4980$ with 34 degrees of freedom. After enlarging the parameter uncertainties as described above, the best-fitting parameters are

$$\begin{aligned} t_0 &= 2455201.790 \pm 0.006 \text{ days}, \\ P_0 &= 0.448438 \pm 0.000006 \text{ days}, \\ {\rm d}P/\,{\rm d}n &= (-2.09 \pm 0.25) \times 10^{-8} \text{ days epoch}^{-1}. \end{aligned}$$

The bottom panel of Figure 2-11 shows the residuals between the observed and calculated times. The implied fractional change in period per epoch, calculated as $\frac{1}{P}\frac{{\rm d}P}{{\rm d}n}$, is equal to -4.66×10^{-8}. If this period change were to continue steadily, the period would shrink to zero after $P_0/\dot{P} \sim 10^4$ years.

2.3 Spectroscopic observations

We monitored the optical spectrum of PTFO 8-8695 on the night of 2013 Dec 12 UT, employing the Keck I telescope and its High Resolution Spectrograph [HIRES; 291]. A total of 22 observations with integration times of 14 min were obtained. This sequence covered 2 hr spanning the event, and 1 hr after the event. HIRES was used in its standard setting, but without an iodine cell in the light path.

To confirm that a fading event was indeed taking place during the spectroscopic

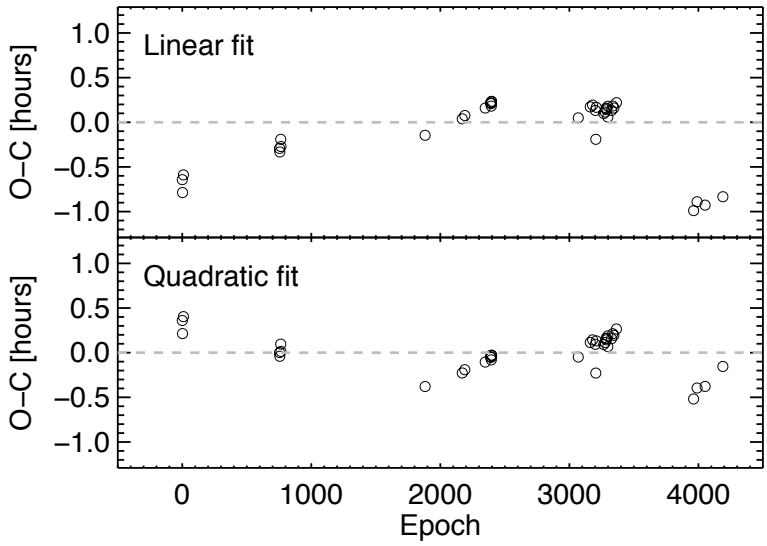

Figure 2-11 *Top panel*: Timing residuals after subtracting the best-fitting linear function of epoch(constant period). *Bottom panel*: Timing residuals after subtracting the best-fitting quadratic function of epoch (steady decrease in period).

observations, we attempted to gather simultaneous photometry with several small telescopes, but in only one case was the weather at least somewhat cooperative. We obtained data in the H band with Mimir, a cryogenic, facility-class near-infrared instrument on the 1.83 m Perkins telescope outside Flagstaff, Arizona [66]. Figure 2-12 shows the light curve. A transit-like dip of $\sim$2% was seen at the expected time, confirming that a fading event did occur, although the data are too noisy to extract much further information. We also note that fading events were seen by TRAPPIST on 2013 Dec 11 and 14, bracketing our Keck observation.

2.3.1 Search for the Rossiter-McLaughlin effect

The primary purpose of the spectroscopic observations was to seek evidence for the Rossiter-McLaughlin (RM) effect, the spectroscopic anomaly that is seen during a planetary transit due to stellar rotation. During a transit, a planet blocks different portions of the rotating stellar photosphere, leaving a particular imprint on the rotationally-broadened stellar absorption lines. The exact shape and time development of the spectral deformations depend on the transit parameters, and in particular

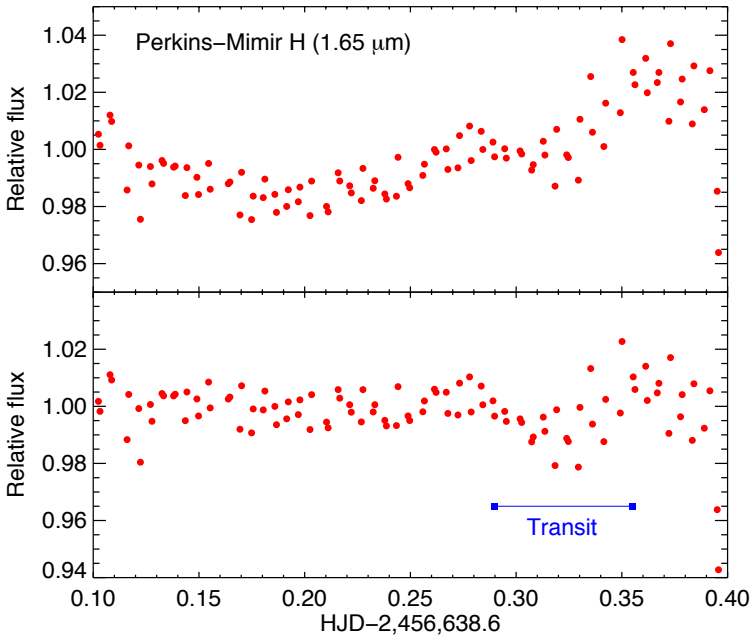

Figure 2-12 *Top panel*: Perkins-Mimir 1.65 μm photometry of PTFO 8-8695 from 2013 Dec 12. Data points are averaged in groups of 5 for clarity. *Bottom panel*: Same, but after rectification to unit flux outside of the transit. A transit signal can be seen in the region marked by the blue bar.

on the angle between the stellar rotation axis and the orbital axis as projected on the sky plane. For PTFO 8-8695, the planet hypothesis requires a large misalignment between these angles. We attempted to detect the RM effect and test that prediction.

After the initial data reduction we corrected for the blaze function by using calibration lamp exposures to estimate the blaze function for each order, and then fitting a linear function of wavelength to remove the residual variations and normalize the continuum to unity. Following the barycentric correction, all of the out-of-transit exposures were co-added to create a single spectrum with a higher signal-to-noise ratio. This was used for a final differential normalization, wherein the summed spectrum was subtracted from each observed spectrum, and a 4th-order polynomial was fitted to the residuals in each order. These polynomials were subsequently subtracted from the corresponding spectrum. This was done to minimize the potential influence of any time variations in the blaze function throughout the night. We verified that the details of this normalization process did not have a significant influence on the

following analysis.

For each spectrum, we calculated the cross-correlation function (CCF) with reference to a synthetic spectrum. The synthetic spectrum was obtained from the PHOENIX database [143], for a star with $T_{\rm eff} = 3500$ K, $\log g = 3.5$ and solar metallicity. We selected the appropriate wavelength ranges for creating the CCF via a visual inspection. We needed to locate areas for which the normalization seemed reliable, and where there were at least a few well-defined absorption lines. As had been reported by VE+12, there are only a few regions between 5000–7000 Å suitable for this work.

We calculated the mean CCF based on all of the out-of-transit observations. Then we subtracted the mean CCF from each individual CCF. When ordered in time, the resulting "differential CCFs" should display the shadow of the transiting object in velocity space. The deformation due to a transiting object would be seen as a dark line. The slope of this line in the velocity-time plane would depend on the projected obliquity. For example, in the case of good spin-orbit alignment, there would be a deficit of blue light (negative radial velocities) in the first half of the transit, followed by a deficit of redshifted light during the second half. As can be seen in Figure 2-13, no such signal — neither aligned nor misaligned — can be discerned.

Could we have detected the spectroscopic transit of the hypothetical planet, given the quality of our data? To answer this question, we simulated the RM signal of a transiting planet with $(R_p/R_\star)^2 = 0.026$, the approximate transit depth measured by TRAPPIST during the events of 2013 Dec 11 and 14, closely bracketing the event observed with Keck. We assumed $v \sin i_\star = 100$ km s^{-1}, a value consistent with the line broadening seen in our Keck spectra, and adopted a macroturbulent velocity of 15 km s^{-1}. Then we injected RM signals into the data, for various choices of λ, the sky-projected stellar obliquity.

Some representative examples of the simulated RM effect are shown in Figure 2-14. The left panel shows the simulated RM signal of a well-aligned planet ($\lambda = 0°$). Such a signal would easily have been detectable with the data at hand. The same is true for $\lambda = 45°$, shown in the middle panel. However, for $\lambda = 90°$, the signal

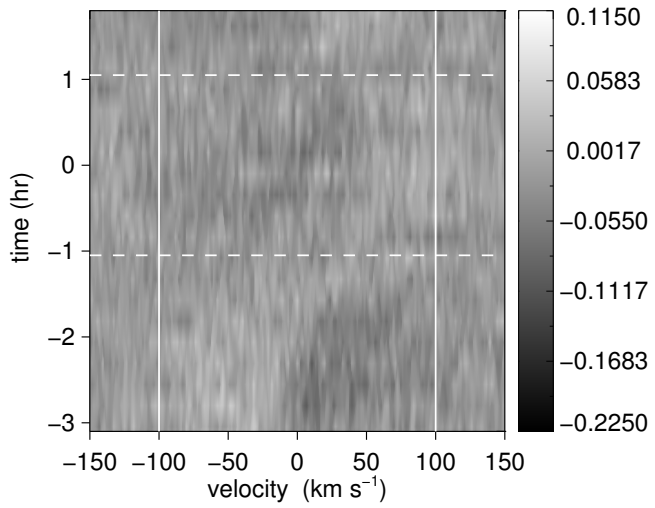

Figure 2-13 Time variations of the CCF during the night of 2013 Dec. 11/12. Dark areas indicate a deficit relative to the mean CCF on that night. The CCFs have been normalized to have a peak value of unity. The dashed lines indicate the predicted times of first and last contact. Vertical lines indicate our estimate for $v \sin i_\star$. One can see variations of the CCFs before, during, and after the transit. No clear sign of a planetary transit is visible.

would have been more difficult to detect. This is because in this case the RM signal is nearly stationary in velocity, as shown in the right panel, making it more difficult to separate from the noise in the velocity–time plane. Based on visual inspection of figures similar to Figure 2-14 we conclude that we can rule out any trajectory except for those within about 15° of perpendicularity ($\lambda = 90°$ or 270°). Given the non-Gaussian and correlated nature of the noise, it is difficult to make a firmer statistical statement.

2.3.2 Projected rotation rate

A secondary goal was to seek changes in the sky-projected rotation rate ($v \sin i_\star$) that would be expected if the star's rotation axis is precessing around the total angular momentum of the system. If PTFO 8-8695 does consist of a star and a planet whose rotation axes and orbits precess around the common angular momentum, then $v \sin i_\star$ should change with time. We searched for such a change between the two epochs for

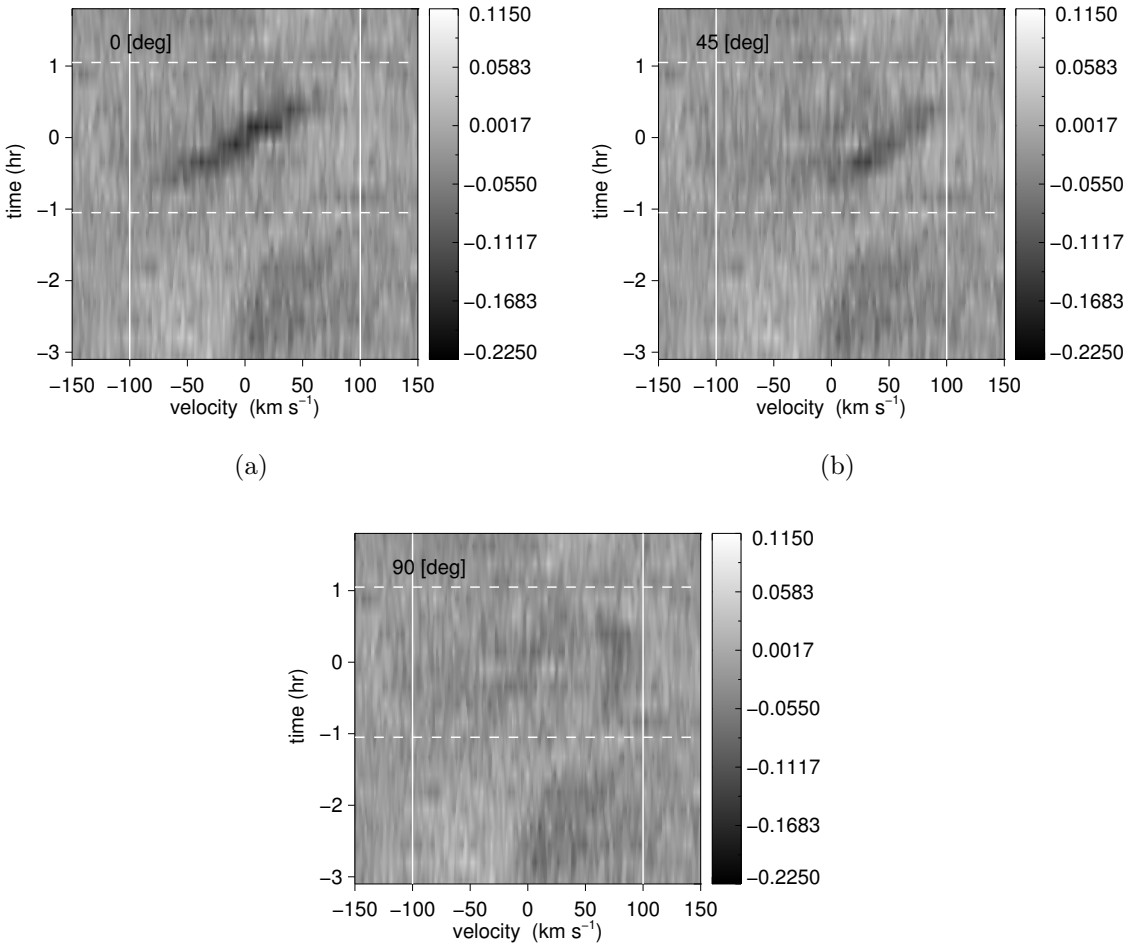

(a) (b) (c)

Figure 2-14 Same as Figure 2-13, but in this case an artificial signal of a transiting planet has been injected. Panel (a) shows the case $\lambda = 0°$ (spin-orbit alignment), panel (b) shows $\lambda = 45°$ and panel (c) shows $\lambda = 90°$.

which Keck/HIRES data have been obtained. Five spectra were obtained in April 2011 and presented by VE+12. Another epoch is represented by our December 2013 data.

We derived CCFs from the 2011 data in exactly the same way as for the 2013 data. We compared the CCFs with theoretical absorption lines taking into account uniform rotation, limb darkening, macroturbulence, and gravity darkening. We adopted the quadratic limb darkening parameters from the tables of Claret et al. [65] for $\log g = 3.5$ and $T_{\rm eff} = 3500$ K, solar metallicity, and the Johnson V band. We adopted a

macroturbulent velocity of 15 $\mathrm{km\,s^{-1}}$. To model the gravity darkening we assumed the same effective temperature, a rotation period of 0.448 days, a stellar mass of 0.4 $M_{\odot}$, a stellar radius of 1.4 $R_{\odot}$, a stellar inclination angle of 90°, and a gravity-darkening exponent of $\beta = 0.25$. We neglected any oblateness of the stellar photosphere. As an example, Figure 2-15 shows the CCF for one of the pre-transit observations from Dec 2013, along with the best-fitting model.

The results for $v \sin i_{\star}$ are 103.6 ± 0.3 $\mathrm{km\,s^{-1}}$ in 2011, and 104.1 ± 0.7 $\mathrm{km\,s^{-1}}$ in 2013. The quoted uncertainties are based on the scatter between the different observations for each epoch, and do not include any additional systematic uncertainties due to the limitations of the model (such as uncertainties in the treatment of limb darkening and gravity darkening, or the neglect of differential rotation and oblateness). Therefore the relative variation in $v \sin i_{\star}$ is bounded to less than a percent, although the absolute value is probably uncertain by at least 10%.

To obtain a better idea about the absolute value of $v \sin i_{\star}$ and its uncertainty, we tried fitting individual absorption lines rather than the CCF. Specifically, we fitted seven apparently isolated lines between 5300 and 7700 Å. The standard deviation in the $v \sin i_{\star}$ measurement form these seven absorption lines varies between $7-15$ $\mathrm{km\,s^{-1}}$ for the different observations, which suggests that an uncertainty of 10 $\mathrm{km\,s^{-1}}$ in $v \sin i_{\star}$ should be a reasonable estimate. This leads to our final estimate of 103 ± 10 $\mathrm{km\,s^{-1}}$.

Our result for $v \sin i_{\star}$ is higher than the value of 80.6 ± 8.1 $\mathrm{km\,s^{-1}}$ reported by VE+12, but we do not think that this necessarily (or even likely) implies that the projected rotation rate is varying in time. This is because it is difficult to compare the results directly, given that VE+12 used a completely different instrument and analysis technique. Our internal comparison is much more sensitive, since it is between two Keck/HIRES spectra obtained at different times and analyzed in exactly the same way.

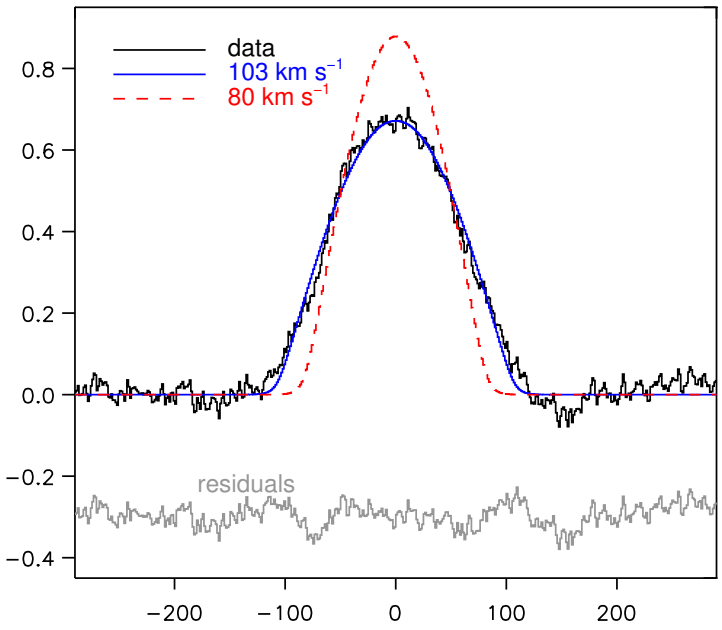

Figure 2-15 CCF for the pre-transit observation from Dec. 2013 (black), along with the best-fitting model with $v \sin i_\star = 103$ km s^{-1} (blue). The red dashed line represents a model with $v \sin i_\star = 80$ km s^{-1}, the value reported by VE+12. The gray line shows the differences between the data and the best-fitting (blue) model, vertically offset by 0.3 units for clarity.

2.3.3 Time variations in emission-line profiles

Our optical spectra also reveal strong emission lines from the hydrogen Balmer series as well as the Ca II H & K transitions. The top panel of Figure 2-16 shows the median Hα line profile, based on all the "out-of-transit" spectra observed on 2013 Dec 12 (at least an hour before or after the time of minimum light). The line is very broad. Most of the emission is confined to velocities $\lesssim$100 km s^{-1}, consistent with the star's rotation rate, but the velocity profile extends to at least 300 km s^{-1}, particularly on the blue side. This is suggestive of at least a low level of ongoing accretion. Material that falls onto the star from large distances could attain the free-fall velocity $\sqrt{2GM_\star/R_\star} \approx 330$ km s^{-1}, given the nominal parameters $M_\star = 0.4\ M_\odot$ and $R_\star = 1.4\ R_\odot$. The equivalent width of the Hα line is 8.7 Å, placing the star near the traditional borderline between the categories of "weak-lined" and "classical" T Tauri stars. For simplicity it is often said that the classical stars are actively accreting while

the weak-lined stars are not accreting, although in reality there seems to be no sharp distinction between these categories, and PTFO 8-8695 presents an intermediate case.

Figure 2-16 also shows the time sequence of observed changes in the Hα line profile. Specifically, for each of the 22 spectra, we plotted the residuals between the observed line profile and the median "out-of-transit" line profile. Also indicated are the times of minimum light, as well as "ingress" (one hour prior) and "egress" (one hour afterward). The red dashed line indicates a slope of 37 km s^{-1} hr^{-1}. This is the expected radial acceleration of any feature attached to the stellar photosphere, which would move from -100 km s^{-1} to $+100$ km s^{-1} over the course of $P_{\rm rot}/2 = 0.224$ days.

Evidently the line profile varied in a complex pattern on a timescale of minutes. Several excess-emission features do seem to be rotating along with the star; for example, a pattern of positive residuals appears in the fourth-to-final spectrum (time coordinate $t = 1.015$) at velocity $+50$ km s^{-1} and shifted redward at the expected rate throughout the final three observations. A similar pattern – perhaps originating from the same feature – is seen starting at minimum light at velocity -50 km s^{-1} and proceeding redward until about an hour after minimum light. These particular components of the emission line seems likely to be caused by active regions on the stellar surface.

During the fading event, the residuals show relative absorption at a redshifted velocity of 25–100 km s^{-1}. The absorption seemed to disappear at around the same time as the end of the fading event. The onset of the absorption feature was at least 2 hours before minimum light, which is at least an hour before what seems to be "ingress" of the fading event. Thus, the transient redshifted absorption does not seem to be exactly coincident with the fading event, although it does at least suggest that the fading event was associated with hot infalling material in front of the star.

The Hγ line profiles (not shown here) tell a similar story but with a lower signal-to-noise ratio. The Hβ line was not observed, given the spectral format. Figure 2-17 shows the median Ca II H line profile, along with the time series of deviations from the median. In this case the fractional variations were even stronger and seemingly faster; there is no straightforward narrative to the sequence of residuals.

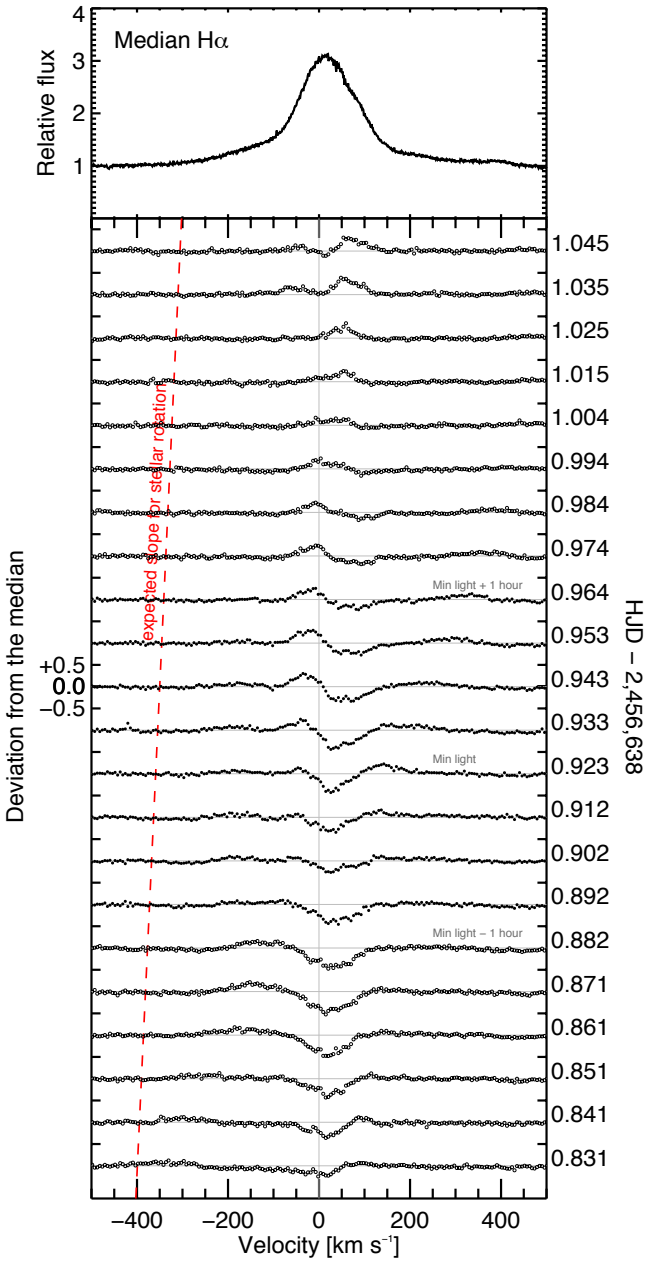

Figure 2-16 The Hα line profile of PTFO 8-8695 on 2013 Dec 12. *Top.*—Median line profile, based on all spectra more than one hour away from minimum light. *Bottom.*—Time series of residuals between each observed spectrum and the median. Open symbols are the "out-of-transit" spectra used to create the median spectrum. Filled symbols are the spectra within one hour of minimum light. On the left axis, each vertical tick mark represents one unit of relative flux, on the same scale as the top panel. The right axis gives the time of each spectrum.

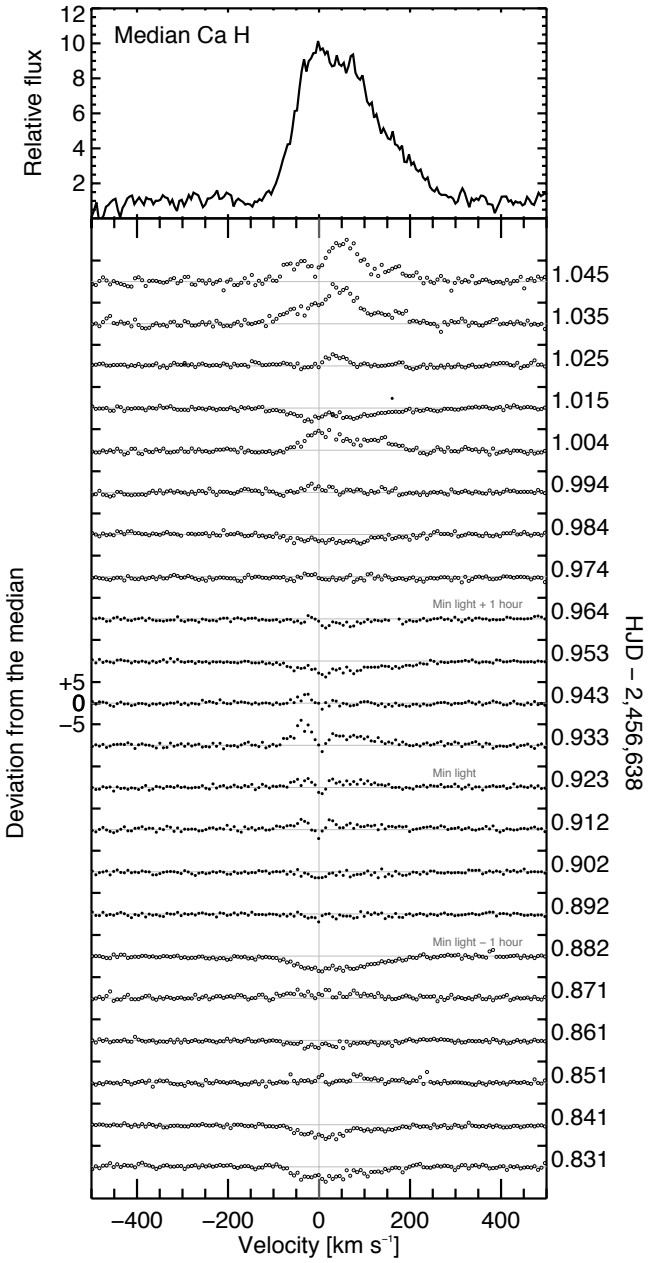

Figure 2-17 The Ca II H line profile of PTFO 8-8695 on 2013 Dec 12. *Top.*—Median line profile, based on all spectra more than one hour away from minimum light. *Bottom.*—Time series of residuals between each observed spectrum and the median. Open symbols are the "out-of-transit" spectra used to create the median spectrum. Filled symbols are the spectra within one hour of minimum light. On the left axis, each vertical tick mark represents 5 units of relative flux, on the same scale as the top panel. The right axis gives the time of each spectrum.

To seek independent evidence for ongoing accretion, we used the available broadband photometry to construct the spectral energy distribution of PTFO 8-8695 and search for any infrared excess. Figure 2-18 shows the result, based on a query of the VizieR website[4], which gave measurements in the $VRJHK$ bands as well as the *WISE* $W1$-$W4$ bands. (The $W4$ observation gave an upper limit.) We corrected for dust extinction with the dust map from the NASA/IPAC website[5], and fitted the results to a grid of zero-metallicity stellar atmosphere models from the library of Castelli & Kurucz [55]. The best-fitting stellar parameters were $T_{\rm eff} = 3500 \pm 120$ K and $\log g = 4.0 \pm 0.9$. The effective temperature is in agreement with the previously reported value of 3470 K [44]. The apparent lack of an infrared excess out to 10 μm is characteristic of weak-lined T Tauri stars. This lack of evidence for the existence of an accretion accretion disk within 1 AU does not necessarily rule out accretion, but does suggest that any accretion is relatively weak.

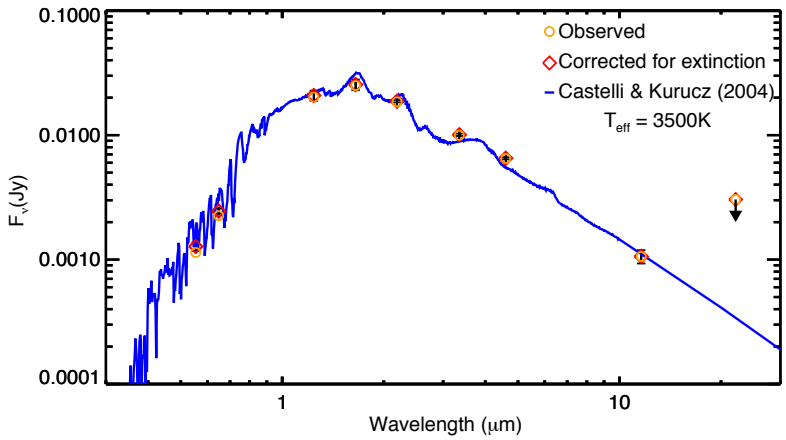

Figure 2-18 Spectral energy distribution of PTFO 8-8695 based on publicly available broadband photometry (orange diamonds), along with the best-fitting stellar atmosphere model (blue line). The data were corrected for extinction (red diamonds) prior to fitting. There is no evidence for any infrared excess that could be attributed to a circumstellar disk.

[4]http://vizier.u-strasbg.fr
[5]http://irsa.ipac.caltech.edu

2.4 Discussion

We now summarize the results of the three tests that we undertook to test the hypothesis that the fading events of PTFO 8-8695 are the transits of a close-in giant planet:

1. The new light curves show variations in depth and duration from event to event. However we did not find strong evidence for asymmetries or other secular changes in morphology indicative of the changing trajectory of a transiting planet. Furthermore, in all cases, a fading event was observed at the appointed time, even though the cessation of transits was predicted to be likely by Barnes et al. [19].

2. Infrared photometry spanning the predicted times of planetary occultations has ruled out signals of the expected amplitude.

3. The Rossiter-McLaughlin effect could not be detected, ruling out a transiting planet with the expected parameters, unless the planet's trajectory is nearly perpendicular to the projected stellar equator. Nor did we detect any changes in $v \sin i_\star$ between 2011 and 2013, which would have been produced by precession of the stellar rotation axis.

Any of these tests could have resulted in a confirmation of the planet hypothesis. In all cases, though, the planet hypothesis was disfavored. In addition we found that the fading events are not strictly periodic. In the most recent observing season the events occurred more than one hour earlier than expected. This finding is incompatible with the strict periodicity that one expects for a planetary orbit.

While this paper was in preparation we learned of the work by Ciardi et al. [63] and Koen [159], who also pursued follow-up observations of PTFO 8-8695. Among the observations of Ciardi et al. [63] was a nondetection of any transit-like event on 2012 Dec 21, based on observations in the r' band. They gave an upper limit of 0.7% on the transit depth. Their simultaneous spectroscopy also revealed no evidence of the Rossiter-McLaughlin effect. They interpreted these nondetections as evidence

for the predicted cessation of the transits. However, our observations reveal that the fading events did indeed take place on 2012 Dec 11, 14, and 15, with a depth of approximately 3% in all cases. It seems unlikely that orbital precession could have abruptly reduced the transit depth from 3% to below 0.7% in less than one week. Therefore our results cast doubt on this aspect of the interpretation of Ciardi et al. [63]. Likewise, Koen [159] reported non-detections of predicted fading events on 2015 Jan 3-4. However, the predicted times were based on the assumption of strict periodicity, which our observations have shown to be false. Judging from Fig. 2 of Koen [159], it seems possible that the fading events were recorded in the SAAO observations a few hours earlier than expected. In any case we detected a clear 2% fading event on 2014 Dec 27, only one week earlier than the SAAO observations.

In summary, our observations have significantly reduced the credibility of the planet hypothesis. However, because the hypothesis invokes an unusual planet in unusual circumstances, it is difficult to rule out definitively. It may be possible to find reasons for the failure of each of the individual tests. For example, the predicted occultation times might have been incorrect, because the planet has a highly eccentric orbit (see § 2.2.3.2). Or perhaps the values of the key parameters $(R_p/R_\star)^2$ and $R_\star/a$ are smaller than the values postulated by [19], which would reduce the predicted occultation depth. The planet's atmosphere might have deep absorption features near 1.7 μm and 4.5 μm that rendered the planetary occultations undetectable. The planet's orbit might have been nearly perpendicular to the stellar equator at the time of our attempt to detect the Rossiter-McLaughlin effect. It remains possible that a comprehensive search of parameter space of the model proposed by [19] — including the effects of gravity darkening and orbital precession — could reveal a configuration that possesses these properties and is also compatible with the lack of detectable change in $v \sin i_\star$, as well as the unexpectedly bland morphologies, strongly chromatic depths, lack of occultation signals, and timing irregularities that are seen in the new light curves. We leave such a computationally intensive search for future work. It is also important to try and develop alternative hypotheses for the fading events of PTFO 8-8695. Below we describe four alternatives, along with their apparent

strengths and weaknesses. Figure 2-19 illustrates these hypotheses.

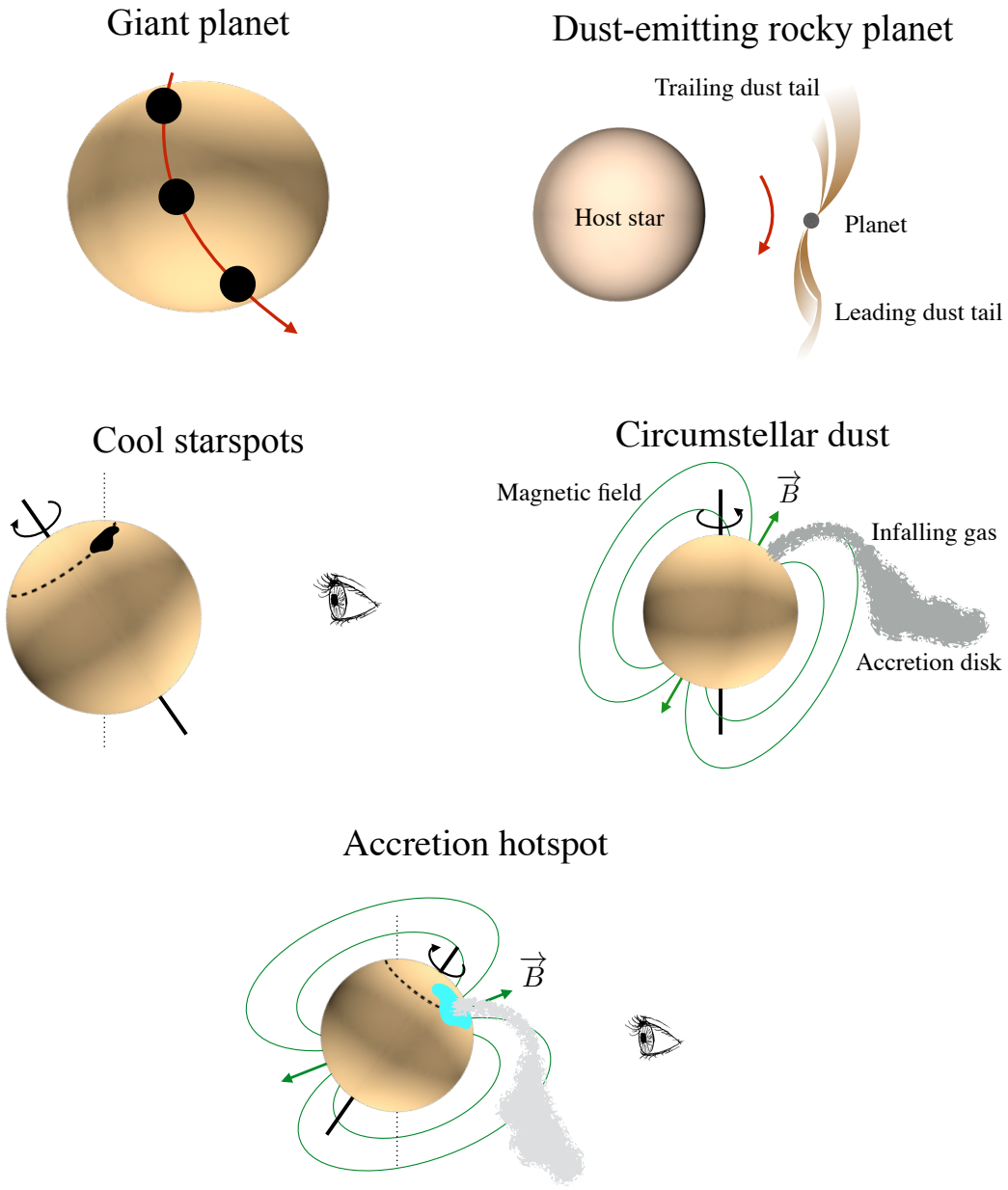

Figure 2-19 Illustrations of the five hypotheses discussed in Section 2.4.

2.4.1 Dust-emitting rocky planet

The seemingly erratic variations in the depth and duration of the fading events, along with the slight asymmetries in the phase-folded light curves (Figure 2-5), bring to mind the case of KIC 12557548 [237]. This object was identified in data from

the *Kepler* spacecraft. It exhibits transit-like flux dips with a very short period (15.7 hours) and duration (1.5 hours), an erratically varying depth ranging from 0–1.3%, and an egress of longer duration than ingress. Rappaport et al. [237] interpreted the dips as transits by a dusty tail being emitted by a small rocky planet. Two other similar cases have since been identified [235, 246]. In at least one case the transit depth has been shown to be smaller at infrared wavelengths, as expected for extinction by small dust grains.

PTFO 8-8695 shares much of the phenomenology that has just been described. The main difference is that the other systems are not rapidly-rotating young stars. They appear to be slowly-rotating main-sequence stars, and are not even close to being synchronized with the transit period. Furthermore it is not clear whether this hypothesis could be reconciled with the apparent change in period that was seen in the most recent season of observations.

It is tempting to invoke tidal dissipation as a mechanism for gradually shrinking the orbit and shortening the period, but this is implausible for a low-mass rocky body. Conceivably, orbital decay could be a consequence of the dust emission. If the dust acquires additional specific angular momentum from radiation pressure while leaving the system, it would be driven into a higher orbit. There it would pull back on the planet and potentially extract angular momentum from the planetary orbit. However, the magnitude of this effective drag is difficult to estimate from first principles, particularly because the dust may represent only a modest fraction of the total mass loss, and the gas need not behave the same way as dust as it leaves the system. In any case the lifetime of $\sim 10^4$ years implied by the observations (see § 2.2.4) is uncomfortably short. It would require a special coincidence to observe such a short-lived phase of evolution.

2.4.2 Starspots

The synchronization of the stellar rotation period and the period of the fading events, along with the changing depth and duration of the fading events, raises the suspicion that the periodic dips are caused by starspots being carried around by rotation. The

star is expected to be heavily spotted, given its youth. Moreover, the photometric variations produced by stellar activity are expected to be weaker in the infrared than in the optical, consistent with our observations. Gradual changes in the spot pattern could be invoked to explain the changes in depth, duration, and timing of the fading events.

VE+12 have already pointed out the main weakness of this hypothesis. Flux variations caused by starspots have a natural timescale of half the rotation period, the interval over which a patch of the stellar surface is typically visible to the observer. In contrast, the fading events of PTFO 8-8695 last only ≈15% of the rotation period. One can arrange for short-duration dips by locating the starspots near one of the rotation poles, and tipping the star such that the spots are only on the visible hemisphere over a narrow range of longitudes. Indeed, T Tauri stars are well known for displaying stable spot patterns near the magnetic poles [e.g. 115]. However, in such a circumstance the spot is highly foreshortened and limb-darkened, and it is difficult to produce variations of several percent. It is also difficult to produce the apparently sharp features that have been occasionally seen in the light curves, such as the apparent point of "fourth contact" in our Magellan H-band time series (see the bottom panel of Figure 2-6). It might be possible to save this hypothesis by invoking multiple spots and in a complex and stable pattern, such that the summation of their photometric variations is coincidentally narrow in time. This model, though, would be rather contrived.

2.4.3 Eclipses by a circumstellar disk or dust

As we have just seen, the basic difficulty of any model in which the variations are due to features on the stellar photosphere is the relatively short duration of the fading events. Eclipses by orbiting bodies avoid this problem because the time spent in front of the star scales as $R_\star/a$, and the orbital distance a can be adjusted to match the observations. This is the basis of the planet hypothesis, for which Barnes et al. [19] found $R_\star/a = 0.5$–0.6. However the eclipsing body need not be a planet. Perhaps it is a feature in the innermost, corotating portion of the stellar magnetosphere.

At an age of a few million years, low-mass T Tauri stars are often still actively

accreting material from their circumstellar disks. PTFO 8-8695 lacks any evidence for an accretion disk, yet, as noted in § 2.3.3, the strength and breadth of the Hα line profile places the star in between the traditional categories of "classical" and "weak-lined" T Tauri stars and suggest that PTFO 8-8695 may be weakly accreting. So we will consider the implications of a small amount of dust that would not be detected as an IR excess, but would still be able to produce the flux dips. The accretion process is thought to proceed as follows [see, e.g., 40, for a review]. First, matter spirals inward through a thin disk, until it reaches an orbital distance of a few stellar radii, at which point the disk is disrupted by the star's magnetosphere. Then, within the magnetosphere, the material is magnetically funneled into narrow tubes or columns, extending from the inner edge of the accretion disk onto the star's magnetic poles. The material falls freely along these columns and crashes onto the star, producing shock waves and a luminous hotspot. In many models, the stellar rotation rate becomes synchronized with the Keplerian orbital velocity at the inner radius of the magnetosphere (the corotation radius), a phenomenon known as disk locking.

This picture contains several elements that could naturally lead to flux variations with a period equal to the stellar rotation period. For example if the accretion disk is warped or has other non-axisymmetric variations in thickness near the innermost, corotating portion of the disk, then the star may be periodically eclipsed by these irregularities. This is thought to be the basic explanation for the quasiperiodic eclipses of AA Tau [38, 39]. Alternatively, periodic eclipses could be produced by stable patterns or concentrations of dust in the accretion flow. This may explain the observed variability of the "short-duration dippers" recently identified by Cody et al. [68] and Stauffer et al. [263]. Those authors studied a number of T Tauri stars in the young cluster NGC 2264 that exhibit short-duration fading events. They found that the flux dips are quasi-periodic and exhibit changes in depth and shape from epoch to epoch over a period of several years. The dips appear shallower in the infrared than in the optical, and the light curves have rounded minima rather than being flat-bottomed [263]. The flux dip periods are usually equal to the rotation periods of the stars,

and some dips have been observed to persist for years. All these properties have been attributed to extinction by infalling material from the innermost portion of the accretion disk [200]. And, all these properties are consistent with our observations of PTFO 8-8695.

In some respects, though, PTFO 8-8695 is different from the rest of the dippers. Its rotation period of 0.45 days is shorter than the 3–10 day periods of most of the stars observed by Cody et al. [68] and Stauffer et al. [263], or the 8 day period of AA Tau. The duration of the fading events is also relatively shorter at 15% of the period, compared to the more typical value of ∼30%. It is also unclear whether disk warps or dust concentrations could produce the apparently sharp features and flat bottoms observed in a few of our light curves. Furthermore, the dippers all have SEDs with a detectable infrared excess, but the currently available data for PTFO 8-8695 show no evidence for any infrared excess (Figure 2-18).

Furthermore, it is questionable whether dust can exist in solid form so close to the star, with an orbital distance less than 2 $R_\star$. Assuming that stellar radiation is the dominant mechanism of heating, the dust sublimation radius R_s is given by [204]

$$R_s = \frac{1}{2}\sqrt{Q_R}\left(\frac{T_\star}{T_s}\right)^2 R_\star \tag{2.7}$$

where T_s is the dust sublimation temperature (≈1500 K), and $Q_R = Q_{\rm abs}(T_\star)/Q_{\rm abs}(T_s)$ is the ratio of the dust absorption efficiencies for radiation at the color temperatures of the incident and reemitted fields, respectively. Adopting the customary value of $T_s = 1500$ K, and assuming Q_R to be of order unity (as expected in this case for silicate grains), this formula gives $R_s = 2.7\ R_\star$. Therefore the hypothesized dust with $R_\star/a$=0.5–0.6, corresponding to a =1.7–2 $R_\star$, would likely be vaporized.

2.4.4 Occultations of an accretion hotspot

Hotspots are another aspect of the magnetospheric accretion model that has previously been invoked to explain some of the quasiperiodic variations of T Tauri stars [129]. We advance here a related hypothesis for the case of PTFO 8-8695: perhaps

the fading events represent occultations of one of the hotspots that is produced by ongoing low-level accretion. In this scenario, the accreting material is funnelled onto a hotspot near one of the star's magnetic poles, which is displaced from the star's rotation pole. Furthermore, the star's rotation pole is tipped toward the observer such that the hotspot is on the visible hemisphere for ≈85% of each rotation period. When the hotspot is hidden from view, we observe a fading event.

This is similar to the starspot hypothesis (§ 2.4.2) in that the photometric modulations are the result of the rotation of a photospheric feature of contrasting intensity. However, replacing the dark starspot with a luminous hotspot could potentially solve some of the problems faced by the starspot model. Hotspots have been inferred to have effective temperatures ranging up to 10^4 K, and thereby present much higher contrast than starspots with the surrounding photosphere. Furthermore, hotspots are probably not confined to a vertically thin surface layer of the photosphere, and as such they are not subject to the effects of limb-darkening or foreshortening. Together these factors may make it easier to produce abrupt modulations of a few percent in the total light even for a small feature near the stellar limb.

If this model is correct, then the mass accretion rate can be estimated from the loss of light during fading events, which is observed to be of order 5%. This requires the accretion luminosity to be

$$L_{\rm acc} = \frac{GM_\star \dot{M}}{R} \sim 0.05\ L_{\rm bol}. \tag{2.8}$$

Using the nominal values $M_\star = 0.4\ M_\odot$, $R = 1.4\ R_\odot$, and $L_{\rm bol} = 0.25\ L_\odot$, we find $\dot{M} \sim 10^{-9}\ M_\odot\ {\rm yr}^{-1}$, at the low end of the range of mass accretion rates that has been inferred for accreting T Tauri stars (10^{-9}–$10^{-7}\ M_\odot\ {\rm yr}^{-1}$). This seems reasonable: a relatively low accretion rate is also consistent with the relatively weak Hα equivalent width of 8.7 Å and the absence of a detectable infrared excess.

One concern with this model is that in the systems where hotspots have been previously invoked to explain photometric variability, the pattern of variability is not as consistent or long-lasting as is seen in PTFO 8-8695 [129]. Oftentimes the hotspot

variability shows no periodicity or, at best, short-lived periodicity, sometimes with period changes of 20% or more. However, those previous results pertain to classical T Tauri stars with much higher inferred accretion rates; perhaps we are seeing the different and more stable behavior of a hotspot in a more weakly accreting system.

2.4.5 Summary

We have discussed five hypotheses for the fading events of PTFO 8-8695. The precessing giant-planet model has failed several key tests, the most serious of which are probably the nondetection of the planetary occultations, and the apparent shift in the phase of the fading events in the most recent season of observations. The planet hypothesis also struggles to explain the observed coincidence of the rotation and orbital periods. This same problem afflicts the hypothesis of the dust-emitting rocky planet.

The other three models share the virtue of a natural explanation for the equality of the rotation period and the period of the fading events. However, the starspot model has difficulty reproducing the observed duration and occasionally sharp ingress/egress of the fading events. The other two models invoke the presence of an accretion disk, for which the evidence is ambiguous or negative: the Hα line profile does extend to higher velocities than can be explained by stellar rotation, but the equivalent width is relatively low and there is no detectable infrared excess.

The occulted-hotspot model seems quantitatively promising, as it is consistent with a low accretion rate of $\sim 10^{-9}$ $M_\odot$ yr^{-1}. There is no deterministic theory for the expected photometric variations due to magnetically-funnelled accretion, making it difficult to achieve a firm confirmation of this hypothesis. Nevertheless all our observations seem at least consistent with this picture. At present, we consider this hypothesis to be the best explanation for PTFO 8-8695. To come to a firmer conclusion will probably require more photometric and spectroscopic observations, seeking changes in the timing and behavior of the fading events, variations in the Hα line profile, and more sensitive searches for any infrared (or ultraviolet) excess or other indicators of low-level accretion.

At the outset of this project, and throughout most of this paper, we have been mainly concerned with the status of the planetary hypothesis for this intriguing planetary candidate. In fact this object may turn out to be useful for understanding magnetospheric accretion, due to a fortuitous geometry, thereby joining the ranks of such systems as AA Tau [38] and KH 15D [122].

Chapter 3

The Road to More Data: *K2* and Data Processing Techniques

The content of this chapter was submitted to AJ *on March 11, 2018 and published [304] on June 21, 2018 as* Planetary Candidates from *K2* Campaign 16*, by Liang Yu, Ian J. M. Crossfield, Joshua E. Schlieder, Molly R. Kosiarek, Adina D. Feinstein, John H. Livingston, Andrew W. Howard, Björn Benneke, Erik A. Petigura, Makennah Bristow, Jessie L. Christiansen, David R. Ciardi, Justin R. Crepp, Courtney D. Dressing, Benjamin J. Fulton, Erica J. Gonzales, Kevin K. Hardegree-Ullman, Thomas Henning, Howard Isaacson, Sébastien Lépine, Arturo O. Martinez, Farisa Y. Morales, and Evan Sinukoff.*

Given that Campaign 16 of the *K2* mission is one of just two *K2* campaigns observed so far in "forward-facing" mode, which enables immediate follow-up observations from the ground, we present a catalog of interesting targets identified through photometry alone. Our catalog includes 30 high-quality planet candidates (showing no signs of being non-planetary in nature), 48 more ambiguous events that may be either planets or false positives, 164 eclipsing binaries, and 231 other regularly periodic variable sources. We have released light curves for all targets in C16, and have also released system parameters and transit vetting plots for all interesting candidates identified in this paper. Of particular interest is a candidate planet orbiting the bright F dwarf HD 73344 ($V = 6.9$, $K = 5.6$) with an orbital period of 15 days. If

confirmed, this object would correspond to a 2.56 ± 0.18 $R_\oplus$ planet and would likely be a favorable target for radial velocity characterization. This paper is intended as a rapid release of planet candidates, eclipsing binaries and other interesting periodic variables to maximize the scientific yield of this campaign, and as a test run for the upcoming *TESS* mission, whose frequent data releases call for similarly rapid candidate identification and efficient follow-up.

3.1 Introduction

By any measure, NASA's *K2* mission [136] has been a success. Out of the ashes of an ailing spacecraft has risen a tremendously productive scientific mission. Sometime this year, *K2* will likely run out of the propellant needed to maintain its stable pointing and deliver precise time-series photometry. 2018 is perhaps an appropriate year for this event, since it marks the 40 year anniversary of the first American summit of K2 — the "Savage Mountain". Hundreds of planets and other astrophysical phenomena have been studied with *K2*, far fewer than the thousands discovered by the original *Kepler* mission [276] — just as thousands of climbers have summited Mount Everest even though only hundreds have ever reached the top of K2. Nonetheless, even after the mission ends, an enduring kinship will remain between those who have been fortunate enough to use *K2* in their research efforts.

In that same communal spirit, we provide a rapid, public release of light curves, planet candidates, and other interesting periodic variables from *K2*'s Campaign 16 (C16) in this paper. Unlike most fields observed by *K2*, C16 was observed in "forward-facing" mode, meaning that the field was observable throughout the night as soon as the campaign ended. We have conducted a quick-look analysis of uncalibrated C16 cadence data and are releasing these data products in order to maximize the scientific yield of this campaign. We hope that this will also provide a test for the imminent *TESS* mission, whose frequent data releases will also benefit from rapid candidate identification and follow-up.

This chapter is organized as follows: in Sec. 3.2, we describe how we compute

time-series photometry and search for transit-like signals; Sec. 3.3 then discusses our approach for discriminating between various astrophysical signals and measurement noise; finally, in Sec. 3.4 we conclude by discussing several particularly interesting systems and reviewing the overall C16 candidate sample.

3.2 *K2* Targets and Photometry

3.2.1 Target Selection and C16 Data Characteristics

K2 target selection is entirely community driven, with all targets selected from Guest Observer (GO) proposals. Our team has proposed large samples of F, G, K, and M dwarfs for every *K2* Campaign up to Campaign 17, but in the analysis that follows we use data from all *K2* GO proposals to maximize the science yield from this campaign.

During C16, *K2* observed 20647 stars in a field centered at RA = 08:54:50, Dec = +18:31:31, for a period of 80 days between 2017 Dec 07 and 2018 Feb 25. This is only the second campaign in which the spacecraft was pointed along the forward-facing direction of its velocity vector (the other, C9, was dedicated mostly to microlensing and was in a dense field unsuited for standard transit searches). Forward-facing observations enable simultaneous observations from the ground and with *K2*, and also allow the field to be accessed from ground-based observatories as soon as compelling targets can be identified. C16 also overlaps with C5 except for a 40 px-wide strip that is not on silicon in C16. We find that 6167 targets observed in C16 were also observed in C5.

3.2.2 Time-Series Photometry

Raw cadence pixel data for C16 became available on the Mikulski Archive for Space Telescopes (MAST)[1] on 2018 Feb 28. We first convert the raw cadence data into target pixel files with `kadenza`[2] [17], following the approach described in Christiansen et al. [61].

[1] https://archive.stsci.edu/k2/
[2] https://github.com/KeplerGO/kadenza

From then on we process the data using a photometric pipeline that has been described in detail in past works by members of our team [e.g. 76, 226, 228]. In brief, we follow an approach similar to that originally outlined by Vanderburg & Johnson [286]. We compute the raw photometry by summing the flux within a soft-edged, stationary, circular aperture centered on each target star. During *K2* operations, solar radiation pressure causes the telescope to roll around its boresight. Consequently, stars trace out small arcs of up to several pixels every ~ 6 hr. Interpixel sensitivity variations and aperture losses can then lead to significant changes in the brightness of stars that dominate *K2* photometry.

To correct for these motion-dependent systematics, we solve for the roll angle between each frame and an arbitrary reference frame using roughly 100 stars of Kepler magnitude $Kp \sim 12$ mag on an arbitrary output channel (we typically use channel 4). Then we use the publicly available `k2phot` photometry code[3] to model the time- and roll-dependent brightness variations using a Gaussian process with a squared-exponential kernel. The models can be individually applied to the raw photometry to produce photometry corrected for motion-dependent systematics or fully detrended photometry. Fig. 3-1 shows an example of raw *K2* photometry for a relatively well-behaved star, along with the same light curve after correction for systematics and subsequent detrending. Some light curves with relatively deep transits, as in this example, show small increases in flux immediately before and after the transits. These are artifacts from the detrending process. The transits are effectively outliers on short timescales that may bias the Gaussian process model, leading to overfitting.

We repeat this photometry process for apertures with radii ranging from 1 to 7 pixels, and also fit a custom, automatically-generated aperture that selects pixels based on how much flux they receive relative to the background. This aperture has an irregular shape and captures most of the flux from each target. For each target we adopt the aperture that minimizes the residual noise on 3 hr timescales. Specifically, we use the median absolute deviation (MAD) of the 3 hr Single Event Statistic (SES) as our noise metric. We define the SES as the depth of a box-shaped

[3] https://github.com/petigura/k2phot

dimming relative to the local photometric level. This method of aperture selection favors smaller apertures, which incur less background noise, for fainter stars and larger apertures for brighter targets. For strongly saturated stars the custom aperture is typically chosen, since in these cases circular apertures miss substantial flux.

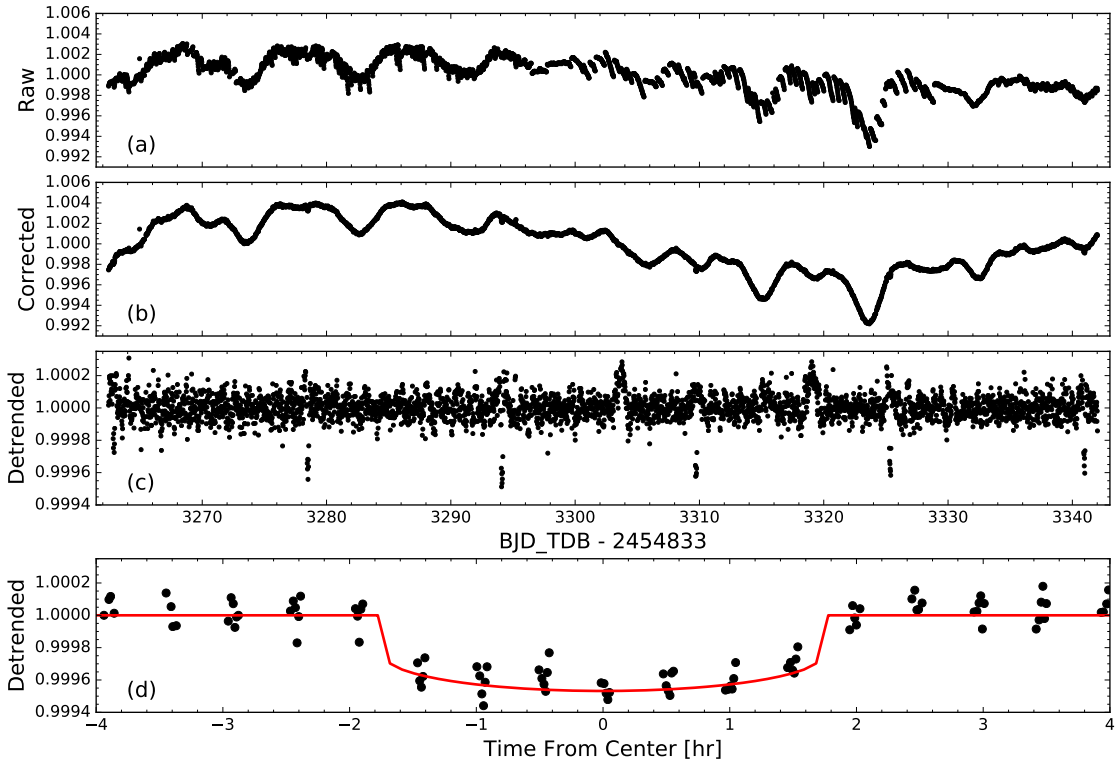

Figure 3-1 *K2* photometry of HD 73344 ($V = 6.9$) and its planet candidate, EPIC 212178066.01. From top to bottom: raw aperture photometry; after removal of telescope systematics, revealing a likely 8.5 ± 0.5 d rotation period; after detrending, clearly revealing candidate transits; and after phase-folding and overplotting a model transit profile (red). The bumps in panel (c) do not occur on the same period as the candidate transit and may be artifacts of the detrending process.

3.2.3 Transit Search

We search our calibrated photometry for transit signals using the publicly available `TERRA` algorithm[4] [224, 225]. `TERRA` flags targets with putative transits as threshold-crossing events (TCEs), which we later examine visually (see Sec. 3.3). Once a TCE is

[4]https://github.com/petigura/terra

detected, TERRA automatically runs again to search for additional signals in the same system [see 228] until no more TCEs are found or until the number of candidates exceeds 5.

Many spurious detections at lower S/N are caused by residual outliers in the photometry. In order to reduce the number of spurious detections, we require that TCEs have orbital periods longer than 0.5 d, and that they also show at least three transits. This last criterion rules out any planets with periods longer than half the campaign baseline, or $\sim$ 40 days. Thus many longer-period planets likely remain to be found in this data set. Furthermore, we adopt a threshold of S/N$\geq$ 12 to yield a good balance between sensitivity to shallow transits and the number of spurious detections. In previous catalog papers produced using the fully processed target pixel files released later by the *K2* project office, we typically vetted candidates down to a lower S/N threshold of 10. We find that spurious detections are more frequent in light curves derived from uncalibrated cadence data than when using fully calibrated pixel files.

In total, TERRA produced a list of 1097 TCEs in C16 with nominal S/N$\geq$12. The distribution of their orbital periods is shown in Fig. 3-2.

3.3 Triage and Vetting

The majority of TCEs identified by TERRA are not caused by genuine transiting planets, but instead by residual instrumental artifacts, eclipsing binary stars, or other periodic stellar variability (e.g. pulsations and spot modulations). We manually vet our entire list of 1097 TCEs to differentiate between these various signals. This process results in a list of robust planet candidates for further follow-up and validation, as well as a list of eclipsing binaries and other periodically variable sources.

We promote TCEs showing no obvious warning signs to the status of "planet candidate" in the spirit of "Kepler Objects of Interest" (KOIs), i.e. events that are almost certainly astrophysical in nature and not obviously false positive scenarios such as eclipsing binaries or variable stars. Details of the vetting process are described in

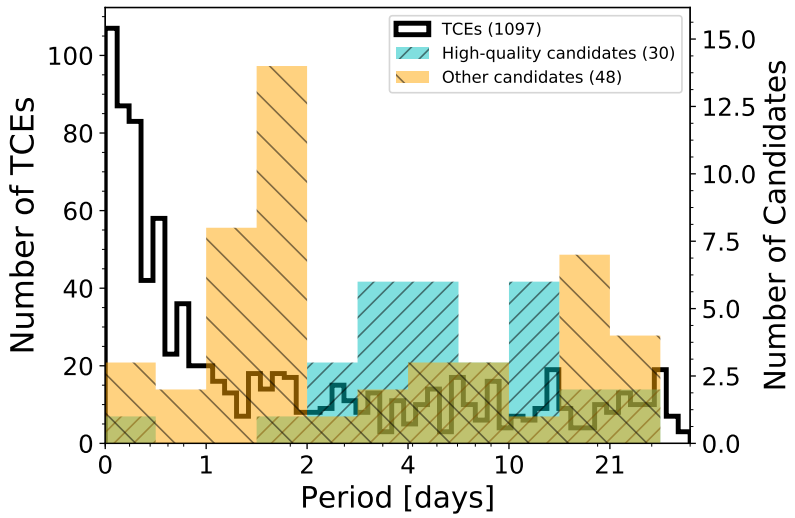

Figure 3-2 Orbital periods of transit-like signals identified in our analysis. The unfilled, narrow-binned histogram (axis at left) shows the Threshold-Crossing Events (TCEs) identified by `TERRA` in our initial transit search (see Sec. 3.2.3). The coarser histograms (axis at right) indicate the distributions of 30 high-quality candidates (blue-green) and 48 remaining, plausibly planetary candidates (orange).

Crossfield et al. [77] and Petigura et al. [228]. `TERRA` produces a set of diagnostics for every TCE, which we use to classify the event as a candidate planet, eclipsing binary, periodic variable, or noise. The diagnostics include a summary of basic fit parameters and a suite of diagnostic plots to visualize the nature of the TCE. These plots include the `TERRA` periodogram, a normalized phase-folded light curve with the best-fit Mandel & Agol [190] model, the light curve phased to 180° to look for eclipses or misidentified periods, the most probable secondary eclipse identified at any phase, and an autocorrelation function. In the era of *TESS*, cross-matching to ground-based surveys will be another excellent way to discover false positives [e.g. 215].

Table 3.2 lists the 30 highest-quality planet candidates whose light curves (shown in Fig. 3-3) show no obvious signs of being non-planetary in nature; our experience with four years of *K2* data leads us to believe that most of these are indeed real planets, ready to be confirmed (e.g., via mass measurements) or statistically validated.

Table 3.3 lists 48 candidates that could also be transiting planets but include some ambiguous warning signs such as a V-shaped transit (frequently caused by eclipsing

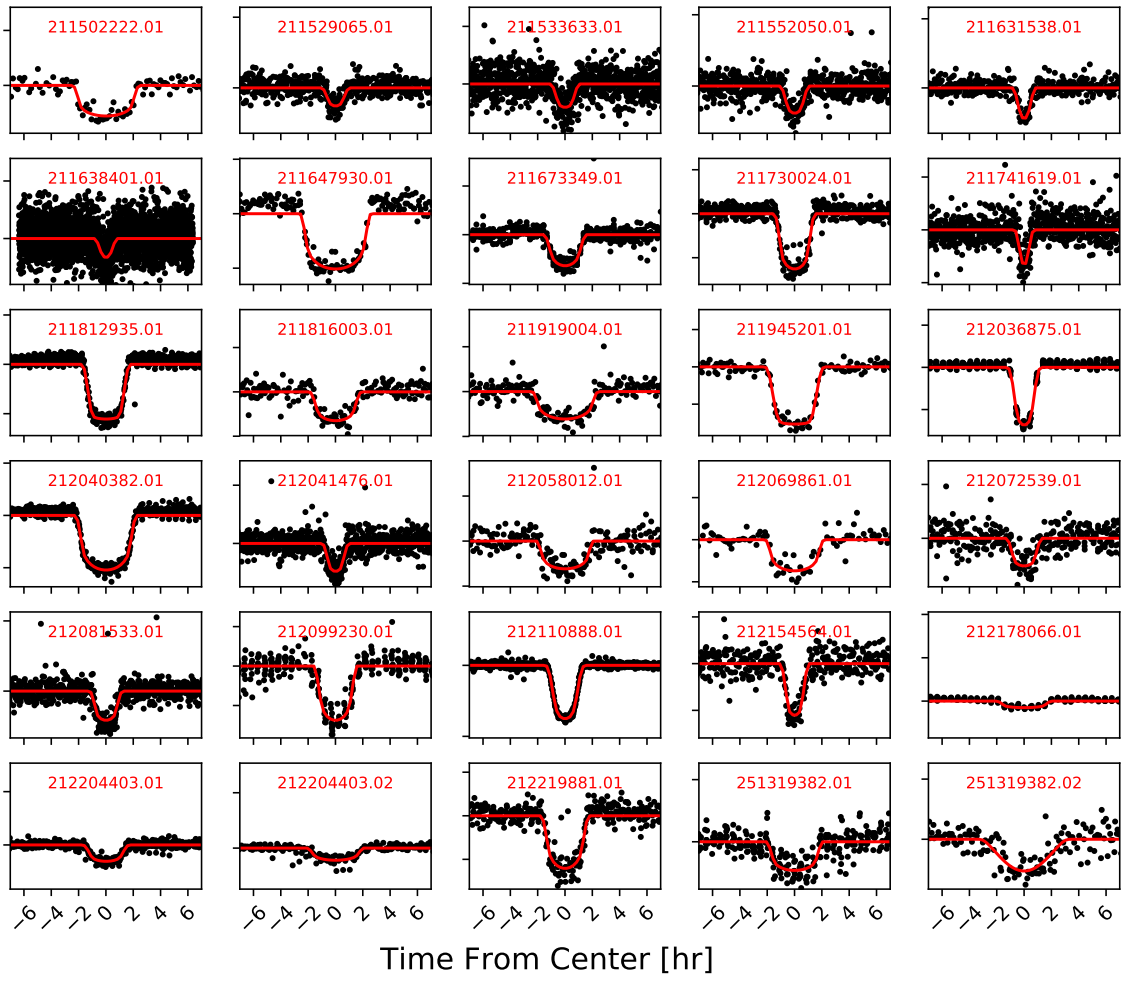

Figure 3-3 Phase-folded light curves of our 30 high-quality planet candidates, and their best-fit Mandel & Agol [190] transit models. To avoid clutter, we did not label the y-axis. Their system parameters are listed in Table 3.2.

binaries). Some candidates in this list may be real planets, but many are likely non-planetary. Following the examples of the KOIs and of Vanderburg et al. [288], we do not classify candidates with very deep transits as false positives even though transit depths $\gtrsim 5\%$ very likely indicate eclipsing binaries. Candidates with radii larger than 1.5 R_J were also included in this category, since giant planet candidates from *Kepler* have a false positive rate as high as 50% [247]. We plot the light curves of these candidates in Fig. 3-4.

Finally, we identify a larger sample of periodic astrophysical signals that are al-

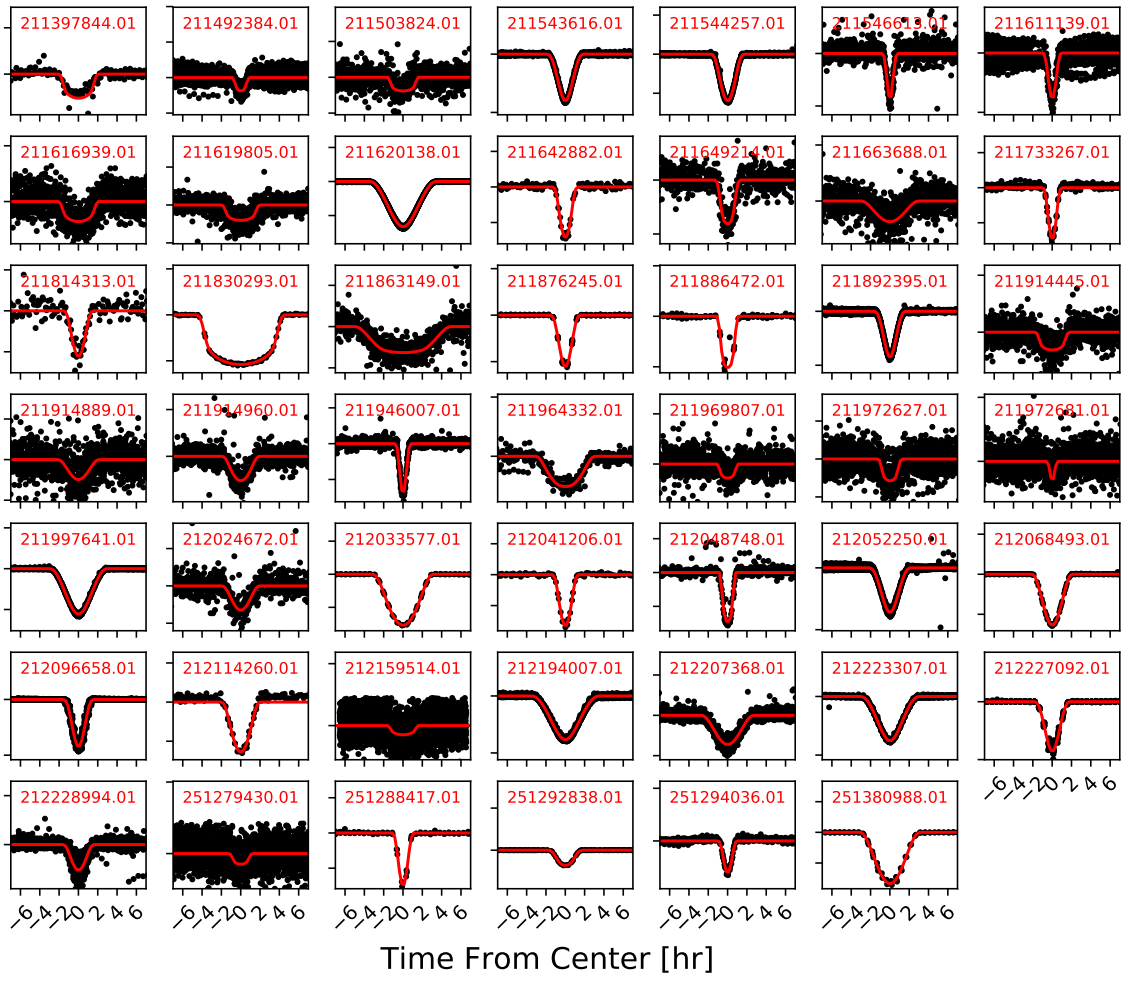

Figure 3-4 Phase-folded light curves of our 48 lower-quality planet candidates, and their best-fit Mandel & Agol [190] transit models. Typical transit depths for these candidates range from 300 ppm to 700000 ppm. Their system parameters are listed in Table 3.3.

most certainly not caused by planets. Table 3.4 lists 164 targets that clearly show both transits and secondary eclipses, while Table 3.5 lists the 231 other periodic, astrophysical signals such as pulsations, coherent stellar rotations, and objects identified as galaxies or quasars in the Ecliptic Plane Input Catalog [EPIC; 141] or GO proposals. There is likely overlap between these last two tables, e.g. for short-period contact/near-contact binaries whose light curves may have been classified as periodic variables.

After constructing the samples of astrophysical TCEs described above, we also

perform ephemeris matching following the approach of [73]. By adopting their recommended thresholds for periods and times-of-transit, we identify a number of transit-like signals with matching ephemerides. We do not discard any of these systems, but indicate them in our target tables. This matching exercise also led us to demote 2 systems that we had originally classified as high-quality candidates (211914445.01 and 211964332.01) down into a lower tier.

To provide the community access to these candidates as rapidly as possible, we have chosen to forego a full MCMC analysis on each candidate's light curve. Instead, we run a Levenberg-Marquardt minimization on each planet candidate to fit a Mandel & Agol [190] transit model. The stellar limb darkening parameters are fixed to values derived using the `PyLDTk` package[5] [220] and stellar parameters derived in Section 3.4.1. We find that this fit gives us a more reliable estimate of the transit ephemerides than `TERRA`. For periodic variables and systems with secondary eclipses, we merely report the parameters found by `TERRA`. In some cases `TERRA` obviously identified a multiple of the true period, and we include a note to that effect where appropriate.

3.4 Discussion

3.4.1 Host Star Parameters

Unlike the original *Kepler* mission, *K2* does not have a homogeneous catalog of stellar parameters. Fortunately, we still have the benefit of the comprehensive classification catalog of *K2* targets produced by Huber et al. [141], who used mainly a combination of colors and galactic population synthesis models to derive stellar parameters such as effective temperatures ($T_{\rm eff}$), surface gravities ($\log g$), metallicities ([Fe/H]), radii, masses, densities, distances and extinctions for *K2* stars. The typical precision of these classifications is $\approx 2\% - 3\%$ in $T_{\rm eff}$ [141]. However, the Huber et al. [141] analysis misclassifies 55-70% of subgiants as dwarfs, and relies on Padova stellar models [194],

[5] https://github.com/hpparvi/ldtk/tree/v1.0

which systematically underestimate the stellar radii of M dwarfs by up to 20%. Many C16 targets, including all of our planet candidate hosts, also have parallaxes from Gaia DR2 [108, 109]. We used the parallaxes and the `isochrones` package[6] [208] in conjunction with the broadband photometry ($BVJHKgri$) from the EPIC to infer the $T_{\rm eff}$, stellar radii, $\log g$, [Fe/H] and masses of all planet candidate hosts. In Tables 3.2 and 3.3, we list the median stellar parameters and their 1σ uncertainties from `isochrones` for all of our candidates. For the vast majority of the candidates, the best-fit $T_{\rm eff}$ is consistent with that from Huber et al. [141] at the 2σ level. But we note that the reported uncertainties are only statistical uncertainties and do not account for any systematic uncertainties in the underlying stellar models, and may therefore be underestimated, especially for cooler stars.

Fig. 3-5 shows the Huber et al. [141] $T_{\rm eff}$ (where available) for the entire C16 sample, along with the `isochrones`-derived $T_{\rm eff}$ distribution among our planet candidate samples. The full campaign shows three distinct populations of targets observed by *K2*, with peaks around 3500 K, 5000 K, and 6100 K. The number of candidates is of course much lower, but the distribution of $T_{\rm eff}$ for these systems appears to roughly track that of the underlying target distribution even though we do not expect it to, given the change in planet detectability as a function of stellar magnitude, radius, and noise.

3.4.2 Characteristics of the Planet Candidate Sample

The period distribution of our planet candidates, along with that of the TCEs, is shown in Fig. 3-2. Whereas the TCE distribution peaks for $P < 1$ d, the number of high-quality candidates increases towards longer periods as expected for real planets [e.g., 209, 105]. A larger fraction of lower-quality candidates have $P < 2$ d; based on the occurrence rates of short-period planets, we expect that many of these shortest-period candidates are not planets.

Fig. 3-6 shows the brightness in the *Kepler* bandpass (Kp) and transit depths for our candidates. The highest-quality candidates typically orbit stars with $Kp =$

[6] https://github.com/timothydmorton/isochrones

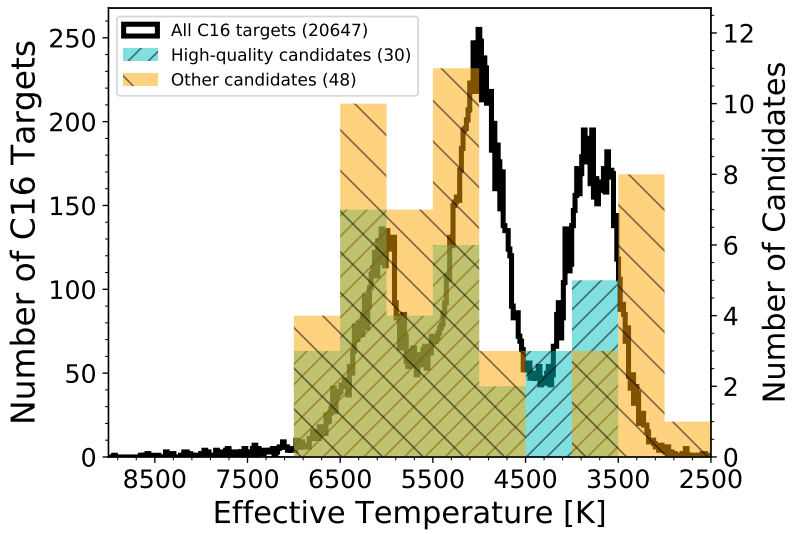

Figure 3-5 Distribution of EPIC stellar $T_{\rm eff}$ for the entire C16 target sample (empty, fine-grained histogram) and for our planet candidate sample (filled, coarser histograms).

$10-15$ mag and have transit depths $\gtrsim 100$ ppm, as is typical for *K2* planet catalogs [e.g., 195]. One candidate has $Kp = 6.8$ mag and is a clear outlier; this would be the brightest host star, by far, for any transiting planet discovered by *K2*. We discuss this candidate, HD 73344, in more detail in Sec. 3.4.3 below.

Adopting the stellar parameters derived in Section 3.4.1, Fig. 3-7 plots the planet radii and incident irradiation of all our candidates.

We detect two possible multi-planet systems. Two high-quality candidates orbit EPIC 212204403, with periods of 4.7 and 12.6 d and sizes of approximately 3.3 and 2.6 $R_\oplus$, respectively. Another two high quality candidates are detected around EPIC 251319382, with periods of 8.2 and 14.9 days, and radii of 2.0 and 4.4 $R_\oplus$. Based on past studies of multi-planet systems these candidates are likely to be real planets [184, 256]. Validating them is beyond the scope of this work, but at $V = 11-12$ mag, these systems could be interesting targets for radial velocity (RV) mass measurements of multi-planet systems.

Another interesting candidate is EPIC 212048748.01 from the lower-quality "plausible planet candidate" list. This candidate transits with a 3155 ppm depth and a

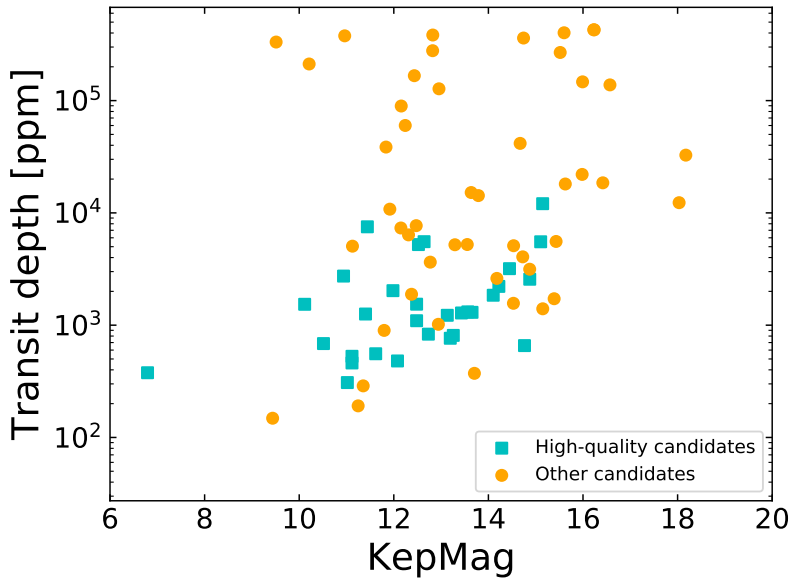

Figure 3-6 Transit depth and stellar magnitude for our high-quality candidates (light blue squares) and lower-quality candidates (orange circles).

period of 5.75 d around a high proper motion, infrared bright ($K = 9.2$) star having optical-IR photometry consistent with an M3 spectral type. If confirmed, this $\sim 2R_\oplus$ candidate will be a priority target for upcoming IR sensitive precision RV instruments and transit spectroscopy with the *James Webb Space Telescope*.

Finally, a comparison with the NASA Exoplanet Archive shows that four of our candidates have already been validated using data from C5. [91] validated two of our high-quality C16 candidates, 212069861.01 (K2-123b) and 212154564.01 (K2-124b); another candidate 212110888.01 is a previously known hot Jupiter K2-34b [180, 130]; and our lower-priority candidate 211969807.01 was validated as K2-104b [191]. One more low-quality candidate, 211946007.01, was confirmed to be a transiting brown dwarf [110]. Our derived system parameters are in approximate agreement with those in the discovery papers. A combined analysis of the C5 and C16 data (possible for many targets in C16) may prove fruitful for these systems.

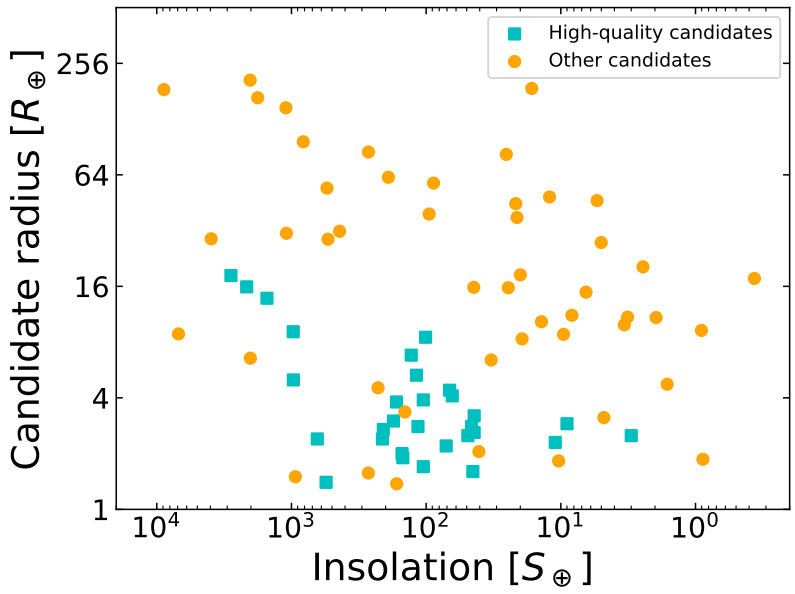

Figure 3-7 Approximate radii and incident insolation for our high-quality candidates (light blue squares) and lower-quality candidates (orange circles).

3.4.3 HD 73344

One candidate of particular interest is HD 73344[7] (HIP 42403, EPIC 212178066), and we show the light curve in Fig 3-1. This bright F star ($V = 6.9$ mag) is highly saturated in the *K2* data, but a custom aperture encompassing the entire saturated PSF shows the clear transit-like signal highlighted in Fig. 3-1. Because the candidate is exceptionally bright, and thus amenable to future characterization, we investigated the signal more closely than others, as explained below.

The star has been characterized by many groups over the years [e.g., 283, 219]. It lies at a distance of 35.296 ± 0.052 pc [109] and its parameters are $T_{\rm eff} = 6120 \pm 50$ K, $R_* = 1.15 \pm 0.04\,R_\odot$, $M_* = 1.26 \pm 0.19\,M_\odot$ [283], in good agreement with our derived values from Gaia DR2 and `isochrones`. The star's projected rotational velocity is $v \sin i = 6.3 \pm 0.5$ km s^{-1} [283], and our light curve shows evidence of stellar rotation at a period (determined via Lomb-Scargle periodogram) of 8.5 ± 0.5 d. This period

[7]This target was proposed by many K2 GO programs: 16009 (PI Charbonneau), 16010 (PI Lund), 16021 (PI Howard), 16028 (PI Cochran), 16063 (PI Redfield), 16068 (PI Jensen), and 16081 (PI Guzik).

would be consistent with the rotation periods of other stars with similar colors, and is consistent with a stellar age of roughly 1 Gyr [10]. Combining all these parameters indicates that the stellar rotation axis is inclined by $i = 62° \pm 10°$. Thus, if the candidate signal comes from an object orbiting HD 73344, the angular momentum of the star and the transiting object's orbit are likely misaligned.

Because the star is strongly saturated, we cannot apply a standard centroid analysis of the stellar position in- vs. out-of-transit. However, a transit analysis with MCMC [identical to that described by 76] implies a stellar density of $\rho_{*,circ} = 2.2 \pm 1.2$ g cm^{-3} — a loose constraint, but consistent with the spectroscopically-inferred stellar density of 1.2 ± 0.2 g cm^{-3} and much higher than the low stellar densities that might be expected from an eclipsed giant star. The results of our transit analysis, which includes dilution as a free parameter, are also consistent with no dilution.

The resulting parameters from our transit analysis of HD 73344 are listed in Table 3.1. If the transits are occurring around the target and not around a background star in the photometric aperture, the stellar radius and transit depth imply a candidate radius of roughly 2.6 $R_\oplus$. This size would imply a corresponding candidate mass of $10 \pm 3\, M_\oplus$ [298] and an RV amplitude of $\sim$2 m s^{-1}. The star was observed 24 times over eleven years as part of the Lick radial velocity survey [99], but these data have an RMS of 32 m s^{-1} (despite internal uncertainties of roughly 6 m s^{-1}) and show no coherent RV signal at the candidate period or at our calculated stellar rotation period. Nightly Keck/HIRES RVs over four consecutive nights in 1999 showed a stellar jitter of 3.9 m s^{-1} [145]. HD 73344 also exhibits moderate chromospheric activity [$S_{HK} = 0.22$, $R'_{HK} = -4.66$; 145], but at this $T_{\rm eff}$ H&K activity is not the main contribution to jitter. It seems likely that precise RV measurements could confirm this planet candidate, despite the fact that it orbits an early-type star, which makes RV measurements more challenging than for later-type stars.

Table 3.1. Candidate Parameters for HD 73344

Parameter	Units	Value
T_0	$\mathrm{BJD_{TDB}} - 2454833$	$3262.8931^{+0.0020}_{-0.0023}$
P	d	$15.61335^{+0.00085}_{-0.00078}$
i	deg	$89.15^{+0.61}_{-1.13}$
R_{circ}/R_*	%	$2.65^{+0.15}_{-0.10}$
T_{14}	hr	$3.46^{+0.20}_{-0.17}$
T_{23}	hr	$3.22^{+0.21}_{-0.18}$
R_*/a	–	$0.0327^{+0.0118}_{-0.0042}$
b	–	0.46 ± 0.32
$\rho_{*,\mathrm{circ}}$	g cm^{-3}	$2.2^{+1.1}_{-1.3}$
a	AU	$0.1321^{+0.0063}_{-0.0070}$
R_{cand}	R_E	2.56 ± 0.18
S_{inc}	S_E	111^{+12}_{-11}

3.4.4 Conclusions

In a short timespan, we have converted cadence-level *K2* data into time-series photometry of 20647 targets, identified 1097 periodic signals (of astrophysical or instrumental origin), and distilled these into 30 high-quality planet candidates, 48 lower-quality candidates, 164 eclipsing binaries, and 231 other periodically-variable astrophysical sources. Four of our candidates have already been validated as planets (see Sec. 3.4.2), suggesting that our approach successfully identifies planet-like signals. One particularly interesting new target is HD 73344, a $V = 6.9$ F dwarf which may host a 2.6 $R_\oplus$ planet on a 15 d orbit (see Sec. 3.4.3). We have released parameters for all identified systems of interest, along with light curves and transit vetting plots[8]. We hope that rapid identification and public dissemination of interesting signals will maximize the scientific productivity of *K2*. If *K2* continues operating through the end of C17 (another forward-facing campaign), it may prove useful to perform a similarly rapid analysis of those data.

This rapid-release model is also somewhat of an analog for the upcoming *TESS* mission [241]. The release of planet catalogs has occurred only irregularly during the *K2* mission, but this paradigm will change once *TESS* operations begin in earnest. Data from *TESS* will be released and processed on a 27-day rhythm for most of the

[8]All available now at `https://exofop.ipac.caltech.edu/k2/`, or by request.

two-year mission duration. With the shorter observing windows, ephemeris decay is also a much larger problem for *TESS* and therefore the importance of securing planet candidates in the same season is even higher. If interesting objects could be rapidly gleaned from *TESS* data and circulated to the community, follow-up observations and analyses could begin a full season earlier and so the full impact of that mission could more quickly be achieved.

Table 3.2: High-quality candidate parameters

Candidate	Kp	P	T_0	T_{14}	$(R_P/R_*)^2$	$R_*^{\rm a}$	$M_*^{\rm a}$	$T_{\rm eff}$ [a]	$\log g$ [a]	R_P	$S_{\rm inc}$	In C5?	Comment
		[d]	[BJD - 2454833]	[d]	[ppm]	$[R_\odot]$	$[M_\odot]$	[K]	[cgs]	$[R_\oplus]$	$[F_\oplus]$		
211502222.01	11.617	22.995920	3280.30425	0.155	470	1.043 ± 0.015	1.054 ± 0.060	6010 ± 170	4.426 ± 0.031	2.5	49		—
211529065.01	13.431	4.399871	3264.73662	0.0532	1076	0.772 ± 0.006	0.852 ± 0.019	4810 ± 30	4.594 ± 0.010	2.8	115	yes	—
211533633.01	13.258	2.126953	3262.66212	0.059	707	0.573 ± 0.018	0.585 ± 0.024	4020 ± 220	4.696 ± 0.015	1.7	105		—
211552050.01	13.194	3.544965	3264.95164	0.061	621	0.701 ± 0.007	0.718 ± 0.037	4860 ± 120	4.602 ± 0.024	1.9	149		—
211631538.01	14.221	5.513327	3266.24778	0.0386	2119	0.770 ± 0.014	0.791 ± 0.046	5020 ± 110	4.562 ± 0.030	3.9	105		—
211638401.01	14.763	0.530270	3262.64176	0.0443	568	0.558 ± 0.006	0.578 ± 0.013	3880 ± 70	4.706 ± 0.011	1.4	553		—
211647930.01	11.982	14.759595	3264.39324	0.1712	1705	1.186 ± 0.024	1.068 ± 0.079	6070 ± 190	4.318 ± 0.043	5.3	118		—
211673349.01	14.446	4.894289	3264.62726	0.0877	3043	0.686 ± 0.008	0.712 ± 0.026	4440 ± 50	4.620 ± 0.018	4.1	64		—
211730024.01	11.402	5.113823	3263.81018	0.0896	1054	1.409 ± 0.036	1.356 ± 0.084	6890 ± 340	4.274 ± 0.041	5.0	968		—
211741619.01	13.564	2.787663	3263.82026	0.0311	1087	0.602 ± 0.005	0.627 ± 0.016	3950 ± 30	4.676 ± 0.013	2.2	71		—
211812935.01[b]	12.64	3.607981	3264.87890	0.1141	5543	2.253 ± 0.081	1.573 ± 0.085	6490 ± 210	3.928 ± 0.042	18.3	2815		—
211816003.01	13.654	14.454034	3265.79062	0.114	1374	0.802 ± 0.012	0.824 ± 0.056	5490 ± 80	4.548 ± 0.036	3.2	44	yes	—
211919004.01	13.131	11.722103	3265.36820	0.1546	958	0.838 ± 0.008	0.920 ± 0.027	5170 ± 60	4.556 ± 0.015	2.8	46	yes	—
211945201.01	10.115	19.491965	3280.94047	0.124	1777	1.485 ± 0.357	1.335 ± 0.183	6320 ± 300	4.219 ± 0.152	6.8	129	yes	—
212036875.01	10.937	5.169887	3265.67929	0.0646	3348	1.450 ± 0.036	1.380 ± 0.084	6830 ± 390	4.256 ± 0.041	9.1	970		—
212040382.01	12.521	4.445559	3266.34866	0.1513	4228	2.237 ± 0.082	1.565 ± 0.082	6520 ± 270	3.932 ± 0.038	15.9	2150		—
212041476.01	12.078	2.783705	3262.55831	0.053	538	0.939 ± 0.013	0.985 ± 0.046	5890 ± 150	4.487 ± 0.025	2.4	643		—
212058012.01	11.018	11.561514	3266.10708	0.1281	255	1.406 ± 0.315	1.305 ± 0.147	6140 ± 220	4.255 ± 0.146	2.4	211		—
212069861.01	14.102	30.954222	3274.10848	0.1368	1496	0.598 ± 0.007	0.609 ± 0.016	4040 ± 80	4.671 ± 0.013	2.5	3	yes	K2-123b [91]
212072539.01	14.874	7.676984	3263.56938	0.0733	2124	0.465 ± 0.010	0.488 ± 0.014	3790 ± 80	4.790 ± 0.011	2.3	11	yes	—
212081533.01	12.731	3.355854	3262.74687	0.0635	670	0.551 ± 0.005	0.579 ± 0.013	3860 ± 10	4.720 ± 0.011	1.6	45		—
212099230.01	10.513	7.112134	3269.13703	0.1046	553	1.042 ± 0.151	1.016 ± 0.109	5800 ± 250	4.409 ± 0.092	2.7	208	yes	—
212110888.01	11.441	2.995653	3263.95700	0.0813	8175	1.398 ± 0.032	1.235 ± 0.095	6380 ± 270	4.239 ± 0.045	13.8	1521	yes	K2-34b [180, 130]
212154564.01	15.105	6.414008	3264.81383	0.0699	4614	0.394 ± 0.010	0.413 ± 0.012	3620 ± 80	4.863 ± 0.014	2.9	9	yes	K2-124b [91]
212178066.01	6.793	15.613426	3262.89291	0.1256	362	1.438 ± 0.218	1.378 ± 0.155	6460 ± 220	4.264 ± 0.090	3.0	175		HD 73344

Table 3.2: High-quality candidate parameters (cont'd)

Candidate	Kp	P	T_0	T_{14}	$(R_P/R_*)^2$	$R_*^{\rm a}$	$M_*^{\rm a}$	$T_{\rm eff}$ [a]	$\log g$ [a]	R_P	$S_{\rm inc}$	In C5?	Comment
		[d]	[BJD - 2454833]	[d]	[ppm]	$[R_\odot]$	$[M_\odot]$	[K]	[cgs]	$[R_\oplus]$	$[F_\oplus]$		
212204403.01	12.482	4.688625	3263.71310	0.0964	1777	0.828 ± 0.010	0.875 ± 0.043	5220 ± 100	4.545 ± 0.029	3.8	166		possible multi
212204403.02	12.482	12.550896	3271.42819	0.1179	858	0.828 ± 0.010	0.875 ± 0.043	5220 ± 100	4.545 ± 0.029	2.6	44		possible multi
212219881.01	15.147	6.924808	3264.18479	0.1189	9578	0.795 ± 0.027	0.817 ± 0.055	5300 ± 70	4.550 ± 0.037	8.5	101		—
251319382.01[c]	11.116	8.236486	3265.71419	0.1293	401	0.923 ± 0.014	0.973 ± 0.046	5930 ± 120	4.497 ± 0.024	2.0	151		possible multi
251319382.02[c]	11.116	14.869943	3270.60950	0.1193	1900	0.923 ± 0.014	0.973 ± 0.046	5930 ± 120	4.497 ± 0.024	4.4	67		possible multi

[a] Note that all uncertainties reported in this table and Table 3.3 are statistical uncertainties only and do not account for systematic uncertainties in the underlying stellar models.

[b] Parameters not in EPIC; classified using `isochrones` as described in Sec. 3.4.1.

[c] We identified hints of a third candidate in this system, with a period of ~ 3.5 d and S/N$\sim$7.

Table 3.3: Plausible candidate parameters

Candidate	Kp	P	T_0	T_{14}	$(R_P/R_*)^2$	R_*	M_*	$T_{\rm eff}$	$\log g$	In C5?	Comment	Ephemeris matching
		[d]	[BJD - 2454833]	[d]	[ppm]	$[R_\odot]$	$[M_\odot]$	[K]	[cgs]			
211397844.01	13.292	16.168833	3274.81174	0.1331	4046	5.653 ± 0.284	2.750 ± 0.454	5186 ± 135	3.371 ± 0.090			
211492384.01	12.375	0.635328	3262.97422	0.0543	1315	1.531 ± 0.047	1.286 ± 0.096	6420 ± 300	4.176 ± 0.050		somewhat V-shaped	
211503824.01	11.246	2.047195	3263.17910	0.0789	255	0.958 ± 0.013	1.000 ± 0.046	6150 ± 110	4.476 ± 0.023		slightly asymmetric	
211543616.01	15.6	1.518232	3263.37623	0.1284	356389	1.209 ± 0.074	0.914 ± 0.073	5510 ± 210	4.237 ± 0.062		V-shaped	
211544257.01	12.242	1.630130	3263.45081	0.0952	46964	1.602 ± 0.047	1.286 ± 0.082	6190 ± 230	4.136 ± 0.041		somewhat V-shaped; spotted star?	
211546613.01	15.982	2.007472	3263.89429	0.0377	16989	0.473 ± 0.012	0.495 ± 0.016	3790 ± 70	4.783 ± 0.013		V-shaped	
211611139.01[a]	12.474	1.882213	3263.60257	0.0402	5678	1.568 ± 0.140	1.355 ± 0.106	6590 ± 380	4.178 ± 0.081		somewhat V-shaped	
211616939.01	11.796	1.855400	3262.61930	0.1167	775	10.091 ± 0.531	3.490 ± 0.558	4990 ± 140	2.964 ± 0.070		V-shaped	211619805.01, 211620138.01, 211663688.01
211619805.01	12.942	1.855827	3262.60966	0.1257	844	0.664 ± 0.010	0.684 ± 0.030	4720 ± 140	4.627 ± 0.021		somewhat V-shaped	211616939.01, 211620138.01, 211663688.01
211620138.01	9.512	1.855421	3262.61863	0.2368	660084	2.734 ± 0.224	3.081 ± 0.529	11500 ± 1960	4.055 ± 0.141		V-shaped	211616939.01, 211619805.01, 211663688.01
211642882.01	13.788	23.897707	3267.90399	0.0618	11511	0.728 ± 0.009	0.738 ± 0.040	5020 ± 120	4.581 ± 0.027		V-shaped	
211649214.01	14.726	3.787950	3265.41821	0.0688	4851	4.182 ± 0.153	1.896 ± 0.435	5126 ± 136	3.476 ± 0.117			
211663688.01	16.419	1.855516	3262.61467	0.1698	14554	0.189 ± 0.010	0.161 ± 0.008	3110 ± 110	5.092 ± 0.026		V-shaped	211616939.01, 211619805.01, 211620138.01
211733267.01	12.15	8.657975	3264.32036	0.041	6106	0.891 ± 0.016	0.819 ± 0.060	5370 ± 140	4.450 ± 0.041	yes	slightly V-shaped	
211814313.01	15.431	15.405101	3265.30794	0.1172	16796	1.475 ± 0.142	1.112 ± 0.099	5910 ± 210	4.145 ± 0.076		V-shaped	

Table 3.3: Plausible candidate parameters (cont'd)

Candidate	Kp	P [d]	T_0 [BJD - 2454833]	T_{14} [d]	$(R_P/R_*)^2$ [ppm]	R_* [$R_\odot$]	M_* [$M_\odot$]	$T_{\rm eff}$ [K]	$\log g$ [cgs]	In C5?	Comment	Ephemeris matching
211830293.01	11.916	20.893526	3281.64853	0.3209	8821	1.765 ± 0.045	1.249 ± 0.085	6020 ± 260	4.041 ± 0.042		possible eclipse at phase 0.53	
211863149.01	14.873	2.612990	3264.30341	0.2776	2779	0.458 ± 0.004	0.480 ± 0.009	3520 ± 20	4.798 ± 0.009		V-shaped	211839430.01, 211839462.01
211876245.01	15.518	8.971460	3266.46199	0.1086	269917	0.872 ± 0.037	0.840 ± 0.063	5330 ± 150	4.481 ± 0.050		Somewhat V-shaped; hint of eclipse	
211886472.01	11.126	19.639750	3281.74841	0.0591	4477	2.183 ± 0.124	1.599 ± 0.096	6730 ± 370	3.963 ± 0.052	yes	V-shaped	
211892395.01	16.238	0.995061	3262.63670	0.1102	445224	0.864 ± 0.039	0.801 ± 0.037	5080 ± 140	4.468 ± 0.038		V-shaped	
211914445.01	14.529	1.810718	3263.47161	0.1002	1366	1.178 ± 0.043	0.914 ± 0.072	5680 ± 200	4.257 ± 0.050	yes	—	211914889.01, 211914960.01, 211915147.01
211914889.01	18.032	1.810420	3263.48113	0.1544	35275	0.313 ± 0.013	0.230 ± 0.070	3050 ± 20	4.808 ± 0.201	yes	somewhat V-shaped	211914445.01, 211914960.01, 211915147.01
211914960.01	14.179	1.810834	3263.46871	0.1185	3433	0.888 ± 0.205	0.241 ± 0.253	3230 ± 690	3.921 ± 0.581	yes	V-shaped	211914445.01, 211914889.01, 211915147.01
211946007.01	16.57	1.982809	3263.84986	0.0568	213762	0.291 ± 0.020	0.281 ± 0.019	3330 ± 160	4.958 ± 0.035	yes	Transiting brown dwarf AD 3116 [110]	
211964332.01	14.533	7.220537	3266.50370	0.1714	3983	0.932 ± 0.035	0.865 ± 0.072	5420 ± 160	4.435 ± 0.053			211964001.01, 211964025.01, 211964555.01, 251809628.01
211969807.01	15.149	1.974991	3262.86291	0.0705	1310	0.484 ± 0.012	0.504 ± 0.016	3820 ± 70	4.773 ± 0.013	yes	K2-104b [191]; marginal detection.	

Table 3.3: Plausible candidate parameters (cont'd)

Candidate	Kp	P [d]	T_0 [BJD - 2454833]	T_{14} [d]	$(R_P/R_*)^2$ [ppm]	R_* [$R_\odot$]	M_* [$M_\odot$]	$T_{\rm eff}$ [K]	$\log g$ [cgs]	In C5?	Comment	Ephemeris matching
211972627.01	11.353	1.092845	3263.45807	0.0677	236	0.951 ± 0.013	0.968 ± 0.058	5620 ± 70	4.468 ± 0.032	yes	V-shaped	211972681.01, 211972837.01
211972681.01	15.39	1.092673	3263.46283	0.0544	833	0.783 ± 0.025	0.807 ± 0.050	5140 ± 160	4.557 ± 0.035		V-shaped (or short transit duration)	211972627.01, 211972837.01
211997641.01	12.821	1.744546	3263.51613	0.1635	206372	2.316 ± 0.133	1.636 ± 0.091	6530 ± 350	3.921 ± 0.049	yes	v-shaped	
212024672.01	18.174	3.697161	3262.87327	0.1397	35827	0.245 ± 0.013	0.216 ± 0.054	3120 ± 20	4.991 ± 0.109	yes	slightly V-shaped; hint of eclipse	212024647.01
212033577.01	11.835	23.702342	3285.09327	0.226	48619	1.869 ± 0.048	1.334 ± 0.076	6280 ± 190	4.021 ± 0.037		V-shaped	
212041206.01	14.671	23.917716	3283.38421	0.0717	32061	0.828 ± 0.019	0.803 ± 0.048	5050 ± 110	4.507 ± 0.033		V-shaped	
212048748.01	12.771	5.745912	3262.55671	0.0472	3155	0.307 ± 0.003	0.302 ± 0.007	3390 ± 20	4.943 ± 0.010		V-shaped	
212052250.01	14.743	0.986765	3262.87581	0.139	305455	1.400 ± 0.067	1.141 ± 0.085	6080 ± 230	4.201 ± 0.050		V-shaped – likely even-odd	
212068493.01	12.955	14.220246	3271.79491	0.1452	101983	1.461 ± 0.045	1.200 ± 0.102	6130 ± 270	4.185 ± 0.050		V-shaped	
212096658.01	10.21	1.466473	3263.68144	0.1062	335755	0.981 ± 0.016	0.911 ± 0.029	4570 ± 110	4.413 ± 0.023	yes	V-shaped	
212114260.01	12.311	20.016917	3265.54619	0.1006	5520	0.970 ± 0.019	0.972 ± 0.066	5790 ± 130	4.451 ± 0.037		likely eclipse	
212159514.01	13.704	0.545702	3262.55728	0.0798	532	4.752 ± 0.307	2.707 ± 0.292	5330 ± 170	3.514 ± 0.071	yes	somewhat asymmetric	
212194007.01	12.824	1.177150	3262.94420	0.1635	294749	2.529 ± 0.105	1.639 ± 0.077	6390 ± 200	3.846 ± 0.036		V-shaped	
212207368.01	15.626	1.190316	3263.29198	0.1358	14098	0.335 ± 0.027	0.338 ± 0.021	3420 ± 200	4.916 ± 0.043		V-shaped	212223307.01
212223307.01	10.962	1.190354	3263.29164	0.1635	363154	2.407 ± 0.048	1.611 ± 0.080	6350 ± 180	3.880 ± 0.030		V-shaped	212207368.01
212227092.01	16.226	5.190254	3266.42803	0.1317	696741	0.645 ± 0.012	0.139 ± 0.006	3120 ± 10	3.970 ± 0.020		V-shaped	
212228994.01	13.553	1.095841	3263.34496	0.0796	3489	1.906 ± 0.050	1.309 ± 0.062	5920 ± 130	3.996 ± 0.030		V-shaped; variable depth	
251279430.01	9.438	0.719597	3262.56479	0.0639	149	1.224 ± 0.016	1.184 ± 0.071	6080 ± 130	4.338 ± 0.033		somewhat V-shaped	
251288417.01	15.991	20.924593	3279.57804	0.0639	119088	0.423 ± 0.004	0.103 ± 0.004	2980 ± 10	4.198 ± 0.018		V-shaped	
251292838.01	12.157	19.581519	3274.28569	0.1132	85946	0.861 ± 0.015	0.900 ± 0.051	5638 ± 121	4.525 ± 0.029			

Table 3.3: Plausible candidate parameters (cont'd)

Candidate	Kp	P	T_0	T_{14}	$(R_P/R_*)^2$	R_*	M_*	$T_{\rm eff}$	$\log g$	In C5?	Comment	Ephemeris matching
		[d]	[BJD - 2454833]	[d]	[ppm]	[$R_\odot$]	[$M_\odot$]	[K]	[cgs]			
251294036.01	13.636	6.854931	3268.73159	0.0526	11053	1.031 ± 0.018	0.854 ± 0.051	5360 ± 130	4.343 ± 0.036		somewhat V-shaped	
251380988.01	12.434	30.921004	3274.20687	0.2285	169142	1.761 ± 0.079	1.425 ± 0.102	6680 ± 380	4.099 ± 0.053		slightly V-shaped	

[a] Parameters not in EPIC; classified using `isochrones` as described in Sec. 3.4.1.

Table 3.4: Systems with secondary eclipses

Candidate	Kp	P [d]	T_0 [BJD$_{TDB}$ - 2454833]	T_{14} [d]	$(R_P/R_*)^2$ [ppm]	In C5?	Comment	Ephemeris matching
211397774.01	15.649	0.967865	3262.83095	0.1047	149235		even-odd – half-period	
211402878.01	14.498	25.236580	3277.84155	0.1427	131088			
211408138.01	12.740	10.337864	3267.82296	0.2954	50598	yes		
211409299.01	11.951	13.919301	3263.16370	0.2036	126507	yes		
211411891.01	12.776	0.954863	3262.53608	0.0928	122533			
211422822.01	15.664	0.554633	3262.67870	0.0547	26770			
211425822.01	14.888	2.153178	3263.18086	0.1114	161675			
211429934.01	14.147	0.565934	3262.47647	0.0817	76907			
211430148.01	14.892	15.091257	3262.98697	0.1731	387212	yes		
211431013.01	14.738	3.102398	3265.15784	0.2575	116056	yes	even-odd – half-period	
211432167.01	8.550	5.817737	3263.03384	0.1202	9442	yes		211432176.01
211432176.01	9.866	5.817854	3263.03296	0.1200	9632			211432167.01
211432946.01	14.398	1.671965	3263.07264	0.0897	321572	yes	even-odd – half-period	
211449931.01	14.659	6.663685	3262.53719	0.1092	77241			
211452175.01	12.406	11.114394	3268.75989	0.2596	140535			
211453076.01	16.341	0.524461	3262.66075	0.0714	8800		twice period	
211453223.01	14.590	9.056947	3264.66347	0.1389	228283			
211468153.01	14.381	0.737735	3262.69611	0.0817	293171			
211471048.01	12.867	0.799768	3262.64738	0.1499	368062			
211477347.01	15.368	1.641114	3263.39459	0.1835	232835			
211490299.01	15.991	0.555516	3262.88867	0.0616	125677			
211492541.01	12.789	1.031746	3262.80400	0.2313	13062			
211493669.01	12.976	0.583370	3262.72350	0.0485	16936			
211509665.01	16.519	3.247194	3263.55605	0.1960	274993		even-odd – half-period	
211524114.01	11.473	0.715676	3262.65638	0.0520	1668			

Table 3.4: Systems with Secondary Eclipses (cont'd)

Candidate	Kp	P [d]	T_0 [BJD$_{TDB}$ - 2454833]	T_{14} [d]	$(R_P/R_*)^2$ [ppm]	In C5?	Comment	Ephemeris matching
211524558.01	14.161	0.546969	3262.99346	0.0817	496880	yes	twice period	
211526186.01	12.814	0.682618	3262.60560	0.0487	10943	yes	even-odd – 1.5× period	
211534342.01	15.873	0.512702	3262.52406	0.0751	259506			
211535481.01	14.979	0.539696	3262.52362	0.0727	101331		V-shaped; likely even-odd	
211538193.01	13.908	0.597258	3262.98601	0.0817	250566			
211540348.01	14.022	0.620388	3262.73962	0.0817	497678			
211563123.01	12.583	17.325857	3265.30498	0.3548	334820	yes		
211589784.01	12.678	1.359386	3263.68715	0.0767	92013	yes		
211600389.01	14.157	0.630717	3263.02647	0.0817	163414			211600632.01
211600632.01	16.688	0.630718	3263.02663	0.0817	164032			211600389.01
211604981.01	12.727	12.427163	3267.32649	0.2241	16631			
211607670.01	12.793	1.348851	3263.01356	0.1584	217820		even-odd – half-period	
211607804.01	13.358	1.490219	3263.43270	0.1635	733825			
211613886.01	12.729	0.958786	3263.10671	0.0522	17691	yes		
211619120.01	13.059	11.100314	3264.29172	0.5242	123582	yes		
211621644.01	15.443	0.921358	3262.74784	0.0694	127918		thrice period	
211621961.01	16.548	11.078847	3265.06284	0.5970	121654			
211625003.01	12.848	0.530431	3262.92711	0.0817	409431		even-odd; 1.5× period	
211626490.01	12.886	0.747734	3262.90935	0.0817	287143			
211630537.01	14.185	0.697190	3262.80305	0.0773	34039			
211631904.01	13.989	0.884004	3262.66371	0.0882	391961	yes		
211638883.01	12.622	0.543877	3262.47515	0.0282	659			
211639283.01	15.088	6.741846	3266.59522	0.3020	55296		slightly V-shaped	
211644647.01	13.304	2.044175	3264.21457	0.2978	71960		even-odd – half-period	
211651743.01	13.962	0.516235	3262.68635	0.0817	111574			

Table 3.4: Systems with Secondary Eclipses (cont'd)

Candidate	Kp	P [d]	T_0 [BJD$_{TDB}$ - 2454833]	T_{14} [d]	$(R_P/R_*)^2$ [ppm]	In C5?	Comment	Ephemeris matching
211662047.01	14.791	0.635238	3262.94146	0.0637	126462			
211663508.01	14.343	0.544418	3262.51405	0.0813	434869		four times period	
211664543.01	15.812	0.698333	3262.97188	0.0550	106429		thrice period	
211710534.01	12.203	3.022569	3263.74324	0.1410	56458			
211718105.01	14.103	2.958763	3264.20177	0.2411	176980		even-odd – half-period	
211721325.01	15.428	1.052364	3262.72164	0.1179	348537			
211732801.01	10.655	2.131554	3263.40544	0.1694	68562	yes	V-shaped; even-odd – half-period	251411166.01
211737652.01	16.354	2.468190	3262.93777	0.2452	483890			
211738534.01	15.604	0.568020	3262.64187	0.1389	13803			
211744153.01	14.861	4.612166	3265.94990	0.0664	5543	yes		
211750072.01	13.005	0.595558	3263.09743	0.0705	51711			
211759163.01	14.804	0.595667	3262.90859	0.0620	129607		five times period	
211764271.01	12.895	3.576744	3262.91264	0.1222	68508			211764373.01
211764373.01	11.409	3.576780	3262.91248	0.1111	31467		likely SE	211764271.01
211768007.01	14.021	0.542912	3262.56186	0.0748	120270		twice period	
211770390.01	12.239	3.790180	3262.68640	0.2469	52183	yes	even-odd – half-period	
211807456.01	14.973	0.504961	3262.86244	0.0756	291504		twice period	
211809568.01	15.456	0.593274	3262.99164	0.0817	636988		twice period	
211812160.01	13.485	1.085097	3262.91626	0.0898	31653	yes		
211814733.01	11.971	14.707213	3268.97802	0.0892	4206	yes		
211822953.01	16.834	1.549381	3262.83336	0.0684	92689	yes		
211828142.01	17.558	20.180269	3268.57729	0.1192	395334			
211829982.01	13.823	5.803439	3264.34997	0.1628	627831			
211838158.01	15.801	0.575349	3262.87166	0.0817	522455		twice period	
211839430.01	10.730	2.612938	3264.30391	0.3813	114984	yes	even-odd – half-period	211863149.01, 211839462.01

Table 3.4: Systems with Secondary Eclipses (cont'd)

Candidate	Kp	P [d]	T_0 [BJD$_{TDB}$ - 2454833]	T_{14} [d]	$(R_P/R_*)^2$ [ppm]	In C5?	Comment	Ephemeris matching
211839462.01	10.037	2.612804	3264.30654	0.3681	91385	yes	even-odd – half-period	211863149.01, 211839430.01
211841496.01	15.486	0.522199	3262.46826	0.0676	35912			
211852187.01	17.636	14.343042	3266.06818	0.0610	110696			
211858408.01	12.427	0.628876	3262.79149	0.0817	109867			
211858489.01	12.270	0.636109	3262.49271	0.0290	1465			
211885185.01	12.493	4.397187	3262.92467	0.2452	203447	yes		
211906940.01	16.368	0.526316	3262.47776	0.0418	364733	yes	thrice period	
211910237.01	14.750	1.108972	3263.36936	0.0760	37369	yes	odd-even – half-period	
211914718.01	11.448	0.582017	3262.66714	0.0817	376942	yes	twice period	
211915147.01	9.023	1.810708	3263.47340	0.1267	35675	yes	odd-even; half-period	211914445.01, 211914889.01, 211914960.01
211919555.01	16.889	9.484994	3264.50601	0.6098	82338			211920528.01, 211920604.01, 251809286.01
211919842.01	15.625	9.510911	3264.32358	0.4087	7834			
211920462.01	19.874	9.516793	3264.29495	0.4087	408803			
211920528.01	12.279	9.486580	3264.50407	0.4341	2153	yes		211919555.01, 211920604.01, 251809286.01
211920604.01	12.258	9.487929	3264.49219	0.5031	8783	yes		211919555.01, 211920528.01, 251809286.01
211920811.01	12.482	9.492590	3264.47004	0.4525	4713	yes		

Table 3.4: Systems with Secondary Eclipses (cont'd)

Candidate	Kp	P [d]	T_0 [BJD$_{TDB}$ - 2454833]	T_{14} [d]	$(R_P/R_*)^2$ [ppm]	In C5?	Comment	Ephemeris matching
211928959.01	16.703	0.858462	3263.16644	0.0845	248568			
211934173.01	18.229	0.520451	3262.60163	0.0259	34196	yes		
211942157.01	12.051	1.324292	3263.37798	0.2452	249317	yes		
211955798.01	14.902	0.616444	3263.06087	0.0290	5674		thrice period	
211964001.01	9.402	7.218071	3266.51847	0.1993	32035			211964332.01, 211964025.01, 211964555.01, 251809628.01
211964025.01	7.605	7.219626	3266.50648	0.2035	31796			211964332.01, 211964001.01, 211964555.01, 251809628.01
211964555.01	18.314	7.220943	3266.50089	0.2204	34667			211964332.01, 211964001.01, 211964025.01, 251809628.01
211972837.01	13.547	1.092917	3263.45491	0.1566	1355446	yes		211972627.01, 211972681.01
212009702.01	13.173	0.923861	3263.37075	0.1382	345965	yes		
212010565.01	14.531	2.851451	3263.72690	0.3877	992969			
212012387.01	13.972	3.244126	3264.32148	0.1609	405896	yes	even-odd – half-period	
212019055.01	12.700	0.821436	3263.14571	0.0991	162008	yes		
212020442.01	13.974	3.888853	3263.60805	0.1295	25872	yes	even-odd – half-period	
212024647.01	10.279	3.696871	3262.87322	0.1286	124336	yes		212024672.01
212026226.01	16.843	1.769505	3263.39804	0.1512	176962		even-odd – half-period	

Table 3.4: Systems with Secondary Eclipses (cont'd)

Candidate	Kp	P [d]	T_0 [BJD$_{TDB}$ - 2454833]	T_{14} [d]	$(R_P/R_*)^2$ [ppm]	In C5?	Comment	Ephemeris matching
212037403.01	13.231	3.408190	3265.44045	0.1191	164327	yes		
212039539.01	11.647	2.229820	3263.61073	0.2225	247831			
212044495.01	12.733	1.830767	3263.40493	0.1187	157032			
212048503.01	13.625	0.617674	3262.65639	0.0817	598171		twice period	
212053988.01	15.028	0.579309	3262.53528	0.0817	471689		twice period	
212060710.01	14.273	1.204338	3262.76086	0.1057	406463			
212060895.01	16.782	0.604228	3262.94672	0.0704	196260		twice period	
212066805.01	10.410	0.816734	3262.60536	0.0505	5075			
212069706.01	14.410	0.547674	3262.88638	0.0239	1629	yes	twice-period	
212071939.01	13.598	1.743013	3262.49990	0.2452	470271			
212075294.01	15.873	0.550820	3262.88533	0.0789	319979		twice period	
212075842.01	14.516	1.153456	3262.92758	0.2072	128377		possible even-odd	
212082682.01	14.611	3.797473	3262.81109	0.1082	118402	yes		
212083250.01	11.967	0.518748	3262.97005	0.0817	157737	yes		212083455.01
212083455.01	12.262	0.518754	3262.96851	0.0344	228	yes		212083250.01
212085654.01	13.900	0.989720	3262.87427	0.1128	168919			
212085740.01	13.688	4.845561	3263.15766	0.1162	77469	yes		
212086717.01	14.757	0.643142	3263.04961	0.0817	450377		twice period	
212109233.01	12.624	1.991357	3262.74598	0.1259	96349			
212110007.01	14.245	16.709659	3264.12649	0.1373	112830	yes		
212115388.01	14.605	1.488249	3262.99356	0.0756	48367		even-odd – half-period	
212116340.01	12.079	0.610205	3262.87662	0.0817	136330	yes		
212117087.01	12.245	1.076390	3262.97882	0.1212	91275		even-odd – half-period	
212154158.01	12.300	1.023613	3263.35564	0.2126	11010			
212163353.01	13.539	5.173531	3265.85411	0.1336	58580	yes		

Table 3.4: Systems with Secondary Eclipses (cont'd)

Candidate	Kp	P [d]	T_0 [BJD$_{TDB}$ - 2454833]	T_{14} [d]	$(R_P/R_*)^2$ [ppm]	In C5?	Comment	Ephemeris matching
212171851.01	14.143	5.489456	3266.59388	0.5965	370025	yes		
212175087.01	13.431	0.699705	3262.85587	0.1975	244959			
212181307.01	15.502	0.555317	3262.74524	0.0817	416594		twice period	
212181460.01	14.620	0.569192	3262.70026	0.0817	276502			
212182233.01	14.991	0.751394	3262.93405	0.0817	628169			
212207194.01	12.285	9.148701	3265.32727	0.2275	119700			
212208163.01	15.437	2.724469	3263.01388	0.2452	665629			
212210390.01	13.136	12.886147	3262.90925	0.1161	62814			
212214592.01	13.803	0.723102	3263.08482	0.0820	58108			
212221986.01	15.093	0.526018	3262.72081	0.0597	236909			
212225413.01	13.937	0.793048	3263.13909	0.1360	200400			
212225806.01	15.251	0.594392	3262.90962	0.0817	406214		double period	
212225986.01	13.668	1.160308	3263.03616	0.0993	205206		even-odd – half-period	
212228588.01	14.794	0.598120	3262.85185	0.0606	108294			251307609.01
228682364.01	19.970	0.872893	3263.15278	0.1432	68394	yes		
251281013.01	14.183	3.287912	3265.59014	0.1247	107725		even-odd – half-period	
251286992.01	15.448	0.505602	3262.78219	0.0740	410848		twice period	
251292508.01	15.238	1.288312	3263.63014	0.0829	241729		even-odd – half-period	
251307609.01	15.183	0.598197	3262.86830	0.0817	379663		twice period	212228588.01
251308775.01	11.989	2.804246	3263.72840	0.1635	69100			
251314585.01	14.440	0.691617	3263.02339	0.0817	98244			
251315031.01	13.537	0.540527	3262.97430	0.0788	333734			
251327548.01	11.636	11.349445	3268.62400	0.2443	59759			
251330444.01	11.202	5.998652	3265.28349	0.4500	83190		odd-even – half-period.	
251345848.01	12.505	2.883162	3263.26254	0.1305	37899			

Table 3.4: Systems with Secondary Eclipses (cont'd)

Candidate	Kp	P [d]	T_0 [BJD$_{TDB}$ - 2454833]	T_{14} [d]	$(R_P/R_*)^2$ [ppm]	In C5?	Comment	Ephemeris matching
251345849.01	16.059	0.545251	3262.96562	0.0817	139220			
251347050.01	12.290	0.493967	3262.55539	0.0895	17723			
251353301.01	14.556	0.504475	3262.67601	0.0772	87373			
251356484.01	14.484	0.781949	3262.81038	0.1084	186838			
251356953.01	14.568	5.214590	3266.48141	0.1706	555674			
251383916.01	16.220	1.332797	3263.21492	0.1635	645357			
251390801.01	13.319	0.592255	3262.47910	0.0817	312313		twice period	
251393748.01	11.256	8.071810	3266.66297	0.1346	190291			
251393916.01	15.093	0.678473	3262.53788	0.0755	58984			
251394139.01	11.763	26.286249	3277.27748	0.3626	110497			
251404897.01	16.029	0.660085	3262.70281	0.0817	273793			
251411166.01	14.179	3.374330	3262.71953	0.2550	23276			
251809286.01	16.200	9.485826	3264.49974	0.6392	52542			211919555.01, 211920528.01, 211920604.01
251809628.01	20.140	7.220585	3266.50127	0.2244	38587			211964332.01, 211964001.01, 211964025.01, 211964555.01

Table 3.5: Systems showing periodic variability

Candidate	Kp	P [d]	In C5?	Comment	Ephemeris matching
211404813.01	16.261	0.560055			
211405917.01	16.664	0.53736	yes		
211417284.01	14.388	0.912345			
211419593.01	14.084	0.544223			
211422471.01	9.95	1.694853			
211432103.01	10.249	0.933482	yes	likely even-odd	
211432905.01	17.747	0.565384	yes		
211433054.01	13.798	0.61983	yes		
211434930.01	14.249	0.619451			
211440296.01	15.179	0.494049		thrice period	
211441441.01	16.838	0.591286			
211442676.01	11.446	0.608446			
211443853.01	14.141	0.561341			
211446249.01	14.273	0.615748		four times period	
211446443.01	16.105	0.592558			212033577.01
211448564.01	14.193	0.601654			
211460030.01	14.43	0.645333			
211460061.01	19.164	0.625954			
211461914.01	14.825	0.65416			
211463443.01	12.52	0.616079			211880558.01
211466875.01	11.368	0.652342			
211467499.01	12.702	0.656892			
211469982.01	16.85	0.610206			
211476633.01	14.316	0.593171			
211478023.01	9.328	0.624181	yes	four times period	
211484212.01	16.047	0.560321	yes		
211489039.01	11.76	0.63247	yes		
211490515.01	14.366	1.028101	yes		
211493788.01	15.443	0.505653			
211497766.01	15.273	0.599943			
211500156.01	14.979	0.512656			
211505322.01	14.512	0.636194			
211505333.01	14.727	0.57382			
211513796.01	14.574	0.497528			211892395.01
211514420.01	14.713	0.625234		thrice period	
211515715.01	13.759	0.656366		four times period	
211523002.01	15.759	0.534137			
211532642.01	17.637	0.6961		thrice period	
211536560.01	16.958	0.549796			
211538914.01	10.11	0.49353	yes		
211548601.01	14.234	0.612276			

Table 3.5: Systems showing periodic variability (cont'd)

Candidate	Kp	P [d]	In C5?	Comment	Ephemeris matching
211557076.01	13.619	0.75719			
211558647.01	13.173	0.643227		twice period	
211600632.01	16.688	0.630718		galaxy	211600389.01
211604764.01	15.381	0.631078	yes	double period	
211620946.01	13.789	0.510214		thrice period	
211626641.01	16.243	0.53009			
211630761.01	12.248	0.866331			
211635890.01	14.755	0.725634			
211637025.01	15.064	0.730568			
211637624.01	13.35	0.870809			
211638042.01	15.258	0.549654		thrice period	
211638623.01	15.882	0.930924			
211647067.01	15.508	0.588719		four times period	
211648739.01	11.346	0.543899			
211655464.01	14.846	0.536933			
211660114.01	15.758	0.571957			
211661302.01	14.459	0.729855			
211661627.01	14.265	0.567284		four times period	
211663508.01	14.343	0.544418		four times period	
211663804.01	11.477	0.504537		marginal. twice period	
211665162.01	14.071	0.509189			
211675538.01	10.902	0.942686			
211675809.01	16.992	0.576179		four times period	
211690514.01	14.863	0.543476		twice period	
211690710.01	10.74	0.546275			
211712111.01	14.052	0.578952			
211719362.01	10.481	0.603347	yes	thrice period	
211723397.01	16.886	0.495563		galaxy	211723536.01
211723536.01	13.946	0.495561			211723397.01
211727340.01	16.741	1.201041			
211731135.01	15.656	0.622298	yes		
211740165.01	12.557	0.506108			
211746225.01	19.166	2.131503		quasar	211732801.01
211761392.01	15.241	0.651541		period multiple	
211763285.01	13.092	0.504204			
211767109.01	14.05	0.602632			
211796365.01	16.387	0.559817			
211812650.01	14.449	0.743778	yes		
211814391.01	15.578	0.514631			
211817361.01	13.595	0.595522	yes		
211821331.01	14.997	0.667574	yes	twice period	
211821355.01	19.48	0.522619	yes		

Table 3.5: Systems showing periodic variability (cont'd)

Candidate	Kp	P [d]	In C5?	Comment	Ephemeris matching
211836630.01	16.206	0.6466			
211845034.01	16.466	1.332803	yes		
211849962.01	14.307	0.546683			
211856772.01	16.732	0.50999		twice period	
211859760.01	16.567	0.50096			
211862434.01	15.915	0.547386			
211863022.01	14.428	0.805189			
211864337.01	16.056	0.496984			
211869527.01	15.525	1.026173			
211871191.01	16.659	0.558281			
211876205.01	17.528	0.601344			
211880558.01	18.228	0.616146			211463443.01
211881456.01	17.431	0.588505			
211894518.01	12.214	1.288034	yes		
211902331.01	9.332	1.03411			211431013.01
211907820.01	16.895	1.646612			
211909322.01	15.311	0.838731	yes	twice period	
211911525.01	12.114	0.597831			
211914343.01	17.21	1.810841		galaxy	211914445.01, 211914889.01, 211914960.01, 211915147.01
211917859.01	17.481	0.574261		galaxy	
211918335.01	10.042	0.574317	yes		
211918516.01	14.408	0.724075			
211918830.01	12.798	0.692784	yes		
211919555.01	16.889	9.484994		galaxy	211920528.01, 211920604.01, 251809286.01, 251809286.01
211920462.01	19.874	9.516793		quasar	
211921309.01	17.026	9.478705		noisy – possibly variable depth. Galaxy	
211926098.01	13.349	0.509329			
211926877.01	18.414	0.571362	yes		
211927125.01	11.2	0.680888	yes		
211931604.01	11.827	0.828348	yes	twice period	
211938003.01	15.133	0.630256	yes		
211945144.01	13.94	0.65699	yes	twice period	
211945831.01	14.875	0.516025	yes		
211946241.01	14.332	1.189492	yes		
211947405.01	13.973	0.604689	yes		
211948134.01	18.646	0.501662		galaxy	

Table 3.5: Systems showing periodic variability (cont'd)

Candidate	Kp	P [d]	In C5?	Comment	Ephemeris matching
211950298.01	16.326	0.510436	yes		
211951418.01	15.433	0.564096			
211957146.01	12.603	0.532536	yes		
211957745.01	16.262	0.507392			
211966619.01	15.166	0.800628			
211973080.01	16.339	1.092902		galaxy	211972627.01, 211972681.01, 211972837.01
211996682.01	12.593	1.36468	yes		
212001688.01	14.116	0.79668	yes		
212005402.01	15.052	0.679429			
212008305.01	13.037	0.615002	yes		
212011476.01	12.743	0.715915	yes		
212013694.01	15.313	0.552221			
212018921.01	14.748	0.519797	yes		212018980.01
212018980.01	17.863	0.519707			212018921.01
212019712.01	14.115	0.952995	yes		
212021237.01	18.791	0.681632		quasar	212043122.01, 212050004.01
212022582.01	15.127	0.834426			
212024898.01	15.509	0.599922			
212027377.01	17.643	1.106476	yes		
212027952.01	11.29	0.949276			
212028041.01	14.321	0.729797	yes	twice period	
212032754.01	15.853	0.558059			
212037558.01	11.882	0.627062	yes		
212041051.01	16.235	0.627561		four times period	
212043122.01	9.899	0.681463			212021237.01, 212050004.01
212048412.01	14.391	0.502575			
212050004.01	16.496	0.681455		twice period	212021237.01, 212043122.01
212050890.01	13.589	0.966599			
212054062.01	16.709	0.944882			
212055545.01	15.058	0.613025			
212060713.01	15.626	0.61537			
212066299.01	11.324	2.609746			
212085240.01	15.164	0.565691			
212086317.01	14.301	0.535092			
212086389.01	16.282	0.493336		thrice period	
212089888.01	15.346	0.681236			
212091210.01	14.526	0.683492			

Table 3.5: Systems showing periodic variability (cont'd)

Candidate	Kp	P [d]	In C5?	Comment	Ephemeris matching
212091834.01	16.122	0.908531			
212095395.01	10.106	0.640683	yes		
212102092.01	14.613	1.227465			
212105446.01	14.448	0.586443			
212106797.01	15.529	0.614616		twice period	
212109327.01	12.477	0.492292			
212110857.01	17.75	0.922879	yes		
212114705.01	19.689	0.610284		twice period; quasar	212116340.01
212118200.01	15.204	0.508903			251391268.01
212118344.01	10.719	0.752885			
212159519.01	12.779	0.717385	yes	twice period	
212159586.01	14.621	0.563176			
212161144.01	13.822	0.723318			
212161874.01	16.807	0.572131			
212163652.01	13.465	0.551515			
212164476.01	14.499	0.67844	yes	twice period	
212172621.01	11.764	0.911485	yes		
212174388.01	14.638	0.665443	yes	twice period	
212174434.01	13.481	0.552321		thrice period	
212177756.01	15.782	0.491506			
212180386.01	17.422	0.718264		double period	
212183082.01	17.322	0.575069			
212194110.01	12.819	0.520576			212194171.01
212194171.01	12.819	0.520576			212194110.01
212199005.01	14.449	0.688457			
212204655.01	15.164	0.709082		likely half-period	
212212241.01	15.624	0.618142			
212222875.01	18.097	1.19013		galaxy	212207368.01, 212223307.01, 212231252.01
212226872.01	16.14	0.516574			
212230240.01	11.887	0.559411			
212231252.01	17.747	1.190356		V-shaped, coincides with 212222875, galaxy	212207368.01, 212223307.01, 212222875.01
251277092.01	12.067	0.502406			
251277701.01	16.014	0.701132			
251278670.01	11.026	0.634153			
251279786.01	16.624	0.503283			
251282021.01	16.24	0.527674			
251283448.01	14.032	0.516848			
251283585.01	15.29	0.497466			

Table 3.5: Systems showing periodic variability (cont'd)

Candidate	Kp	P [d]	In C5?	Comment	Ephemeris matching
251284270.01	13.642	0.688028			
251284826.01	13.557	0.534658			
251290111.01	16.013	0.515451			
251297292.01	14.451	0.521537		thrice period	
251307454.01	16.142	0.551316			211631538.01
251316666.01	14.396	0.567813			
251321168.01	14.203	0.606779			
251321696.01	15.703	0.631561			
251323035.01	14.221	0.596242		thrice period	
251330643.01	19.247	5.997937		quasar	251330444.01
251336933.01	12.952	1.166224			
251342381.01	15.777	0.878144			
251347997.01	14.102	0.497745			
251348935.01	12.852	0.562005			
251349510.01	12.286	0.605516			
251350556.01	16.267	0.699118			
251351108.01	14.098	0.732705			
251355465.01	16.019	0.574342			
251356578.01	11.493	0.788145			
251365170.01	13.313	0.902363			251365173.01
251365173.01	13.563	0.902431		twice period	251365170.01
251374534.01	13.993	0.890305			
251384067.01	17.67	0.527066			
251390658.01	15.332	0.716276			
251391268.01	13.759	0.508759		thrice period	212118200.01
251392383.01	16.699	0.567376			
251397356.01	15.266	1.170258			
251397429.01	12.393	0.542076			
251400494.01	12.922	0.715199		twice period	
251401983.01	14.39	0.836151		twice period	
251402361.01	15.0	0.809957			
251403257.01	16.493	0.638882			
251403570.01	14.633	1.036362			
251809170.01	18.41	0.553061		twice period	
251809263.01	18.93	0.650882			
251809286.01	16.2	9.485826		galaxy	211919555.01, 211920528.01, 211920604.01, 211919555.01

Table 3.5: Systems showing periodic variability (cont'd)

Candidate	Kp	P [d]	In C5?	Comment	Ephemeris matching
251809628.01	20.14	7.220585		galaxy	211964332.01, 211964001.01, 211964025.01, 211964555.01

Chapter 4

New Discoveries: Two Warm, Low-density Sub-Jovian Planets Orbiting Bright Stars in K2 Campaigns 13 and 14

The content of this chapter was submitted to AJ *on March 6, 2018 and published [305] on August 29, 2018 as* Two Warm, Low-density Sub-Jovian Planets Orbiting Bright Stars in *K2* Campaigns 13 and 14*, by Liang Yu, Joseph E. Rodriguez, Jason D. Eastman, Ian J. M. Crossfield, Avi Shporer, B. Scott Gaudi, Jennifer Burt, Benjamin J. Fulton, Evan Sinukoff, Andrew W. Howard, Howard Isaacson, Molly R. Kosiarek, David R. Ciardi, Joshua E. Schlieder, Kaloyan Penev, Andrew Vanderburg, Keivan G. Stassun, Allyson Bieryla, R. Paul Butler, Perry Berlind, Michael L. Calkins, Gilbert A. Esquerdo, David W. Latham, Gabriel Murawski, Daniel J. Stevens, Erik A. Petigura, Laura Kreidberg, and Makennah Bristow.*

We report the discovery of two planets transiting the bright stars HD 89345 (EPIC 248777106, $V = 9.376$, $K = 7.721$) in *K2* Campaign 14 and HD 286123 (EPIC 247098361, $V = 9.822$, $K = 8.434$) in *K2* Campaign 13. Both stars are G-type stars, one of which is at or near the end of its main sequence lifetime, and the other that

is just over halfway through its main sequence lifetime. HD 89345 hosts a warm sub-Saturn (0.66 $R_{\rm J}$, 0.11 $M_{\rm J}$, $T_{\rm eq}$ = 1100 K) in an 11.81-day orbit. The planet is similar in size to WASP-107b, which falls in the transition region between ice giants and gas giants. HD 286123 hosts a Jupiter-sized, low-mass planet (1.06 $R_{\rm J}$, 0.39 $M_{\rm J}$, $T_{\rm eq}$ = 1000 K) in an 11.17-day, mildly eccentric orbit, with $e = 0.255 \pm 0.035$. Given that they orbit relatively evolved main-sequence stars and have orbital periods longer than 10 days, these planets are interesting candidates for studies of gas planet evolution, migration, and (potentially) re-inflation. Both planets have spent their entire lifetimes near the proposed stellar irradiation threshold at which giant planets become inflated, and neither shows any sign of radius inflation. They probe the regime where inflation begins to become noticeable and are valuable in constraining planet inflation models. In addition, the brightness of the host stars, combined with large atmospheric scale heights of the planets, makes these two systems favorable targets for transit spectroscopy to study their atmospheres and perhaps provide insight into the physical mechanisms that lead to inflated hot Jupiters.

4.1 Introduction

Giant planets have historically been an important class of transiting exoplanets, and many questions have been raised about their formation and evolution. The discovery of the first hot Jupiters immediately upended all existing giant planet formation models, which were based on observations of the Solar System. One of the most pressing open questions is how hot Jupiters, or Jupiter-mass planets orbiting at only a few percent of an astronomical unit from their host stars, are able to reach such short orbital periods. Although *in situ* formation has been considered as a possibility [e.g. 30, 23], hot Jupiters are most commonly thought to have formed at large radial distances and subsequently migrated inward to their present orbits. There have been several theories attempting to explain hot Jupiter migration. Some invoke interactions with a planetary or stellar companion: the gas giant planet is first injected into an eccentric orbit, which then undergoes tidal circularization [e.g. 238, 97]. Other

theories suggest processes where the gas giant planet gradually moves inward by interacting with the protoplanetary disk, during which the orbit is kept circular [e.g. 181, 6]. The two theories predict different orbital eccentricities and stellar obliquities as the planet migrates inward, yet it appears that stellar obliquities in hot Jupiter systems may be erased by tides raised by the planet on the star [e.g. 251, 296]. We would then expect warm Jupiters - gas giants with orbital periods of 10 days or longer - which experience weaker tidal effects, to have retained the obliquity they had when emplaced in their current orbits. In reality, however, the interpretation is not that simple, as Mazeh et al. [197] found that warm Jupiters seem to be showing effects of tidal realignment even at orbital distances where tidal effects should be negligible.

Another long-standing mystery is the anomalously large radii of "inflated" close-in giant planets. Many of the known transiting hot Jupiters have radii larger than expected by standard models of giant planets [see, e.g., 52, 31, 121]. Dozens of inflated hot Jupiters with radii $> 1.2\ R_{\rm J}$ have been observed to orbit stars several Gyr old [120]. Although very young planets (< 10 Myr) are expected to have radii this large, it is unclear how such inflated planets can exist around mature main sequence and even evolved stars [e.g. 119].

Various mechanisms have been proposed to explain the large radii of hot Jupiters. Following Lopez & Fortney [188], the suggested mechanisms for inflating gas giants can be divided into two categories: in class I mechanisms, stellar irradiation incident on a planet is transported into the planet's deep interior, driving adiabatic heating of the planet and causing it to expand [e.g. 24, 13]; in class II mechanisms, the inflationary mechanism simply acts to slow radiative cooling through the atmosphere, allowing a planet to retain its initial heat and inflated radius from formation [delayed contraction, e.g. 51]. The observation that the radii of giant planets increase with incident stellar irradiation hints that giant planet inflation is intimately linked to irradiation [50, 31, 188]. We can distinguish between these two classes of models by studying warm Jupiters around stars that have recently evolved off the main sequence [e.g., 254, 259]. The irradiation levels experienced by warm Jupiters around main sequence stars are not high enough to cause inflation, but as their host stars move up

the subgiant and red-giant branches, they will experience enormous increases in their irradiation levels. If class I mechanisms are responsible for giant planet inflation, then warm Jupiters should inflate in response to the increased irradiation [14, 261, 124]. On the other hand, an exclusively non-inflated population of warm Jupiters around evolved stars would favor class II mechanisms [188].

Finally, we have yet to even understand the formation mechanism of giant planets. The positive correlation between the fraction of stars with short-period giant planets and stellar metallicity hints that planets form through core accretion [e.g. 248, 148]. In the core accretion scenario, a rocky core forms through the coagulation of planetesimals; when the mass of the gaseous envelope relative to the solid core mass reaches a critical ratio, rapid gas accretion occurs and a giant planet is formed [e.g. 231]. Gas accretion is expected to start in the mass regime between Neptune and Saturn [206], the transition zone between ice giants and gas giants. Yet this regime is not very well understood given the small number of known planets that fall within this mass range. In particular, the core accretion model struggles to explain why ice giants do not undergo the runaway gas accretion that would have turned them into gas giants [127].

In this chapter, we present the discovery of two exoplanets observed by *K2*, which are pertinent to the problems described above: one sub-Saturn transiting a bright star HD 89345 (EPIC 248777106), and a warm Saturn orbiting a similarly bright star HD 286123 (EPIC 247098361), with both stars well into or nearing the ends of their main sequence lifetimes. Despite their large radii, both planets have low masses, which make them promising targets for atmospheric characterization. They are also interesting additions to the currently available set of giant planets to study radius inflation, which consists primarily of Jupiter-massed objects. We describe our discovery and observations in Section 4.2, our derivation of stellar and planetary parameters in Sections 4.3 and 4.4, and potential implications for giant planet migration, inflation and formation theories in Section 4.5.

Table 4.1. Stellar parameters of HD 89345 and HD 286123 from the literature and spectroscopy

Parameter	HD 89345	HD 286123	Source
Identifying Information			
α_{J2000} R.A. (hh:mm:ss)	10:18:41.06	04:55:03.96	
δ_{J2000} Dec. (dd:mm:ss)	10:07:44.5	18:39:16.33	
Other identifiers	TYC 840-840-1	TYC 1284-745-1	
	2MASS J10184106+1007445	2MASS J04550395+1839164	
	EPIC 248777106	EPIC 247098361	
	K2-234	K2-232	
K2 campaign	14	13	
Photometric Properties			
B (mag).....	10.148 ± 0.039	10.520 ± 0.051	1
V (mag)	9.376 ± 0.028	9.822 ± 0.038	1
J (mag).....	8.091 ± 0.020	8.739 ± 0.030	2
H (mag)	7.766 ± 0.040	8.480 ± 0.018	2
Ks (mag)	7.721 ± 0.018	8.434 ± 0.017	2
W1 (mag)	7.763 ± 0.028	8.380 ± 0.024	3
W2 (mag)	7.759 ± 0.020	8.419 ± 0.019	3
W3 (mag)	7.729 ± 0.019	8.391 ± 0.027	3
Spectroscopic and Derived Properties			
Spectral Type	G5V-G6V	F9V-G0V	4
μ_α (mas yr^{-1})	5.348 ± 0.079	62.064 ± 0.077	5
μ_δ (mas yr^{-1})	-42.449 ± 0.071	-48.245 ± 0.051	5
Parallax (mas)	7.528 ± 0.046	7.621 ± 0.044	5
Barycentric RV (km s^{-1})	2.4 ± 0.1	22.4 ± 0.1	TRES; this paper
$v \sin i$ (km s^{-1})	3 ± 1	3 ± 1	APF; this paper
Space motion (U^*,V,W) (km s^{-1})	(21.5±0.1, -9.8±0.1, 1.5±0.1)	(-14.9±0.1, -34.5±0.3, 13.5±0.1)	this paper

References: (1) Høg et al. [132]; (2) Skrutskie et al. [258]; (3) Cutri et al. [79]; (4) Pecaut & Mamajek [222], (5) Gaia Collab. et al. [108, 109].
* Positive U is in the direction of the Galactic center

4.2 Observations

HD 286123 was proposed as a *K2* target in Campaign 13 (C13) in four programs: GO13071 (PI Charbonneau), GO13122 (PI Howard), GO13024 (PI Cochran) and GO13903 (GO Office). HD 89345 was proposed as a target in Campaign 14 (C14) in five programs: GO14010 (PI Lund), GO14009 (PI Charbonneau), GO14028 (PI Cochran), GO14021 (PI Howard) and GO14901 (GO Office). C13 was observed from 2017 Mar 08 to May 27, and C14 was observed from 2017 Jun 01 to Aug 19. HD 89345 and HD 286123's photometric and spectroscopic properties are given in Table 4.1.

4.2.1 *K2* Photometry

We converted the processed *K2* target pixel files into light curves using an approach identical to that described in Crossfield et al. [76]. In brief, we computed the raw photometry by summing the flux within a soft-edged circular aperture centered around the target star, and used the publicly available `k2phot` photometry code[1] to model out the time- and roll-dependent variations with a Gaussian process. We then used the publicly available `TERRA` algorithm[2] [224, 225] to search for transit-like events and manually examined diagnostic plots for all signals with S/N ≥ 10. `TERRA` identified a planet candidate orbiting HD 89345 with $P = 11.81$ days and S/N = 24 in Campaign 14, and another candidate orbiting HD 286123 with $P = 11.17$ days and S/N = 495 in Campaign 13.

After identifying the transits, we produced new light curves by simultaneously fitting the transits, the *K2* roll systematics, and long-timescale stellar/instrumental variability. Reprocessing the *K2* light curves in this way prevents the shape of the transits from being biased by the removal of *K2* systematics. We used light curves and systematics corrections derived using the method of Vanderburg & Johnson [286] as initial guesses for our simultaneous fits, which we then performed following Vanderburg et al. [288]. Throughout the rest of this paper, we use these simultaneously-fit light curves in our analysis and our plots. Fig. 4-1 shows the flattened[3] and detrended light curves of HD 89345 and HD 286123.

[1] https://github.com/petigura/k2phot

[2] https://github.com/petigura/terra

[3] We flattened the light curves by dividing away the best-fit long-timescale variability from our simultaneously-fit light curve.

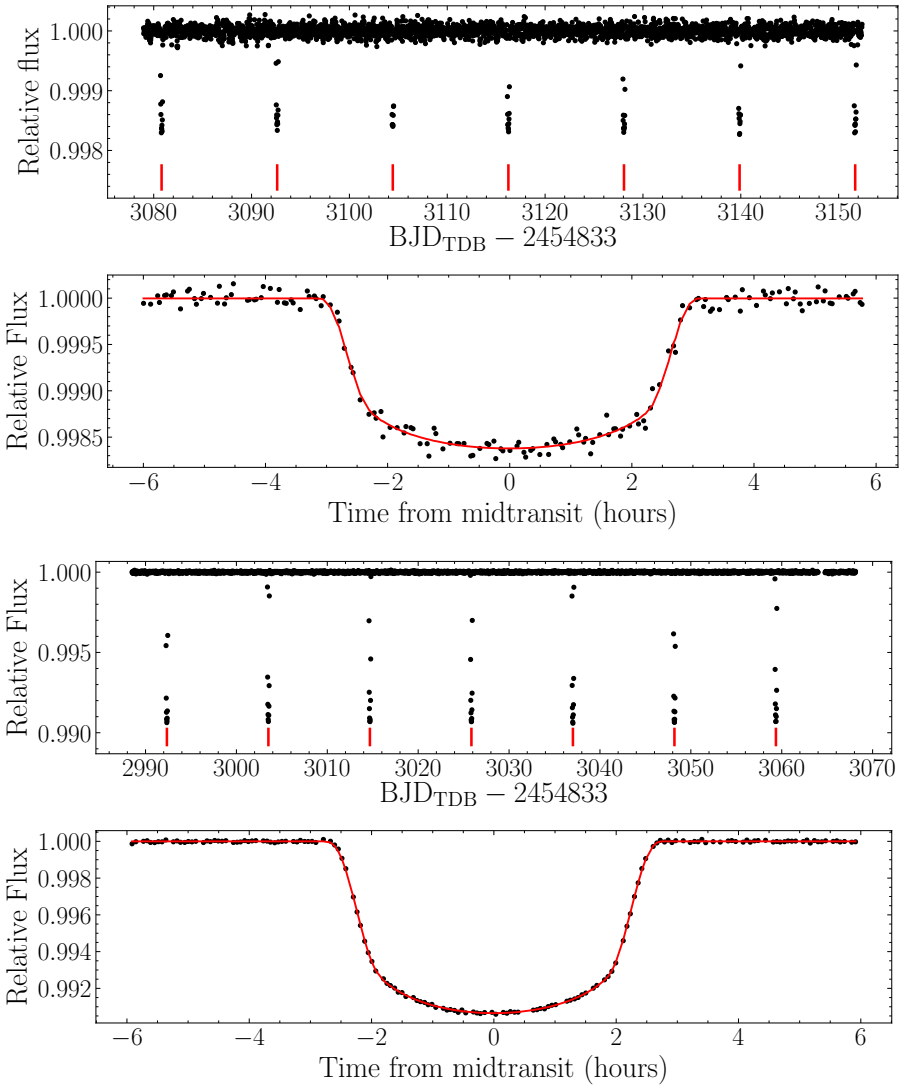

Figure 4-1 *Upper panels*: Calibrated *K2* photometry for HD 89345 (top), with vertical ticks indicating the locations of the transits, and phase-folded photometry and best-fit light curve model (bottom). *Lower panels:* Same, but for HD 286123.

4.2.2 Ground-based Followup

In this section, we present our ground-based photometric and spectroscopic observations used to confirm the planetary nature of HD 89345b and HD 286123b.

4.2.2.1 Spectroscopic followup

We used the HIRES spectrograph [291] at the W. M. Keck Observatory to measure high-resolution optical spectra of the two targets. Observations and data reduction followed the standard procedures of the California Planet Search [CPS; 134]. For both stars, the 0.86″× 14″ "C2" decker was placed in front of the slit and the exposures were terminated once an exposure meter reached 10,000 counts, yielding a signal-to-noise ratio (SNR) of 45 per pixel at 550 nm. Additional spectra of HD 89345 were collected to measure precise radial velocities (RVs), by placing a cell of gaseous iodine in the converging beam of the telescope, just ahead of the spectrometer slit. The iodine cell is sealed and maintained at a constant temperature of 50.0 ±0.1°C to ensure that the iodine gas column density remains constant over decades. The iodine superimposes a rich forest of absorption lines on the stellar spectrum over the 500-620 nm region, thereby providing a wavelength calibration and proxy for the point spread function (PSF) of the spectrometer. Once extracted, each spectrum of the iodine region is divided into ∼700 chunks, each of which is 2 Å wide. Each chunk produces an independent measure of the wavelength, point spread function, and Doppler shift, determined using the spectral synthesis technique described by [54]. The final reported Doppler velocity for a stellar spectrum is the weighted mean of the velocities of all the individual chunks. The final uncertainty of each velocity is the weighted average of all 700 chunk velocities. These iodine exposures were terminated after 50,000 counts (SNR = 100 per pixel), typically lasting 2 min. For both stars, a single iodine-free "template" spectrum with a higher SNR of 225 was also collected using the narrower "B3" decker (0.57″× 14″). RVs were measured using the standard CPS Doppler pipeline [192, 282, 54, 133]. Each observed spectrum was forward modeled as the product of an RV-shifted iodine-free spectrum and a high-resolution/high-SNR iodine transmission spectrum convolved with a PSF model. Typical internal RV uncertainties were 1.5 m s^{-1}.

We obtained additional spectra for the two targets with the Tillinghast Reflector Echelle Spectrograph [TRES; 273] on the 1.5 m telescope at the Fred L. Whipple

Observatory on Mt. Hopkins, AZ. The TRES spectra have a resolution of 44,000 and were extracted as described in Buchhave et al. [47]. We obtained 8 TRES spectra of HD 286123 in Oct 2017. The average S/N per resolution element (SNRe) was 46, which was determined at the peak continuum of the Mgb region of the spectrum near 519 nm. HD 89345 was observed twice, once in 2017 Nov and again in 2017 Dec, with an average SNR of 54. The TRES spectra were not used to determine an orbital solution but were used to determine stellar parameters (see Section 4.3).

The RV dataset for HD 286123 is comprised of 19 velocities obtained between 2018 Oct and 2019 Feb using the Automated Planet Finder (APF), a 2.4m telescope located atop Mt. Hamilton at Lick Observatory. One of the 19 measurements was discarded due to cloudy observing conditions. The telescope is paired with the Levy echelle spectrograph, and is capable of reaching 1 m s^{-1} precision on bright, quiet stars. The Levy spectrograph is operated at a resolution of ∼90,000 for RV observations and covers a wavelength range of 370-900 nm, though only the 500-620 nm Iodine region is used in extracting Doppler velocities [292]. APF RVs were collected using the same iodine-based methodology described above.

The APF is a dedicated exoplanet facility, and employs a dynamic scheduler to operate without the aid of human observers [53]. Due to the large expected RV semi-amplitude of the transiting planet (K ∼26 m s^{-1}) and the desire to use the telescope as efficiently as possible, we set the desired RV precision in the dynamic scheduler to 4 m s^{-1}. The exposure times necessary to achieve this precision were automatically calculated in real time to account for changing atmospheric conditions, and the resulting RV data set has a mean internal uncertainty of 3.9 m s^{-1}. In our analysis, we chose to omit data taken on one night due to a low number of photons in the iodine region, caused by cloudy observing conditions.

APF RVs for HD 89345 were collected in exactly the same way between Nov 2017 and Feb 2018 except that we used fixed 30-min exposure times giving SNR ∼ 80. We also utilized the iodine-free “template" observations collected on Keck during the RV extraction in order to avoid duplication of data. All RV measurements for the two systems are reported in Tables 4.2 and 4.3.

Table 4.2. Radial velocities for HD 89345

BJD_{TDB}	RV (m s^{-1})	σ_{RV} (m s^{-1})	Instrument
2458088.069276	9.1	2.5	APF
2458089.027427	14.0	2.4	APF
2458092.004495	-7.8	1.9	HIRES
2458093.080794	-4.4	4.8	APF
2458094.982520	-2.0	2.5	APF
2458099.986259	5.6	1.7	HIRES
2458107.007150	-9.6	2.4	APF
2458109.930945	-6.0	3.5	APF
2458113.049078	2.9	1.4	HIRES
2458114.005711	6.4	2.8	APF
2458114.048573	2.3	1.7	HIRES
2458115.846145	-0.5	3.6	APF
2458116.934534	-8.5	1.2	HIRES
2458118.934942	-8.0	1.6	HIRES
2458120.050818	-8.9	2.8	APF
2458125.024846	1.0	1.7	HIRES
2458161.055191	1.7	1.2	HIRES
2458181.912190	5.3	1.6	HIRES
2458194.946988	14.0	1.6	HIRES
2458199.783821	-14.7	1.8	HIRES
2458209.952119	-0.3	1.8	HIRES

Table 4.3. Radial velocities for HD 286123

BJD_{TDB}	RV (m s^{-1})	σ_{RV} (m s^{-1})	Instrument
2458054.788204482	8.5	3.0	APF
2458055.777755827	17.3	3.1	APF
2458070.726872717	-19.5	3.6	APF
2458076.725079441	2.3	4.7	APF
2458079.684109405	10.4	2.9	APF
2458085.796427525	-22.1	3.1	APF
2458089.686568968	11.0	2.7	APF
2458097.641511793	-7.1	4.4	APF
2458098.690433952	0.8	3.3	APF
2458099.705764488	9.1	2.8	APF
2458102.620387156	15.1	3.3	APF
2458114.740644814	-6.8	4.0	APF
2458151.84598876	-45.9	6.8	APF
2458153.616766337	-8.1	4.1	APF
2458154.626598141	6.8	3.6	APF
2458158.828482109	14.9	3.7	APF
2458163.626207308	-36.4	3.3	APF
2458164.630352368	-17.5	3.7	APF

4.2.2.2 Keck/NIRC2 Adaptive Optics Imaging

We obtained NIR adaptive optics (AO) imaging of HD 89345 through clear skies with $\sim 0.8''$ seeing on the night of 2017 Dec 29 using the 10m Keck II telescope at the W. M. Keck Observatory. The star was observed behind the natural guide star AO system using the NIRC2 camera in narrow angle mode with the large hexagonal pupil. We observed using the narrow-band Br-γ filter ($\lambda_c = 2.1686$ μm; $\Delta\lambda = 0.0326$ μm) with a 3-point dither pattern that avoids the noisier lower left quadrant of the NIRC2 detector. Each dither was offset from the previous position by $0.5''$ and the star was imaged at 9 different locations across the detector. The integration time per dither was 1s for a total time of 9s. The narrow angle mode of NIRC2 provides a field-of-view of $10''$ and a plate scale of about $0.01''$ pixel^{-1}. We used the dithered images to remove sky-background, then aligned, flat-fielded, dark subtracted and combined the individual frames into a final combined image (see Fig. 4-2 inset). The final images had a FWHM resolution of $\sim$60 mas, near the diffraction limit at $\sim$2.2 μm.

We also obtained NIR high-resolution AO imaging of HD 286123 at Palomar Observatory with the $200''$ Hale Telescope at Palomar Observatory on 2017 Sep 06 using the NIR AO system P3K and the infrared camera PHARO [125]. PHARO has a pixel scale of $0.025''$ per pixel with a full field of view of approximately $25''$. The data were obtained with a narrow-band Br-γ filter ($\lambda_o = 2.166; \Delta\lambda = 0.02$ μm). The AO data were obtained in a 5-point quincunx dither pattern with each dither position separated by $4''$. Each dither position is observed 3 times with each pattern offset from the previous pattern by $0.5''$ for a total of 15 frames. The integration time per frame was 9.9s for a total on-source time of 148.5s. We use the dithered images to remove sky background and dark current, and then align, flat-field, and stack the individual images. The PHARO AO data have a resolution of $0.10''$ (FWHM).

To determine the sensitivity of the final combined images, we injected simulated sources at positions that were integer multiples of the central source FWHM scaled to brightnesses where they could be detected at 5σ significance with standard aperture photometry. We compared the Δ-magnitudes of the injected 5σ sources as a function

of their separation from the central star to generate contrast sensitivity curves (Fig. 4-2). We were sensitive to close companions and background objects with ΔBr-$\gamma \approx 6$ at separations $\geq$200 mas. No additional sources were detected down to this limit in the field-of-view of HD 89345, and the target appears single at the limiting resolution of the images.

A stellar companion was detected near HD 286123 in the Br-γ filter with PHARO. The companion separation was measured to be $\Delta\alpha = -1.39'' \pm 0.01''$ and $\Delta\delta = 0.28'' \pm 0.03''$. The companion has a measured differential brightness in comparison to the primary star of $\Delta_K = 6.75 \pm 0.05$ mag, which implies deblended stellar 2MASS K-band magnitudes of $K_S = 8.45 \pm 0.02$ mag and $K_S = 15.2 \pm 0.1$ mag for the primary and the companion respectively. Utilizing Kepler magnitude (K_p)-K_S relationships from Howell et al. [135], we derive approximate deblended Kepler magnitudes of $K_p = 9.81 \pm 0.01$ mag for the primary and $K_p = 17.3 \pm 0.8$ mag for the companion. The resulting Kepler magnitude difference is $\Delta K_p = 7.5 \pm 0.8$ mag. The companion star therefore cannot be responsible for the transit signals, but is potentially a bound stellar companion. At a separation of $1.4''$, the projected separation of the companion is approximately 175 AU. This translates to an orbital period of about a $\sim$2300 yr (10^6 days), which is near the peak of the period distribution of binaries [234] and within the 80% likelihood of AO-detected companions being bound for these separations [131]. With an infrared magnitude difference of $\Delta_K = 6.75$ mag and assuming the distance of HD 286123, the companion star has an infrared magnitude similar to that of an M7V dwarf [222].

The AO imaging rules out the presence of any additional stars within $\sim 0.5''$ of HD 286123 ($\sim$ 30 AU) and the presence of any brown dwarfs, or widely-separated tertiary components down to $K_S = 16.4$ beyond $0.5''(\sim 30 - 1000$ AU). All data and sensitivity curves are available on the ExoFOP-K2 site[4].

We also searched for any faint sources within the *K2* apertures used but beyond the field of view of the AO imaging by examining archival images from imaging surveys including SDSS9, 2MASS, Pan-STARRS and DECaLS/DR3, and catalogs including

[4]https://exofop.ipac.caltech.edu

UCAC, GSC2.3, 2MASS and SDSS12. Across all surveys and catalogs, we identified no sources brighter than 19 magnitudes in the g'-band and 18 magnitudes in the r'-band within 40″ of either star. The optical flux contribution of any faint companion is below the precision of *K2* and can be safely ignored in our transit fits.

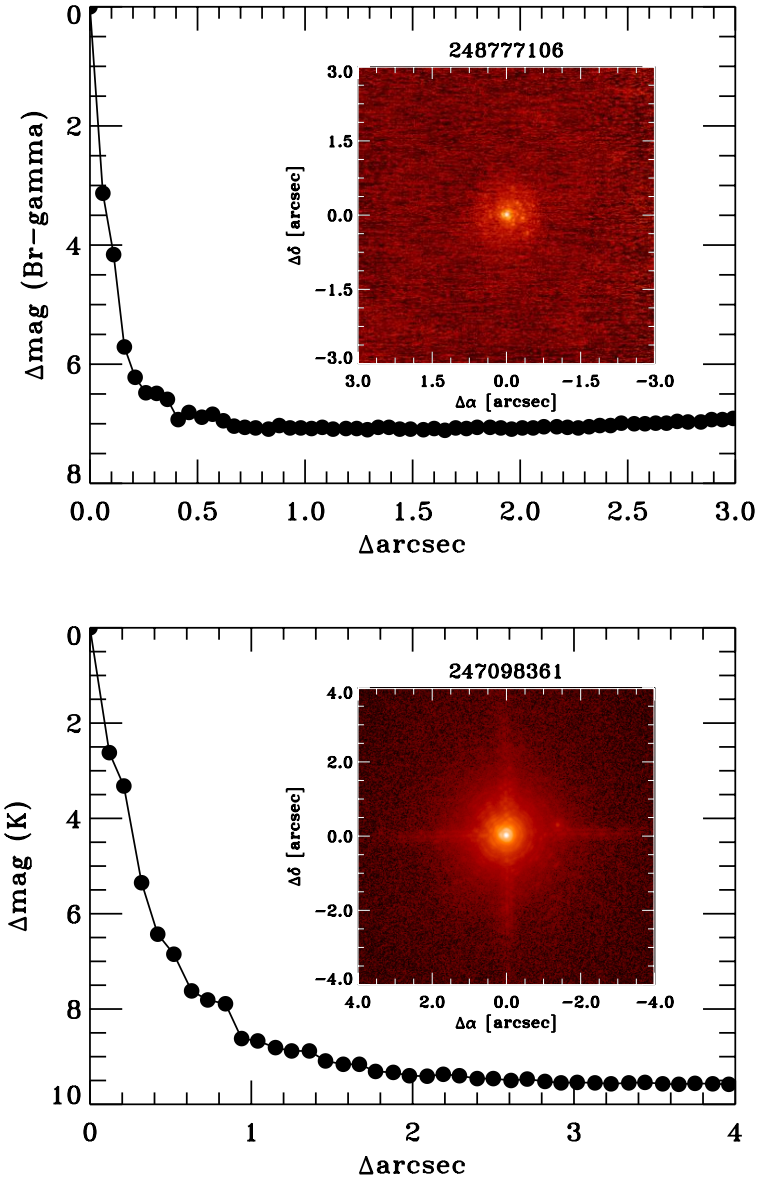

Figure 4-2 AO images (inset) and K_S-band contrast curves for HD 89345 (top) and HD 286123 (bottom). HD 89345 was imaged with Keck/NIRC2, and HD 286123 was imaged with Palomar/PHARO. The right image shows a faint companion at about $\sim 1.4''$ away from HD 286123, but this cannot be the source of the observed transit signals (see Section 4.2.2.2).

4.2.2.3 Ground-Based Photometry

We obtained additional ground-based photometric observations of HD 286123 on the night of 2017 Sep 29. One of us (G.M.) observed the second half of the transit from Suwałki, Poland using a 78mm ASI178MM-cooled camera with a 1/1.8″CMOS IMX178 sensor and Canon FD 300mm f/2.8 lens. The images have pixel scales of 1.65″/pixel. No filter was used, and each measurement consists of 100 binned 3s exposures.

Dark and flat calibrations were applied to each frame. The aperture used was a circular aperture with a radius corresponding to 8.7″. Two stable stars within the field of view were used as reference stars, and the flux of HD 286123 was divided by the sum of the reference stars' fluxes. We modeled the out-of-transit variations with a quadratic function, which was also divided out to obtain the detrended light curve. Fig. 4-3 shows the resulting light curve overplotted with the *K2* light curve, phase-folded to the same ephemeris. The data clearly show the transit egress and so confirm the ephemeris of this planet, but in the rest of our analysis we use only the *K2* light curve.

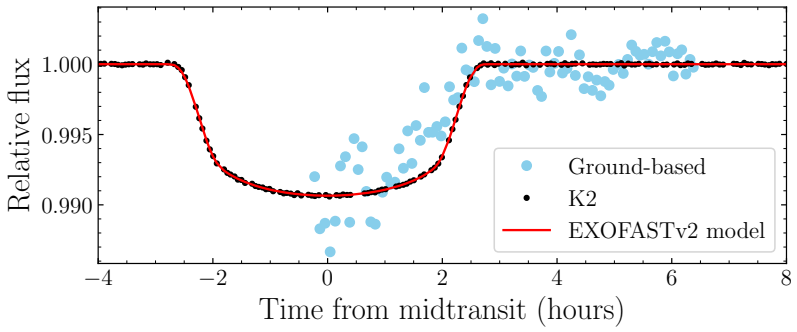

Figure 4-3 Detrended ground-based light curve of HD 286123 (blue) and *K2* light curve (black) phase-folded to the same ephemeris and overplotted with the transit model (red) from our global fit in Section 4.4.1.

4.3 Host Star Characterization

4.3.1 Spectral Analysis

We searched the iodine-free Keck/HIRES for spectroscopic blends using the algorithm of Kolbl et al. [160], which is sensitive to secondary stars with $> 1\%$ flux and ΔRV > 10 km s^{-1} relative to the primary star. No secondary lines were detected in either spectrum.

We calculated initial estimates of the spectroscopic parameters of the host stars from our iodine-free Keck/HIRES spectra using the SpecMatch procedure [223]. SpecMatch searches a grid of synthetic model spectra [69] to fit for the effective temperature ($T_{\rm eff}$), surface gravity ($\log g$), metallicity ([Fe/H]) and projected equatorial rotation velocity of the star ($v \sin i$). The resulting values are $T_{\rm eff} = 5532 \pm 100$ K, $\log g = 3.71 \pm 0.10$, [Fe/H]$= +0.44 \pm 0.06$, $v \sin i = 3 \pm 1$ km/s for HD 89345, and $T_{\rm eff} = 5909 \pm 100$ K, $\log g = 4.25 \pm 0.10$, [Fe/H]$= +0.05 \pm 0.06$, $v \sin i = 3 \pm 1$ km/s for HD 286123. We adopt these values as starting points and/or priors for the `isoclassify` fits described in Section 4.3.2 and the global fit described in Section 4.4.1.

As a consistency check, we also estimated the spectroscopic parameters using our TRES spectra and the Stellar Parameter Classification tool [SPC; 48, 49]. SPC works by cross-correlating observed spectra with a grid of synthetic model spectra generated from Kurucz [166] model atmospheres. From these fits, we obtained weighted averages of $T_{\rm eff} = 5676 \pm 50$ K, $\log g = 4.13 \pm 0.10$, [Fe/H]$= +0.50 \pm 0.08$, $v \sin i = 3.3 \pm 0.5$ km/s for HD 89345, and $T_{\rm eff} = 5877 \pm 53$ K, $\log g = 4.27 \pm 0.10$, [Fe/H]$= +0.03 \pm 0.08$, $v \sin i = 3.9 \pm 0.5$ km/s for HD 286123. The values from SPC are in agreement with those from SpecMatch, except for the slightly higher $\log g$ value for HD 89345 from SPC. Given that HD 89345 is a slightly evolved star, spectroscopic $\log g$ estimates are expected to be less reliable. As shown by Torres et al. [277], reliance on spectroscopically determined $\log g$ can lead to considerable biases in the inferred evolutionary state, mass and radius of a star. Therefore we avoid imposing any priors on $\log g$ for our global fit in Section 4.4.1.

4.3.2 Evolutionary Analysis

We then use the stellar parameters derived from HIRES spectra as well as broad-band photometry and parallax as inputs for the grid-modeling method implemented in the stellar classification package `isoclassify` [142]. `isoclassify` derives posterior distributions for stellar parameters ($T_{\rm eff}$, $\log g$, [Fe/H], radius, mass, density, luminosity and age) through direct integration of isochrones from the MIST database [90, 60] and synthetic photometry. Both target stars have parallaxes from Gaia DR2, but are saturated in the Sloan z band. We therefore input for each star its 2MASS JHK and Tycho BV magnitudes, Gaia parallax, and $T_{\rm eff}$, $\log g$, and [Fe/H] from SpecMatch. The V-band extinction A_V is left as a free parameter. From this fit, we obtained $R_\star = 1.720 \pm 0.051 R_\odot$ and $M_\star = 1.147 \pm 0.034 M_\odot$ for HD 89345 and $R_\star = 1.214 \pm 0.043 R_\odot$ and $M_\star = 1.063 \pm 0.047 M_\odot$ for HD 286123. These values are consistent with the final determined stellar parameters from our EXOFASTv2 global fit (See Table 4.4).

4.3.3 UVW Space Motions, Galactic Coordinates, and Evolutionary States of the Host Stars

To calculate the absolute radial velocities of the two host stars, we used the TRES observation with the highest SNR for each and corrected for the gravitational redshift by adding -0.61 km/s. This gives us an absolute velocity of 2.4 km s^{-1} for HD 89345 and 22.4 km s^{-1} for HD 286123. We quote an uncertainty of 0.1 km/s which is an estimate of the residual systematics in the IAU radial velocity standard star system.

4.3.3.1 HD 89345

HD 89345 is located at equatorial coordinates $\alpha = 10^h18^m41\farcs06$, and $\delta = +10°07'44\farcs5$ (J2000), which corresponds to Galactic coordinates of $\ell = 230.8°$ and $b = 50.2°$. Given the Gaia distance of $\sim$ 127 pc, HD 89345 lies roughly 100 pc above the Galactic plane. Using the Gaia DR2 proper motion of $(\mu_\alpha, \mu_\delta) = (5.348 \pm 0.079, -42.449 \pm 0.071)$ mas yr^{-1}, the Gaia parallax, and the absolute radial velocity as determined

from the TRES spectroscopy of 2.4 ± 0.1 km s^{-1}, we find that HD 89345 has a three-dimensional Galactic space motion of $(U, V, W) = (21.5 \pm 0.1, -9.8 \pm 0.1, 1.5 \pm 0.1)$ km s^{-1}, where positive U is in the direction of the Galactic center, and we have adopted the Coşkunoğlu et al. [67] determination of the solar motion with respect to the local standard of rest. These values yield a 99.4% probability that HD 89345 is a thin disk star, according to the classification scheme of Bensby et al. [26].

Note that stars of the mass of HD 89345 ($M_* \sim 1.2\ M_\odot$) that are close to the zero age main sequence typically have spectral types of roughly F5V-F8V [222], but in fact HD 89345 has a $T_{\rm eff}$ and colors that are more consistent with a much later spectral type of G5V-G6V [222]. Furthermore, it has a radius of $R \sim 1.74\ R_\odot$; much larger than one would expect of its mass if it were on the zero age main sequence. All of this implies that HD 89345 has exhausted or nearly exhausted its core hydrogen, and is currently in or close to the relatively short subgiant phase of its evolution, as it moves toward the giant branch. The location of HD 89345 above the disk [41] and Galactic velocities are all consistent with this scenario.

This conclusion is corroborated by the properties of the star inferred from the global fit to the transit, radial velocity, spectral energy distribution (SED), and parallax data described in Section 4.4.1. A joint fit to these data measure, nearly directly and empirically, the stellar radius, density, surface gravity, and luminosity. As we note in Section 4.4.1, the global fit in fact yields two solutions, one on the main sequence and one on the subgiant branch. Together with the $T_{\rm eff}$ and [Fe/H], we can locate both of these solutions on a "theoretical" Hertzsprung-Russell diagram (see Figure 4-7). When comparing these values to MIST evolutionary tracks [90, 60], we infer that HD 89345 has an age of either ~ 4.2 Gyr or 7.5 Gyr and is indeed either near or just past the end of its main-sequence lifetime.

4.3.3.2 HD 286123

HD 286123 is located at equatorial coordinates $\alpha = 4^h55^m03\overset{s}{.}9$, and $\delta = +18°39'16\overset{''}{.}33$ (J2000), which correspond to the Galactic coordinates of $\ell = 182.1°$ and $b = -15.3°$. Given the Gaia distance of ~ 126 pc, HD 89345 lies roughly 34 pc below the Galactic

plane. Using the Gaia DR2 proper motion of $(\mu_\alpha, \mu_\delta) = (62.064 \pm 0.077, -48.245 \pm 0.051)$ mas yr^{-1}, the Gaia parallax, and the absolute radial velocity as determined from the TRES spectroscopy of 22.4 ± 0.1 km s^{-1}, we find that HD 286123 has a three-dimensional Galactic space motion of $(U, V, W) = (-14.9 \pm 0.1, -34.5 \pm 0.3, 13.5 \pm 0.1)$ km s^{-1}, where again positive U is in the direction of the Galactic center, and we have adopted the Coşkunoğlu et al. [67] determination of the solar motion with respect to the local standard of rest. These values yield a 98.3% probability that HD 286123 is a thin disk star, according to the classification scheme of Bensby et al. [26].

Note that stars of the mass of HD 286123 typically have spectral types of roughly G1V [222], and in fact HD 286123 has a $T_{\rm eff}$ and colors that are roughly consistent with this spectral type [222]. The radius and luminosity of HD 286123 are $R_* \sim 1.23\ R_\odot$ and $L_* \sim 1.65\ L_\odot$; again, these are roughly consistent, although slightly larger, than would be expected for a zero age main sequence star of its mass and spectral type [222]. The Galactic velocities of HD 286123 are somewhat larger than typical thin disk stars. Together, these pieces of information suggest that HD 286123 is likely a roughly solar-mass star, with an age that is somewhat larger than the average age of the Galactic thin disk, that is roughly 70% of the way through its main-sequence lifetime. Indeed, when combined with the estimate of its metallicity, we can roughly characterize HD 286123 as a slightly older, slightly more massive analog of the sun.

As with HD 89345, this conclusion is corroborated by the properties of HD 286123 inferred from the global fit to the transit, radial velocity, SED, and parallax data described in 4.4.1. When comparing the $\log g$ and $T_{\rm eff}$ from the global fit to MIST evolutionary tracks [90, 60], we infer that HD 286123 has an age of ~ 7.1 Gyr and is indeed just over halfway through its main sequence lifetime.

4.4 Planet Characterization

4.4.1 EXOFASTv2 Global Fit

To determine the system parameters for both HD 89345 and HD 286123, we perform a simultaneous fit using exoplanet global fitting suite EXOFASTv2 [92]. EXOFASTv2 is based largely on the original EXOFAST [93] but is now more flexible and can, among many other features, simultaneously fit multiple RV instruments and the spectral energy distribution (SED) along with the transit data. Specifically, for each system we fit the flattened *K2* light curve, accounting for the long cadence smearing; the SED; and the radial velocity data. To constrain the stellar parameters, we used the MESA Isochrones & Stellar Tracks [MIST, 90, 60], the broad band photometry, and the parallax from Gaia summarized in Table 4.1. In addition, we set priors on $T_{\rm eff}$ and [Fe/H] from the Keck/HIRES spectra described in Section 4.3.1 and enforced upper limits on the V-band extinction from the Schlegel et al. [252] dust maps of 0.035 for HD 89345 and 0.4765 for HD 286123. We used the online EXOFAST tool[5] to refine our starting values prior to the EXOFASTv2 fit.

We note that the fit yielded bimodal posterior distributions for the age and mass of HD 89345, with the age distribution showing peaks at 7.53 and 4.18 Gyr, and the mass peaking at 1.157 $M_\odot$ and 1.324 $M_\odot$. The two peaks correspond to two solutions with the star being a subgiant and a main sequence dwarf respectively. This degeneracy is also present when we repeat our global fits using the integrated Yale-Yonsei stellar tracks [301] instead of MIST. We also attempted an empirical fit using only the transits, RVs, SED, broadband photometry and Gaia parallax but no isochrones, and the resulting mass distribution, with error bars as large as 80%, does not offer any useful insight. This degeneracy may be broken with better constraints on the eccentricity of the planet or asteroseismic analyses[6], but in this paper, we report both solutions agnostically. Even so, the resulting planet masses from these two solutions are consistent to within 1σ because the error on planet mass is dominated

[5] `http://astroutils.astronomy.ohio-state.edu/exofast/exofast.shtml`

[6] In an independent discovery paper, Van Eylen et al. [285] found a stellar mass consistent with the lower of the two masses through asteroseismology.

by the uncertainty on the RV semi-amplitude.

See Fig. 4-1 for the final transit fits, Figs. 4-4 & 4-5 for the final RV fits, Fig. 4-6 for the final SED fit from our EXOFASTv2 global fit, and Fig. 4-7 for the best-fit evolutionary tracks. The median values of the posterior distributions of the system parameters are shown in Table 4.4.

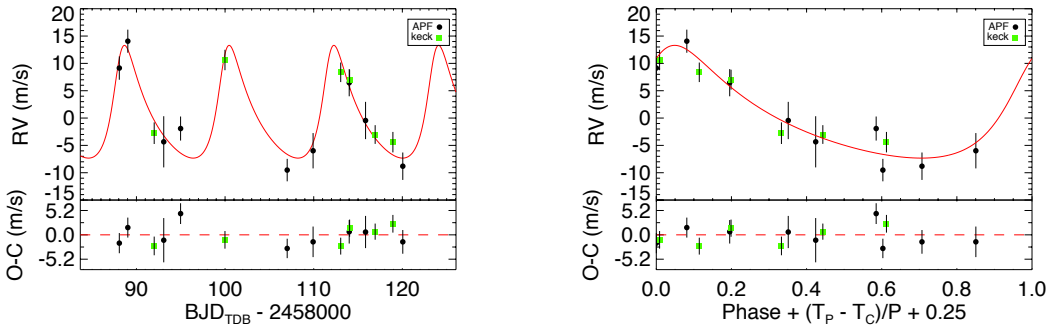

Figure 4-4 *Left*: The RV time series of HD 89345. In each panel, the green squares are the HIRES data and black circles are the APF data. The maximum-likelihood eccentric Keplerian orbital model is plotted in red. The instrumental offset has been subtracted from each data set and the model. The uncertainties plotted include the RV jitter terms listed in Table 4.4 added in quadrature with the measurement uncertainties for all RVs. Below are the residuals to the maximum-likelihood eccentric orbit model. *Right*: same as the left panel, but phase-folded to the best-fit ephemeris. The X-axis is defined such that the primary transit occurs at 0.25, where T_P is the time of periastron, T_C is the time of transit, and P is the period.

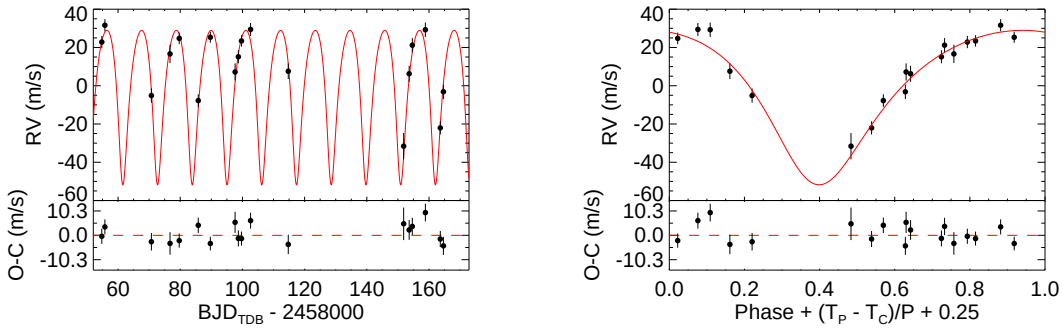

Figure 4-5 Same as Fig. 4-4, but for HD 286123.

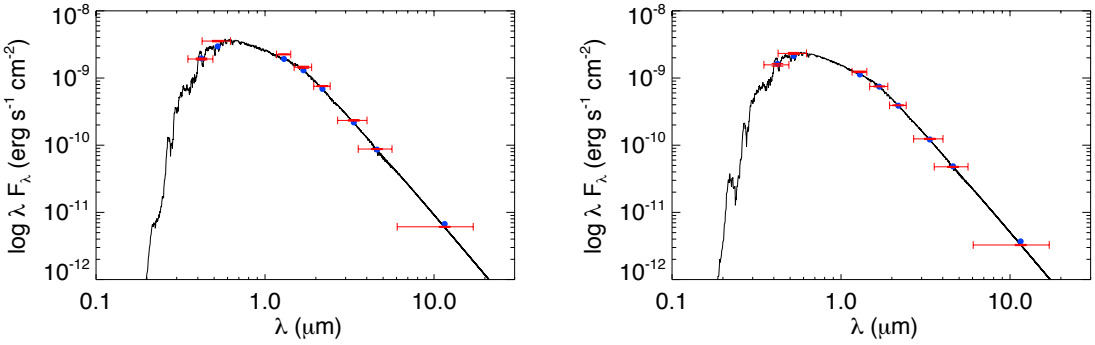

Figure 4-6 SED fits to HD 89345 (left) and HD 286123 (right) from EXOFASTv2. The red points show observed values, with the vertical error bars representing 1σ measurement uncertainties and horizontal error bars representing the widths of the bandpasses. The blue points are the model fluxes in the observed bandpasses. The solid lines show the model fits.

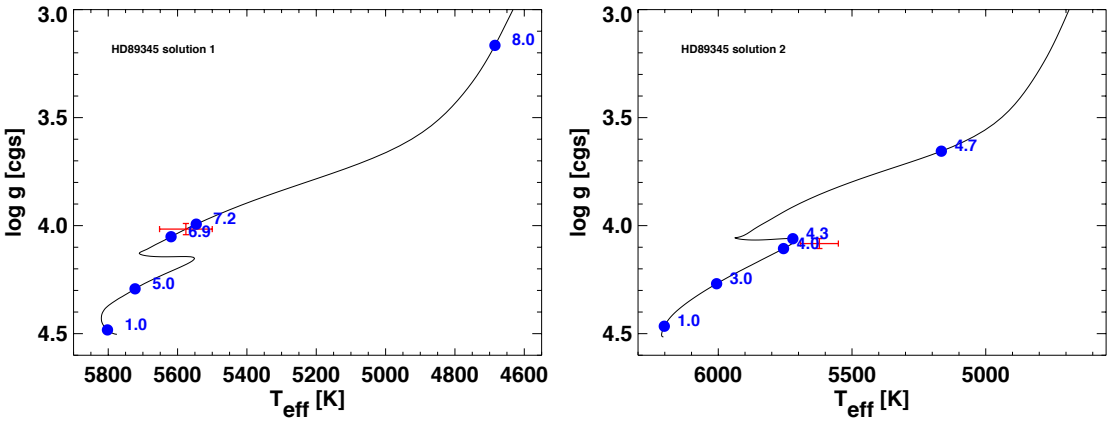

(a) (b)

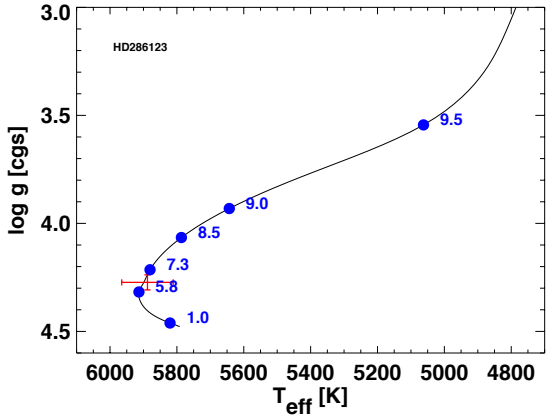

(c)

Figure 4-7 The locations of HD 89345 solution 1 (a), HD 89345 solution 2 (b) and HD 286123 (c) in the Kiel diagram. The median $T_{\rm eff}$ and $\log g$ from the global model fit are shown as red points, while the black lines show MIST evolutionary tracks for stars with the best-fit values of $M_\star$ and [Fe/H]; the locations on the best-fit model corresponding to several values of stellar age are shown as blue points, with ages quoted in Gyr. The red points do not fall exactly on the evolutionary tracks at the median ages quoted in Table 4.4, because the median values in Table 4.4 are drawn from individual posterior distributions and are not always exactly self-consistent.

Table 4.4: Median values and 68% confidence intervals for the physical and orbital parameters of the HD 89345 and HD 286123 systems

Parameter	Units	HD 89345		HD 286123
		Solution 1 (subgiant)	Solution 2 (main sequence)	
Stellar Parameters				
M_*	Mass ($M_\odot$)	$1.157^{+0.040}_{-0.045}$	$1.324^{+0.044}_{-0.041}$	$1.039^{+0.071}_{-0.065}$
R_*	Radius ($R_\odot$)	$1.747^{+0.049}_{-0.050}$	1.733 ± 0.047	$1.233^{+0.026}_{-0.025}$
L_*	Luminosity ($L_\odot$)	$2.66^{+0.15}_{-0.16}$	2.71 ± 0.15	$1.646^{+0.080}_{-0.079}$
ρ_*	Density (cgs)	$0.305^{+0.027}_{-0.025}$	$0.359^{+0.029}_{-0.026}$	$0.782^{+0.077}_{-0.070}$
$\log g$	Surface gravity (cgs)	4.016 ± 0.026	$4.083^{+0.023}_{-0.022}$	4.273 ± 0.035
$T_{\rm eff}$	Effective Temperature (K)	5576^{+73}_{-76}	5622^{+70}_{-71}	5888^{+71}_{-77}
[Fe/H]	Metallicity	$0.421^{+0.046}_{-0.054}$	$0.436^{+0.040}_{-0.050}$	$0.051^{+0.058}_{-0.056}$
Age	Age (Gyr)	$7.53^{+1.3}_{-0.99}$	$4.18^{+0.64}_{-0.69}$	$7.1^{+3.1}_{-2.7}$
A_v	V-band extinction	$0.017^{+0.012}_{-0.011}$	0.017 ± 0.012	$0.017^{+0.012}_{-0.011}$
σ_{SED}	SED photometry error scaling	$5.4^{+2.2}_{-1.3}$	$5.2^{+2.1}_{-1.3}$	$3.28^{+1.3}_{-0.82}$
d	Distance (pc)	$132.8^{+1.8}_{-1.7}$	132.7 ± 1.7	131.7 ± 1.7
π	Parallax (mas)	7.533 ± 0.098	$7.533^{+0.098}_{-0.097}$	$7.594^{+0.10}_{-0.098}$
Planet Parameters				
P	Period (days)	11.81430 ± 0.00020	$11.81430^{+0.00020}_{-0.00019}$	11.168459 ± 0.000017
R_P	Radius ($R_{\rm Jup}$)	$0.660^{+0.028}_{-0.030}$	$0.648^{+0.029}_{-0.028}$	$1.058^{+0.023}_{-0.022}$
T_C	Time of Transit ($\rm BJD_{TDB}$)	$2457913.8052^{+0.0011}_{-0.0010}$	$2457913.80504^{+0.0011}_{-0.00094}$	$2457858.856812^{+0.000042}_{-0.000046}$
a	Semi-major axis (AU)	$0.1066^{+0.0012}_{-0.0014}$	0.1115 ± 0.0012	$0.0991^{+0.0022}_{-0.0021}$
i	Inclination (Degrees)	$87.21^{+0.43}_{-0.22}$	$87.56^{+0.59}_{-0.24}$	$89.61^{+0.26}_{-0.29}$
e	Eccentricity	$0.220^{+0.095}_{-0.13}$	$0.22^{+0.10}_{-0.12}$	$0.255^{+0.034}_{-0.036}$
ω_*	Argument of Periastron (Degrees)	-13^{+58}_{-27}	-16^{+56}_{-27}	$170.9^{+5.7}_{-340}$
T_{eq}	Equilibrium temperature (K)	1089^{+15}_{-16}	1068^{+14}_{-15}	1001 ± 14
M_P	Mass ($M_{\rm J}$)	$0.110^{+0.017}_{-0.018}$	$0.121^{+0.018}_{-0.019}$	$0.387^{+0.044}_{-0.042}$
K	RV semi-amplitude (m/s)	9.2 ± 1.5	9.2 ± 1.5	$35.4^{+4.6}_{-4.3}$
$logK$	Log of RV semi-amplitude	$0.962^{+0.064}_{-0.080}$	$0.965^{+0.064}_{-0.078}$	$1.550^{+0.053}_{-0.056}$

R_P/R_*	Radius of planet in stellar radii	$0.0389^{+0.0011}_{-0.0012}$	0.0384 ± 0.0012	$0.08811^{+0.00031}_{-0.00017}$
a/R_*	Semi-major axis in stellar radii	$13.11^{+0.38}_{-0.36}$	$13.84^{+0.36}_{-0.34}$	$17.28^{+0.55}_{-0.53}$
δ	Transit depth (fraction)	$0.001509^{+0.000085}_{-0.000091}$	$0.001477^{+0.000094}_{-0.000090}$	$0.007764^{+0.000054}_{-0.000030}$
$Depth$	Flux decrement at mid transit	$0.001509^{+0.000085}_{-0.000091}$	$0.001477^{+0.000094}_{-0.000090}$	$0.007764^{+0.000054}_{-0.000030}$
τ	Ingress/egress transit duration (days)	$0.0149^{+0.0045}_{-0.0037}$	$0.0135^{+0.0046}_{-0.0034}$	$0.01717^{+0.00047}_{-0.00020}$
T_{14}	Total transit duration (days)	$0.2389^{+0.0037}_{-0.0033}$	$0.2378^{+0.0038}_{-0.0030}$	$0.20959^{+0.00033}_{-0.00028}$
T_{FWHM}	FWHM transit duration (days)	0.2239 ± 0.0016	0.2241 ± 0.0016	$0.19233^{+0.00026}_{-0.00027}$
b	Transit Impact parameter	$0.645^{+0.089}_{-0.15}$	$0.60^{+0.11}_{-0.19}$	$0.108^{+0.080}_{-0.072}$
b_S	Eclipse impact parameter	$0.568^{+0.057}_{-0.079}$	$0.509^{+0.051}_{-0.077}$	$0.114^{+0.082}_{-0.076}$
τ_S	Ingress/egress eclipse duration (days)	$0.0129^{+0.0018}_{-0.0020}$	$0.0114^{+0.0013}_{-0.0016}$	$0.0182^{+0.0011}_{-0.0010}$
$T_{S,14}$	Total eclipse duration (days)	$0.232^{+0.030}_{-0.021}$	$0.226^{+0.039}_{-0.026}$	$0.221^{+0.013}_{-0.012}$
$T_{S,FWHM}$	FWHM eclipse duration (days)	$0.219^{+0.029}_{-0.018}$	$0.215^{+0.038}_{-0.024}$	$0.202^{+0.012}_{-0.011}$
$\delta_{S,3.6\mu m}$	Blackbody eclipse depth at 3.6μm (ppm)	$40.0^{+3.1}_{-3.3}$	36.0 ± 2.9	$136.9^{+7.6}_{-7.4}$
$\delta_{S,4.5\mu m}$	Blackbody eclipse depth at 4.5μm (ppm)	$65.3^{+4.7}_{-5.1}$	$59.7^{+4.6}_{-4.5}$	$239^{+11}_{-10.}$
ρ_P	Density (cgs)	$0.471^{+0.094}_{-0.084}$	$0.547^{+0.11}_{-0.096}$	$0.405^{+0.046}_{-0.044}$
$logg_P$	Surface gravity	$2.795^{+0.068}_{-0.079}$	$2.852^{+0.066}_{-0.076}$	$2.933^{+0.045}_{-0.048}$
$\langle F \rangle$	Incident Flux (10^9 erg s^{-1} cm^{-2})	$0.303^{+0.021}_{-0.022}$	$0.280^{+0.019}_{-0.020}$	0.214 ± 0.011
T_P	Time of Periastron (BJD$_{\rm TDB}$)	$2457911.30^{+1.5}_{-0.89}$	$2457911.23^{+1.4}_{-0.89}$	$2457860.59^{+0.24}_{-0.20}$
T_S	Time of eclipse (BJD$_{\rm TDB}$)	$2457909.29^{+0.65}_{-1.1}$	$2457909.33^{+0.63}_{-1.1}$	$2457862.67^{+0.25}_{-0.23}$
T_A	Time of Ascending Node (BJD$_{\rm TDB}$)	$2457911.42^{+0.36}_{-0.43}$	$2457911.40^{+0.35}_{-0.42}$	2457855.32 ± 0.17
T_D	Time of Descending Node (BJD$_{\rm TDB}$)	$2457917.54^{+1.0}_{-0.84}$	$2457917.62^{+1.1}_{-0.88}$	$2457860.70^{+0.15}_{-0.14}$
$ecos\omega_*$		$0.185^{+0.087}_{-0.15}$	$0.189^{+0.084}_{-0.15}$	$-0.252^{+0.036}_{-0.033}$
$esin\omega_*$		$-0.03^{+0.12}_{-0.13}$	$-0.04^{+0.12}_{-0.14}$	0.026 ± 0.029
$M_P \sin i$	Minimum mass ($M_{\rm J}$)	$0.110^{+0.017}_{-0.018}$	$0.121^{+0.018}_{-0.019}$	$0.387^{+0.044}_{-0.042}$
M_P/M_*	Mass ratio	$0.000091^{+0.000014}_{-0.000015}$	$0.000087^{+0.000013}_{-0.000014}$	$0.000355^{+0.000047}_{-0.000044}$
d/R_*	Separation at mid transit	$13.1^{+1.4}_{-1.5}$	$13.9^{+1.5}_{-1.6}$	$15.8^{+1.1}_{-1.0}$
Wavelength Parameters	Kepler			
$u_{1,Kepler}$	linear limb-darkening coeff	0.437 ± 0.038	$0.432^{+0.037}_{-0.038}$	0.412 ± 0.011
$u_{2,Kepler}$	quadratic limb-darkening coeff	$0.206^{+0.046}_{-0.045}$	0.214 ± 0.046	0.211 ± 0.027
Telescope Parameters	Kepler			

γ	APF instrumental offset (m/s)	$0.2^{+1.8}_{-1.7}$	0.2 ± 1.7	-11.8 ± 2.2
γ	HIRES instrumental offset (m/s)	$-3.0^{+1.7}_{-1.6}$	$-3.1^{+1.7}_{-1.6}$	—
σ_J	APF RV jitter	$4.2^{+2.9}_{-2.2}$	$4.1^{+2.9}_{-2.2}$	$3.7^{+1.6}_{-1.4}$
σ_J	HIRES RV jitter	$4.1^{+1.5}_{-1.1}$	$4.0^{+1.5}_{-1.1}$	—
σ_J^2	APF RV jitter variance	17^{+33}_{-14}	16^{+33}_{-13}	$13.8^{+15}_{-8.4}$
σ_J^2	HIRES RV jitter variance	$16.4^{+15}_{-7.5}$	$16.3^{+14}_{-7.4}$	—
Transit Parameters	Kepler			
σ^2	Added Variance	$0.00000000007^{+0.00000000050}_{-0.00000000045}$	$0.00000000006^{+0.00000000051}_{-0.00000000045}$	$0.00000000038^{+0.00000000015}_{-0.00000000013}$
F_0	Baseline flux	0.9999984 ± 0.0000050	0.9999983 ± 0.0000051	0.9999994 ± 0.0000027

4.4.2 RV Analysis with `RadVel`

For comparison with EXOFASTv2, we also analyze the RV time series using another widely used, publicly available RV fitting package `RadVel`[7] [103]. We impose a Gaussian prior on the orbital period and times of conjunction of HD 89345 and HD 286123 with means and standard deviations derived from transit photometry and given in Table 4.4. We initially included a constant radial acceleration term, dv/dt, but the result is consistent with zero for both systems. Therefore we fix dv/dt to zero. The remaining free parameters are the velocity semi-amplitudes, the zero-point offsets for each instrument, and the jitter terms for each instrument. The jitter terms are defined in Equation 2 of Fulton et al. [104] and serve to capture the stellar jitter and instrument systematics such that the reduced χ^2 of the best-fit model is close to 1. To calculate $M_P \sin i$, we adopt the median stellar masses in Table 4.4 and their quoted error bars.

The fitting procedure is identical to that described in Sinukoff et al. [256]. The best-fit Keplerian orbital solutions are in agreement with those from EXOFASTv2 at the 1σ level.

4.5 Discussion

4.5.1 Potential for Atmospheric Characterization

Sub-Jovian gas giants are particularly interesting targets for atmospheric studies because a wide range of atmospheric compositions are possible. Yet the atmospheres of such planets, especially those more massive than Neptune but less massive than Saturn, have not been thoroughly studied, both because the host stars of most such systems are too faint for atmospheric characterization, and because the mass regime of sub-Saturns is relatively unpopulated. The two systems presented in this paper are therefore important additions to the small sample of sub-Jovian gas giants amenable to atmospheric characterization.

[7] `http://radvel.readthedocs.io/en/master/index.html`

With their bright host stars and low planet densities, both systems are promising targets for transit transmission spectroscopy. Such observations could provide insight into the planets' bulk composition and formation histories by measuring the elemental composition of their atmospheres, and overall metal enrichment. We calculated the expected SNR per transit compared to the expected scale height of each planet's atmosphere, and compared the results with other known transiting planets with 0.01 $M_{\rm J} < M_p < 0.5\ M_{\rm J}$. Specifically, we calculated the SNR as

$$\mathrm{SNR} \propto \frac{R_p H \sqrt{F t_{14}}}{R_\star^2} \tag{4.1}$$

$$H = \frac{k_{\rm b} T_{\rm eq}}{\mu g} \tag{4.2}$$

where R_p is the planet's radius, $R_\star$ is the star's radius, H is the planet atmosphere's scale height, $k_{\rm b}$ is Boltzmann's constant, $T_{\rm eq}$ is the planet's equilibrium temperature, μ is the atmosphere's mean molecular weight, g is the planet's surface gravity, t_{14} is the transit duration, and F is the flux from the star. To simplify the comparison, we assumed the planets' atmospheres were dominated by molecular hydrogen and $\mu = 2$ for all cases. We also calculated F from the host stars' H-band magnitudes to test suitability for observations with the Hubble Space Telescope's Wide Field Camera 3 instrument. Fig. 4-8 shows the expected SNR for transmission spectroscopy (normalized such that the predicted SNR for WASP-107b is unity) against planet masses for HD 89345b, HD 286123b, and 30 known planets with the highest estimated SNR. For reference, Kreidberg et al. [164] detected water features at 6.5σ confidence with a single HST/WFC3 transit observation of WASP-107b, the benchmark for comparison. HD 286123b appears to be one of the coolest Saturn-sized planets that are amenable to transmission spectroscopy. Notably, many known planets with the highest expected SNR, including GJ 1214b [165], GJ 3470b [96] and GJ 436b [156], were found to show essentially featureless transmission spectra, indicating the existence of hazes, clouds, or atmospheres with high molecular weight. So the estimated SNR does not necessarily mean that we will detect spectral features in the atmospheres of HD 89345b and HD 286123b. Nevertheless, not all such planets have featureless

spectra [75]. Past works have found that a planet's likelihood of being cloudy/hazy is correlated with its equilibrium temperature: at temperatures below roughly 1000 K, methane is abundant and can easily photolyze to produce hydrocarbon hazes [e.g. 101, 207]. These predictions are borne out in observations of transmission spectra showing that hotter planets tend to have larger spectral features [e.g. 265, 75, 102]. At $T_{\rm eq} \approx 1000$ K, HD 89345b and HD 286123b are less likely to be hazy and there are fewer condensible cloud species. It is therefore scientifically compelling to pursue transmission spectroscopy for these planets, both to increase the small sample of Neptune- to Saturn-sized planets with well-characterized atmospheres and to inform the choice of which *TESS* planets to observe to efficiently study the atmospheric composition of sub-Jovian planets.

In addition to transit spectroscopy, HD 286123b is also a good candidate for secondary eclipse detection. Table 4.4 shows the blackbody eclipse depths at 3.6 μm and 4.5 μm, derived using the planet's equilibrium temperature assuming perfect redistribution and zero albedo, to test the feasibility of secondary eclipse observations with *Spitzer*. HD 286123b probes a different period, mass and temperature range from most other planets with secondary eclipse detections, and is one of the few targets that are good candidates for both transmission spectroscopy and secondary eclipse observations.

4.5.2 The Evolutionary History of Close-in Giant Planets

Both planets fall in the same period range as warm Jupiters, giant planets with incident irradiation levels near or below 2×10^8 erg s^{-1} cm^{-2}, corresponding to orbital periods longer than 10 days around Sun-like stars [254]. Like hot Jupiters, they may have formed *in situ*, or migrated inward through high eccentricity migration or disk migration. But at wider orbital separations than hot Jupiters, the orbits of warm Jupiters are less likely to be perturbed by tides raised on the star, and their eccentricity and stellar obliquity distributions may serve as the primordial (after emplacement) distributions for hot Jupiters. Previous works have found that the eccentricity distribution of warm Jupiters contains a low eccentricity component and a

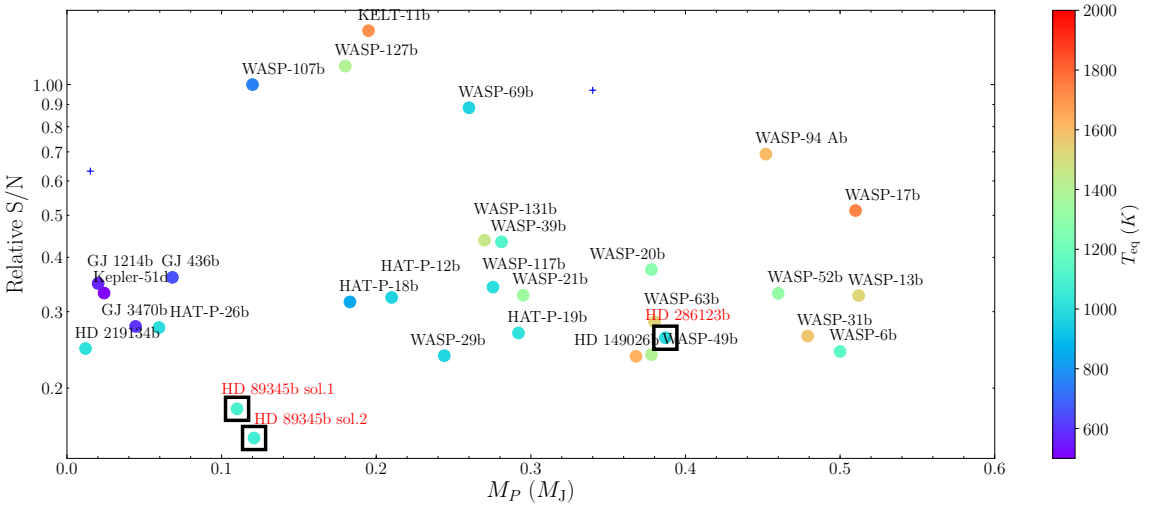

Figure 4-8 Estimated SNR per transit for transmission spectroscopy, relative to that of WASP-107b, as a function of planetary mass for planets with 0.01 $M_J < M_p < 0.5$ M_J. Both solutions are shown for HD 89345b. Small plus symbols denote planets with uncertain mass and/or radius measurements (error $> 20\%$). Data retrieved from the NASA Exoplanet Archive on May 21, 2018.

component with an approximately uniform distribution [229]. The former component cannot be easily explained by the high eccentricity tidal migration hypothesis, and the latter is a challenge for *in situ* formation or disk migration. This suggests that perhaps there is more than one migration mechanism at work.

Fig. 4-9 shows HD 89345b and HD 286123b in a period-eccentricity diagram along with other known planets. HD 286123b has a moderately high eccentricity compared to planets at similar periods. The eccentricity of HD 89345b is only weakly constrained and driven away from zero largely by one data point. Given that, and the Lucy-Sweeney bias that tends to overestimate eccentricity due to the boundary at $e = 0$ [189], we cannot consider the eccentricity of HD 89345b to be significant without additional RV measurements. If these planets arrived at their present locations via high eccentricity migration, they must each be accompanied by a strong enough perturber to overcome precession caused by general relativity [89]. Moreover, Dong et al. [89] predicted that for warm Jupiters with orbital distances of 0.1-0.5 AU, the perturbers must have separations of $\sim$1.5-10 AU (period 2-30 years). Although we detected no significant linear trend in the RVs of HD 89345 or HD 286123, long-term

RV monitoring may be able to reveal the existence of any distant companions.

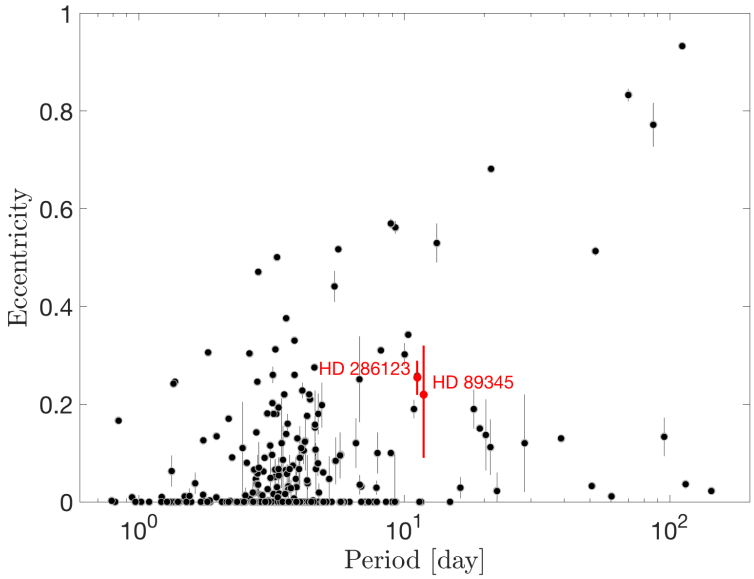

Figure 4-9 Orbital eccentricity versus the log of the orbital period for transiting planets. The two new planets described in this paper are labeled and marked in red. Data retrieved from the NASA Exoplanet Archive on April 20, 2018.

Both planets are also favorable targets for stellar obliquity measurements. Among hot Jupiter systems, spin-orbit misalignment is more commonly seen among hot stars [$T_{\rm eff} \geq 6100$ K; 251, 296, 5], and among the cooler stars, those hosting misaligned hot Jupiters are all in the zone $a_{\rm min}/R_\star \geq 8$ [80]. Hot Jupiters also tend to be more misaligned at longer orbital periods [177]. These observations have been construed as evidence for tidal realignment at work, but tidal realignment suffers from problems pointed out by Mazeh et al. [197], who found that the hot/cool obliquity distinction persists even in cases where tidal interactions should be negligible. The interpretation of warm Jupiters' stellar obliquities remains an outstanding problem. Resolving this problem requires a larger observational sample size, yet the set of warm Jupiters (and smaller planets) currently available for obliquity studies is very small. Both planets in this paper have $a/R_\star$ values beyond the threshold for alignment found by Dai & Winn [80], and the tidal effects on them are expected to be relatively weak. Measuring their stellar obliquities can potentially offer insight into their migration history and tidal

realignment theories. One possible method is to measure the Rossiter-McLaughlin (RM) effect, whose maximum semi-amplitude is approximately

$$\Delta V_{\rm RM} \approx \left(\frac{R_P}{R_\star}\right)^2 \sqrt{1-b^2}(v \sin i) \tag{4.3}$$

where b is the impact parameter and $v \sin i$ is the projected equatorial rotation velocity of the star. Substituting values in Tables 4.1 and 4.4, we obtain $V_{\rm RM} \approx 4$ m s^{-1} for HD 89345b and $V_{\rm RM} \approx 23$ m s^{-1} for HD 286123b. Both should be detectable by modern spectrographs .

4.5.3 Constraining Planet Inflation Models

Many of the proposed mechanisms for explaining the inflated radii of giant planets are related to the irradiation the planet receives from its host star [c.f. 51, 100]. The relation to irradiation seems to be empirically confirmed. For example, radius enhancement is common if the planet receives at least $\sim 2 \times 10^8$ erg s^{-1} cm^{-2}, and mostly absent below that threshold [202, 86], and Hartman et al. [124] argued that planets appear to re-inflate when their stars increase in luminosity as they leave the main sequence.

HD 89345b and HD 286123b are gas giants on roughly 11-day period orbits around moderately evolved stars. At ages of roughly 4-7 Gyr, the host stars are near the end of or already leaving the main sequence. The time-averaged incident flux on the planets are given in Table 4.4 as $(3.03 \pm 0.22) \times 10^8$ erg s^{-1} cm^{-2} (solution 1) or $(2.80 \pm 0.20) \times 10^8$ erg s^{-1} cm^{-2} (solution 2) for HD 89345b and $(2.14 \pm 0.11) \times 10^8$ erg s^{-1} cm^{-2} for HD 286123b, all just above the observed radius inflation threshold found by Miller & Fortney [202] and Demory & Seager [86]. Yet, when shown in a mass-radius diagram (Fig. 4-10) alongside other planets with measured masses and radii, neither appears unusually large for its mass. The same conclusion can be drawn from Fig. 4-11, where the radii of the two planets are compared with those of other planets at similar irradiation levels. Thus, despite being slightly above the critical insolation required for radius inflation, neither planet is significantly inflated.

To further examine the irradiation history of these two planets, we estimate the change in stellar irradiation over time using MIST evolutionary tracks [90, 60] interpolated to stellar masses and metallicities derived in Section 4.4.1. Fig. 4-12 shows the irradiation history of both planets as their host stars evolve. We conclude that for both planets, the orbit-averaged incident flux has been within a factor of two of the empirical critical value of $\sim 2 \times 10^8\,\mathrm{erg\ s^{-1}\ cm^{-2}}$ at least as far back as the zero-age main sequence phase of the host stars.

The above calculation ignores possible evolution in the orbits of the planets. This is justified in the absence of other bodies in the systems, since the only other mechanism for orbital evolution is tidal decay after the disk disappears, and for both systems the timescales of this process are rather long, even assuming efficient dissipation (tidal quality factors of $Q'_\star \sim 10^5$ and $Q'_{\mathrm{planet}} \sim 10^6$) and taking the present day planetary and stellar radii, which must have been smaller in the past. In particular, using Equations 1 and 2 from Jackson et al. [146], the timescales for the evolution of the semi-major axis and the orbital eccentricity are approximately

$$\left(\frac{1}{a}\frac{da}{dt}\right)^{-1} \approx 210\,\mathrm{Gyr\ (sol.1)\ or\ 290\,Gyr\ (sol.2)} \tag{4.4}$$

$$\left(\frac{1}{e}\frac{de}{dt}\right)^{-1} \approx 40\,\mathrm{Gyr\ (sol.1)\ or\ 50\,Gyr\ (sol.2)} \tag{4.5}$$

for HD 89345b, and

$$\left(\frac{1}{a}\frac{da}{dt}\right)^{-1} \approx 85\,\mathrm{Gyr} \tag{4.6}$$

$$\left(\frac{1}{e}\frac{de}{dt}\right)^{-1} \approx 20\,\mathrm{Gyr} \tag{4.7}$$

for HD 286123b. Using $Q'_{\mathrm{planet}} \sim 10^5$ for HD 286123b results in an eccentricity decay timescale of just 3 Gyr, which conflicts with the observed non-zero eccentricity of the system.

The results of our calculation therefore apply to any dissipation less efficient that

$Q'_\star \sim 10^5$ and $Q'_{\rm planet} \sim 10^6$. In this regime, both planets have been very close to the critical irradiation threshold throughout their lifetimes. Lopez & Fortney [188] found that if the inflation mechanism operates by depositing some fraction of a planet's incident irradiation into its deep interior (class I), then a Saturn-mass planet on a 20-day orbit around a 1.5 $M_\odot$ star can rapidly inflate to more than 2 Jupiter radii as the host star leaves the main sequence. In contrast, a class II inflation mechanism that operates by delayed cooling should not cause a planet to inflate as its host evolves off the main sequence. We stress that the critical irradiation threshold is not known to better than a factor of two. That the two planets presented here are not inflated shows that if class I mechanisms are indeed responsible for planet inflation, then these planets have not yet reached high enough irradiation levels or have not had time to inflate in response to increasing irradiation. Regardless, they probe the regime where inflation begins to be noticeable, and provide two new additions to the currently very small sample of warm gas giants to test the two theories. Moreover, most existing gas giant inflation studies have focused on Jupiter-mass objects, but these new detections are lower mass and could potentially provide interesting new insight into the physical processes governing inflation.

4.5.4 HD 89345b and the Transition between Ice Giants and Gas Giants

HD 89345b has a radius 0.8 times that of Saturn and a mass $\sim$ 0.1 times that of Jupiter. It may therefore be a rare example of a sub-Saturn ($4\ R_\oplus < R_p < 8\ R_\oplus$, and $0.02\ M_{\rm J} \lesssim M_p \lesssim 0.2\ M_{\rm J}$, using the definition of Petigura et al. [227]). Apart from HD 89345b, there are only $\sim$ 20 known sub-Saturns with masses determined to within 50% accuracy. In the core accretion scenario, rapid accretion of a gaseous envelope is expected to start in this mass regime [e.g. 206]. Sub-Saturns are therefore an important mass regime for studying the transition between ice giants and gas giants.

Sub-Saturns have no analogs in the Solar System, but may shed light on the forma-

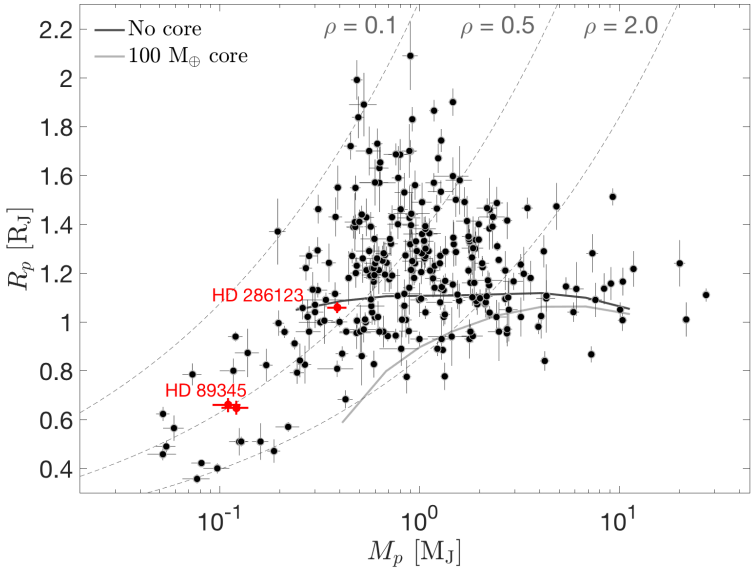

Figure 4-10 Radius-Mass diagram (X-axis in log scale) of transiting planets with measured masses and radii, for planets with $R_p > 0.3$ R_J. The two new planets described in this paper are labeled and marked in red. For HD 89345 both solutions are marked in the plot. The thick solid and dashed lines show radius-mass models from [100] for gas giants with no solid core (thick solid black line) and a large core of 100 $M_\oplus$ (thick solid gray line). Also plotted are three equal density lines (dashed thin gray lines) with mean densities of $<\rho>$ = 0.1, 0.5, and 2.0 g cm^{-3}. Data retrieved from the NASA Exoplanet Archive on April 20, 2018.

tion mechanisms of similar intermediate-mass planets in the Solar System (Uranus and Neptune). It is commonly assumed that ice giants like Uranus and Neptune formed via core accretion. Under this assumption, the accretion rate must be high enough to ensure that enough gas is accreted, but with high accretion rates, such planets would become gas giants the size of Jupiter and Saturn, instead of ice giants [e.g. 127]. To explain the formation of ice giants, core accretion models must prematurely terminate their growth by dispersal of the gaseous disk during envelope contraction [231, 87].

At a period of 11.8 days, HD 89345b is much closer to its host star than the Solar System ice giants. Under the core accretion scenario, at such small radial distances, where the solid surface density is high, planets are even more likely to undergo runaway accretion that turns them into gas giants. It would therefore be

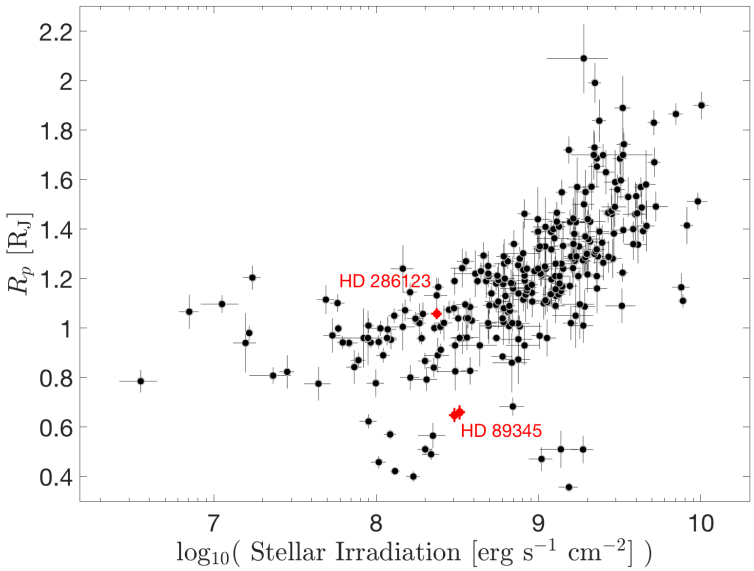

Figure 4-11 Planet radius vs. stellar irradiation at the planets' orbits for transiting planets with measured mass and radius, for planets with $R_p > 0.3\ R_J$. The two new planets described in this paper are labeled and marked in red. For HD 89345 both solutions are marked in the plot. Data retrieved from the NASA Exoplanet Archive on April 20, 2018.

interesting to see whether the composition of HD 89345b more closely resembles that of ice giants or gas giants. One way to test this is to measure the atmospheric metallicity of the planet through transmission spectroscopy, since the Solar System's ice giants have significantly higher atmospheric metallicities compared to the gas giants [120].

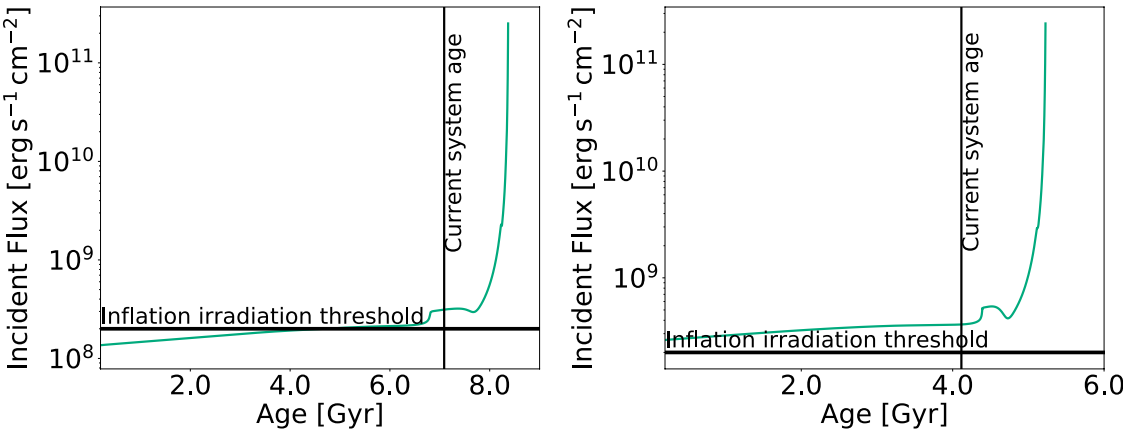

(a)

(b)

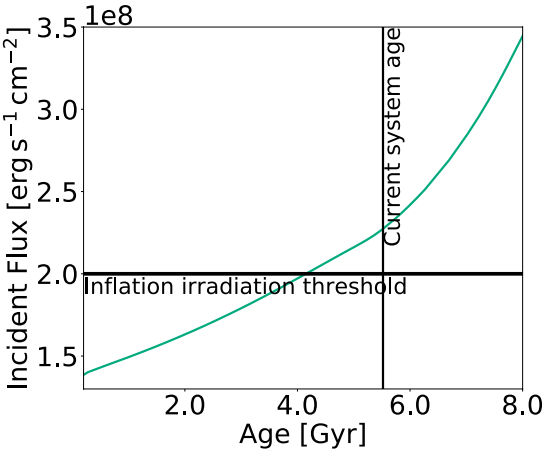

(c)

Figure 4-12 Models of the orbital evolution of HD 89345b solution 1 (a), HD 89345b solution 2 (b) and HD 286123b (c) for tidal quality factors $Q'_\star \sim 10^5$ and $Q'_{\rm planet} \sim 10^6$. The horizontal line represents the threshold value of 2×10^8 erg s^{-1} cm^{-2} for radius inflation from Miller & Fortney [202] and Demory & Seager [86]. The vertical lines show the current ages of the systems.

Chapter 5

Constraining Giant Planet Migration Pathways through Spin-Orbit Alignment and Stellar Companions

The content of this chapter was submitted to AJ *on July 25, 2018 and published [303] on November 7, 2018 as* EPIC 246851721 b: A Tropical Jupiter Transiting a Rapidly Rotating Star in a Well- aligned Orbit *by Liang Yu, George Zhou, Joseph E. Rodriguez, Chelsea X. Huang, Andrew Vanderburg, Samuel N. Quinn, B. Scott Gaudi, Charles A. Beichman, Perry Berlind, Allyson Bieryla, Michael L. Calkins, David R. Ciardi, Ian J. M. Crossfield, Jason D. Eastman, Gilbert A. Esquerdo, David W. Latham, Keivan G. Stassun, and Steven Villanueva, Jr.*

We report the discovery of EPIC 246851721 b, a “tropical" Jupiter in a 6.18-day orbit around the bright ($V = 11.439$) star EPIC 246851721 (TYC 1283-739-1). We present a detailed analysis of the system using *K2* and ground-based photometry, radial velocities, Doppler tomography and adaptive optics imaging. From our global models, we infer that the host star is a rapidly rotating ($v \sin i = 74.92$ km s^{-1}) F dwarf with $T_{\rm eff} = 6202$ K, $R_\star = 1.586\ R_\odot$ and $M_\star = 1.317\ M_\odot$. EPIC 246851721 b has a radius of $1.051 \pm 0.044 R_{\rm J}$, and a mass of $3.0^{+1.1}_{-1.2}\ M_{\rm J}$. Doppler tomography reveals an aligned spin-orbit geometry, with a projected obliquity of $-1.47^{\circ}\ ^{+0.87}_{-0.86}$, making EPIC 246851721 the fourth hottest star to host a Jovian planet with $P > 5$ days and

a known obliquity. Using quasi-periodic signatures in its light curve that appear to be spot modulations, we estimate the star's rotation period, and thereby infer the true obliquity of the system to be $3.7^{\circ}{}^{+3.7}_{-1.8}$. We argue that this near-zero obliquity is likely to be primordial rather than a result of tidal damping. The host star also has a bound stellar companion, a 0.4 $M_{\odot}$ M dwarf at a projected separation of 2100 AU, but the companion is likely incapable of emplacing EPIC 246851721 b in its current orbit via high eccentricity Kozai-Lidov migration.

5.1 Introduction

Ever since their initial discovery in 1995, the formation and evolution history of hot Jupiters have been the subjects of intense study. We have yet to understand how hot Jupiters, giant planets orbiting at just a few percent of an astronomical unit from their host stars, are able to reach such close-in orbits. Their origin theories fall into three categories: *in situ* formation [e.g. 30, 23, 32], high eccentricity migration via gravitational perturbations by bound stellar companions [e.g. 300] or by other planets in the system [e.g. 238, 211], and smooth disk migration [e.g. 181, 6]. Among these mechanisms, high eccentricity migration is capable of altering the planet's orbital orientation and driving up the stellar obliquity (i.e. the angle between the planetary orbit and the host star's spin axis), while *in situ* formation and disk migration are likely to preserve or even reduce the initial obliquity, although this initial obliquity may not necessarily be small [see e.g. 22, 169]. Therefore the measurement of stellar obliquities is a key to understanding the migration of hot Jupiters [e.g. 5]. Only the sky projection of this angle, λ, can be directly measured via the Rossiter-McLaughlin effect [201, 243], Doppler tomography [70], or star spot crossings [245], among other techniques. As of June 2018, 125 planets have measured projected obliquities[1], the majority of which are hot Jupiters with orbital periods shorter than 5 days. The projected obliquity is only a lower bound on the true, three-dimensional obliquity, of which only 23 planets have measurements.

[1] http://www.astro.keele.ac.uk/jkt/tepcat/obliquity.html

As was first noted by Winn et al. [296], Schlaufman [251] and others, among hot Jupiter hosts, stars with cool photospheres ($\lesssim$ 6100 K) are generally in spin-orbit alignment, while hotter stars ($\gtrsim$ 6100 K) span a wide range of obliquities. The temperature boundary coincides with the "Kraft break", the transition between convective and radiative stars [163]. This dichotomy is commonly thought to arise from differences in internal structures between hot and cool stars. Under this hypothesis, hot Jupiter systems acquire a wide range of obliquities through the migration process of the planet [e.g. 238, 97], magnetic star-disk interactions [169], or torques from distant stellar companions [21]. But stars cooler than $\sim$ 6100 K have thick convective envelopes and high rates of tidal dissipation, and are able to quickly realign orbits through tidal interactions. Hot stars, on the other hand, can only weakly dampen orbital obliquities and cannot realign the planets on Gyr timescales.

Recently, however, this tidal realignment hypothesis has been challenged by new observations. Using ensemble measurements, Mazeh et al. [197] found that the hot/cool obliquity distinction persists even for long-period planets, where tidal interactions should be negligible. Theoretically, it is also difficult to explain how a planet can realign its host star without sacrificing all of its angular momentum and leading to orbital decay [e.g. 168, 82, 182]. Therefore the interpretation of hot Jupiters' obliquities remains an outstanding problem, which calls for an expansion of the parameter space for which we have obliquity measurements. In particular, we need to measure the obliquities of planets with longer orbital periods than typical hot Jupiters, including warm Jupiters (with orbital periods $\gtrsim$ 10 days) and Jovian planets with periods between 5 and 10 days, which we dub "tropical" Jupiters.

Unlike typical hot Jupiters, which have periods shorter than 5 days, tropical Jupiters may provide important insight into the dynamic evolution of close-in giant planets. At farther distances from their host stars, tropical Jupiters experience weaker tidal effects, and thus may have retained both the obliquity and eccentricity they had when emplaced in their current orbits. The tidal circularization timescale scales with the orbital period as $\tau_{\rm circ} \propto P^{13/3}$ [2]. For a tropical Jupiter with a period of 5 days, the circularization timescale is as long as $\sim$ 2 Gyr. This means that

if close-in Jovian planets arrive through high eccentricity migration, we should be able to detect non-zero primordial eccentricities and obliquities in tropical Jupiters. Tropical Jupiters are also distinct from warm Jupiters, which are often defined in the literature as giant planets with incident irradiation levels below 2×10^8 erg s^{-1} cm^{-2}.

In this chapter, we present the discovery and obliquity measurement of a tropical Jupiter, EPIC 246851721 b, using Doppler tomography. The planet transits a rapidly rotating ($v \sin i = 74.92$ km s^{-1}), bright F dwarf on a 6.18-day orbit. Despite having an effective temperature just above the Kraft break, the planet appears to be very well aligned. Using what appears to be spot modulations in the *K2* light curve, we were able to estimate the true obliquity of this system. Interestingly, the host star also has a distant, bound stellar companion, which enables us to examine the role of stellar Kozai-Lidov oscillations in the planet's migration history. This paper is organized as follows: we describe our discovery and observations in Section 5.2, our derivation of stellar and planetary parameters in Sections 5.3 and 5.4, and our interpretation of the stellar companion and well-aligned planetary orbit and future prospects in Section 5.5.

5.2 Observations

EPIC 246851721 was observed by *Kepler* between March 8 and May 27, 2017 during Campaign 13 of its *K2* mission. It was proposed as a target in three programs: GO13071 (PI Charbonneau), GO13122 (PI Howard) and GO13024 (PI Cochran). A summary of EPIC 246851721's photometric and kinematic properties is given in Table 5.1.

5.2.1 K2 Light Curve

We extracted photometry for EPIC 246851721 from pixel-level data, which we downloaded from the Mikulski Archive for Space Telescopes (MAST)[2]. We computed the raw aperture photometry by summing the flux inside an irregularly shaped aper-

[2]https://archive.stsci.edu/k2/

ture consisting of all pixels that are within some distance away from the centroid of the star. For EPIC 246851721, a distance of 5 pixels yielded the best-calibrated photometry.

K2 photometry is dominated by systematics resulting from spacecraft motion. During spacecraft rolls, stars move over different pixels with varying sensitivities, leading to apparent changes in stellar brightness. As shown by Vanderburg & Johnson [286], these systematics are strongly correlated with centroid positions of the stars. Our light curve detrending process is similar to that described in detail in Huang et al. [140]. In brief, we used the averaged centroid motions of 4 bright stars to represent the centroid positions of all stars in the same campaign. Short-term variations in flux due to spacecraft motion are fitted as the sum of a set of cosine and sine functions of centroid position and the first 10 principal components of fluxes of stars in the same channel. The systematics model is then removed from the raw light curve.

We then filtered out any remaining low-frequency variability (mostly intrinsic stellar variability) using a set of cosine and sine functions, following the method described in Huang et al. [139]. In order to avoid distorting the transit profiles, we set the minimum timescale of the harmonic filter to 0.5 days. We used the box-least-squares (BLS) algorithm [161] to search for periodic transit signals in the filtered light curve, following procedures outlined in Huang et al. [139], and selected candidates according to statistics produced with the VARTOOLS [123] implementation of BLS. This search yielded a signal with a SNR of 61.9 and a preliminary period of 6.18 days.

After identifying the transits, we produced new light curves by simultaneously fitting the transits, the *K2* roll systematics, and long-timescale stellar/instrumental variability. Reprocessing the *K2* light curves in this way prevents the shape of the transits from being biased by the removal of *K2* systematics. We used light curves and corrections of systematics derived using the method of Vanderburg & Johnson [286] as initial guesses for our simultaneous fits, which we then performed following Vanderburg et al. [288]. Throughout the rest of this paper, we use these simultaneously-fit light curves in our analysis and our plots. Fig. 5-1 shows the systematics-corrected,

flattened[3] and detrended light curves of EPIC 246851721.

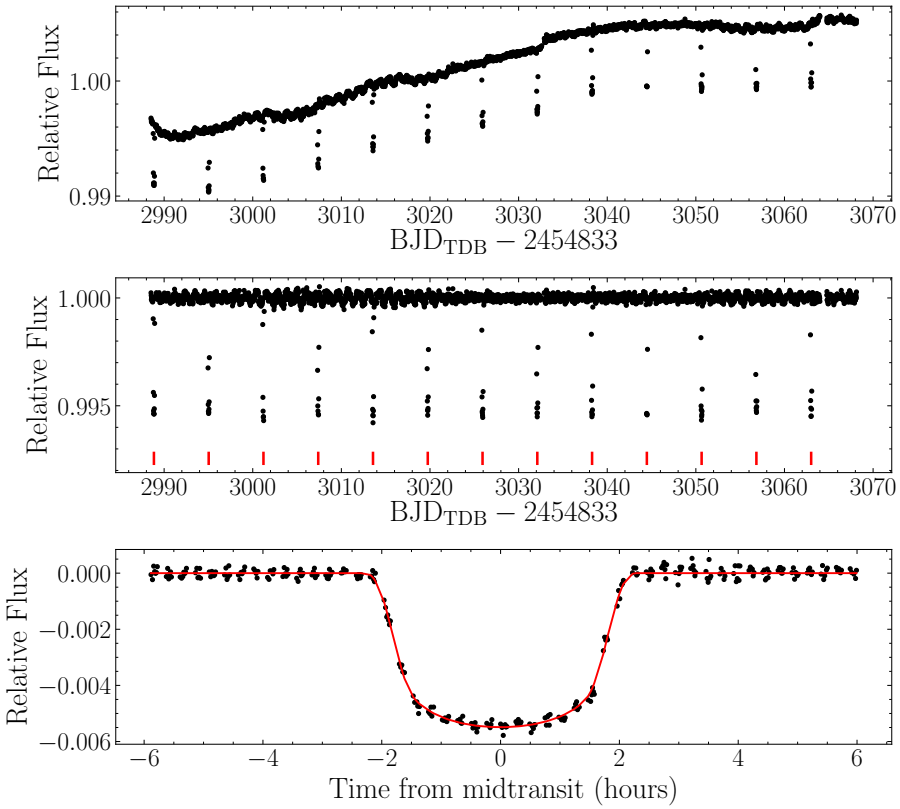

Figure 5-1 *K2* light curves of EPIC 246851721. From top to bottom: *K2* photometry after decorrelation against centroid motion; the full light curve after removing low-frequency stellar variability, with vertical ticks indicating the locations of transits (note the residual high-frequency stellar activity in the baseline); the phase-folded photometry and best-fit transit model.

5.2.2 Ground-Based Follow-Up

In this section, we present our ground-based photometric and spectroscopic observations used to confirm the planetary nature of EPIC 246851721 b. Section 5.2.2.1 describes our radial velocity measurements with TRES and Doppler tomography with MIKE; Section 5.2.2.2 presents adaptive optics imaging follow-up with NIRC2; Sec-

[3]We flattened the light curve by dividing away the best-fit long-timescale variability from our simultaneously-fit light curve.

Table 5.1. Parameters of EPIC 246851721 from the literature and spectroscopy

Parameter	Value	Source
Identifying Information		
α_{J2000} R.A. (hh:mm:ss)	05:15:40.74	
δ_{J2000} Dec. (dd:mm:ss)	+16:16:43.47	
Other identifiers	TYC 1283-739-1	
	2MASS J05154075+1616435	
	K2-267	
Photometric Properties		
B (mag).....	11.990 ± 0.011	1
V (mag)	11.439 ± 0.053	1
J (mag).....	10.199 ± 0.042	2
H (mag)	9.967 ± 0.021	2
K (mag)	9.893 ± 0.018	2
W1 (mag)	9.813 ± 0.023	3
W2 (mag)	9.816 ± 0.020	3
W3 (mag)	9.754 ± 0.056	3
Spectroscopic and Derived Properties		
Spectral Type	F5V	4
μ_α (mas yr^{-1})	2.72 ± 0.11	5
μ_δ (mas yr^{-1})	-12.983 ± 0.094	5
Parallax (mas)	2.66 ± 0.13	5
Barycentric RV (km s^{-1})	$36.85^{+0.13}_{-0.12}$	TRES; this paper
$v \sin i$ (km s^{-1})	77.70 ± 0.78	TRES; this paper
Space motion (U^*, V, W) (km s^{-1})	$(-22.6 \pm 0.3, -12.6 \pm 1.1, -10.1 \pm 0.5)$	this paper

tion 5.2.2.3 describes additional ground-based photometry obtained with the DEMONEXT telescope.

5.2.2.1 Spectroscopy

To constrain the mass of the planet and measure the stellar atmosphere properties of the host star, we obtained a series of spectroscopic observations with the Tillinghast Reflector Echelle Spectrograph [TRES; 273, 106] on the 1.5 m telescope at Fred Lawrence Whipple Observatory, Mt Hopkins, Arizona. TRES is a fibre-fed echelle spectrograph with a resolving power of $R \equiv \lambda/\Delta\lambda \sim 44,000$, over the wavelength range $3900 - 9100$ Å, spanning 51 echelle orders. A total of 17 observations were obtained with TRES over the time period 2017 September 24 - 2017 November 14, covering multiple orbital phases of the planet. The spectra were reduced as per Buchhave et al. [47]. Relative radial velocities were extracted by cross-correlating against the median observed TRES spectrum. In order to avoid regions of the spectra containing low SNR telluric lines, or little information content, cross-correlations were

carried out across only 12 echelle orders in the wavelength range $4290 - 5485\,\text{Å}$. We track and correct for TRES instrumental zero point shifts using nightly observations of RV standard stars; the shifts ($\lesssim 10$ m s^{-1}) are small compared to the RV uncertainties of EPIC 246851721. The final relative velocities are reported in Table 5.2. To translate the relative RVs to an absolute scale, we calculate two additional offsets: that between the relative and absolute TRES RVs; and that between the absolute TRES and IAU scales. Absolute TRES RVs are calculated by cross-correlating the spectra against synthetic templates, and these absolute TRES RVs are used to calculate the weighted mean offset between relative and absolute TRES RVs. The offset from TRES to the IAU scale is calculated from the absolute TRES velocities of the RV standards. The final absolute center-of-mass velocity for the system is given in Table 5.1, but the offsets applied carry additional uncertainties not representative of our sensitivity to orbital motion. For this reason, we perform our analysis on the relative RVs, and report the fitted center-of-mass velocity (i.e., on the relative scale) in Table 5.3. Due to the rapid rotation ($v \sin I_\star = 74.92\,\text{km}\,\text{s}^{-1}$) of the host star, the radial velocities were of lower precision than that typically achieved with TRES. With the velocities, we can only detect the mass of the planet at 2.5σ significance, with a value of $3.0^{+1.1}_{-1.2}\ M_\text{J}$.

For planets around rapidly rotating stars that are not conducive to a mass measurement via traditional radial velocity techniques, spectroscopic detections of planetary transits can be used to eliminate blend scenarios. During the transit, the planet casts a shadow on the rotating stellar surface, distorting the rotationally-broadened spectroscopic line profile that we observe. By obtaining a time series of spectroscopic observations during transit, we can track the changes in the line profiles, and detect the Doppler tomographic shadow cast by the planet [243, 201, 70]. Such a detection, when consistent with the amplitude expected based on the stellar $v \sin i$ and transit depth, as well as the impact parameter from the transit, confirms that the occultor is indeed transiting the primary star. This, combined with an upper limit on the occultor's mass from the Doppler measurements, confirms the planetary nature of the occultor [70, 29]

Table 5.2. TRES radial velocities

BJD_{TDB}	RV (m s^{-1})	σ_{RV} (m s^{-1})
2458020.970114	-593	264
2458024.001740	-156	440
2458030.867169	182	236
2458039.840741	167	271
2458042.843727	1136	428
2458051.906756	-590	287
2458052.901266	109	282
2458053.855002	97	342
2458054.907031	166	225
2458055.960418	429	176
2458056.910076	487	386
2458060.896728	-514	397
2458067.923497	172	372
2458068.961460	85	157
2458069.858188	143	346
2458070.770534	-433	271
2458071.786275	399	269
2458099.839901	-8	216
2458099.862025	492	315
2458099.884305	350	279
2458099.906481	457	241
2458106.891022	-288	222

We obtained a series of spectroscopic observations during the transit of EPIC 246851721 on 2018 Jan 04 with the Magellan Inamori Kyocera Echelle [MIKE, 27], located at Las Campanas Observatory, Chile. MIKE is a slit-fed echelle spectrograph, with a wavelength coverage of $3200 - 10000$ Å obtained over the red and blue arms of the instrument. Our observations were obtained using the $0.''50 \times 5.''00$ slit, yielding a spectroscopic resolving power of $R = 43,000$ in the red, and $R = 48,000$ in the blue. A total of 29 observations were obtained through the transit, at an integration time of 600 s in both the blue and red cameras. Wavelength solutions are provided by ThAr arc lamp exposures every 30 minutes. Flat fielding corrections are applied using Quartz lamp exposures taken during the afternoon. The spectral reductions and extractions were performed using the Carnegie *CarPy* package [152, 151].

The Doppler tomographic analysis largely follows that described in Zhou et al. [308]. To measure the spectroscopic line profiles, we perform a least-squares deconvolution between the observed spectra and a non-rotating spectral template [88, 70]. The resulting kernel from the deconvolution describes the line broadening profile, including effects from stellar rotation, macroturbulence, and instrumental broadening.

The unbroadened infinite resolution spectral template is synthesised with the *SPECTRUM* code [117], using the ATLAS9 atmosphere models [55], at the measured stellar parameters of the host star. The deconvolution is performed over individual echelle orders spanning the spectral range $4900-6200$ Å, and the resulting broadening kernels from each order are averaged into a master broadening kernel for each observation.

Changes in the line broadening kernel derived from the deconvolutions reveal the Doppler tomographic shadow of the planet. An averaged out-of-transit kernel is subtracted from each observation, and the resulting line profile residuals are plotted in the Doppler tomographic map in Fig. 5-2. The dark trail represents the Doppler tomographic shadow of the transiting planet. The angle of the trail describes the projected spin-orbit angle of the planet, and is fitted for in the global model in Section 5.4.

5.2.2.2 Keck/NIRC2 Adaptive Optics Imaging

As part of our standard process for validating transiting exoplanets, we observed EPIC 246851721 with infrared high-resolution adaptive optics (AO) imaging at Keck Observatory. The Keck Observatory observations were made with the NIRC2 instrument on Keck-II behind the natural guide star AO system. The observations were first made on 2017 Aug 20 in $Br-\gamma$ and the repeat follow-up observations were made on 2017 Oct 30 in both $Br-\gamma$ ($\lambda_\circ = 2.1686$ μm, $\Delta\lambda = 0.0326$ μm) and in the J band ($\lambda_\circ = 1.248$ μm, $\Delta\lambda = 0.163$ μm) filters. The observation sequence utilized the standard 3-point dither pattern that is used with NIRC2 to avoid the left lower quadrant of the detector which is typically noisier than the other three quadrants. The dither pattern step size was $3''$ and was repeated three times, with each dither offset from the previous dither by $0.5''$.

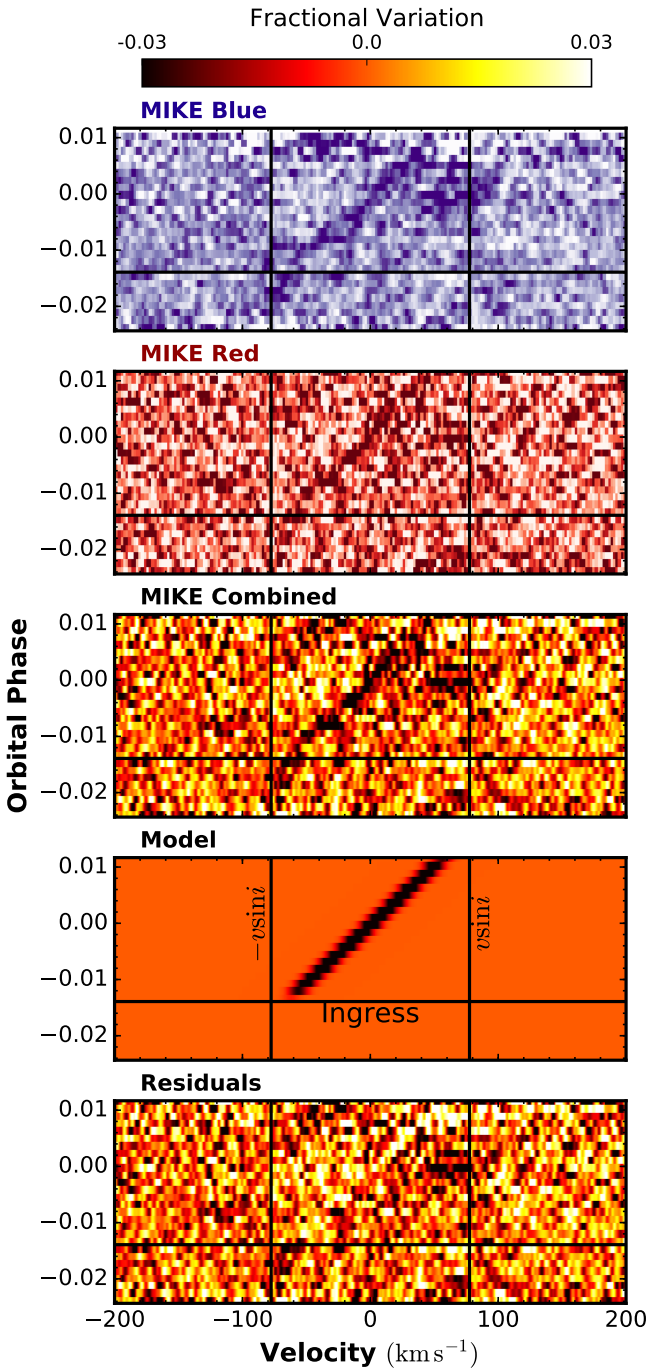

Figure 5-2 Doppler tomographic map for the transit of EPIC 246851721 b, as observed with MIKE/Magellan on 2018 Jan 04. The tomographic maps show the temporal variations of the stellar line profile as a function of orbital phase and stellar rotational velocity. The top two panels show the planetary signal as seen from the blue and red arms of the spectrograph. The middle panel shows the combined tomographic signal. The bottom two panels show the best fit transit model and the residuals after model subtraction.

The August 2018 observations utilized an integration time of 7.8 seconds with one coadd per frame for a total of 70.2 seconds and detected a companion 5.8″ to the southwest (Fig. 5-3). The additional follow-up observations made in October 2018 utilized a 10 second integration (1 coadd) in the $Br-\gamma$ filter for a total of 90 seconds and a 1 second integration (1 coadd) in the J band filter for a total of 9 seconds. In all observations, the camera was in the narrow-angle mode with a full field of view of 10″ and a pixel scale of approximately 0.009942″ per pixel. We use the dithered images to remove sky background and dark current, and then align, flat-field, and stack the individual images. The NIRC2 AO data have a full-width half-maximum (FWHM) resolution of 0.051″ in $Br-\gamma$ and 0.039″ in the J band. The sensitivities of the AO data were determined by injecting fake sources into the final combined images with separations from the primary targets in integer multiples of the central source's FWHM [107, 64]. The companion star is $\sim$ 4 magnitudes fainter than the primary star in the Ks band.

The stellar companion at 5.8″ southwest of the primary star is also detected in the 2MASS imaging (2MASS J05154048+1616394, see right panel of Fig. 5-3). In agreement with the Keck observations, the companion star is approximately 3.9 magnitudes fainter than the primary star at Ks and 4.4 magnitudes fainter at J. Utilizing Kepler magnitude (Kp)-Ks relationships from Howell et al. [135], we derive approximate deblended Kepler magnitudes of $Kp = 11.3$ mag for the primary and $Kp = 16.4$ mag for the companion. The resulting Kepler magnitude difference is $\Delta Kp = 5.1$ mag.

Doppler tomography shows that the transiting planet orbits the primary star and the AO imaging rules out the presence of any additional stars within $\sim$ 0.25″ of the primary and the presence of any additional brown dwarfs or widely-separated tertiary components beyond 0.25″. The presence of the blended 5.8″ stellar companion is taken into account to obtain the correct transit depth and planetary radius [62].

In addition, we also examined archival images from POSS-I, POSS-II and Pan-STARRS (Fig. 5-4). POSS-I and Pan-STARRS both show another possible faint source northeast of the primary, right at the edge of the *K2* aperture, but the corre-

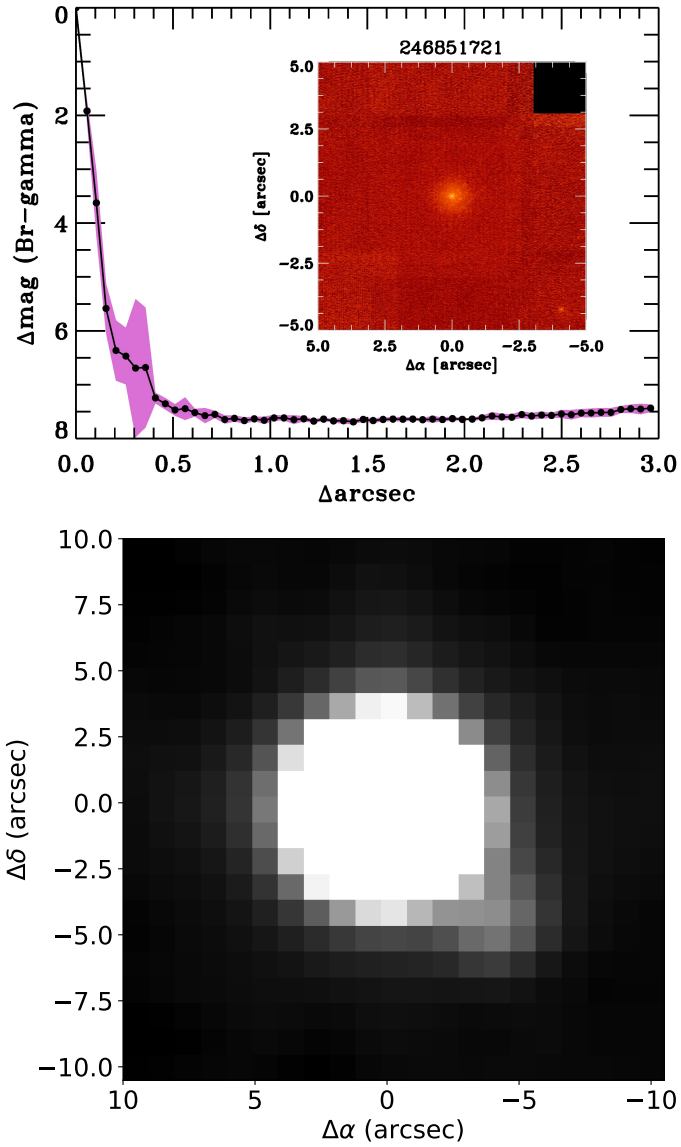

Figure 5-3 *Top:* AO images (inset) and K_S-band contrast curves for EPIC 246851721, taken with Keck/NIRC2. To assess the effect of azimuthal structure on the sensitivity analysis, the image was divided into 45° "pie-wedges" and the radial sensitivity was calculated in each of the eight wedges. The shading represents the rms azimuthal dispersion of the sensitivities for each of the radial steps. A companion is visible at 5.8″ southwest of the primary. *Bottom:* 2MASS J-band image showing EPIC 246851721 and its nearby companion.

sponding catalogs as well as UCAC, 2MASS, SDSS12 and GSC2.3 all indicate that there are no other sources brighter than 20 magnitudes in the g'-band and 19 magnitudes in the r'-band within 30″ of the primary, apart from the companion at 5.8″. The

optical flux contribution of any other possible nearby sources is below the precision of *K2* and can be safely ignored in our transit fits.

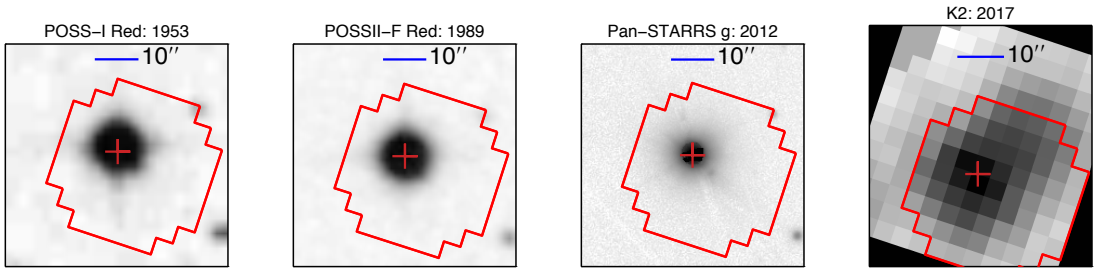

Figure 5-4 Left to right: POSS-I red band image showing EPIC 246851721, with the *K2* aperture overplotted in red; same, but for POSS-II red band; same, but for Pan-STARRS g band; *K2* pixel-level image from which we extracted the *K2* photometry, with the aperture overplotted in red.

5.2.2.3 Ground-Based Photometry

We obtained additional ground-based photometry for EPIC 246851721 using the DEMONEXT telescope [290] at Winer Observatory in Sonoita, Arizona. DEMONEXT is a 0.5 m PlaneWave CDK20 $f/6.8$ Corrected Dall-Kirkham Astrograph telescope. It has a 2048×2048 pixel FLI Proline CCD3041 camera, with a $30.7' \times 30.7'$ field of view and a pixel scale of $0.90''$ pixel^{-1}.

EPIC 246851721 was placed in the DEMONEXT automated queue beginning in December 2017 through February 2018 with observations requested in i'. Using the ephemerides derived from the *K2* light curves, RA, DEC, and magnitude, DEMONEXT automatically scheduled transits on 5 nights where at least 1.5 hours of observations could be made that included 30 minutes of either pre-ingress or post-egress data, and 60 minutes of in-transit data. Observations ranged from 2 to 6 hours. An exposure time of 20 seconds was used and DEMONEXT was defocused to avoid saturation. In February 2018, DEMONEXT was also used in alternating filter mode with observations alternating between g' and i' for the transit occurring on UT 2018 Feb 05. A total of 1882 observations were made, with 1769 in i' and 113 in g'.

All observations were reduced using standard bias, dark, and flat-fielding tech-

niques. Relative aperture photometry was performed using AIJ [71] on the defocused images to obtain the time-series light curves. No detrending parameters were used in the initial reductions. The resulting light curves are shown in Fig. 5-5. The stellar companion at 5.8″ southwest of the primary star is not resolved in the defocused images.

5.3 Host Star Characterization

5.3.1 Spectral Analysis

We obtain initial estimates of some of EPIC 246851721's physical properties from the TRES spectra using the Spectral Parameter Classification (SPC) procedure of Buchhave et al. [48]. However, since the star is rapidly rotating, SPC yields less reliable results than for slowly rotating stars. We ran SPC with no parameters fixed, and obtain the following error-weighted mean values: effective temperature $T_{\rm eff} = 6565 \pm 203$ K, surface gravity $\log g = 3.92 \pm 0.44$ (cgs) and metallicity $[m/H] = 0.14 \pm 0.09$. We adopt these values as starting points and/or priors for the global fit described in Section 5.4.

Since an accurate measurement of the projected stellar rotational velocity $v \sin i$ directly affects the measured spin-orbit angle of the planet, we performed a detailed modelling of the line profile to derive the broadening velocities of the host star. We derive a series of line broadening kernels from the TRES spectra via a least-squares deconvolution against synthetic non-rotating templates (similar to the process described in Section 5.2.2.1). We make use of the TRES spectra since TRES is a fibre-fed spectrograph with a stable instrument profile. We model the line broadening profiles via a numerical disk integration, accounting for the varying radial-tangential macroturbulence, rotational broadening, and limb darkening in our model [following 116]. The disk-integrated line broadening kernel is then convolved with a Gaussian function of width $6.8\,{\rm km\,s^{-1}}$ to account for the instrument broadening. The disk integration process is computationally intensive, as such we only compute a grid of broadening

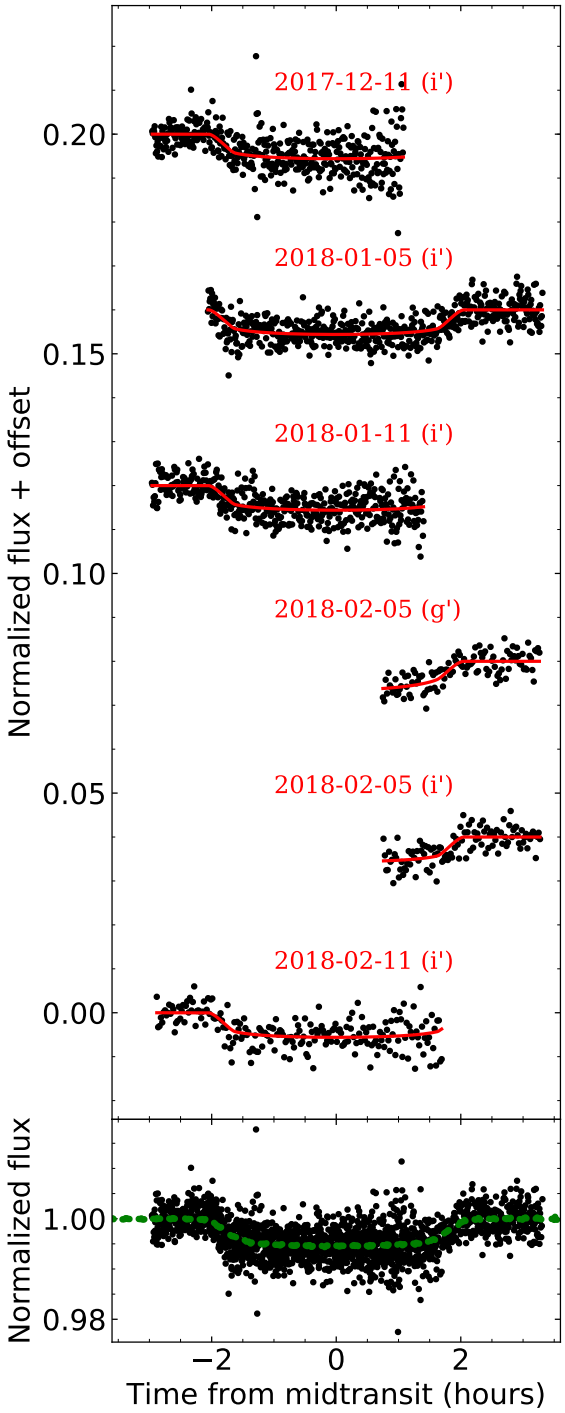

Figure 5-5 Top: Individual transit observations of EPIC 246851721 from DEMONEXT with the best-fit model from the global fit (Section 5.4) overplotted in red. A vertical offset is applied to each light curve for clarity. Bottom: The phase-folded DEMONEXT light curves, with the phase-folded *K2* light curve overplotted in green.

kernels spanning $2 < v \sin I_\star < 100\,\mathrm{km\,s^{-1}}$ and $1 < v_{\mathrm{macro}} < 20\,\mathrm{km\,s^{-1}}$, and interpolate within the grid during our model fit [309]. By modeling the line profiles, we derive a projected stellar rotation rate of $v \sin I_\star = 74.77 \pm 0.63\,\mathrm{km\,s^{-1}}$, and a macroturbulent broadening of $v_{\mathrm{macro}} = 6.79 \pm 0.62\,\mathrm{km\,s^{-1}}$. The uncertainties are determined by the scatter of the broadening velocities from observation to observation, and may be underestimated as they do not account for systematic offsets due to model mismatch. These broadening velocities are used in the global modeling of the system described in Section 5.4.

5.3.2 UVW Space Motion

We calculate the star's Galactic space-velocity components U, V and W to locate it kinematically within the Galaxy. We use the Gaia DR2 parallax [109] (uncorrected for the Stassun & Torres [262] systematic offset of 80 μarcseconds), to infer a distance to EPIC 246851721 of 375 ± 18 pc. Note that the Stassun & Torres [262] offset is slightly smaller than the DR2-quoted uncertainty of this star of 130 μarcseconds. We find that EPIC 246851721 is located about 80 parsecs below the plane, which is entirely typical for a thin disk star of this spectral type [41]. Using the absolute systemic RV of this system from TRES of $36.85^{+0.13}_{-0.12}$ km s^{-1}, we infer that $(U, V, W) = (-22.6 \pm 0.3, -12.6 \pm 1.1, -10.1 \pm 0.5)$ km s^{-1}; again entirely normal kinematics for a star of this spectral type and confirming that it is, indeed, a thin disk star [26].

Had we applied the Stassun & Torres [262] offset, we would have inferred a distance of 373 ± 18 pc, well within 1σ of the uncorrected result; doing so would have had a negligible impact on our inferences about the location and kinematics of this star.

5.4 EXOFASTv2 Global Fit

To properly determine the final system parameters for EPIC 246851721 and its planet, we use the exoplanet global fitting suite EXOFASTv2 [92], to perform a global analysis of all the available data. Specifically, we perform a simultaneous fit of the flattened *K2* light curve, accounting for the long cadence smearing; the DEMONEXT light

curves; the Doppler tomographic map; and the radial velocity data. Within the fit, we use the spectral energy distribution (SED), the integrated YY stellar tracks [301], and the parallax from Gaia DR2 summarized in Table 5.1 to constrain the host star properties with priors set on $T_{\rm eff}$ and [Fe/H] from the TRES spectra described in Section 5.2.2.1. We enforce an upper limit on the V-band extinction from the Schlegel et al. [252] dust maps of 0.328. Since the high $v \sin i$ is causing higher than typical errors on our radial velocity measurements from TRES, we do not attempt to fit for the eccentricity and fix it to zero. To correct for the flux contribution from the nearby blended stellar companion, we separately fit its SED and determine the following deblending coefficients (B/A) for the *K2* and DEMONEXT light curves: Kepler = 0.001597, $g' = 0.005259$, $i' = 0.000792$. We include these deblending coefficients in our EXOFASTv2 global fit to properly account for the contamination on each light curve. We note that our final determined parallax from the global fit is 2.970±0.072 mas, which is $\sim 2\sigma$ different from the value reported by Gaia (2.66±0.13 mas). It is not clear what is causing this discrepancy, but the higher than typical error on the Gaia parallax and the blending nearby companion may be responsible.

See Fig. 5-1 for the final *K2* transit fit, Fig. 5-6 for the final RV fit, Fig. 5-7 for the final SED fit from our EXOFASTv2 global fit, and Fig. 5-8 for the best-fit evolutionary track. The median values of the posterior distributions of the system parameters are shown in Table 5.3, and the telescope parameters are shown in Table 5.4.

5.5 Discussion

5.5.1 The Stellar Companion

The stellar companion to EPIC 246851721 has a parallax of 2.70 ± 0.31 mas and proper motions of $\mu_\alpha = 5.69 \pm 0.48$ mas yr^{-1} and $\mu_\delta = -14.81 \pm 0.35$ mas yr^{-1} [109]. The parallax places the companion at a distance of 370 ± 42 pc, consistent with the distance of the primary within 1σ. Their proper motions are also sufficiently

Table 5.3 Median values and 68% confidence interval for EPIC 246851721

Parameter	Units	Values		
Stellar Parameters:				
M_*	Mass ($M_\odot$)	$1.317^{+0.041}_{-0.040}$		
R_*	Radius ($R_\odot$)	$1.586^{+0.034}_{-0.033}$		
L_*	Luminosity ($L_\odot$)	$3.36^{+0.20}_{-0.18}$		
ρ_*	Density (cgs)	$0.465^{+0.025}_{-0.024}$		
$\log g$	Surface gravity (cgs)	4.157 ± 0.016		
$T_{\rm eff}$	Effective Temperature (K)	6202^{+52}_{-50}		
[Fe/H]	Metallicity	$0.141^{+0.082}_{-0.085}$		
Age	Age (Gyr)	$3.02^{+0.44}_{-0.46}$		
$vsinI_*$	Projected rotational velocity (km/s)	$74.92^{+0.62}_{-0.60}$		
$macturb$	Macroturbulence (m/s)	7220 ± 590		
A_v	V-band extinction	$0.315^{+0.014}_{-0.030}$		
σ_{SED}	SED photometry error scaling	$1.21^{+0.49}_{-0.29}$		
d	Distance (pc)	$336.7^{+8.4}_{-8.0}$		
π	Parallax (mas)	2.970 ± 0.072		
$\dot{\gamma}$	RV slope (m/s/day)	$2.8^{+3.0}_{-2.9}$		
Planetary Parameters:				
P	Period (days)	6.180235 ± 0.000014		
R_P	Radius ($R_{\rm Jup}$)	1.051 ± 0.044		
T_C	Time of conjunction ($\rm BJD_{TDB}$)	$2457858.93009 \pm 0.00010$		
T_0	Optimal conjunction Time ($\rm BJD_{TDB}$)	$2457865.11032 \pm 0.00010$		
a	Semi-major axis (AU)	$0.07229^{+0.00074}_{-0.00075}$		
i	Inclination (Degrees)	86.21 ± 0.17		
T_{eq}	Equilibrium temperature (K)	1401 ± 16		
M_P	Mass ($M_{\rm J}$)	$3.0^{+1.1}_{-1.2}$		
K	RV semi-amplitude (m/s)	270^{+100}_{-110}		
$logK$	Log of RV semi-amplitude	$2.44^{+0.14}_{-0.21}$		
R_P/R_*	Radius of planet in stellar radii	$0.0681^{+0.0025}_{-0.0026}$		
a/R_*	Semi-major axis in stellar radii	9.80 ± 0.17		
δ	Transit depth (fraction)	0.00464 ± 0.00035		
$Depth$	Flux decrement at mid transit	0.00464 ± 0.00035		
τ	Ingress/egress transit duration (days)	$0.01810^{+0.00092}_{-0.00093}$		
T_{14}	Total transit duration (days)	$0.17117^{+0.00074}_{-0.00075}$		
T_{FWHM}	FWHM transit duration (days)	$0.15307^{+0.00052}_{-0.00050}$		
b	Transit Impact parameter	$0.647^{+0.017}_{-0.018}$		
$\delta_{S,3.6\mu m}$	Blackbody eclipse depth at 3.6μm (ppm)	251 ± 20		
$\delta_{S,4.5\mu m}$	Blackbody eclipse depth at 4.5μm (ppm)	355 ± 27		
ρ_P	Density (cgs)	3.1 ± 1.3		
$loggP$	Surface gravity	$3.82^{+0.14}_{-0.21}$		
λ	Projected Spin-orbit alignment (Degrees)	$-1.47^{+0.87}_{-0.86}$		
Θ	Safronov Number	0.31 ± 0.12		
$\langle F \rangle$	Incident Flux (10^9 erg s^{-1} cm^{-2})	$0.874^{+0.041}_{-0.039}$		
T_P	Time of Periastron ($\rm BJD_{TDB}$)	$2457858.93009 \pm 0.00010$		
T_S	Time of eclipse ($\rm BJD_{TDB}$)	$2457862.02021 \pm 0.00010$		
T_A	Time of Ascending Node ($\rm BJD_{TDB}$)	$2457857.38503 \pm 0.00010$		
T_D	Time of Descending Node ($\rm BJD_{TDB}$)	$2457860.47515 \pm 0.00010$		
$M_P \sin i$	Minimum mass ($M_{\rm J}$)	$3.0^{+1.1}_{-1.2}$		
M_P/M_*	Mass ratio	$0.00215^{+0.00081}_{-0.00086}$		
d/R_*	Separation at mid transit	9.80 ± 0.17		
P_T	A priori non-grazing transit prob	0.0951 ± 0.0017		
$P_{T,G}$	A priori transit prob	0.1090 ± 0.0019		
Wavelength Parameters:		Kepler	g'	i'
u_1	linear limb-darkening coeff	0.250 ± 0.031	$0.500^{+0.051}_{-0.050}$	0.228 ± 0.023
u_2	quadratic limb-darkening coeff	0.270 ± 0.042	0.267 ± 0.050	0.291 ± 0.022
A_D	Dilution from neighboring stars	$-0.109^{+0.078}_{-0.089}$	$-0.22^{+0.14}_{-0.16}$	$-0.134^{+0.088}_{-0.100}$
Telescope Parameters:		TRES		
$\gamma_{\rm rel}$	Relative RV Offset (m/s)	90^{+73}_{-71}		
σ_J	RV Jitter (m/s)	200^{+110}_{-130}		
σ_J^2	RV Jitter Variance	40000^{+58000}_{-34000}		

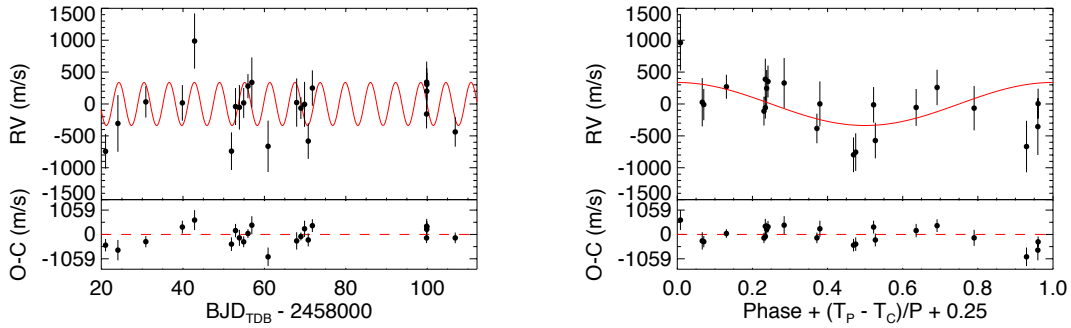

Figure 5-6 *Left*: The RV time series of EPIC 246851721 from TRES. The maximum-likelihood Keplerian orbital model is plotted in red. The instrumental offset has been subtracted from each data set and the model. The uncertainties plotted include the RV jitter terms listed in Table 5.3 added in quadrature with the measurement uncertainties for all RVs. Below are the residuals to the maximum-likelihood orbit model. *Right*: same as the left panel, but phase-folded to the best-fit ephemeris. The X-axis is defined such that the primary transit occurs at 0.25, where T_P is the time of periastron, T_C is the time of transit, and P is the period.

Table 5.4 Median values and 68% confidence interval for the Telescope parameters of EPIC 246851721

Transit Parameters: Observation	Added Variance σ^2	Baseline flux F_0	Additive detrending coeff C_0
UT 2017 K2 C13 (Kepler)	$-1.229^{+0.060}_{-0.055} \times 10^{-8}$	1.0000013 ± 0.0000048	–
DEMONEXT UT 2017-12-11 (i')	$8.8^{+1.1}_{-1.0} \times 10^{-6}$	$1.00373^{+0.00022}_{-0.00023}$	0.00038 ± 0.00052
DEMONEXT UT 2018-01-05 (i')	$1.39^{+0.43}_{-0.39} \times 10^{-6}$	1.00371 ± 0.00017	$0.00104^{+0.00036}_{-0.00037}$
DEMONEXT UT 2018-01-11 (i')	$3.50^{+0.63}_{-0.58} \times 10^{-6}$	1.00388 ± 0.00019	0.00025 ± 0.00042
DEMONEXT UT 2018-02-05 (g')	$1.14^{+0.77}_{-0.65} \times 10^{-6}$	$1.00207^{+0.00030}_{-0.00029}$	0.00144 ± 0.00067
DEMONEXT UT 2018-02-05 (i')	$1.9^{+8.8}_{-7.4} \times 10^{-7}$	1.00205 ± 0.00024	$0.00057^{+0.00066}_{-0.00065}$
DEMONEXT UT 2018-02-11 (i')	$2.91^{+0.95}_{-0.84} \times 10^{-7}$	1.00389 ± 0.00025	$-0.00118^{+0.00061}_{-0.00062}$

similar that we can conclude that the companion is most likely bound. The projected separation of 5.842″ translates to a physical separation of $\sim$ 2100 AU. This places the system just beyond the range of separations examined by the Friends of Hot Jupiters collaboration in a series of papers [212, and references therein], which found that stars hosting hot Jupiters are more likely to have stellar companions between 50 and 2000 AU compared to field stars. EPIC 246851721 b therefore adds to the sample of hot and tropical Jupiters with bound stellar companions.

However, the properties of hot Jupiters' stellar companions are incompatible with high eccentricity migration through stellar Kozai-Lidov oscillations being the domi-

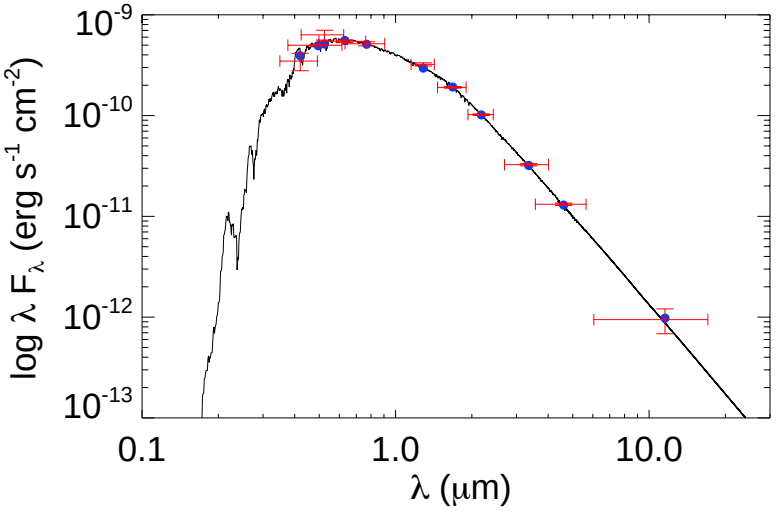

Figure 5-7 SED fits to EPIC 246851721 from EXOFASTv2. The red points show observed values, with the vertical error bars representing 1σ measurement uncertainties and horizontal error bars representing the widths of the bandpasses. The blue points are the model fluxes in the observed bandpasses. The solid lines show the model fits.

nant channel of giant planet migration. Ngo et al. [212] determined that only 16%±5% of hot Jupiters have stellar companions capable of inducing Kozai-Lidov oscillations, assuming initial semi-major axes between 1 and 5 AU. Dawson & Murray-Clay [85] also showed that giant planets orbiting metal-poor stars are confined to lower eccentricities than those orbiting metal-rich stars. This is more compatible with planet-planet interactions than with planet-stellar Kozai-Lidov interactions, because giant planet formation is strongly correlated with stellar metallicity but stellar multiplicity is not.

Nonetheless, we can explore the feasibility of stellar Kozai-Lidov emplacement in this system. In order to excite Kozai-Lidov oscillations on the planet, the precession caused by the perturber must be able to overcome other perturbing forces, including due to general relativity (GR), tides, and the oblateness of the star [98]. For Jupiter-sized planets with periods $\gtrsim 3$ days, apsidal precession due to GR typically dominates over other sources of precession, so the Kozai-Lidov oscillation timescale must be shorter than the GR precession timescale in order for eccentricity excitation to take

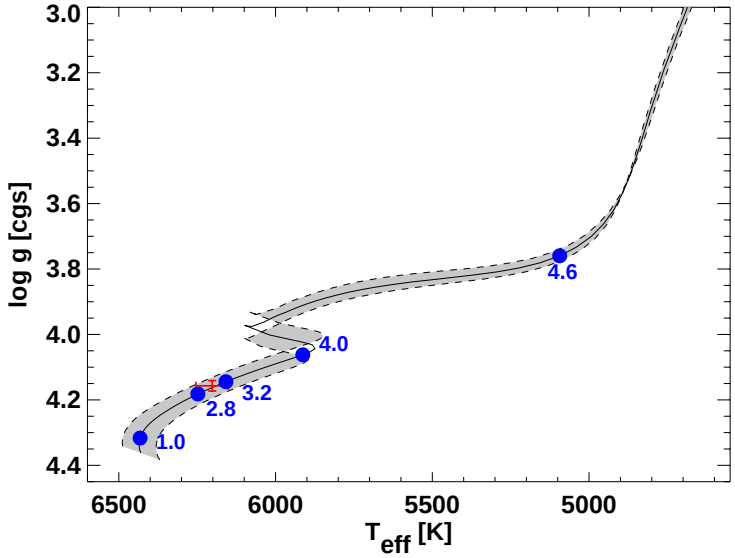

Figure 5-8 The location of EPIC 246851721 in the Kiel diagram. The median $T_{\rm eff}$ and $\log g$ from the global model fit are shown as the red point, while the grey swath shows the YY evolutionary track for a star with the best-fit values of $M_\star$ and [Fe/H]; the locations on the best-fit model corresponding to several values of stellar age are shown as blue points, with ages quoted in Gyr.

place. The former is on the order of [155]

$$t_{KL} = \frac{2P_{\rm per}^2}{3\pi P}\frac{M_* + M_P + M_{\rm per}}{M_{\rm per}}(1-e_{\rm per}^2)^{3/2} \tag{5.1}$$

and the GR precession rate can be estimated as [Eq. 23 from 97]

$$\dot{\omega}_{\rm GR} = \frac{3G^{3/2}(M_* + M_P)^{3/2}}{a_P^{5/2}c^2(1-e_P^2)} \tag{5.2}$$

where P, a_P and e_P are the planet's initial orbital period, semi-major axis and eccentricity, and $M_{\rm per}$, $P_{\rm per}$ and $e_{\rm per}$ are the stellar perturber's mass, orbital period and eccentricity respectively. The inverse of this rate gives an estimate of the GR precession timescale.

Using broadband photometry from 2MASS and SDSS, and Gaia parallaxes, we fit for the mass of the companion, $M_{\rm per}$, with the `isochrones` package[4] [208]. The

[4]https://github.com/timothydmorton/isochrones

companion appears to be an M dwarf with a mass of $\sim 0.4\ M_{\odot}$. Without eccentricity constraints for the planet and the stellar companion, we assume a circular orbit for the planet and an orbital eccentricity of 0.5 for the companion, following Ngo et al. [212]. Substituting these values and the sky-projected separation of 2100 AU into Eqs. 5.1 and 5.2, we find that if the planet had a starting semi-major axis of 1 AU, the GR timescale is three orders of magnitude smaller than the Kozai-Lidov timescale and stellar Kozai-Lidov emplacement is therefore impossible. At a starting semi-major axis of 5 AU, the two timescales are comparable so that stellar Kozai-Lidov emplacement is in theory plausible. Yet if stellar Kozai-Lidov oscillations were really responsible for the migration of EPIC 246851721 b, it seems unlikely that the system should have such a low obliquity (see Section 5.5.2). These mysteries can be solved with a larger sample of hot Jupiters with "friends" and well-constrained obliquities.

5.5.2 Spin-Orbit Alignment

Doppler tomography also enabled us to measure the sky-projected spin-orbit misalignment λ for EPIC 246851721. Our global fit reveals that EPIC 246851721 b has a very small projected obliquity of $-1.48^{\circ} \pm 0.85^{\circ}$. Fig. 5-9 shows EPIC 246851721 b alongside all other planets with known obliquities. EPIC 246851721 b joins a small group of known Jovian-sized planets at periods longer than 5 days (corresponding to $a/R_{*} \gtrsim 10$) orbiting stars near or above the Kraft break ($T_{\rm eff} \gtrsim 6100$ K). Among these, only seven systems have measured projected obliquities. The other six are HAT-P-2 b [297], HAT-P-34 b [5], KELT-6 b [81], KOI-12 b [37], KOI-94 d [4] and WASP-38 b [46]. EPIC 246851721 is the fourth hottest star in the group, and Fig. 5-8 suggests it has been even hotter in the past. The angle λ is only the sky-projected angle between the stellar spin and orbital angular momentum vectors. To date, very few planets have known three-dimensional spin-orbit angles ψ, which cannot be directly measured. We can attempt to derive the true three-dimensional obliquity for this system using the information we have.

To estimate ψ, we need to know the inclination of the stellar rotation axis with

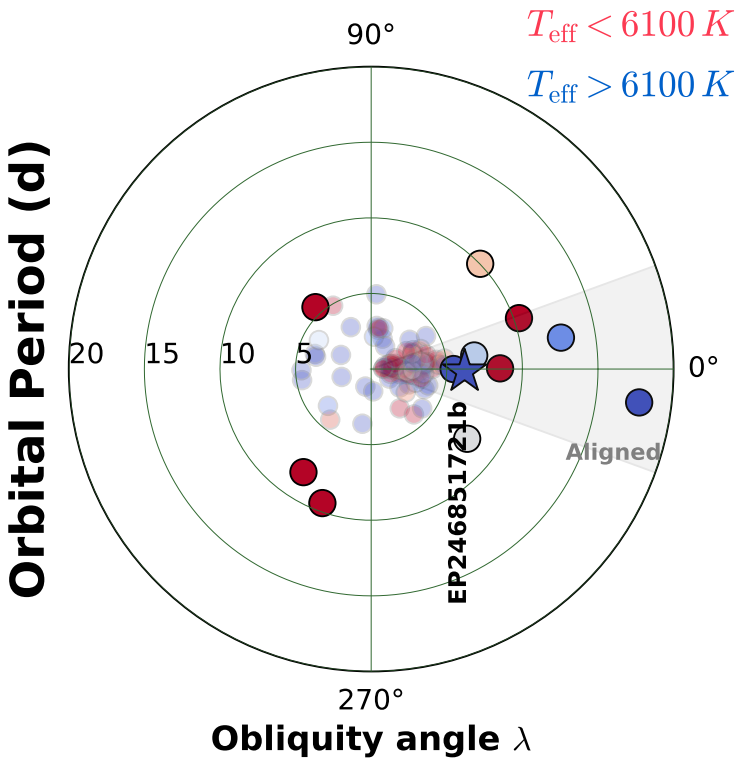

Figure 5-9 Polar plot showing all planets with known obliquities. The angle shows the sky-projected obliquity λ while the radius corresponds to the orbital period of each system. The colors scale with the $T_{\rm eff}$ of the host stars. Planets with $P \geq 5$ days are shown in bold. Figure format inspired by J. Winn.

respect to the line of sight (I_*), which can be calculated if we know the rotation period of the star. The systematics-corrected light curve of EPIC 246851721 shows a clear quasi-periodic variability with a peak-to-peak amplitude of ~ 600 ppm. While we cannot be absolutely sure that this signal is induced by spot modulations rather than pulsations, since EPIC 246851721 resides in the typical $T_{\rm eff}$ and $\log g$ range for γ Dor variables [e.g. 43], the light curve strongly resembles those of spotted, rotating stars. We calculate a Lomb-Scargle periodogram [187, 249, 307] of the *K2* light curve with the transits masked out and low-frequency trends removed (see Fig. 5-11). The periodogram shows three strong, closely-spaced peaks around ~ 1.15 days. But if we divide the light curve into segments of ~ 10 days in length and produce a periodogram for each, every periodogram shows a single, clear peak in the vicinity of 1.15 days. We adopt the mean of the peaks from the seven segments, resulting in a period of

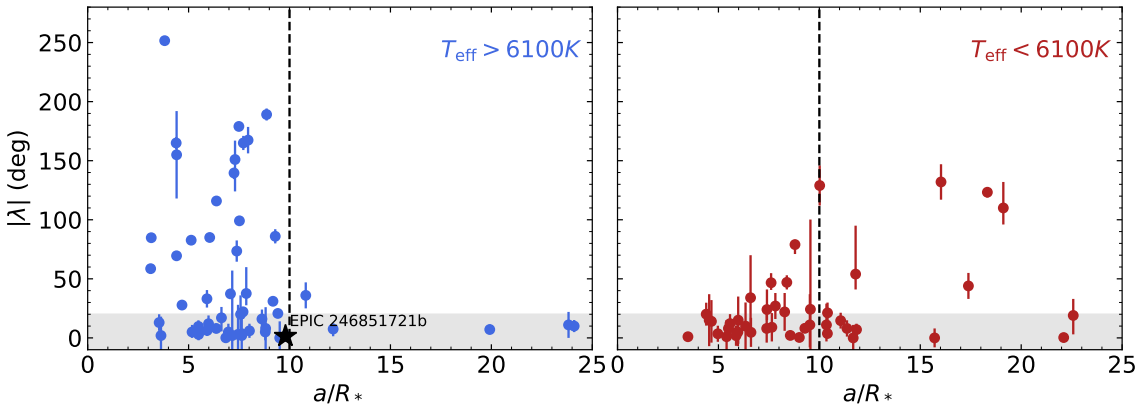

Figure 5-10 Absolute values of the projected obliquities, λ, of Jovian planets as a function of scaled orbital distance, a/R_*, for systems with $T_{\rm eff} > 6100$ K (left) and $T_{\rm eff} < 6100$ K (right). The star shows the location of EPIC 246851721 b. The grey shaded region corresponds to $|\lambda| < 20°$ (aligned). Data retrieved from TEPCat[5] in June 2018.

1.152 ± 0.023 days. Again, the photometric variability may come from pulsations rather than spot modulations, but the rotation period of the star is related to the spectroscopically derived $v \sin i$ and stellar radius by $\sin I_\star = v \sin i P_{rot}/2\pi R_\star$. A rotation period of 1.152 days would give us $\sin I_\star \simeq 1$. This coincidence gives us some confidence that the 1.152-day peak is close to the true rotation period of the star.

To deduce the full three-dimensional spin-orbit alignment, we perform a Monte Carlo simulation with 2×10^6 samples assuming independent Gaussian distributions for λ, $R_\star$, $v \sin i$, the planet's orbital inclination and P_{rot}, and discarding any combination of parameters that leads to $\sin I_\star > 1$. The resulting distribution for ψ implies that the true obliquity of the system is very close to zero, with $\psi = 3.7^{\circ +3.7^\circ}_{-1.8^\circ}$. For reference, the spin-orbit misalignment between the Earth and the Sun is about 7°, and that between Jupiter and the Sun is about 6°.

Interestingly, six of the seven Jovian planets with $T_{\rm eff} > 6100$ K, $P > 5$ days and known obliquities are well aligned ($|\lambda| < 20°$), while only four out of ten such planets orbiting cooler stars are aligned. We can observe this apparent difference between the two populations more clearly in Fig. 5-10, which shows the obliquity distributions of Jovian planets above and below the Kraft break as a function of a/R_*. The obliquity

[5]http://www.astro.keele.ac.uk/jkt/tepcat/obliquity.html

distributions at $a/R_* \gtrsim 10$ appear to contradict the empirical rule found by Winn et al. [296] stating that stars with $T_{\rm eff} \gtrsim 6100$ K are more likely to host planets with high obliquities. Albrecht et al. [5] and others reasoned that the original dichotomy found by Winn et al. [296] is caused by differing amounts of mass in the stellar convective envelope, which acts to tidally dampen orbital obliquities. Cooler stars have a thicker convective envelope than hotter stars, resulting in stronger planet-star tidal interactions and shorter realignment timescales.

But as we gather more planets with known obliquities at $a/R_* \gtrsim 10$, we observe that the fraction of misaligned planets around cooler stars starts to increase (right panel of Fig. 5-10). This trend was first described by Anderson et al. [9], who reasoned that tides become ineffective with sufficient distance from the star, so the population at large a/R_* may retain their initial spin-orbit angles instead of being tidally aligned. But Anderson et al. [9] did not comment on the distribution around hot stars, presumably because there were too few planets with known obliquities at $a/R_* > 10$. Our sample of planets in that regime is limited, but they are mostly aligned, including EPIC 246851721 b. We note that measured inner-disk-clearing timescales have been shown to be dependent on stellar mass [e.g. 153, 240], potentially due to the rate of photo-evaporation clearing the inner disk. A shorter disk clearing timescale for early-type stars may mean that the stopping distances of Jovian planets migrating in-disk are longer for early-type stellar hosts than for later-type hosts. These Jovian planets at larger semi-major axes may also be part of a group of giant planets that formed *in situ* [e.g. 32], whose accretion timescales depend on the viscosity and lifetime of the disk. We must caution, however, that the current sample of early-type stars bearing well characterized Jovian planets at longer orbital periods is severely limited. A simple Student's T-test of the hot and cool star samples shows that the distinction between the two populations at distances of $a/R_* > 10$ is not yet statistically significant. We expect this parameter space to be populated with planets from the *TESS* mission, allowing a more statistically meaningful comparison to be made in the near future.

Is it possible that EPIC 246851721 b initially had a higher obliquity and subse-

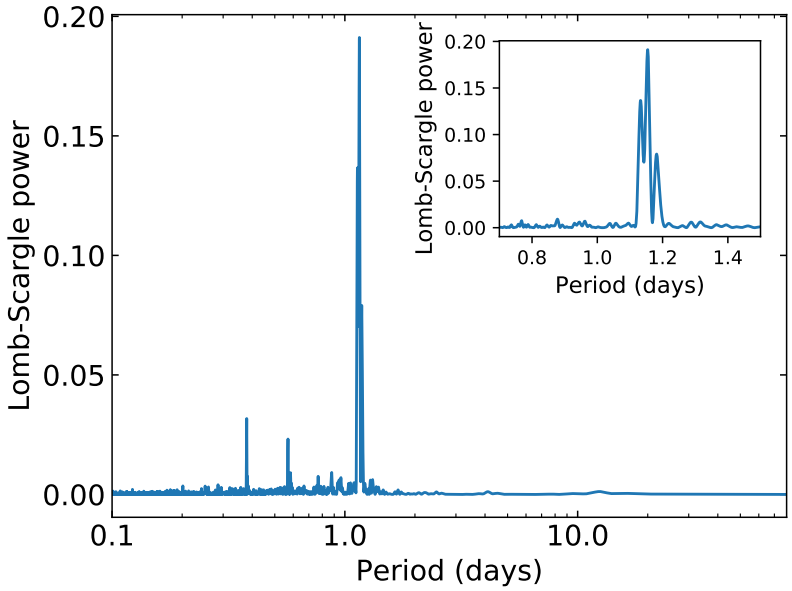

Figure 5-11 Lomb-Scargle periodogram of the *K2* light curve, with transits masked out. A zoom into the region around the tallest peaks is shown in the inset panel.

quently underwent tidal realignment? The $T_{\rm eff}$ of EPIC 246851721 places it near the Kraft break [163], the boundary between convective and radiative stars. The convective layer thins gradually with higher $T_{\rm eff}$, resulting in a smooth transition. So we consider tidal dissipation timescales for both convective and radiative stars [Eqs. 2 and 3 from 5]:

$$\frac{1}{\tau_{\rm CE}} = \frac{1}{10 \times 10^9 \text{ yr}} q^2 \left(\frac{a/R_\star}{40}\right)^{-6}, \tag{5.3}$$

$$\frac{1}{\tau_{\rm RA}} = \frac{1}{0.25 \times 5 \times 10^9 \text{ yr}} q^2 (1+q)^{5/6} \left(\frac{a/R_\star}{6}\right)^{-17/2} \tag{5.4}$$

where $\tau_{\rm CE}$ and $\tau_{\rm RA}$ are the tidal dissipation timescales for stars with convective and radiative envelopes respectively, and q is the planet-to-star mass ratio ($M_P/M_\star$). For EPIC 246851721 b, we estimate that $\tau_{\rm CE} \sim 10^{12}$ yrs and $\tau_{\rm RA} \sim 10^{16}$ yrs. Hence tidal dissipation is expected to be very weak whether the star is predominantly radiative or convective, though its rapid rotation suggests that it has a radiative envelope. Additionally, Li & Winn [177] also found that realignment through tidal effects would lead to a significant increase in the stellar rotation period, so a rapidly rotating star

like EPIC 246851721 should not have undergone tidal realignment. The long tidal dissipation timescales, combined with the rapid rotation of the host star, suggest that EPIC 246851721 b did not attain spin-orbit alignment through tidal interactions. It is therefore likely that the alignment we observe is primordial, which suggest that the planet formed *in situ* or underwent disk migration. This may be the case for all other aligned planets orbiting hot stars at $a/R_* \gtrsim 10$.

5.5.3 Future Prospects

The lack of planet-bearing early-type stars at longer orbital periods is a selection bias. Planets around the larger, early-type host stars at longer orbital periods are currently beyond the reach of ground-based surveys. With the successful launch of the Transiting Exoplanet Survey Satellite [*TESS*, 241], we will soon begin to discover thousands of planets orbiting bright stars, including many Jovian planets with periods longer than 5 days, and sub-Jovian planets amenable to obliquity measurements. Both populations are relatively unexplored with respect to spin-orbit misalignment. A larger, more diverse sample may show us whether the primordial alignment in EPIC 246851721 is common among longer-period giant planets, and thereby reveal the dominant migration mechanism of close-in giant planets. Approximately 200 giant planets with periods longer than 5 days are expected to be discovered around stars brighter than $T_{\mathbf{mag}} = 12$ in the *TESS* primary mission [137].

Chapter 6

Identifying New Planet Candidates in the Era of *TESS*: Deep Learning

The content of this chapter was submitted [306] to AJ *on April 2, 2019 and accepted for publication on May 14, 2019 as* Identifying Exoplanets with Deep Learning III: Automated Triage and Vetting of TESS Candidates *by Liang Yu, Andrew Vanderburg, Chelsea Huang, Christopher J. Shallue, Ian J. M. Crossfield, B. Scott Gaudi, Tansu Daylan, Anne Dattilo, David J. Armstrong, George R. Ricker, Roland K. Vanderspek, David W. Latham, Sara Seager, Jason Dittmann, John P. Doty, Ana Glidden, and Samuel N. Quinn*

NASA's *Transiting Exoplanet Survey Satellite* (*TESS*) presents us with an unprecedented volume of space-based photometric observations that must be analyzed in an efficient and unbiased manner. With at least $\sim 1,000,000$ new light curves generated every month from full frame images alone, automated planet candidate identification has become an attractive alternative to human vetting. Here we present a deep learning model capable of performing triage and vetting on *TESS* candidates. Our model is modified from an existing neural network designed to automatically classify *Kepler* candidates, and is the first neural network to be trained and tested on real *TESS* data. In triage mode, our model can distinguish transit-like signals (planet candidates and eclipsing binaries) from stellar variability and instrumental noise with an average precision (the weighted mean of precisions over all classification thresh-

olds) of 97.0% and an accuracy of 97.4%. In vetting mode, the model is trained to identify only planet candidates with the help of newly added scientific domain knowledge, and achieves an average precision of 69.3% and an accuracy of 97.8%. We apply our model on new data from Sector 6, and present 288 new signals that received the highest scores in triage and vetting and were also identified as planet candidates by human vetters. We also provide a homogeneously classified set of *TESS* candidates suitable for future training.

6.1 Introduction

The advent of large-scale transit surveys revolutionized our understanding of exoplanets. Both ground-based and space-based telescopes, such as OGLE [281], TrES [7], HATNET/HATS [16], WASP [230], KELT [257], and CoRoT [15], have provided us with an unprecedented volume and rate of new discoveries. Perhaps the most notable of all these surveys is NASA's *Kepler* space telescope [34, 158]. Over the course of its four-year mission, *Kepler* observed a total of 200,000 stars, including hosts of more than 2,000 confirmed planets [33]. After the failure of two of its reaction wheels, the repurposed spacecraft [*K2;* 136] yielded another $\sim$ 360 confirmed planets across the ecliptic plane [e.g. 77, 195, 185, 186]. *Kepler*'s successor, the recently launched *Transiting Exoplanet Survey Satellite* [*TESS*; 241] will likely more than double the number of known exoplanets [268, 137]. During its two-year mission duration, *TESS* will observe the sky in $24^\circ \times 96^\circ$ sectors and downlink data twice during every 27-day sector, eventually covering 20 million stars and 90% of the sky [268]. Because *TESS* observes in the anti-Sun direction [241], *TESS* targets can be immediately observed from the ground if identified sufficiently rapidly. Prompt follow-up observations are rendered even more crucial by *TESS*'s shorter observing windows, which mean that ephemeris decay (increasing uncertainty in future transit times as we extrapolate our predictions beyond the data used to determine the ephemeris) presents a much bigger problem for *TESS* than for *Kepler* and *K2* (Dragomir et al. in prep.).

Despite the need for rapid and accurate planet candidate identification, space

surveys like *TESS* continue to rely on human vetting. Typically, teams of experts manually examine possible planet signals and vote on their final dispositions [e.g. 304, 78, Guerrero et al. in prep]. This process can be quite time-consuming: for a typical *TESS* sector, it may take a few experienced humans up to a few days to perform triage, i.e. the procedure of rapidly eliminating the obvious false positives, on tens of thousands of candidates. Then, a team of ~ 10 vetters may spend up to a week classifying the remaining $\sim 1,000$ high-quality candidates if we require each one to be viewed by at least three different people. Furthermore, human vetters may not always maintain a consistent set of criteria when judging potential planetary signals. Even an experienced team of vetters may sometimes disagree on the disposition of a TCE, and dispositions given to the same object may vary depending on, for example, the manner of presentation, other TCEs viewed recently, or even the time of day, as we have seen both in *Kepler* vetting [e.g. 74] and in our own experience with *TESS*.

In response to these shortcomings in human vetting, a number of efforts have emerged to classify light curves automatically and uniformly. Non-machine learning methods make use of classical tree diagrams with criteria designed to mimic the manual process for rejecting false positives [74, 210]. These were completely automated by the end of the *Kepler* mission. Early works on using machine learning to classify *Kepler* light curves have explored techniques such as k-nearest neighbors [275], random forests [198, 203], and self-organizing maps [12]. Convolutional neural networks (CNNs), a class of deep neural networks that has proven successful in image recognition and classification, emerged as another possible method. Zucker & Giryes [310] and Pearson et al. [221] investigated the feasibility of using CNNs to detect transiting planets by applying them to simulated data. The first successful CNN that identified planets in real data from *Kepler* was `AstroNet` [253]. Ansdell et al. [11] further improved upon the model by incorporating scientific domain knowledge. Since then, researchers have either modified the original `AstroNet` model or created their own CNNs to classify candidates from ground-based surveys [250] and *K2* [83]. Osborn et al. [216] registered the first attempt to adapt `AstroNet` for *TESS* candidates, but the model was trained on simulated data, which are likely to have very different

systematics from real *TESS* data. As a result, the model suffers a deterioration in performance when applied to real *TESS* data, recovering about 61% of the previously identified *TESS* objects of interest.

Here we present the first CNN trained and tested on real *TESS* data. Our model takes as inputs human-labeled light curves produced by the MIT Quick Look Pipeline (Huang et al. in prep.), and can be trained to perform either triage or vetting on *TESS* candidates. This paper is organized as follows: In Section 6.2, we describe the creation of the data set used in this study, including how we produced and labeled the light curves; Section 6.3 describes the architecture and training of our neural network for triage and vetting purposes; in Section 6.4, we evaluate the ability of our neural network to identify planet-like events in the test set; in Section 6.5, we apply our neural network to new data from *TESS* Sector 6 and present a number of new planet candidates; finally, we discuss some potential improvements to our model in Sector 6.6. All of our code and the list of labeled *TESS* targets used in this paper are publicly available[1].

6.2 Data set

Since our goal is to create a neural network capable of performing triage and vetting on *TESS* light curves, we train and test our models using *TESS* light curves from Sectors 1-5. Here, we give a brief overview of how these light curves are produced and processed prior to training. We also describe some additional criteria we use to refine this data set.

6.2.1 Identifying Threshold-Crossing Events

Like Shallue & Vanderburg [253], we work with possible planet signals, which are called "threshold-crossing events" or TCEs. These are periodic dimming events potentially consistent with signals produced by transiting planets, and are typically

[1] `AstroNet-Triage:` https://github.com/yuliang419/AstroNet-Triage. `AstroNet-Vetting`: https://github.com/yuliang419/AstroNet-Vetting. A CSV file containing the list of labeled TCEs used in this study is included in the repositories.

identified by an algorithm designed to find such signals. In this study, we adopt the MIT Quick Look Pipeline (QLP; Huang et al. in prep) for light curve production and transit searches. The QLP is partially based on `fitsh` [218], and is designed to process *TESS* full-frame images (FFIs) that are obtained with 30-minute time sampling. Immediately upon data downlink, the QLP produces light curves using internal calibrated images from the MIT Payload Operation Center and identifies TCEs. It has already been used to find and alert planet candidates from early *TESS* sectors [e.g. 138, 289, 242].

6.2.1.1 Light Curve Production

The QLP uses a catalog-based circular aperture photometry method to extract light curves for all stars in the *TESS* Input Catalog (TIC) with *TESS*-band magnitudes brighter than 13.5. The apertures are centered based on a predetermined astrometric solution derived on each observed frame using stars with *TESS* magnitudes between 8-10. The light curves are extracted using five circular apertures. The background is estimated using annuli around the target star on difference images and a photometric reference frame. The photometric reference is computed using the median of 40 frames with minimal scattered light. The difference images are computed using a direct subtraction of the photometric reference frame from the observed frames.

The light curves produced this way usually contain low-frequency variability from stellar activity or instrumental noise. Following Vanderburg & Johnson [286], the QLP removes this variability by fitting a B-spline to the light curve and dividing the light curve by the best-fit spline. Outlier points caused by momentum dumps or other instrumental anomalies are masked out prior to detrending. To avoid distorting any transits present, we iteratively fit the spline, remove 3σ outliers, and refit the spline while interpolating over these outliers (see Fig. 3 in [286]). We then select an optimal aperture for stars in each magnitude range (13 linear bins between *TESS* magnitudes of 6-13.5) by determining which aperture size produces the smallest photometric scatter in the magnitude bins.

The light curves are extracted and detrended one *TESS* orbit at a time, and then

stitched together into multi-sector light curves after dividing out the median levels of the detrended light curves. By Sector 6, stars observed in *TESS*'s continuous viewing zone have light curves with baselines of ≈ 166 days, while stars observed in camera 1 (closest to the ecliptic plane) have baselines of only a single ≈ 27 day TESS sector.

6.2.1.2 Transit Search

After producing a detrended light curve for each star using its optimal aperture, the QLP searches the light curves for periodic dipping signals using the Box Least Squares algorithm (BLS; [161]). We perform the search for periods ranging from 0.1 days, to half the length of the longest baseline expected for the given camera. The number and spacing of frequencies searched by BLS is adapted to the total baseline in the light curves as well, following Vanderburg et al. [288]. We designate any signal with a signal-to-pink-noise ratio (SNR, as defined by [123]) > 9 and BLS peak significance > 10 as a TCE. The BLS peak significance is defined as the height of the BLS peak in the spectrum compared to the noise floor of the BLS spectrum.

6.2.2 "Ground Truth" Labels

Unlike the *Kepler* DR24 data set used by Shallue & Vanderburg [253], our *TESS* TCEs do not come with a complete set of human-assigned labels. A small fraction of TCEs underwent group vetting, in which a team of human vetters closely examined the signals using candidate reports created by the QLP and voted on their dispositions, but even this process can yield inconsistent results: a TCE that appears in more than one sector can have different dispositions in different sectors. To ensure homogeneity in the labeling, one of us (LY) visually inspected the light curves of all the TCEs and assigned each to one of four categories: planet candidates (PC), eclipsing binaries (EB), stellar variability (V) and instrumental noise (IS). We used the following set of rules to guide our classification:

- Any planet-like signal that does not have a strong secondary eclipse, odd/even transit shape differences, or transit depths that increase with aperture size (in-

dicating that the source of the transit is off-target) is classified as PC.

- Some transiting brown dwarfs and M dwarfs have previously been identified as eclipsing binaries in ground-based surveys [e.g. 279, 72] and assigned EB labels in group vetting, but without information beyond the *TESS* data, even experienced human vetters cannot distinguish these systems from transiting giant planets. We relabel these TCEs as PCs in the data set.

- Our data set contains one known planet with visible secondary eclipses, namely the hot Jupiter WASP-18b [128, 255]. We assigned this planet to the PC class.

- Off-target transit signals whose depths increase with aperture size are always labeled as EBs, regardless of whether the signals could be consistent with planetary transits after correcting for dilution.

- Some eclipsing binary systems also exhibit stellar variability. We classify such systems as V if the amplitude of the variability is more than half the eclipse depth, and as EB otherwise.

- Any TCEs that are so ambiguous that even human vetters cannot decide whether they are viable planet candidates or false positives are removed from the training set.

- PCs and EBs that are significantly distorted by detrending (i.e. if the transits are no longer recognizable as transits, or if their depths change by 50% or more) are removed from the training set.

- We do not make any cuts on transit depth. Deep transit signals that do not show any other signs of being eclipsing binaries are still classified as PCs. The deepest transit in our data set has a depth of 8%.

- Unusual signals that do not fit well into any of the four categories are classified as V.

For the rest of the paper, we assume that these dispositions are the ground truth, even though they may not be perfect. It is likely that a small number of TCEs are misclassified, especially ones that exhibit both stellar variability and eclipses. There may also be a few duplicates in the data set. But since the number of such errors is very small, we expect their impact on our model and performance metrics to be minimal. There are also cases where BLS misidentified the period of a TCE. We corrected as many of these as possible by hand. Occasionally, BLS identifies single-transit events at a fraction of the true period. Our dataset included 20 such singly-transiting EBs and 9 singly-transiting PCs. We do not know the exact periods of these objects, so we use the smallest integer multiple of the BLS period that exceeds the baseline as a guess for the true period. Since the duty cycle of the transit provides information on the density of the host star, which may be useful in distinguishing PCs from EBs (large duty cycles typically indicate that the host star is a giant, and therefore more likely to host EBs), any inaccurate estimates of the period would only be a potential concern in vetting, not in triage. But the number of PCs affected is also small, so again we do not expect them to have a large impact on our model's performance.

After manually assigning labels to all TCEs, we binarize the labels as "planet-like" and "non planet-like". When using our neural network to perform triage, both the PC and EB classes are considered to be "planet-like", so that we retain as many potential planet candidates as possible. When using the network for vetting, we perform a more rigorous selection and only consider PCs as "planet-like".

We make use of TCEs from *TESS* Sectors 1-4, but because the V and IS classes drastically outnumber both PCs and EBs, we supplemented our data set with 296 PCs and EBs from Sector 5. In total, we have 16,516 TCEs for triage, including 493 PCs, 2,155 EBs and 13,868 V and IS combined. If an object is identified as a TCE in multiple sectors, we break up the light curve into individual sectors and count each sector as a separate object. For vetting, another 65 TCEs were discarded due to an insufficient number of points (< 5) to construct secondary eclipse views, resulting in 492 PCs, 2,154 EBs and 13,805 V and IS combined. We randomly shuffle and

partition them into three subsets: training (80%), validation (10%) and test (10%). The validation set is used to choose model hyperparameters during training, and the test set to evaluate final model performance.

6.2.3 Preparing Input Representations

Following Shallue & Vanderburg [253], we process each light curve into a standardized input representation before feeding it into the neural network. Since the QLP already removes low-frequency variability from the light curves, we skip the detrending step. The light curve is then phase-folded at the period identified by BLS, such that the transits are lined up and centered. We remove any points corresponding to images with non-zero data quality flags, and any upward outliers that are more than 5 times the median absolute deviation away from the median.

We then binned the data into two views, similar to those described in Shallue & Vanderburg [253]: a "global view", which shows the light curve over an entire orbital period; and a "local view", which is a close-up of the transit event, spanning no more than two transit durations on either side of the transit mid-point. Shallue & Vanderburg [253] grouped their phase-folded light curves into 2,001 bins for the global view, and 201 bins for the local view. The *Kepler* light curves used by Shallue & Vanderburg [253] span up to 4 years in duration and contain approximately 70,000 points each. Many *TESS* light curves, on the other hand, only span about 27 days and have far fewer data points. The resulting phase-folded light curves are therefore much sparser than those from *Kepler*. For this reason, we reduced the number of bins in the global and local views to 201 and 61 respectively, and linearly interpolated the data over empty bins.

In vetting mode, we also prepare a "secondary eclipse view", which was not present in the original `AstroNet` model, but was suggested as a possible improvement to the model by Shallue & Vanderburg [253]. We first perform a search for the most likely secondary eclipse by masking the transits in the phase-folded light curves and using a BLS-like algorithm to fit a box (whose width is fixed to that of the primary transit) to various positions between orbital phases 0.1 and 0.9 in the masked and folded light

curve. The position that yields the highest S/N is assumed to be the midpoint of the most likely secondary eclipse. We then normalize and bin the folded light curve within up to two transit durations on either side of this location into 61 bins, following the exact same procedure we use to produce the local views.

Fig. 6-1 shows examples of global, local and secondary eclipse views for different classes of signals.

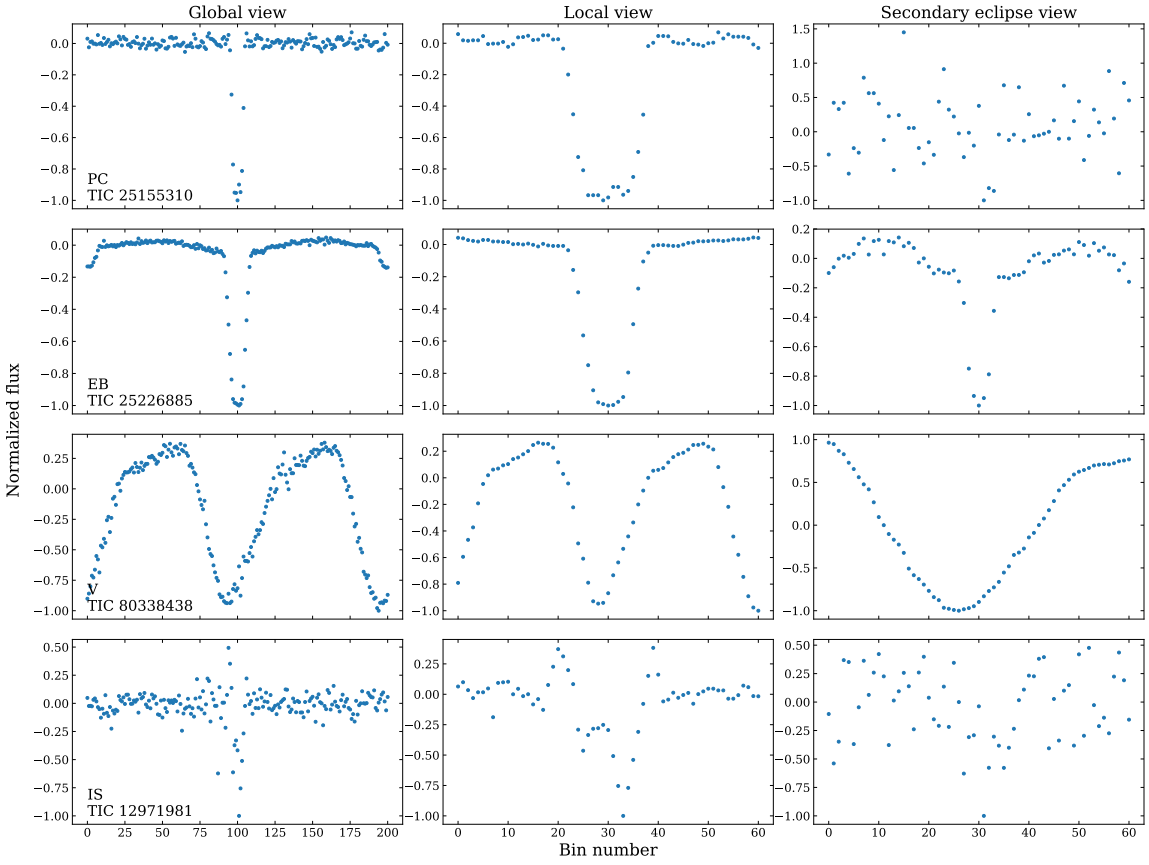

Figure 6-1 For each TCE, we prepare three phase-folded, depth-normalized representations of the light curve: the “global view" (left column) is a fixed-length representation of the entire period; the “local view" (middle column) is a close-up view of the putative transit; the “secondary eclipse view" (right column), only present in vetting mode, is a close-up view of the most likely secondary eclipse. Each row presents an example from one of the four categories of TCEs: PC (planet candidates), EB (eclipsing binaries), V (stellar variability) and IS (instrumental artifact).

6.3 Neural Network

6.3.1 Architecture

Our neural network architecture is based on `AstroNet`, a deep convolutional neural network (CNN) developed by Shallue & Vanderburg [253]. CNNs are a class of deep learning model used for inputs with spatial structure (e.g. images or time series). A CNN contains a hierarchy of "convolutional layers." Each convolutional layer performs a cross-correlation operation by sliding a small filter over the input, summing the result, and adding it to a feature map. Each filter activates in response to a specific feature or pattern in its input. A CNN typically contains many consecutive convolutional layers. In the deeper layers, simpler features learned in previous layers are combined into more complex features. During training, the parameters of the convolutional filters are adjusted to minimize a cost function, a measure of how far the model's predictions are from the true labels in its training set.

`AstroNet` is implemented in TensorFlow [1], an open source machine learning framework developed at Google Brain. The global and local view vectors (and secondary eclipse view in vetting mode) are passed through disjoint convolutional columns with max pooling, and then combined in shared fully connected layers ending in a sigmoid activation function. The model outputs a value in $(0, 1)$, with values close to 1 indicating high confidence that the input is a transiting planet and values close to 0 indicating high confidence that the input is a false positive. Shallue & Vanderburg [253] trained 10 independent copies of the model with different random parameter initializations and averaged the outputs from these 10 copies for all predictions. This technique, known as "model averaging", improves the robustness of the predictions by averaging over the stochastic differences between the individual models. We refer the interested reader to the Shallue & Vanderburg [253] paper for a more detailed description of convolutional neural networks and the associated terminology.

We have made a few key modifications to the original `AstroNet` architecture, depending on whether the model is used for triage or vetting. Here we describe the two different modes in detail.

6.3.1.1 Triage Mode

The main goal of triage is to eliminate all the obvious non-planetary signals among the TCEs. Most TCEs are caused by instrumental artifacts and stellar variability. The remaining TCEs (usually a mix of planet candidates, eclipsing binaries and blended eclipsing binaries) are then passed on to the vetting stage, where they are examined in more detail. Typically, triage is performed by a human who visually inspects the light curve of each TCE and separates the signals that do not look remotely planet-like at first glance. There are usually a large number of TCEs to be triaged (a few thousand per *TESS* sector). Our neural network's triage mode, which we dub `AstroNet-Triage`, is designed to automate the triage process.

`AstroNet-Triage` serves to classify TCEs into "planet-like" (including PCs and EBs) and everything else. We find that the original `AstroNet` architecture works well for triage purposes, and that changing the architecture does not yield any significant improvement over the original model, so we make no modifications to the architecture in triage mode. We pass both the global and local views, described in Section 6.2.3, through separate convolutional columns before concatenating them in the fully connected layers. We reproduce this architecture in Fig. 6-2.

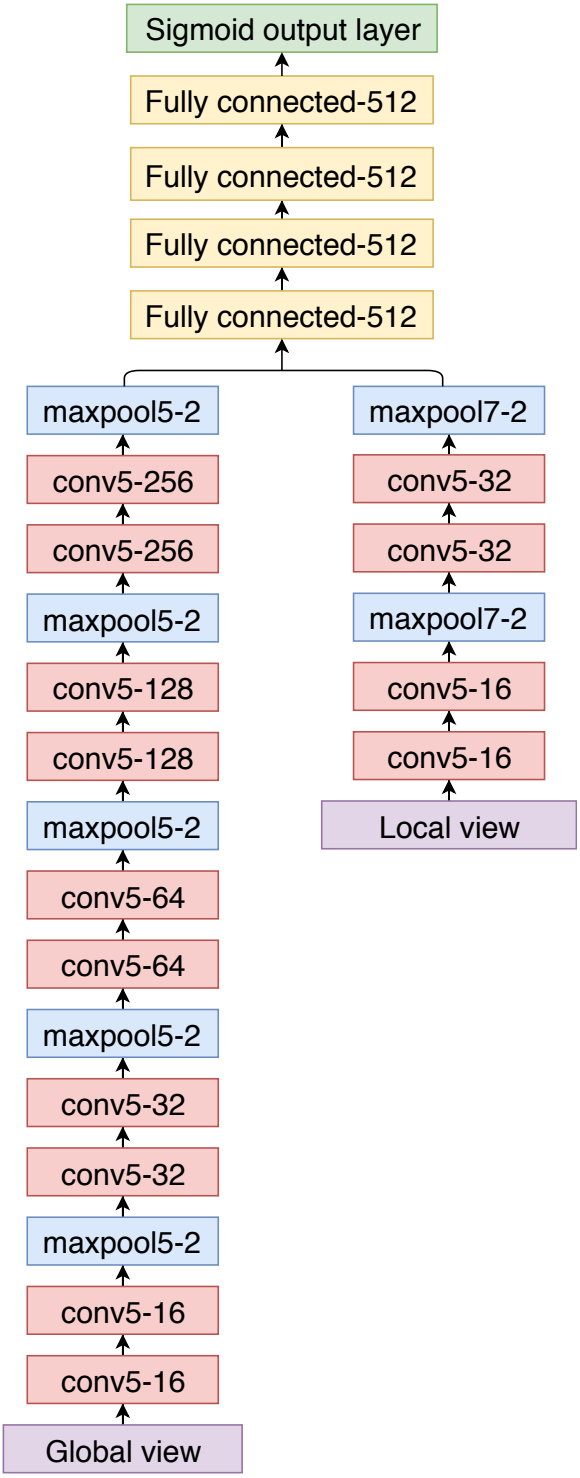

Figure 6-2 The architecture of `AstroNet-Triage` (identical to that of the best-performing neural network from Shallue & Vanderburg [253]). Convolutional layers are denoted conv<kernel size>-<number of feature maps>, maxpooling layers are denoted maxpool<window length>-<stride length>, and fully connected layers are denoted Fully connected-<number of units>.

6.3.1.2 Vetting Mode

When used for vetting, the model (dubbed `AstroNet-Vetting`) must also be able to distinguish EBs from PCs. Here we feed the global and local views to the neural network as we do in triage mode, but we also include a close-up of the most likely secondary eclipse (described in Section 6.2.3) in a disjoint convolutional column. In addition, we also concatenate a scalar feature to the outputs of the convolutional columns, namely the difference in transit depths measured in two apertures with radii of 2.75 and 3 pixels, divided by the out-of-transit standard deviation measured in the smaller aperture. We chose these two apertures because we find that they are generally large enough to encompass most of the flux from the target star, yet small enough to not include too much flux from background stars. The transit depths are estimated by fitting a box-shaped model to the light curves. This "depth change" feature is normalized by subtracting the mean of the entire training set and dividing by the standard deviation. The motivation behind adding a transit depth difference between different apertures is to help the model identify potential blends. When the source of a transit is off-target, a larger aperture typically produces a deeper transit than a smaller one. Transit depth differences are a simpler alternative to including the entire centroid time series, which Ansdell et al. [11] and Osborn et al. [216] used in their model. Also unlike Ansdell et al. [11] and Osborn et al. [216], we chose not to incorporate stellar parameters because a substantial fraction of our TCEs simply do not have stellar parameters available. This is because we search all stars in the FFIs, not just those selected for 2-minute-cadence observations. We also experimented with adding the *TESS* magnitude as a scalar feature, but its effect on the output is negligible. The architecture of the `AstroNet-Vetting` model is illustrated in Fig. 6-3.

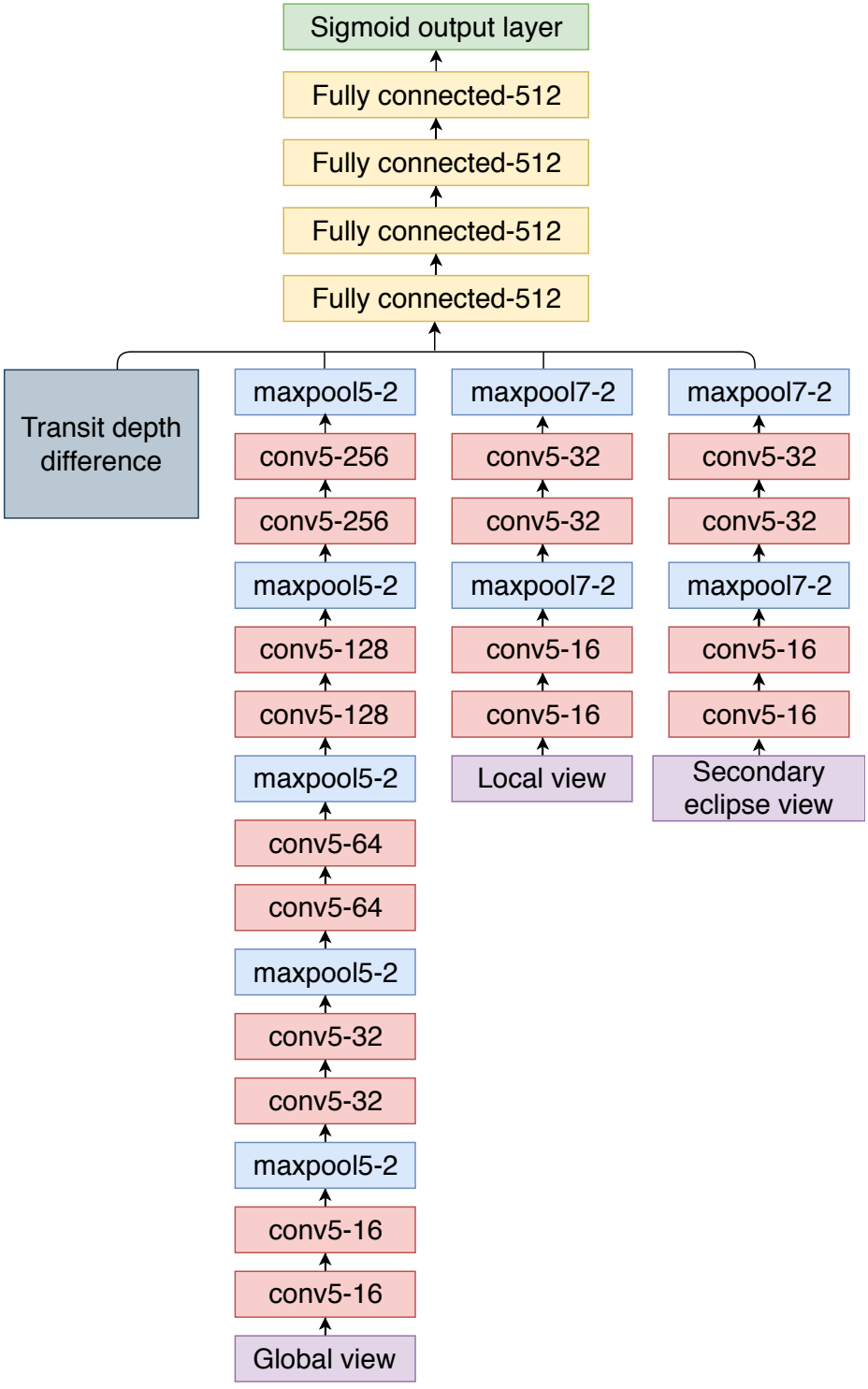

Figure 6-3 Same as Fig. 6-2, but for `AstroNet-Vetting`.

6.3.2 Training

We trained the model for 14,000 steps on the training set in both the triage and vetting modes. We used the Adam optimization algorithm [154] to minimize the cross-entropy error function over the training set. The number of training steps was chosen to minimize this error function over the validation set. During training, we augmented our training data by applying random horizontal reflections to the light curves with a 50% probability. This process generates similar but not identical samples with the same labels as the originals, thereby increasing the effective size of our training set and reducing the risk of overfitting. We trained the model with a batch size of 64, a learning rate of $\alpha = 10^{-5}$, and exponential decay rates of $\beta_1 = 0.9$, $\beta_2 = 0.999$ and $\epsilon = 10^{-8}$ (for more details on these parameters, see [154]).

Like Shallue & Vanderburg [253], we also make use of "model averaging" to improve the robustness of our predictions. We trained 10 independent, randomly initialized copies of the same model and used the average outputs of all copies for all predictions. Each copy may perform better or worse in different regions of parameter space due to its random parameter initialization, but model averaging averages over these differences. It also minimizes the stochastic differences that exist between individual models, thus making different configurations more comparable.

6.4 Evaluation of Neural Network Performance

We assess the performance of our neural network using the test set, the 10% of TCEs that were randomly left out of the training/validation sets and were thus not used to tune the model or its hyperparameters. Given the highly imbalanced nature of our training set, accuracy - the fraction of TCEs that the model correctly classified - is not a very useful measure of the model's performance, because we can achieve high accuracy simply by classifying everything as negative (not planet-like). The same can be said of the AUC (area under the receiver-operator characteristic curve, equivalent to the probability that a randomly selected positive is assigned a higher prediction than a randomly selected negative). We therefore make use of three additional met-

rics: precision (reliability), recall (completeness) and average precision. Precision is defined as the fraction of all objects classified as positives that are indeed true positives. Recall is defined as the fraction of all positives in the test set that were correctly classified as positives. There is a trade-off between precision and recall depending on the classification threshold (the score above which we consider an object to be a positive): increasing the threshold typically raises the precision while lowering the recall, and vice versa. Average precision is the weighted mean of precisions achieved at each threshold, with the increase in recall from the previous threshold used as the weight.

In Fig. 6-4, we show the precision-recall (PR) curves for triage and vetting on our test set. Each point on a curve corresponds to the precision and recall values for that model at a different choice of classification threshold. For `AstroNet-Vetting`, we also plot separate PR curves for the original `AstroNet` model architecture and models with the two new features added individually to show the impact of each on model performance. Table 6.1 shows the accuracies (calculated for a classification threshold of 0.5), AUC, and average precisions achieved by all of these models on the test set. As mentioned earlier, the models can achieve very high accuracy and AUC in vetting mode and yet still struggle to produce a reliable planet sample.

Table 6.1 Ensembled results achieved on the test set

Model	Accuracy	AUC	Average precision
Triage	0.974	0.992	0.970
Vetting - `AstroNet` plain	0.977	0.973	0.605
Vetting - depth change	0.978	0.980	0.669
Vetting - secondary eclipse	0.976	0.978	0.642
Vetting - depth change + secondary eclipse	0.978	0.984	0.693

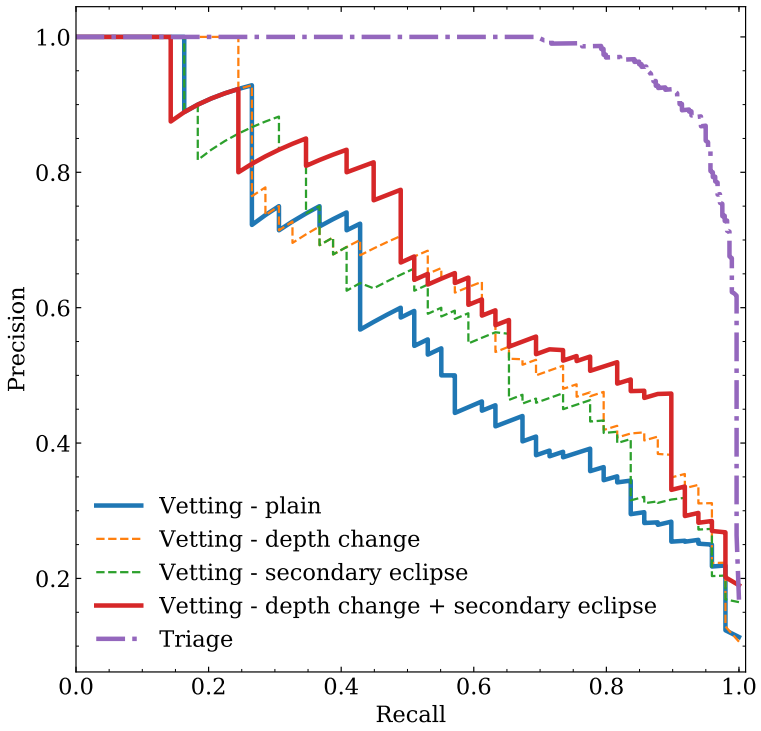

Figure 6-4 Precision-recall curve of our neural network in both triage and vetting modes. The triage model is trained to distinguish PCs and EBs from obvious false positives, and the vetting model is trained to identify only PCs. The line labeled "vetting - plain" shows the original `AstroNet` model applied to vetting without the addition of any new features. The two dashed lines show the individual contributions of new features we added: "vetting - depth change" is the addition of transit depth differences alone, and "vetting - secondary eclipse" is the addition of secondary eclipse views. "Vetting - depth change + secondary eclipse" is the final `AstroNet-Vetting` model that combines both features.

We can also visualize the results in a different way. Fig. 6-5 shows a histogram of predictions given by the model to our test sets. The prediction loosely represents the probability that the model considers a given TCE to be a "positive", meaning either a PC or EB in triage mode, or a PC in vetting mode. The color of each bar corresponds to the fraction of TCEs in that bin that are truly positives: a yellow bin contains mostly TCEs that are positives, while a blue bin contains mostly negatives. A good classifier would assign high predictions to positives and low predictions to negatives, so as to produce a histogram with yellow bins on the right side and blue

bins on the left side. This is indeed what we see in both histograms.

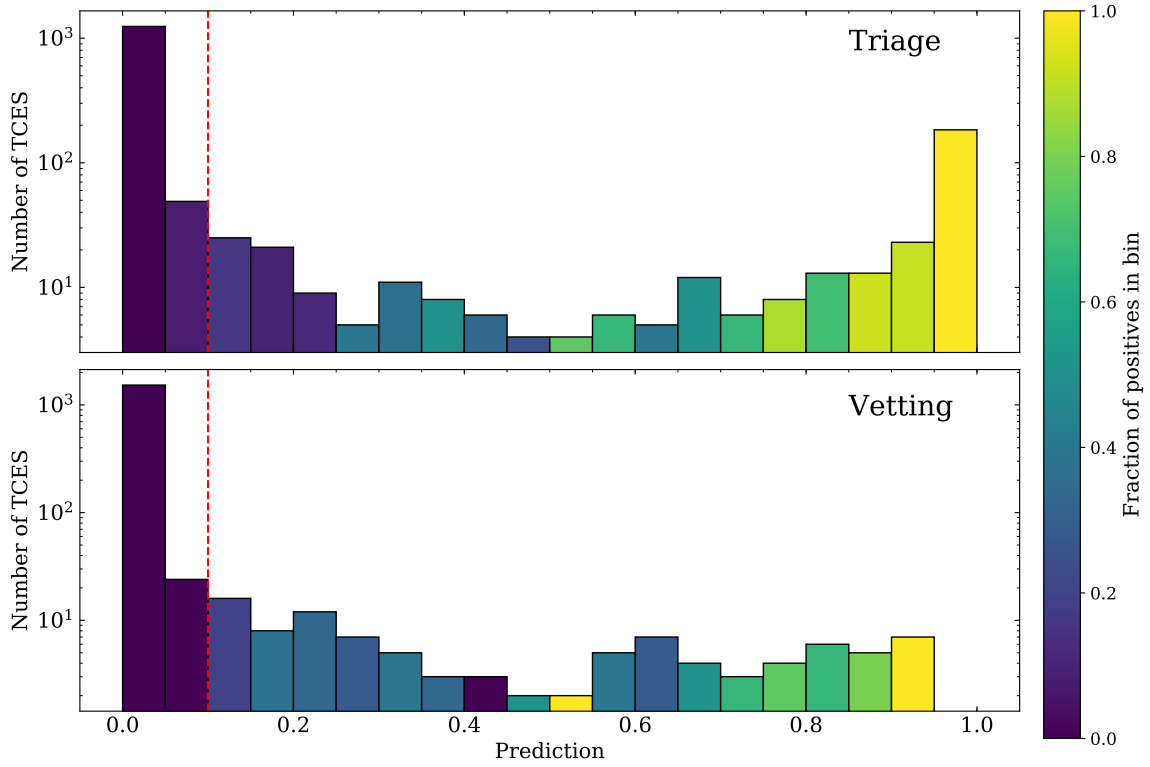

Figure 6-5 Histogram of predictions on the test set by `AstroNet-Triage` (top) and `AstroNet-Vetting` (bottom). The color of each bar represents the fraction of TCEs in that bin that are actually positives (PCs and EBs in triage mode, and just PCs in vetting mode). A yellow bin contains mostly TCEs that are positives, while a blue bin contains mostly negatives. The red dashed line marks a classification threshold of 0.1, which we find to maximize the fraction of false positives eliminated while still retaining almost all of the PCs.

`AstroNet-Triage` is already capable of achieving high precision and recall. Since the primary goal of triage is to cull the list of candidates while preserving most or all true PCs, we choose a classification threshold of 0.1 in order to discard only TCEs that the model is confident are false positives. With this classification threshold, we reach a precision of 0.749 and a recall of 0.975 on our test set of 1,650 TCEs. We recover all of the 49 PCs and the vast majority of EBs, while still eliminating 93% of the negatives. The model can therefore be used to automatically eliminate obvious false positives in a set of TCEs with a minimal loss of PCs, allowing human vetters to focus instead on the strong candidate planets. The MIT *TESS* Team has

already started using this model to perform triage on new TCEs from Sector 6 (see Section 6.5) and onward.

`AstroNet-Vetting`, on the other hand, is less successful and not ready to be used in production. A natural classification threshold for vetting would be 0.5, which would select only those TCEs that the model considers more-likely-than-not planets. However, we find that the vetting model has difficulty distinguishing some PCs from EBs: at a threshold of 0.5, we recover just 28 of the 49 PCs from the same test set with a precision of 0.651. Since *TESS* is a mission designed with follow-up in mind, we would rather retrieve as many PCs as possible at the expense of more false positives, which can be easily vetted out by follow-up programs. We therefore choose to evaluate our vetting model at the more conservative threshold of 0.1. At this threshold, we recover 44 of the 49 PCs with a precision of 0.449. Of the 5 missed PCs, three have systematics in their light curves that could have been mistaken for secondary eclipses, one is very V-shaped, and the last shows residual out-of-transit variability from imperfect detrending. 54 of the 69 false positives are EBs. A visual examination of the input representations of these misclassified EBs reveals that most do not have visible secondary eclipses nor exhibit significant changes in eclipse depth with aperture size. Most of these objects received EB labels during the initial inspection because they had odd-even transit differences or had synchronized out-of-transit variability that was later removed during detrending. These features are not captured in our input representation, so the model lacks sufficient information to distinguish these particular EBs from PCs. We discuss several ideas for improving the input representation in Section 6.6. The inability of the vetting model to separate EBs from PCs may also be due to the small number of PCs present in the training set. With the addition of new PCs from later *TESS* sectors, the model's performance in vetting mode may continue to improve. Still, our current results and success in triage mode indicate that our approach to automated vetting is a promising one.

We note that even though `AstroNet-Vetting` cannot replace human vetting in its current state, and may never be able to do so completely, it can serve as a valuable complement to human vetting. This can help neutralize the shortcomings in both

human and machine vetting. For example, it is difficult for human vetters to maintain a constant set of criteria when judging potential planet candidates, but machine learning can assign dispositions in a self-consistent, unbiased manner. On the other hand, a neural network can only detect patterns it was trained to detect. Unusual and interesting astrophysical signals that humans would recognize, such as WD 1145+017 b [287] and KIC 8462852 [42], would likely be classified as IS or V and discarded by neural networks. It would be useful to compare lists of PCs produced by humans and neural networks.

6.5 Application to Previously Unseen TCEs

TESS finished observing Sector 6 on Jan 7, 2019. We directly applied the trained `AstroNet-Triage` model to 59,719 new TCEs with the strongest BLS signals from Sector 6. Among these, 11,895 TCEs received a triage score of 0.1 or higher. We manually examined a random subset of 3,177 TCEs with triage scores of 0.1 or higher, and *TESS* magnitudes brighter than 12. Among these, we labeled 2,223 as EBs, 415 as PCs and 539 as IS or V. So if we accept these manually assigned labels as the ground truth, the precision of our model is 0.83 at a threshold of 0.1. Therefore our model is able to successfully eliminate a large number of false positives from Sector 6 TCEs, despite being trained on previous sectors that may have different systematics. It is worth noting that Sector 6 also covers a different stellar population compared to Sectors 1-5: because of its proximity to the Galactic plane, there are more evolved and variable stars in Sector 6. That our model was able to attain a precision comparable to that from Sectors 1-5 indicates that the model generalizes well to previously unseen sectors. We are also starting to see similar systematics from sector to sector now, so once we have built up a large sample from data taken using the same pointing strategy, we may achieve an even better performance when extrapolating to future sectors.

Although `AstroNet-Vetting` is not quite ready to be used in production, we generated scores for the manually examined subset of 3,177 TCEs with `AstroNet-`

`Vetting` as a demonstration of what we can achieve with purely automated vetting at this stage. 700 of these TCEs received vetting predictions of 0.1 or higher, including 288 of the 415 PCs. Fig. 6-6 shows 25 TCEs with the highest PC class probabilities that were also labeled as PCs by humans. At first glance, these do not show any warning signs of being non-planetary in nature (e.g. V-shaped transits or synchronized stellar activity). Our experience with *Kepler*, *K2* and earlier *TESS* sectors leads us to believe that most of these are indeed planetary in nature, and can quickly be confirmed via follow-up observations. The transit properties from BLS for these TCEs and the remainder of the 273 highly ranked PCs are given in Table 6.2.

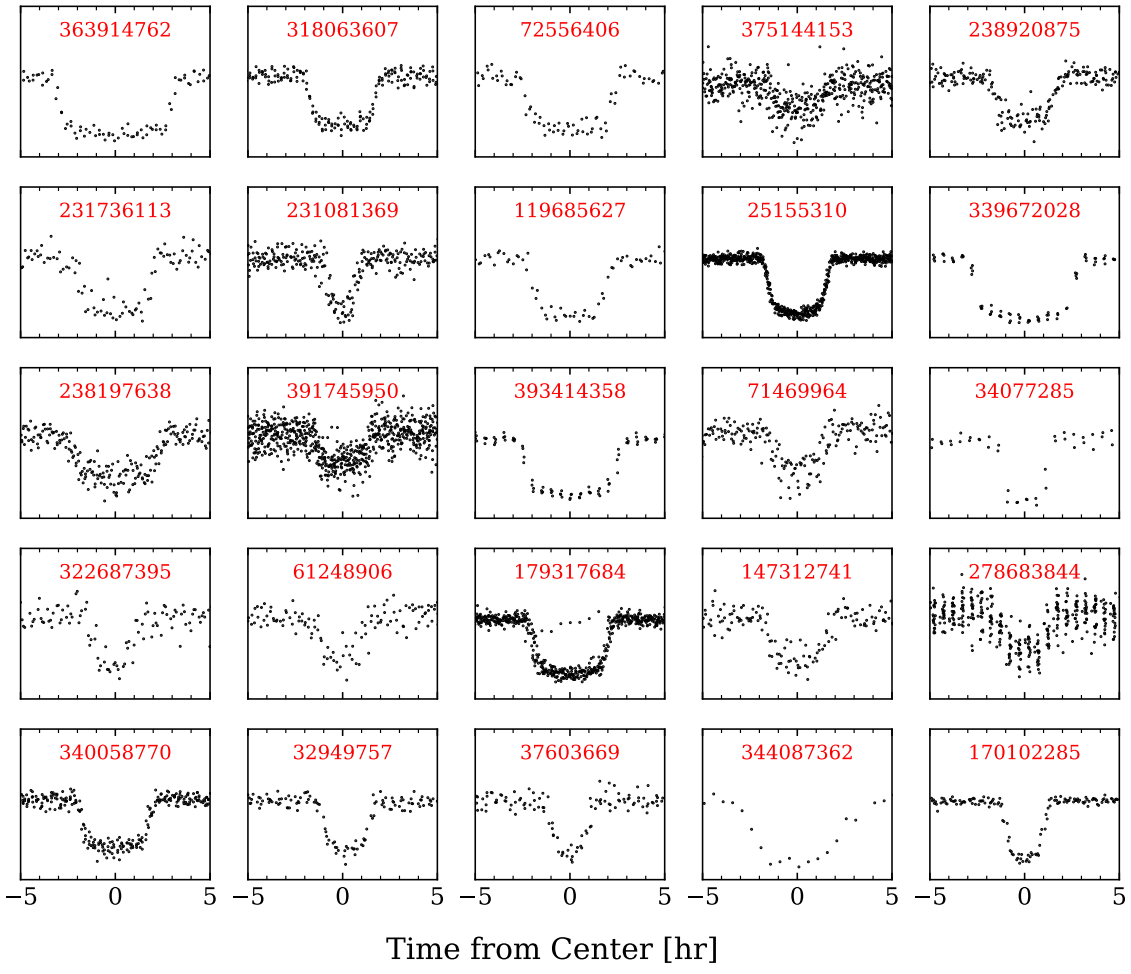

Figure 6-6 Phase-folded light curves of our 25 highest-quality planet candidates from Sector 6, along with their TIC IDs. To avoid clutter, we did not label the y-axis. Their transit parameters are listed in Table 6.2.

6.6 Future Work

`AstroNet-Triage` is already quite successful at distinguishing "planet-like" TCEs (PCs and EBs) from instrumental noise and stellar variability, but both `AstroNet-Triage` and `AstroNet-Vetting` have room for improvement going forward. We have identified a few ways to improve these models in the future:

- Currently, our training set only contains about $\sim 14,000$ TCEs, all of which are labeled by hand. It is therefore highly likely that there are some incorrectly labeled TCEs in the training set. Moreover, only ~ 500 of the TCEs are PCs. A larger, more accurately labeled data set would likely improve the performance of our model. Specifically, having more PCs on which to train should boost the accuracy of `AstroNet-Vetting`. One way to do this is to incorporate simulated transits injected into *TESS* light curves, but it is challenging to realistically simulate transit depth changes in different apertures, or to add simulated PCs with correct distributions of orbital periods and transit durations. If the simulated signals are sufficiently different from real PCs, including them may be detrimental to the model's performance. Future work may either explore how to accurately simulate TCEs, or retrain the model with new TCEs from future sectors.

- Ansdell et al. [11] showed that the inclusion of features such as stellar effective temperature, surface gravity, metallicity, radius, mass and density will likely improve our model's vetting accuracy. This is therefore a promising avenue for improving the model. In the future, we may amass a large enough sample of TCEs with stellar parameters from Gaia DR2 or the TIC to make this feasible.

- Including separate views of even- and odd-numbered transits may help `AstroNet-Vetting` identify eclipsing binaries with a true orbital period twice that reported by BLS and deep secondary eclipses present at phase 0.5.

- The interpolation method used to produce our input representations is not yet ideal. When generating binned views of light curves, we estimate the values of

empty bins by linearly interpolating over neighboring bins (see Section 6.2.3). This can distort the shapes of signals when there are large gaps in the data. A more intelligent interpolation method may be able to improve the model's performance. Alternatively, we could modify the model to take empty bins into account and avoid interpolation altogether.

Although our models currently only perform binary classification, they only require minor adjustments to perform multi-class classification. This may be of interest to researchers studying eclipsing binaries or stellar variability.

Table 6.2: New TCEs from Sector 6 with the highest likelihood of being planet candidates and manually assigned PC labels

TIC ID	Tmag	P [d]	T_0 [BJD$_{TDB}$ - 2457000]	Duration [hr]	Depth [ppm]	Triage prediction	Vetting prediction
363914762	10.931	13.862950	1445.332277	6.57	7490	0.894	0.935
318063607	11.591	1.972508	1470.574615	3.98	6900	0.994	0.93
72556406	10.763	5.564581	1470.665685	5.36	3590	0.976	0.926
375144153	11.611	3.349557	1328.947672	3.20	1370	0.989	0.913
238920875	11.740	6.534533	1326.067219	3.70	6610	0.935	0.911
231736113	11.371	10.576018	1414.601978	4.52	5180	0.798	0.906
231081369	11.686	7.632922	1329.841961	2.04	4880	0.968	0.906
119685627	11.396	5.033517	1472.754875	4.71	9400	0.97	0.899
25155310	10.555	3.288961	1327.516978	3.72	7020	0.996	0.894
339672028	9.370	10.330855	1387.669219	5.89	4580	0.893	0.89
238197638	11.729	7.276679	1355.883202	5.23	3270	0.945	0.89
391745950	11.078	2.429812	1327.492932	3.07	1630	0.991	0.889
393414358	10.417	4.374266	1469.700462	5.58	7210	0.994	0.886
71469964	9.543	2.048315	1468.865706	3.15	900	0.978	0.878
34077285	9.210	6.381659	1471.137677	2.93	3220	0.58	0.872
322687395	11.415	4.002862	1471.141177	2.32	4300	0.967	0.871
61248906	11.792	2.993511	1469.423987	2.64	3790	0.982	0.864
179317684	10.843	4.231651	1328.874103	4.67	7190	0.992	0.862
147312741	11.391	2.816972	1471.197891	3.57	3380	0.99	0.861
278683844	9.234	5.542128	1327.600005	3.01	480	0.829	0.861
340058770	11.874	2.758566	1385.912920	4.22	12690	0.996	0.857
32949757	11.927	3.767558	1468.974521	2.86	11620	0.939	0.847
37603669	11.584	2.969808	1468.864996	2.47	5020	0.99	0.845
344087362	10.030	13.962886	1481.818801	6.84	3740	0.922	0.845
170102285	11.682	2.941959	1470.667403	2.64	20280	0.982	0.844
349789882	11.301	10.016470	1329.628043	1.69	1980	0.84	0.842
443539530	11.158	2.719387	1470.030341	2.24	3290	0.97	0.832
52640302	11.988	1.572030	1469.592407	2.55	16770	0.996	0.83
235067594	11.276	8.296909	1438.933450	2.96	3750	0.892	0.826
34371411	10.938	3.881647	1472.485586	4.54	8780	0.99	0.82
172409263	9.995	2.111086	1469.560165	2.20	1140	0.974	0.816
317924729	11.067	1.998197	1468.957994	3.61	11510	0.993	0.816
255704097	10.585	6.014029	1470.980421	1.72	7740	0.86	0.815
49079670	9.875	1.891807	1470.207475	1.44	770	0.887	0.809
172464366	11.056	2.920137	1470.049317	3.17	14790	0.991	0.808
443452168	11.857	4.634948	1472.707943	9.59	6880	0.986	0.808
119170373	8.860	3.231364	1470.577387	1.65	1430	0.786	0.803
25250808	11.515	3.323634	1468.782982	5.80	13550	0.995	0.803
34466256	11.970	0.702749	1468.973241	1.20	2470	0.965	0.802
150098860	9.656	10.692789	1335.921402	2.54	570	0.881	0.801

Table 6.2: New TCEs from Sector 6 with the highest likelihood of being planet candidates and manually assigned PC labels (cont'd)

TIC ID	Tmag	P [d]	T_0 [BJD_{TDB} - 2457000]	Duration [hr]	Depth [ppm]	Triage prediction	Vetting prediction
322740947	11.883	1.750530	1470.221519	2.90	2120	0.987	0.799
172193428	10.328	2.939634	1470.250746	1.25	1940	0.89	0.798
38846515	10.307	2.849407	1326.744696	3.98	7730	0.998	0.797
63571763	11.979	3.657340	1470.778793	3.04	3820	0.986	0.791
79292541	9.373	2.275200	1470.742574	2.09	1490	0.946	0.79
167418898	10.179	10.979537	1335.776524	1.92	2680	0.925	0.783
157533118	11.733	2.519023	1470.833981	3.72	1510	0.782	0.776
317483660	11.494	3.331287	1471.200359	4.10	11740	0.983	0.771
54064834	11.495	6.057196	1470.396892	2.48	2960	0.92	0.768
156836699	10.463	5.175336	1473.410078	3.05	3100	0.949	0.763
201493205	10.619	4.063323	1472.533860	2.58	8260	0.97	0.757
142523514	11.701	2.920137	1470.496760	2.34	7970	0.963	0.754
339769761	11.442	4.604645	1386.570095	2.45	1520	0.949	0.752
21725655	11.641	4.015693	1439.318766	2.39	3970	0.974	0.748
67196573	10.729	2.556024	1469.400820	1.06	3280	0.689	0.734
35644550	9.453	5.430301	1469.685013	3.83	2060	0.931	0.733
139444326	11.474	3.526167	1440.702014	2.47	1300	0.641	0.732
61404104	10.698	4.116773	1469.622464	3.64	1280	0.984	0.732
63199675	10.425	2.833525	1470.244562	1.88	3530	0.954	0.723
279644164	11.495	7.441509	1469.869921	4.49	15190	0.95	0.718
200324182	10.342	1.297000	1411.750103	1.53	1890	0.991	0.716
97279976	11.547	1.530326	1469.171958	3.44	5560	0.996	0.713
172521714	11.279	3.831710	1470.174757	4.01	32160	0.99	0.712
350445771	10.998	3.190404	1326.799310	1.57	2850	0.967	0.711
317277995	11.873	2.433191	1470.987509	2.09	3610	0.92	0.708
279425357	11.544	9.017454	1358.154457	1.44	4120	0.52	0.703
279645722	10.369	2.220812	1469.322319	1.61	930	0.925	0.699
78953309	9.725	1.931130	1470.346593	2.60	560	0.923	0.698
38696105	10.482	5.577113	1326.104199	2.42	590	0.723	0.694
232038804	11.217	4.154500	1471.244532	2.12	8930	0.96	0.693
100589632	11.070	3.946770	1439.568240	1.81	1780	0.8	0.69
192831602	11.381	9.790579	1447.827549	5.09	7200	0.927	0.686
119544485	11.603	2.322156	1469.287125	2.93	1840	0.896	0.684
63572800	11.829	2.021734	1470.356296	3.22	38350	0.991	0.674
120165978	11.422	1.465310	1469.752267	3.06	2250	0.994	0.667
24887574	11.001	1.771662	1468.921754	2.17	1020	0.718	0.66
259701232	11.529	2.485701	1384.181439	3.18	4190	0.988	0.655
443369587	11.885	2.085436	1470.142533	1.34	9360	0.965	0.652
300116105	11.596	2.075595	1469.703864	1.42	3080	0.944	0.651
346316941	11.412	1.688926	1469.289457	1.40	5510	0.918	0.651
71728593	11.536	2.392378	1470.782565	2.53	13730	0.988	0.646

Table 6.2: New TCEs from Sector 6 with the highest likelihood of being planet candidates and manually assigned PC labels (cont'd)

TIC ID	Tmag	P [d]	T_0 [BJD_{TDB} - 2457000]	Duration [hr]	Depth [ppm]	Triage prediction	Vetting prediction
443164624	11.764	2.525427	1469.482256	1.91	2620	0.921	0.641
346574001	10.591	5.450762	1468.878060	3.64	820	0.699	0.641
149603524	9.716	4.412208	1326.074373	3.95	14710	0.996	0.64
200321330	11.143	1.815170	1411.405135	2.16	5130	0.987	0.635
220459826	11.762	2.239526	1355.728967	1.26	1040	0.549	0.632
124201045	11.899	7.157484	1474.437824	4.44	6760	0.85	0.631
288078795	9.347	2.055383	1469.367685	1.68	2690	0.971	0.63
147263084	11.743	0.614515	1468.868150	1.76	5660	0.956	0.624
350623356	11.469	2.871340	1328.054642	2.66	660	0.944	0.618
231969683	10.616	13.986153	1481.389627	3.54	13590	0.893	0.618
238129783	11.277	4.849406	1469.394608	2.00	1680	0.3	0.612
123742935	11.640	1.712055	1469.065779	1.81	2310	0.944	0.607
47911178	9.776	3.586105	1470.300149	2.83	11850	0.98	0.605
299742843	11.927	3.351131	1470.590447	1.89	8980	0.762	0.601
140691463	11.976	2.084444	1326.551771	2.26	12920	0.992	0.6
300146940	11.988	0.355657	1438.097487	1.31	5320	0.996	0.596
63665162	11.783	3.985532	1471.517260	2.55	9520	0.969	0.59
147977348	10.002	5.000113	1469.747290	3.51	6900	0.974	0.581
123898871	9.831	4.901942	1470.359873	4.29	12330	0.98	0.576
32925763	11.042	1.679960	1469.859626	1.45	2250	0.842	0.572
306477840	10.981	5.522099	1469.524965	3.78	9700	0.939	0.57
21725658	11.200	4.015693	1439.320057	2.48	2460	0.925	0.566
48242396	11.709	0.865599	1468.736100	1.67	1760	0.943	0.566
61341442	11.624	1.918690	1469.833807	3.79	2660	0.984	0.564
339958786	11.703	7.497688	1389.519061	3.64	16280	0.954	0.561
382626661	9.649	8.810778	1333.461016	3.79	280	0.712	0.553
30031594	11.588	4.806822	1330.384295	2.70	1300	0.856	0.55
142522973	11.821	7.097287	1473.393670	4.90	5790	0.969	0.54
146918469	11.984	3.523713	1469.853577	3.34	8590	0.971	0.539
200387965	11.673	0.550108	1411.443175	1.15	1300	0.979	0.536
157568289	10.341	1.840512	1468.735923	5.17	3010	0.996	0.529
443556801	11.266	1.508082	1470.123856	1.36	1550	0.7	0.523
443115550	11.067	2.924354	1469.496132	3.25	1800	0.925	0.52
97056348	11.956	2.898275	1471.068489	2.00	9330	0.949	0.518
52452979	11.803	12.540751	1472.832850	4.19	5160	0.817	0.509
32606889	11.585	4.684260	1440.937721	4.85	11120	0.987	0.502
124331723	11.956	1.403180	1469.811385	3.58	10520	0.995	0.502
35299896	11.809	7.057715	1470.284406	3.78	10120	0.734	0.499
49187106	11.953	1.712634	1468.924649	3.14	1510	0.789	0.498
14091704	9.136	0.764880	1438.420081	1.50	1900	0.995	0.493
382101339	11.739	0.268842	1325.740785	0.74	630	0.895	0.492

Table 6.2: New TCEs from Sector 6 with the highest likelihood of being planet candidates and manually assigned PC labels (cont'd)

TIC ID	Tmag	P [d]	T_0 [BJD$_{TDB}$ - 2457000]	Duration [hr]	Depth [ppm]	Triage prediction	Vetting prediction
130613909	11.924	2.240024	1470.162214	1.79	11610	0.954	0.483
349271454	11.575	0.716456	1325.793257	1.10	870	0.851	0.482
238926217	11.983	3.351340	1326.984089	2.16	1370	0.948	0.481
52639431	11.061	1.475015	1469.544384	2.18	3550	0.992	0.474
78669071	11.280	1.516892	1469.596999	2.26	2990	0.988	0.469
95418277	9.545	2.902560	1470.810932	3.41	460	0.808	0.465
427352241	9.969	1.264720	1468.823180	2.31	2360	0.992	0.46
33100834	11.332	5.741253	1473.985525	1.79	9060	0.841	0.459
33797807	11.376	7.446982	1468.788619	4.27	1730	0.714	0.459
35491505	11.987	2.714285	1471.002712	3.03	3080	0.979	0.458
119024411	11.095	0.973156	1469.121692	1.93	5860	0.992	0.456
232038798	11.275	4.154500	1471.244036	2.14	10810	0.902	0.456
260268672	11.066	2.199328	1326.994207	1.31	550	0.81	0.452
124493296	11.393	0.462865	1468.916825	1.65	3710	0.994	0.452
46312336	11.418	4.592904	1439.292303	1.76	1730	0.813	0.447
147478809	11.844	1.593514	1469.999134	2.70	3520	0.988	0.445
10001673159	11.388	2.091282	1326.962632	5.19	690	0.888	0.441
443129289	11.610	0.510670	1468.851587	1.56	3470	0.97	0.44
14092291	11.802	1.908158	1439.077233	2.72	12650	0.993	0.435
220397831	11.936	7.048540	1359.766935	11.43	810	0.924	0.434
349576483	11.856	0.259746	1325.701037	0.99	740	0.981	0.433
124106074	11.285	5.586068	1469.075132	4.38	6830	0.295	0.433
157661381	11.533	0.911638	1469.024954	2.17	1620	0.98	0.428
120544415	11.782	1.911447	1468.968402	3.25	4210	0.776	0.423
142468550	11.850	6.658610	1469.047725	3.37	5190	0.959	0.421
279322914	11.542	9.434735	1328.214438	6.12	21230	0.921	0.419
134198986	11.648	1.012970	1468.802921	1.57	4530	0.933	0.417
34366697	11.428	0.746141	1469.256947	1.83	5290	0.989	0.416
72490088	11.895	0.944827	1469.220860	2.55	1520	0.918	0.413
238082493	10.065	0.876523	1468.667915	1.91	1210	0.989	0.413
72580791	11.379	1.754168	1469.274700	2.21	1690	0.945	0.411
443115574	10.523	2.925198	1469.481622	2.73	1500	0.805	0.411
461840150	11.424	0.538105	1468.549807	1.02	1620	0.931	0.408
391745951	11.804	2.429695	1327.495315	3.14	1620	0.935	0.406
20178111	10.244	1.734102	1468.622076	2.18	2290	0.994	0.406
172308091	11.242	1.224808	1469.622611	2.57	1880	0.985	0.405
333340702	11.292	2.029839	1469.033238	2.32	1450	0.906	0.405
375090561	11.381	5.423940	1330.698602	3.15	2840	0.585	0.403
339733013	10.038	5.620686	1328.386377	2.52	550	0.709	0.403
63113815	10.432	1.738210	1469.892651	2.41	1590	0.986	0.401
79142467	10.751	1.003933	1468.769629	3.30	1500	0.988	0.393

Table 6.2: New TCEs from Sector 6 with the highest likelihood of being planet candidates and manually assigned PC labels (cont'd)

TIC ID	Tmag	P [d]	T_0 [BJD_{TDB} - 2457000]	Duration [hr]	Depth [ppm]	Triage prediction	Vetting prediction
157311499	11.142	2.010626	1470.124626	3.29	1050	0.744	0.392
49669244	11.763	1.708877	1469.344553	4.68	9240	0.995	0.392
30321299	11.105	3.864392	1327.954251	3.27	720	0.953	0.388
350274840	11.624	1.597868	1326.048299	2.33	3230	0.99	0.386
72090501	6.832	1.070700	1469.473875	2.16	3820	0.986	0.383
49379306	11.418	2.116823	1469.224144	3.94	3460	0.983	0.382
150437346	11.557	1.392659	1326.870639	2.05	7120	0.993	0.381
79941130	11.975	1.698273	1469.433447	3.58	1920	0.903	0.38
7420600	11.211	1.014010	1439.016749	2.30	2430	0.991	0.376
238197709	10.260	6.864081	1354.344756	2.86	4030	0.918	0.374
47711963	11.225	2.318965	1468.682246	1.68	1280	0.66	0.373
63665158	11.785	3.987102	1471.515918	2.81	9270	0.944	0.366
66915559	11.196	1.127067	1469.542826	3.45	3470	0.985	0.358
34196883	11.631	1.617181	1469.404646	3.54	8310	0.996	0.355
157129452	11.309	1.182573	1468.527976	3.32	1940	0.931	0.355
35582553	9.840	0.935488	1468.837040	1.73	1360	0.98	0.348
389920949	9.888	11.917522	1335.248973	3.96	5930	0.341	0.343
278775625	11.215	5.128430	1328.941195	2.19	670	0.746	0.342
421900585	11.449	6.903744	1472.660729	5.42	1990	0.873	0.339
219151731	10.086	1.485150	1438.985678	2.37	1120	0.971	0.33
443130801	10.576	2.169894	1470.664990	4.12	1270	0.942	0.326
130415266	7.281	13.473506	1481.792518	6.39	8360	0.941	0.324
35290793	10.970	0.280211	1468.827125	1.14	640	0.761	0.311
52324253	10.318	1.676432	1469.319684	2.21	2510	0.992	0.307
150186145	11.788	0.270739	1325.764847	0.93	2580	0.993	0.302
157041282	11.995	6.491574	1474.795888	2.70	9010	0.805	0.302
317548889	6.781	6.861642	1469.573795	3.75	230	0.488	0.301
78820372	10.373	0.812993	1469.265872	1.37	800	0.874	0.293
101144450	11.487	4.368986	1470.701150	2.17	1600	0.59	0.292
348995211	11.333	0.345693	1325.753557	1.34	2260	0.996	0.29
79682476	11.748	3.357798	1470.594351	4.10	1850	0.916	0.288
219421728	11.154	0.671078	1411.370168	1.65	3950	0.996	0.287
284288080	10.783	1.834544	1469.906630	2.99	970	0.593	0.284
30538087	11.740	4.136415	1355.799976	5.80	830	0.713	0.284
317022315	11.968	2.226672	1469.258933	4.81	4500	0.983	0.28
124323593	11.305	5.589151	1469.077755	4.23	5160	0.249	0.279
79139296	11.697	1.516437	1468.911918	2.44	1550	0.865	0.279
157404343	8.352	3.139683	1470.492164	3.63	450	0.972	0.271
172410994	11.392	0.453232	1468.691820	1.19	1490	0.795	0.268
346488066	10.601	0.834499	1469.438340	1.95	840	0.9	0.267
200326413	10.356	0.455446	1411.412194	1.07	900	0.975	0.266

Table 6.2: New TCEs from Sector 6 with the highest likelihood of being planet candidates and manually assigned PC labels (cont'd)

TIC ID	Tmag	P [d]	T_0 [BJD_{TDB} - 2457000]	Duration [hr]	Depth [ppm]	Triage prediction	Vetting prediction
52812339	11.831	5.513609	1473.895818	3.90	2000	0.611	0.266
32641207	11.536	0.407934	1438.509538	1.83	1710	0.992	0.265
48752342	10.087	1.614603	1469.310972	2.33	5170	0.985	0.263
35410741	11.047	1.049614	1469.351019	3.37	1130	0.954	0.262
156992575	10.520	0.486501	1468.795743	2.05	1180	0.991	0.259
52169698	10.885	0.622254	1468.530363	1.53	1300	0.979	0.257
157566468	11.288	1.067850	1468.617298	2.32	6830	0.992	0.257
443257841	11.943	2.697654	1471.092085	1.94	2700	0.543	0.257
47773319	11.797	0.693984	1468.691629	1.72	8850	0.993	0.257
231717034	10.771	2.198655	1384.483532	3.35	2440	0.229	0.248
388128308	11.955	1.194126	1325.815270	2.09	8620	0.993	0.246
31142436	11.714	5.271984	1440.303827	4.11	1080	0.453	0.245
35488933	11.880	2.173153	1469.109265	2.52	1730	0.696	0.245
388850377	11.094	2.467580	1469.295266	1.95	1040	0.577	0.245
34377352	11.594	7.142339	1469.185327	3.51	4860	0.828	0.243
287995512	11.938	0.938523	1468.930512	2.34	10560	0.965	0.242
34521303	11.848	1.891453	1469.549945	3.47	1660	0.743	0.24
220397824	11.379	7.049527	1359.742831	10.45	510	0.495	0.238
37770169	10.650	6.097314	1474.488281	3.85	1860	0.835	0.238
369517674	11.714	0.713896	1469.042390	2.15	1730	0.733	0.237
32643071	10.570	2.161556	1470.560955	3.85	1090	0.972	0.234
348995212	11.471	0.345693	1325.753438	1.34	2580	0.994	0.233
34790951	11.363	4.974178	1473.246406	3.85	5310	0.579	0.227
443451099	11.829	3.133377	1470.767509	3.70	6890	0.981	0.225
120540763	11.908	2.261481	1470.124763	3.31	2900	0.672	0.225
25413404	11.333	1.921603	1469.926743	4.07	4410	0.989	0.221
123457307	11.995	2.870472	1469.458499	4.63	14430	0.974	0.217
31852980	9.821	7.412709	1327.144736	4.09	350	0.203	0.214
33602950	10.780	0.816532	1468.952009	2.70	770	0.46	0.213
92845561	11.352	5.651537	1442.294869	3.08	1350	0.897	0.212
255588086	10.869	0.896959	1438.655066	1.80	2760	0.992	0.211
30848598	10.791	0.753911	1326.409307	3.29	570	0.974	0.211
79143083	10.314	1.503826	1468.975437	3.09	3170	0.993	0.208
120540056	11.158	1.522823	1469.819949	1.76	2560	0.959	0.207
124022931	11.994	5.589151	1469.072801	4.63	19330	0.83	0.206
48806546	11.074	0.932731	1468.802668	1.91	600	0.51	0.196
219205407	10.804	6.125959	1327.329607	1.82	34050	0.977	0.187
150066562	10.186	0.978050	1325.961256	1.11	420	0.404	0.185
63423599	10.661	1.185797	1469.632930	4.90	4070	0.997	0.184
147375101	10.741	1.586524	1469.185487	3.01	730	0.432	0.184
299655932	11.433	1.331064	1468.785574	1.76	1750	0.77	0.179

Table 6.2: New TCEs from Sector 6 with the highest likelihood of being planet candidates and manually assigned PC labels (cont'd)

TIC ID	Tmag	P [d]	T_0 [BJD_{TDB} - 2457000]	Duration [hr]	Depth [ppm]	Triage prediction	Vetting prediction
124097546	11.479	0.750065	1469.124751	1.85	1870	0.818	0.177
238192097	11.919	1.227093	1325.744153	2.20	24100	0.996	0.177
172409594	11.869	0.341709	1468.731897	1.33	2290	0.919	0.175
349483495	11.643	0.998846	1326.031092	2.31	7380	0.997	0.173
167714792	11.072	0.929267	1438.106543	1.58	1030	0.822	0.171
382302241	10.976	1.598020	1326.041226	2.40	2010	0.98	0.168
94989423	11.697	0.977006	1438.996675	1.11	1240	0.899	0.164
260708537	9.342	1.744675	1326.979158	1.26	190	0.566	0.16
333426440	11.379	2.423293	1470.386555	3.75	15780	0.99	0.157
404965758	11.854	0.663947	1326.128108	3.48	2000	0.973	0.155
143350974	11.608	1.081449	1439.142065	2.23	10260	0.98	0.154
34443859	11.583	1.676900	1469.862528	2.61	1800	0.789	0.154
349311188	11.291	5.608167	1326.174989	4.66	510	0.507	0.151
340797848	11.702	7.387224	1474.903044	5.04	4030	0.669	0.15
201508515	11.480	0.986094	1468.913865	1.71	1250	0.278	0.149
48176862	11.412	1.925622	1469.928224	4.17	20480	0.993	0.146
151628217	11.022	1.111059	1438.206509	2.38	9600	0.995	0.145
92880568	10.924	0.588447	1438.538668	1.40	3470	0.993	0.144
33002823	11.063	0.737931	1469.091985	1.96	1840	0.97	0.143
55272169	11.385	1.008285	1326.298004	1.93	430	0.68	0.141
260709785	11.896	1.156873	1325.754191	1.76	650	0.274	0.138
53823382	11.671	3.452825	1470.817027	4.69	7590	0.984	0.135
31109502	11.411	4.077800	1329.635600	3.44	520	0.731	0.134
31054498	9.879	1.411197	1439.448140	3.06	520	0.949	0.132
93123746	11.991	0.634459	1438.554379	3.70	1960	0.952	0.131
32050278	10.889	9.040116	1325.996384	3.51	6510	0.864	0.131
79439026	11.621	0.787574	1468.899673	2.00	4470	0.978	0.13
201369213	11.508	2.809158	1469.713993	3.63	10470	0.961	0.125
78672342	10.118	2.976792	1471.303365	3.44	910	0.872	0.123
25191560	9.787	2.150539	1469.403285	3.83	910	0.856	0.121
78956561	11.109	2.028213	1469.845112	4.02	930	0.321	0.12
393159572	10.821	1.403214	1469.733819	2.57	2490	0.991	0.119
123958679	11.426	5.589151	1469.074462	4.14	4210	0.164	0.119
238006656	11.314	0.877241	1354.366910	1.73	880	0.935	0.116
71917644	11.394	1.109653	1468.838374	2.67	1680	0.798	0.115
364395234	11.708	1.375841	1326.602612	2.70	7660	0.998	0.114
124543547	10.486	5.355631	1471.746463	7.07	3300	0.866	0.114
120027834	11.518	2.996169	1471.466335	3.66	2570	0.6	0.111
375032908	9.328	8.518659	1333.616043	3.21	530	0.26	0.11
143218704	11.692	1.857112	1469.812388	5.55	30850	0.997	0.106
317876382	10.966	2.150539	1470.621890	4.18	950	0.774	0.104

Table 6.2: New TCEs from Sector 6 with the highest likelihood of being planet candidates and manually assigned PC labels (cont'd)

TIC ID	Tmag	P [d]	T_0 [BJD_{TDB} - 2457000]	Duration [hr]	Depth [ppm]	Triage prediction	Vetting prediction
382068562	11.293	12.129942	1330.347472	2.15	16680	0.959	0.102
4616346	11.498	0.690059	1468.773630	1.77	1230	0.409	0.1

Chapter 7

Conclusion

In this thesis, my colleagues and I have discovered and characterized new giant planets using data from the *K2* space mission (see Chapters 4 and 5). These are valuable additions to the population of known giant planets, probing the regimes of low stellar irradiation, long periods, moderate eccentricity, and high stellar effective temperature. In Chapter 2, we have analyzed in detail and ruled out a potential young hot Jupiter caught in the middle of migration. We also developed methods and tools to facilitate the discovery of more transiting planets, including giant planets like these, in *K2* and *TESS* data. These methods have already been applied to the latest sectors of *TESS* data. My personal contribution to all of these projects includes the following:

- Performing aperture photometry on image-level data of PTFO 8-8695, removing systematics in light curves, fitting models to transit and occultation data, and carrying out statistical analyses to deduce the non-planetary nature of the object.

- Processing all raw *K2* photometry used in this thesis, producing light curves, and searching for threshold-crossing events with the Box Least Squares algorithm.

- Performing triage and vetting on *K2* light curves from Campaigns 10-17, including all of those used in Chapters 3-5, and training other team members to do so.

- Developing my own *K2* pipeline, which automatically extracts light curves from raw images and performs detrending with polynomial splines and Gaussian processes. This code later became part of the pipeline used to discover the planets in Chapters 4 and 5.

- Carrying out remote observations of PTFO 8-8695 (photometry) with the 1.2 m telescope at the Fred Lawrence Whipple Observatory, and on-site observations of EPIC 246851721 (Doppler tomography) with the Magellan Inamori Kyocera Echelle.

- Synthesizing and interpreting observational data presented in Chapters 4 and 5 to place our newly discovered planets into context.

- Modifying the original `AstroNet` model to work on *TESS* data, preparing data sets used in the training and testing of `AstroNet-Triage` and `AstroNet-Vetting`, determining the best-performing architectures for these models, and evaluating their performances.

This thesis also lays the foundation for some future work. The lists of candidates presented in Chapters 3 and 6 are good opportunities for follow-up. Since the publication of Chapter 3, a number of candidates from that paper have become the subjects of proposals to measure radial velocities and spin-orbit alignment. One has already been confirmed by radial velocity measurements to be a long-period ($P = 19.5$ days) sub-Saturn [57], and three more have been statistically validated [186]. The methods developed in Chapters 3 and 6 are easily generalizable to other missions dedicated to the detection of transiting exoplanets.

An exciting array of missions are currently underway or in the planning phases. *Kepler* and *K2*'s immediate successor, *TESS* [241], is among them. Launched in April 2018, *TESS* has already begun surveying nearly the entire sky in 28-day sectors, as discussed in Chapter 6. The planet hosts discovered by *TESS* will typically be 10-100 times brighter than those from *Kepler*, making follow-up easier and much more feasible. Indeed, *TESS* has already found a number of unusual and interesting

giant planets. For example, HD 1397b [214], a warm Jupiter on an 11-day orbit around a subgiant star, has a moderate eccentricity despite the lack of any observable planetary or stellar companions. HD 202772Ab [293] is one of the most strongly irradiated hot Jupiters known. Since it orbits an evolved star, its inflated radius may provide evidence supporting the "re-inflation hypothesis", which states that if class I mechanisms are responsible for giant planet inflation, planets that were not inflated during their host stars' main sequence lifetimes can inflate after the host stars become subgiants or giants, in response to rising levels of stellar irradiation [261, 188, 264]. TOI-172b [242] is a rare massive giant planet on an orbit with an eccentricity greater than 0.3, and helps constrain the migration pathways of close-in giant planets. Many of *TESS*'s new discoveries are also amenable to atmospheric characterization, which will allow us to understand the formation and migration mechanisms of these planets from a chemical perspective. The soon-to-be-launched *James Webb Space Telescope* (*JWST*), equipped with multiple infrared spectrographs, will offer a unique opportunity to study exoplanet atmospheres through transit spectroscopy [e.g. 25, 118].

In the near future, ESA will launch three more space missions: the *CHaracterising ExOPlanet Satellite* (*CHEOPS*; [45]) in 2019, the *PLAnetary Transits and Oscillations* (*PLATO*) mission [239] in 2026, and the *Atmospheric Remote-sensing Infrared Exoplanet Large-survey* (*ARIEL*; [232]) in 2028. Unlike *Kepler* and *TESS*, *CHEOPS* is the first mission dedicated to performing ultra-high precision photometry on bright stars already known to host planets, one star at a time. *CHEOPS* will be the most efficient instrument to measure accurate radii for planets in the super-Earth to Neptune mass range, spanning the mass regime in which core accretion is expected to start. *CHEOPS*'s measurements may provide some key insight into how giant planets form and grow. *PLATO*, on the other hand, will conduct a large-scale transit survey like *Kepler* and *TESS*. *PLATO* will target brighter stars than *Kepler*. Its dwell time is also longer than that of *TESS*, lasting from a few months up to three years, making it sensitive to long-period planets. Even though *PLATO*'s focus is on smaller, Earth-like planets, it will most likely discover a significant number of giant exoplanets around

the brightest nearby stars, including many prime candidates for further characterization through radial velocity, spectroscopy or asteroseismology [56]. *ARIEL* is also designed to observe transits of known planets. As the first large-scale survey of the chemistry of exoplanet atmospheres, *ARIEL* aims to characterize at least 1000 known planets using transmission spectroscopy. Undertanding the chemical compositions of planets' atmospheres will help answer fundamental questions about how planetary systems form and evolve.

This new generation of missions, combined with state-of-the-art ground-based telescopes, will provide us with many more giant planet samples in regions of parameter space that are relatively unpopulated today. For example, we currently have fewer than 10 long-period giant planets ($P \gtrsim 10$ days) available for atmospheric characterization, ~ 20 giant planets with $P \gtrsim 5$ days and measured stellar obliquities, and ~ 30 giant planets with irradiation levels below the radius inflation threshold of 2×10^8 erg s^{-1} cm^{-2}. But thanks to recent progress in instrumentation, we will soon be able to detect and study these currently underrepresented planets using the same techniques that have been honed for hot Jupiters.

Four hundred years ago, when Giordano Bruno speculated about the existence of other worlds, little could he have imagined that one day, humanity really would come to discover thousands of planets orbiting other stars in the universe, the majority of which have no analog in the Solar System. It was only two decades ago that we learned of the existence of planets around other stars. In merely twenty years, we have formed a much deeper understanding of planet formation and evolution, and of our place in the cosmos. I look forward to the new discoveries that the next twenty years will bring.

Bibliography

[1] Abadi, M., Agarwal, A., Barham, P., et al. 2016, arXiv e-prints, arXiv:1603.04467

[2] Adams, F. C., & Laughlin, G. 2006, ApJ, 649, 1004

[3] Addison, B. C., Tinney, C. G., Wright, D. J., et al. 2013, ApJ, 774, L9

[4] Albrecht, S., Winn, J. N., Marcy, G. W., et al. 2013, ApJ, 771, 11

[5] Albrecht, S., Winn, J. N., Johnson, J. A., et al. 2012, ApJ, 757, 18

[6] Alibert, Y., Mordasini, C., Benz, W., & Winisdoerffer, C. 2005, A&A, 434, 343

[7] Alonso, R., Brown, T. M., Torres, G., et al. 2004, ApJ, 613, L153

[8] Anderson, D. R., Hellier, C., Gillon, M., et al. 2010, ApJ, 709, 159

[9] Anderson, D. R., Triaud, A. H. M. J., Turner, O. D., et al. 2015, ApJ, 800, L9

[10] Angus, R., Aigrain, S., Foreman-Mackey, D., & McQuillan, A. 2015, MNRAS, 450, 1787

[11] Ansdell, M., Ioannou, Y., Osborn, H. P., et al. 2018, ApJ, 869, L7

[12] Armstrong, D. J., Pollacco, D., & Santerne, A. 2017, MNRAS, 465, 2634

[13] Arras, P., & Socrates, A. 2010, ApJ, 714, 1

[14] Assef, R. J., Gaudi, B. S., & Stanek, K. Z. 2009, ApJ, 701, 1616

[15] Auvergne, M., Bodin, P., Boisnard, L., et al. 2009, A&A, 506, 411

[16] Bakos, G., Noyes, R. W., Kovács, G., et al. 2004, PASP, 116, 266

[17] Barentsen, Geert; Cardoso, J. V. d. M. 2018, Kadenza: Kepler/K2 Raw Cadence Data Reader, Astrophysics Source Code Library, doi:10.5281/zenodo.344973

[18] Barnes, J. W. 2009, ApJ, 705, 683

[19] Barnes, J. W., van Eyken, J. C., Jackson, B. K., Ciardi, D. R., & Fortney, J. J. 2013, ApJ, 774, 53

[20] Batalha, N. M., Rowe, J. F., Bryson, S. T., et al. 2013, ApJS, 204, 24

[21] Batygin, K. 2012, Nature, 491, 418

[22] Batygin, K., & Adams, F. C. 2013, ApJ, 778, 169

[23] Batygin, K., Bodenheimer, P. H., & Laughlin, G. P. 2016, ApJ, 829, 114

[24] Batygin, K., & Stevenson, D. J. 2010, ApJ, 714, L238

[25] Beichman, C., Benneke, B., Knutson, H., et al. 2014, PASP, 126, 1134

[26] Bensby, T., Feltzing, S., & Lundström, I. 2003, A&A, 410, 527

[27] Bernstein, R., Shectman, S. A., Gunnels, S. M., Mochnacki, S., & Athey, A. E. 2003, in Proc. SPIE, Vol. 4841, Instrument Design and Performance for Optical/Infrared Ground-based Telescopes, ed. M. Iye & A. F. M. Moorwood, 1694–1704, doi:10.1117/12.461502

[28] Bhattacharya, A., Beaulieu, J.-P., Bennett, D. P., et al. 2018, AJ, 156, 289

[29] Bieryla, A., Collins, K., Beatty, T. G., et al. 2015, AJ, 150, 12

[30] Bodenheimer, P., Hubickyj, O., & Lissauer, J. J. 2000, Icarus, 143, 2

[31] Bodenheimer, P., Lin, D. N. C., & Mardling, R. A. 2001, ApJ, 548, 466

[32] Boley, A. C., Granados Contreras, A. P., & Gladman, B. 2016, ApJ, 817, L17

[33] Borucki, W. J. 2016, Reports on Progress in Physics, 79, 036901

[34] Borucki, W. J., Koch, D., Basri, G., et al. 2010, Science, 327, 977

[35] Borucki, W. J., Koch, D. G., Basri, G., et al. 2011, ApJ, 728, 117

[36] —. 2011, ApJ, 736, 19

[37] Bourrier, V., Lecavelier des Etangs, A., Hébrard, G., et al. 2015, A&A, 579, A55

[38] Bouvier, J., Chelli, A., Allain, S., et al. 1999, A&A, 349, 619

[39] Bouvier, J., Grankin, K. N., Alencar, S. H. P., et al. 2003, A&A, 409, 169

[40] Bouvier, J., Alencar, S. H. P., Boutelier, T., et al. 2007, A&A, 463, 1017

[41] Bovy, J. 2017, MNRAS, 470, 1360

[42] Boyajian, T. S., LaCourse, D. M., Rappaport, S. A., et al. 2016, MNRAS, 457, 3988

[43] Bradley, P. A., Guzik, J. A., Miles, L. F., et al. 2015, AJ, 149, 68

[44] Briceño, C., Calvet, N., Hernández, J., et al. 2005, AJ, 129, 907

[45] Broeg, C., Fortier, A., Ehrenreich, D., et al. 2013, in European Physical Journal Web of Conferences, Vol. 47, European Physical Journal Web of Conferences, 03005, arXiv:1305.2270

[46] Brown, D. J. A., Collier Cameron, A., Díaz, R. F., et al. 2012, ApJ, 760, 139

[47] Buchhave, L. A., Bakos, G. Á., Hartman, J. D., et al. 2010, ApJ, 720, 1118

[48] Buchhave, L. A., Latham, D. W., Johansen, A., et al. 2012, Nature, 486, 375

[49] Buchhave, L. A., Bizzarro, M., Latham, D. W., et al. 2014, Nature, 509, 593

[50] Burrows, A., Guillot, T., Hubbard, W. B., et al. 2000, ApJ, 534, L97

[51] Burrows, A., Hubeny, I., Budaj, J., & Hubbard, W. B. 2007, ApJ, 661, 502

[52] Burrows, A., Marley, M., Hubbard, W. B., et al. 1997, ApJ, 491, 856

[53] Burt, J., Holden, B., Hanson, R., et al. 2015, Journal of Astronomical Telescopes, Instruments, and Systems, 1, 044003

[54] Butler, R. P., Marcy, G. W., Williams, E., et al. 1996, PASP, 108, 500

[55] Castelli, F., & Kurucz, R. L. 2004, ArXiv Astrophysics e-prints, astro-ph/0405087

[56] Catala, C. 2009, Communications in Asteroseismology, 158, 330

[57] Chakraborty, A., Roy, A., Sharma, R., et al. 2018, AJ, 156, 3

[58] Chambers, J. E. 2006, ApJ, 652, L133

[59] Charbonneau, D., Brown, T. M., Latham, D. W., & Mayor, M. 2000, ApJ, 529, L45

[60] Choi, J., Dotter, A., Conroy, C., et al. 2016, ApJ, 823, 102

[61] Christiansen, J. L., Crossfield, I. J. M., Barentsen, G., et al. 2018, AJ, 155, 57

[62] Ciardi, D. R., Beichman, C. A., Horch, E. P., & Howell, S. B. 2015, ApJ, 805, 16

[63] Ciardi, D. R., van Eyken, J. C., Barnes, J. W., et al. 2015, ApJ, 809, 42

[64] Ciardi, D. R., Crossfield, I. J. M., Feinstein, A. D., et al. 2018, AJ, 155, 10

[65] Claret, A., Hauschildt, P. H., & Witte, S. 2012, A&A, 546, A14

[66] Clemens, D. P., Sarcia, D., Grabau, A., et al. 2007, PASP, 119, 1385

[67] Coşkunoğlu, B., Ak, S., Bilir, S., et al. 2011, MNRAS, 412, 1237

[68] Cody, A. M., Stauffer, J., Baglin, A., et al. 2014, AJ, 147, 82

[69] Coelho, P., Barbuy, B., Meléndez, J., Schiavon, R. P., & Castilho, B. V. 2005, A&A, 443, 735

[70] Collier Cameron, A., Guenther, E., Smalley, B., et al. 2010, MNRAS, 407, 507

[71] Collins, K. A., Kielkopf, J. F., Stassun, K. G., & Hessman, F. V. 2017, AJ, 153, 77

[72] Collins, K. A., Collins, K. I., Pepper, J., et al. 2018, AJ, 156, 234

[73] Coughlin, J. L., Thompson, S. E., Bryson, S. T., et al. 2014, AJ, 147, 119

[74] Coughlin, J. L., Mullally, F., Thompson, S. E., et al. 2016, ApJS, 224, 12

[75] Crossfield, I. J. M., & Kreidberg, L. 2017, AJ, 154, 261

[76] Crossfield, I. J. M., Petigura, E., Schlieder, J. E., et al. 2015, ApJ, 804, 10

[77] Crossfield, I. J. M., Ciardi, D. R., Petigura, E. A., et al. 2016, ApJS, 226, 7

[78] Crossfield, I. J. M., Guerrero, N., David, T., et al. 2018, ApJS, 239, 5

[79] Cutri, R. M., et al. 2012, VizieR Online Data Catalog, 2311

[80] Dai, F., & Winn, J. N. 2017, AJ, 153, 205

[81] Damasso, M., Esposito, M., Nascimbeni, V., et al. 2015, A&A, 581, L6

[82] Damiani, C., & Lanza, A. F. 2015, A&A, 574, A39

[83] Dattilo, A., Vanderburg, A., Shallue, C. J., et al. 2019, AJ, 157, 169

[84] Dawson, R. I., & Johnson, J. A. 2018, ARA&A, 56, 175

[85] Dawson, R. I., & Murray-Clay, R. A. 2013, ApJ, 767, L24

[86] Demory, B.-O., & Seager, S. 2011, ApJS, 197, 12

[87] Dodson-Robinson, S. E., & Bodenheimer, P. 2010, Icarus, 207, 491

[88] Donati, J.-F., Semel, M., Carter, B. D., Rees, D. E., & Collier Cameron, A. 1997, MNRAS, 291, 658

[89] Dong, S., Katz, B., & Socrates, A. 2014, ApJ, 781, L5

[90] Dotter, A. 2016, ApJS, 222, 8

[91] Dressing, C. D., Vanderburg, A., Schlieder, J. E., et al. 2017, AJ, 154, 207

[92] Eastman, J. 2017, EXOFASTv2: Generalized publication-quality exoplanet modeling code, Astrophysics Source Code Library, ascl:1710.003

[93] Eastman, J., Gaudi, B. S., & Agol, E. 2013, PASP, 125, 83

[94] Eastman, J., Siverd, R., & Gaudi, B. S. 2010, PASP, 122, 935

[95] Eggleton, P. P., Kiseleva, L. G., & Hut, P. 1998, ApJ, 499, 853

[96] Ehrenreich, D., Bonfils, X., Lovis, C., et al. 2014, A&A, 570, A89

[97] Fabrycky, D., & Tremaine, S. 2007, ApJ, 669, 1298

[98] Fabrycky, D. C. 2010, ArXiv e-prints, arXiv:1006.3834

[99] Fischer, D. A., Marcy, G. W., & Spronck, J. F. P. 2014, ApJS, 210, 5

[100] Fortney, J. J., Marley, M. S., & Barnes, J. W. 2007, ApJ, 659, 1661

[101] Fortney, J. J., Mordasini, C., Nettelmann, N., et al. 2013, ApJ, 775, 80

[102] Fu, G., Deming, D., Knutson, H., et al. 2017, ApJ, 847, L22

[103] Fulton, B., Blunt, S., Petigura, E., et al. 2017, California-Planet-Search/radvel: Version 1.0.4, doi:10.5281/zenodo.1127792

[104] Fulton, B. J., Weiss, L. M., Sinukoff, E., et al. 2015, ApJ, 805, 175

[105] Fulton, B. J., Petigura, E. A., Howard, A. W., et al. 2017, AJ, 154, 109

[106] Furész, G. 2008, PhD thesis, University of Szeged

[107] Furlan, E., Ciardi, D. R., Everett, M. E., et al. 2017, AJ, 153, 71

[108] Gaia Collab., Brown, A. G. A., Vallenari, A., et al. 2016, A&A, 595, A2

[109] —. 2018, A&A, 616, A1

[110] Gillen, E., Hillenbrand, L. A., David, T. J., et al. 2017, ApJ, 849, 11

[111] Gillon, M., Jehin, E., Magain, P., et al. 2011, in European Physical Journal Web of Conferences, Vol. 11, European Physical Journal Web of Conferences, 6002, arXiv:1101.5807

[112] Gillon, M., Anderson, D. R., Collier-Cameron, A., et al. 2013, A&A, 552, A82

[113] Goldreich, P., & Tremaine, S. 1980, ApJ, 241, 425

[114] Gould, A., Dong, S., Gaudi, B. S., et al. 2010, ApJ, 720, 1073

[115] Granzer, T., Schüssler, M., Caligari, P., & Strassmeier, K. G. 2000, A&A, 355, 1087

[116] Gray, D. F. 2005, The Observation and Analysis of Stellar Photospheres

[117] Gray, R. O., & Corbally, C. J. 1994, AJ, 107, 742

[118] Greene, T. P., Chu, L., Egami, E., et al. 2016, in Proc. SPIE, Vol. 9904, Space Telescopes and Instrumentation 2016: Optical, Infrared, and Millimeter Wave, 99040E, arXiv:1606.04161

[119] Grunblatt, S. K., Huber, D., Gaidos, E., et al. 2017, AJ, 154, 254

[120] Guillot, T., & Gautier, D. 2014, ArXiv e-prints, arXiv:1405.3752

[121] Guillot, T., & Showman, A. P. 2002, A&A, 385, 156

[122] Hamilton, C. M., Johns-Krull, C. M., Mundt, R., Herbst, W., & Winn, J. N. 2012, ApJ, 751, 147

[123] Hartman, J. D., & Bakos, G. Á. 2016, Astronomy and Computing, 17, 1

[124] Hartman, J. D., Bakos, G. Á., Bhatti, W., et al. 2016, AJ, 152, 182

[125] Hayward, T. L., Brandl, B., Pirger, B., et al. 2001, PASP, 113, 105

[126] Hebb, L., Collier-Cameron, A., Loeillet, B., et al. 2009, ApJ, 693, 1920

[127] Helled, R., & Bodenheimer, P. 2014, ApJ, 789, 69

[128] Hellier, C., Anderson, D. R., Collier Cameron, A., et al. 2009, Nature, 460, 1098

[129] Herbst, W., Herbst, D. K., Grossman, E. J., & Weinstein, D. 1994, AJ, 108, 1906

[130] Hirano, T., Nowak, G., Kuzuhara, M., et al. 2016, ApJ, 825, 53

[131] Hirsch, L. A., Ciardi, D. R., Howard, A. W., et al. 2017, AJ, 153, 117

[132] Høg, E., Fabricius, C., Makarov, V. V., et al. 2000, A&A, 355, L27

[133] Howard, A. W., Johnson, J. A., Marcy, G. W., et al. 2009, ApJ, 696, 75

[134] —. 2010, ApJ, 721, 1467

[135] Howell, S. B., Rowe, J. F., Bryson, S. T., et al. 2012, ApJ, 746, 123

[136] Howell, S. B., Sobeck, C., Haas, M., et al. 2014, PASP, 126, 398

[137] Huang, C. X., Shporer, A., Dragomir, D., et al. 2018, arXiv e-prints, arXiv:1807.11129

[138] Huang, C. X., Burt, J., Vanderburg, A., et al. 2018, ApJ, 868, L39

[139] Huang, X., Bakos, G. Á., & Hartman, J. D. 2013, MNRAS, 429, 2001

[140] Huang, X., Penev, K., Hartman, J. D., et al. 2015, MNRAS, 454, 4159

[141] Huber, D., Bryson, S. T., Haas, M. R., et al. 2016, ApJS, 224, 2

[142] Huber, D., Zinn, J., Bojsen-Hansen, M., et al. 2017, ApJ, 844, 102

[143] Husser, T.-O., Wende-von Berg, S., Dreizler, S., et al. 2013, A&A, 553, A6

[144] Ida, S., & Lin, D. N. C. 2004, ApJ, 604, 388

[145] Isaacson, H., & Fischer, D. 2010, ApJ, 725, 875

[146] Jackson, B., Barnes, R., & Greenberg, R. 2009, ApJ, 698, 1357

[147] Jehin, E., Gillon, M., Queloz, D., et al. 2011, The Messenger, 145, 2

[148] Johnson, J. A., Aller, K. M., Howard, A. W., & Crepp, J. R. 2010, PASP, 122, 905

[149] Kamiaka, S., Masuda, K., Xue, Y., et al. 2015, PASJ, 67, 94

[150] Kant, I. 1755, Universal Natural History and Theory of the Heavens

[151] Kelson, D. D. 2003, PASP, 115, 688

[152] Kelson, D. D., Illingworth, G. D., van Dokkum, P. G., & Franx, M. 2000, ApJ, 531, 159

[153] Kim, K. H., Watson, D. M., Manoj, P., et al. 2009, ApJ, 700, 1017

[154] Kingma, D. P., & Ba, J. 2014, CoRR, arXiv:1412.6980

[155] Kiseleva, L. G., Eggleton, P. P., & Mikkola, S. 1998, MNRAS, 300, 292

[156] Knutson, H. A., Benneke, B., Deming, D., & Homeier, D. 2014, Nature, 505, 66

[157] Knutson, H. A., Charbonneau, D., Allen, L. E., Burrows, A., & Megeath, S. T. 2008, ApJ, 673, 526

[158] Koch, D. G., Borucki, W. J., Basri, G., et al. 2010, ApJ, 713, L79

[159] Koen, C. 2015, MNRAS, 450, 3991

[160] Kolbl, R., Marcy, G. W., Isaacson, H., & Howard, A. W. 2015, AJ, 149, 18

[161] Kovács, G., Zucker, S., & Mazeh, T. 2002, A&A, 391, 369

[162] Kozai, Y. 1962, AJ, 67, 591

[163] Kraft, R. P. 1967, ApJ, 150, 551

[164] Kreidberg, L., Line, M. R., Thorngren, D., Morley, C. V., & Stevenson, K. B. 2017, ArXiv e-prints, arXiv:1709.08635

[165] Kreidberg, L., Bean, J. L., Désert, J.-M., et al. 2014, Nature, 505, 69

[166] Kurucz, R. L. 1992, in IAU Symposium, Vol. 149, The Stellar Populations of Galaxies, ed. B. Barbuy & A. Renzini, 225

[167] Lafrenière, D., Doyon, R., Marois, C., et al. 2007, ApJ, 670, 1367

[168] Lai, D. 2012, MNRAS, 423, 486

[169] —. 2014, MNRAS, 440, 3532

[170] Laplace, P.-S. 1796, Exposition du système du monde

[171] Lardner, D. 1853, Hand-book of Natural philosophy and Astronomy (Walton and Maberly, London)

[172] Lendl, M., Anderson, D. R., Collier-Cameron, A., et al. 2012, A&A, 544, A72

[173] Levison, H. F., & Stewart, G. R. 2001, Icarus, 153, 224

[174] Lewis, J. S. 1972, Icarus, 16, 241

[175] —. 1972, Earth and Planetary Science Letters, 15, 286

[176] —. 1974, Science, 186, 440

[177] Li, G., & Winn, J. N. 2016, ApJ, 818, 5

[178] Lidov, M. L. 1962, Planet. Space Sci., 9, 719

[179] Lieman-Sifry, J., Hughes, A. M., Carpenter, J. M., et al. 2016, ApJ, 828, 25

[180] Lillo-Box, J., Demangeon, O., Santerne, A., et al. 2016, A&A, 594, A50

[181] Lin, D. N. C., Bodenheimer, P., & Richardson, D. C. 1996, Nature, 380, 606

[182] Lin, Y., & Ogilvie, G. I. 2017, MNRAS, 468, 1387

[183] Lissauer, J. J., & Stevenson, D. J. 2007, Protostars and Planets V, 591

[184] Lissauer, J. J., Marcy, G. W., Rowe, J. F., et al. 2012, ApJ, 750, 112

[185] Livingston, J. H., Endl, M., Dai, F., et al. 2018, AJ, 156, 78

[186] Livingston, J. H., Crossfield, I. J. M., Petigura, E. A., et al. 2018, AJ, 156, 277

[187] Lomb, N. R. 1976, Ap&SS, 39, 447

[188] Lopez, E. D., & Fortney, J. J. 2016, ApJ, 818, 4

[189] Lucy, L. B., & Sweeney, M. A. 1971, AJ, 76, 544

[190] Mandel, K., & Agol, E. 2002, ApJ, 580, L171

[191] Mann, A. W., Gaidos, E., Vanderburg, A., et al. 2017, AJ, 153, 64

[192] Marcy, G. W., & Butler, R. P. 1992, PASP, 104, 270

[193] Marcy, G. W., Weiss, L. M., Petigura, E. A., et al. 2014, Proceedings of the National Academy of Science, 111, 12655

[194] Marigo, P., Girardi, L., Bressan, A., et al. 2008, A&A, 482, 883

[195] Mayo, A. W., Vanderburg, A., Latham, D. W., et al. 2018, AJ, 155, 136

[196] Mayor, M., & Queloz, D. 1995, Nature, 378, 355

[197] Mazeh, T., Perets, H. B., McQuillan, A., & Goldstein, E. S. 2015, ApJ, 801, 3

[198] McCauliff, S. D., Jenkins, J. M., Catanzarite, J., et al. 2015, ApJ, 806, 6

[199] McCullough, P. R., Stys, J. E., Valenti, J. A., et al. 2005, PASP, 117, 783

[200] McGinnis, P. T., Alencar, S. H. P., Guimarães, M. M., et al. 2015, A&A, 577, A11

[201] McLaughlin, D. B. 1924, ApJ, 60, 22

[202] Miller, N., & Fortney, J. J. 2011, ApJ, 736, L29

[203] Mislis, D., Bachelet, E., Alsubai, K. A., Bramich, D. M., & Parley, N. 2016, MNRAS, 455, 626

[204] Monnier, J. D., & Millan-Gabet, R. 2002, ApJ, 579, 694

[205] Mordasini, C., Alibert, Y., & Benz, W. 2009, A&A, 501, 1139

[206] Mordasini, C., Mollière, P., Dittkrist, K.-M., Jin, S., & Alibert, Y. 2015, International Journal of Astrobiology, 14, 201

[207] Morley, C. V., Fortney, J. J., Kempton, E. M.-R., et al. 2013, ApJ, 775, 33

[208] Morton, T. D. 2015, isochrones: Stellar model grid package, Astrophysics Source Code Library, ascl:1503.010

[209] Morton, T. D., Bryson, S. T., Coughlin, J. L., et al. 2016, ApJ, 822, 86

[210] Mullally, F., Coughlin, J. L., Thompson, S. E., et al. 2016, PASP, 128, 074502

[211] Naoz, S., Farr, W. M., Lithwick, Y., Rasio, F. A., & Teyssandier, J. 2011, Nature, 473, 187

[212] Ngo, H., Knutson, H. A., Hinkley, S., et al. 2016, ApJ, 827, 8

[213] Nielsen, E. L., & Close, L. M. 2010, ApJ, 717, 878

[214] Nielsen, L. D., Bouchy, F., Turner, O., et al. 2019, A&A, 623, A100

[215] Oelkers, R. J., Rodriguez, J. E., Stassun, K. G., et al. 2018, AJ, 155, 39

[216] Osborn, H. P., Ansdell, M., Ioannou, Y., et al. 2019, arXiv e-prints, arXiv:1902.08544

[217] O'Toole, S. J., Tinney, C. G., Jones, H. R. A., et al. 2009, MNRAS, 392, 641

[218] Pál, A. 2009, PhD thesis, Department of Astronomy, Eötvös Loránd University

[219] Paletou, F., Böhm, T., Watson, V., & Trouilhet, J.-F. 2015, A&A, 573, A67

[220] Parviainen, H., & Aigrain, S. 2015, MNRAS, 453, 3821

[221] Pearson, K. A., Palafox, L., & Griffith, C. A. 2018, MNRAS, 474, 478

[222] Pecaut, M. J., & Mamajek, E. E. 2013, ApJS, 208, 9

[223] Petigura, E. A. 2015, PhD thesis, University of California, Berkeley

[224] Petigura, E. A., Howard, A. W., & Marcy, G. W. 2013, Proceedings of the National Academy of Science, 110, 19273

[225] Petigura, E. A., Marcy, G. W., & Howard, A. W. 2013, ApJ, 770, 69

[226] Petigura, E. A., Schlieder, J. E., Crossfield, I. J. M., et al. 2015, ApJ, 811, 102

[227] Petigura, E. A., Howard, A. W., Lopez, E. D., et al. 2016, ApJ, 818, 36

[228] Petigura, E. A., Crossfield, I. J. M., Isaacson, H., et al. 2018, AJ, 155, 21

[229] Petrovich, C., & Tremaine, S. 2016, ApJ, 829, 132

[230] Pollacco, D. L., Skillen, I., Collier Cameron, A., et al. 2006, PASP, 118, 1407

[231] Pollack, J. B., Hubickyj, O., Bodenheimer, P., et al. 1996, Icarus, 124, 62

[232] Puig, L., Pilbratt, G. L., Heske, A., Escudero Sanz, I., & Crouzet, P.-E. 2016, in Proc. SPIE, Vol. 9904, Space Telescopes and Instrumentation 2016: Optical, Infrared, and Millimeter Wave, 99041W, doi:10.1117/12.2230964

[233] Rafikov, R. R. 2006, ApJ, 648, 666

[234] Raghavan, D., McAlister, H. A., Henry, T. J., et al. 2010, ApJS, 190, 1

[235] Rappaport, S., Barclay, T., DeVore, J., et al. 2014, ApJ, 784, 40

[236] Rappaport, S., Sanchis-Ojeda, R., Rogers, L. A., Levine, A., & Winn, J. N. 2013, ApJ, 773, L15

[237] Rappaport, S., Levine, A., Chiang, E., et al. 2012, ApJ, 752, 1

[238] Rasio, F. A., & Ford, E. B. 1996, Science, 274, 954

[239] Rauer, H., Catala, C., Aerts, C., et al. 2014, Experimental Astronomy, 38, 249

[240] Ribas, Á., Bouy, H., & Merín, B. 2015, A&A, 576, A52

[241] Ricker, G. R., Winn, J. N., Vanderspek, R., et al. 2014, in Proc. SPIE, Vol. 9143, Space Telescopes and Instrumentation 2014: Optical, Infrared, and Millimeter Wave, 914320, arXiv:1406.0151

[242] Rodriguez, J. E., Quinn, S. N., Huang, C. X., et al. 2019, arXiv e-prints, arXiv:1901.09950

[243] Rossiter, R. A. 1924, ApJ, 60, 15

[244] Ruan, S. C., Zhang, F., Zhu, Q., & Zhu, G. P. 2000, in SPIE Conference Series, Vol. 4087, SPIE Conference Series, ed. A. R. Lessard & G. A. Lampropoulos, 817R

[245] Sanchis-Ojeda, R., Winn, J. N., Holman, M. J., et al. 2011, ApJ, 733, 127

[246] Sanchis-Ojeda, R., Rappaport, S., Pallé, E., et al. 2015, ArXiv e-prints, arXiv:1504.04379

[247] Santerne, A., Moutou, C., Tsantaki, M., et al. 2016, A&A, 587, A64

[248] Santos, N. C., Israelian, G., & Mayor, M. 2004, A&A, 415, 1153

[249] Scargle, J. D. 1982, ApJ, 263, 835

[250] Schanche, N., Collier Cameron, A., Hébrard, G., et al. 2019, MNRAS, 483, 5534

[251] Schlaufman, K. C. 2010, ApJ, 719, 602

[252] Schlegel, D. J., Finkbeiner, D. P., & Davis, M. 1998, ApJ, 500, 525

[253] Shallue, C. J., & Vanderburg, A. 2018, AJ, 155, 94

[254] Shporer, A., Zhou, G., Fulton, B. J., et al. 2017, AJ, 154, 188

[255] Shporer, A., Wong, I., Huang, C. X., et al. 2019, AJ, 157, 178

[256] Sinukoff, E., Howard, A. W., Petigura, E. A., et al. 2016, ApJ, 827, 78

[257] Siverd, R. J., Pepper, J., Stanek, K., et al. 2009, in IAU Symposium, Vol. 253, Transiting Planets, ed. F. Pont, D. Sasselov, & M. J. Holman, 350–353, doi:10.1017/S1743921308026628

[258] Skrutskie, M. F., Cutri, R. M., Stiening, R., et al. 2006, AJ, 131, 1163

[259] Smith, A. M. S., Gandolfi, D., Barragán, O., et al. 2017, MNRAS, 464, 2708

[260] Socrates, A. 2013, arXiv e-prints, arXiv:1304.4121

[261] Spiegel, D. S., & Madhusudhan, N. 2012, ApJ, 756, 132

[262] Stassun, K. G., & Torres, G. 2018, ApJ, 862, 61

[263] Stauffer, J., Cody, A. M., McGinnis, P., et al. 2015, AJ, 149, 130

[264] Stephan, A. P., Naoz, S., & Gaudi, B. S. 2018, AJ, 156, 128

[265] Stevenson, K. B. 2016, ApJ, 817, L16

[266] Stevenson, K. B., Harrington, J., Fortney, J. J., et al. 2012, ApJ, 754, 136

[267] Struve, O. 1952, The Observatory, 72, 199

[268] Sullivan, P. W., Winn, J. N., Berta-Thompson, Z. K., et al. 2015, ApJ, 809, 77

[269] Suzuki, D., Bennett, D. P., Ida, S., et al. 2018, ApJ, 869, L34

[270] Swedenborg, E. 1734, Opera Philosophica et Mineralia

[271] Szabó, G. M., Pál, A., Derekas, A., et al. 2012, MNRAS, 421, L122

[272] Szabó, G. M., Szabó, R., Benkő, J. M., et al. 2011, ApJ, 736, L4

[273] Szentgyorgyi, A. H., & Furész, G. 2007, in Revista Mexicana de Astronomia y Astrofisica, vol. 27, Vol. 28, Revista Mexicana de Astronomia y Astrofisica Conference Series, ed. S. Kurtz, 129–133

[274] Thommes, E. W., Duncan, M. J., & Levison, H. F. 2002, AJ, 123, 2862

[275] Thompson, S. E., Mullally, F., Coughlin, J., et al. 2015, ApJ, 812, 46

[276] Thompson, S. E., Coughlin, J. L., Hoffman, K., et al. 2017, ArXiv e-prints, arXiv:1710.06758

[277] Torres, G., Fischer, D. A., Sozzetti, A., et al. 2012, ApJ, 757, 161

[278] Triaud, A. H. M. J., Collier Cameron, A., Queloz, D., et al. 2010, A&A, 524, A25

[279] Triaud, A. H. M. J., Martin, D. V., Ségransan, D., et al. 2017, A&A, 608, A129

[280] Tsiganis, K., Gomes, R., Morbidelli, A., & Levison, H. F. 2005, Nature, 435, 459

[281] Udalski, A., Paczynski, B., Zebrun, K., et al. 2002, Acta Astronomica, 52, 1

[282] Valenti, J. A., Butler, R. P., & Marcy, G. W. 1995, PASP, 107, 966

[283] Valenti, J. A., & Fischer, D. A. 2005, ApJS, 159, 141

[284] van Eyken, J. C., Ciardi, D. R., von Braun, K., et al. 2012, ApJ, 755, 42

[285] Van Eylen, V., Dai, F., Mathur, S., et al. 2018, MNRAS, 478, 4866

[286] Vanderburg, A., & Johnson, J. A. 2014, PASP, 126, 948

[287] Vanderburg, A., Johnson, J. A., Rappaport, S., et al. 2015, Nature, 526, 546

[288] Vanderburg, A., Latham, D. W., Buchhave, L. A., et al. 2016, ApJS, 222, 14

[289] Vanderspek, R., Huang, C. X., Vanderburg, A., et al. 2019, ApJ, 871, L24

[290] Villanueva, Jr., S., Gaudi, B. S., Pogge, R. W., et al. 2018, PASP, 130, 015001

[291] Vogt, S. S., Allen, S. L., Bigelow, B. C., et al. 1994, in Proc. SPIE, Vol. 2198, Instrumentation in Astronomy VIII, ed. D. L. Crawford & E. R. Craine, 362, doi:10.1117/12.176725

[292] Vogt, S. S., Radovan, M., Kibrick, R., et al. 2014, PASP, 126, 359

[293] Wang, S., Jones, M., Shporer, A., et al. 2019, AJ, 157, 51

[294] Weidenschilling, S. J., & Marzari, F. 1996, Nature, 384, 619

[295] Winn, J. N. 2010, Exoplanet Transits and Occultations, ed. S. Seager (University of Arizona Press), 55–77

[296] Winn, J. N., Fabrycky, D., Albrecht, S., & Johnson, J. A. 2010, ApJ, 718, L145

[297] Winn, J. N., Johnson, J. A., Peek, K. M. G., et al. 2007, ApJ, 665, L167

[298] Wolfgang, A., Rogers, L. A., & Ford, E. B. 2016, ApJ, 825, 19

[299] Wu, Y., & Lithwick, Y. 2011, ApJ, 735, 109

[300] Wu, Y., & Murray, N. 2003, ApJ, 589, 605

[301] Yi, S., Demarque, P., Kim, Y.-C., et al. 2001, ApJS, 136, 417

[302] Yu, L., Winn, J. N., Gillon, M., et al. 2015, ApJ, 812, 48

[303] Yu, L., Zhou, G., Rodriguez, J. E., et al. 2018, AJ, 156, 250

[304] Yu, L., Crossfield, I. J. M., Schlieder, J. E., et al. 2018, AJ, 156, 22

[305] Yu, L., Rodriguez, J. E., Eastman, J. D., et al. 2018, AJ, 156, 127

[306] Yu, L., Vanderburg, A., Huang, C., et al. 2019, arXiv e-prints, arXiv:1904.02726

[307] Zechmeister, M., & Kürster, M. 2009, A&A, 496, 577

[308] Zhou, G., Latham, D. W., Bieryla, A., et al. 2016, MNRAS, 460, 3376

[309] Zhou, G., Rodriguez, J. E., Vanderburg, A., et al. 2018, AJ, 156, 93

[310] Zucker, S., & Giryes, R. 2018, AJ, 155, 147